UNIVERSIDAD NACIONAL DEL LITORAL
Facultad de Bioquímica y Ciencias Biológicas
TECHNISCHE UNIVERSITÄT DRESDEN
Bereich Mathematik und Naturwissenschaften

Thesis presented as part of the requirements of the UNL and TUD to obtain the
Academic Degree Doctor in Biochemistry and Applied Biology
/
Doctor Rerum Naturalium

OPTIMISATION OF BIOTECHNOLOGICAL PROCESSES RELATED TO THE CULTIVATION OF MICROALGAE IN PHOTOBIOREACTORS FOR OBTAINING METABOLITES OF INDUSTRIAL INTEREST

Manuel Vicente Ibañez

Argentine Director: Prof. Dr. Josué Miguel Heinrich

German Director: Prof. Dr. Thomas Walther

Places of execution: Laboratorio de Operaciones y Procesos Biotecnológicos - FBCB - UNL - CONICET and Institut für Naturstofftechnick – ZINT - TU Dresden

-2022-

(Intentionally left empty page)

Acknowledgements

It is a great pleasure to express my gratitude and appreciation to Prof. Josué Miguel Heinrich and Prof. Thomas Walther for their supervision during my PhD work. Furthermore, much obliged to Prof. Günter Vollmer, Ms Katrin Simmank, Prof. Gabriela Micheloud, Prof. Adriana Ortolani, Prof. Elina Welchen and Prof. Carlos Brondino for their kind guidance over these last years in every step.

In addition, thanks to Dr Felix Krujatz and Dr Rodrigo Leonardi. You were the true pillars of this Thesis.

Thanks to Dr Marlen Zschaetzsch for having me in your thoughts across all the distance.

Also, I would like to thank CONICET and CUAA-DHAZ-DAAD for the financial support, the INTEC CCT Santa Fe, FBCB-UNL and ZINT for providing an excellent working place, and my colleagues from ZINT and GiiB.

In closing, I would further like to thank FBCB-UNL and TU Dresden for accepting me into their PhD program.

Lastly, thank you, Clara, for being breathtaking and kind to me daily.

Academic production during the thesis

- **Ibañez M. V.**, Leonardi R. J., Krujatz F., Heinrich, J. M. (2022). *The assessment of the real-time radiative properties and productivity of Arthrospira platensis in Tubular Photobioreactors*. Life MDPI. https://doi.org/10.3390/life12071014.
- **Ibañez M. V.**, Leonardi R. J., Steingroewer, J., Walther, T., Heinrich, J. M., Krujatz F. (2020). *A rapid assessment of the radiative properties from a suspension of Chromochloris zofingiensis*. Journal of Photochemistry and Photobiology. DOI 10.1016/j.jpap.2020.100007.
- **Ibañez M. V.**, Morelli M.N., Leonardi R. J., Irazoqui H., Heinrich J.M. (2019). *A colourimetric method for the measuring of the mass transfer kinetics of carbon dioxide in aqueous media*. Algal Research. DOI 10.1016/j.algal.2019.101717.

- Leonardi R. J., **Ibañez M. V.**, Morelli M. N., Heinrich J. M. (2022). *Evaluation of the phototrophic growth of Haematococcus pluvialis under outdoor lighting conditions inside a bubble column reactor at a laboratory scale*. Algal Research. DOI 10.1016/j.algal.2022.102800.
- Leonardi R. J., **Ibañez M. V.**, Morelli M. N., Irazoqui H. A., Heinrich J. M. (2021). *Laboratory-scale reproduction of lighting conditions for an outdoor vertical column photobioreactor: Theoretical fundamentals and operation of a programmable LED module. Algal Research*. DOI 10.1016/j.algal.2021.102227.
- Morelli, M., **Ibañez M. V.**, Leonardi R. J., Santiago L. G., Irazoqui H., Heinrich J. M. (2019). *Design of a biodegradable carrier for the application of controller bacteria on air–water interfaces*. Pest Manag Sci. DOI 10.1002/ps.5514.
- Leonardi R. J., **Ibañez M. V.**, Morelli M. N., Irazoqui H. A., Heinrich J. M. (2019). *Influence of light stratification on the growth of Scenedesmus quadricauda*. Biochemical Engineering Journal. DOI 10.1016/j.bej.2019.04.022.

Table of contents

Abbreviations and symbols

General and common abbreviations

3G	third-generation fuel
A	surface/area [m^2]
V	volume [m^3] [L]
A/V	area-to-volume ratio [m^{-1}]
ASTM	*American Society for Testing and Materials*
Car	carotenoid
CCAP	Culture Collection of Algae and Protozoa
REF	radiant energy field/light field
Chls, Chl *a*, Chl *b*	chlorophyll, chlorophyll *a*, chlorophyll *b*
RC	photosystem reaction centre
RTE	radiative transfer equation
PBR	photobioreactor
Fd	ferredoxin
HTL	hydrothermal liquefaction
LED	*Light-Emitting Diode*
LHC	light-harvesting complex
MC	Monte Carlo
PAR	*Photosynthetically Active Radiation*, $400 \leq \lambda \leq 700$ [nm]
PPFD	photosynthetic photon flux density [$\mu mol\ s^{-1}\ m^{-2}$]
PPF	photosynthetic photon flux [$\mu mol\ s^{-1}$]
PQ	plastoquinone
dw	dry weight
PS, PSI, PSII	photosystem, photosystem I, photosystem II
RuBisCO	Ribulose-1,5-bisphosphate carboxylase-oxygenase
UV	ultraviolet radiation
VIS	visible radiation, $400 \leq \lambda \leq 700$ [nm]
vvm	air volume per unit of liquid medium per minute

Chapter (1)

m_{CR}: Molar concentration of Cresol Red [moles L^{-1}].

m_i^0: Molar concentration of the i species at initial state [moles of i L^{-1}].

m_i : Molar concentration of the i species at non-equilibrium [moles of i L^{-1}].

$m_{NaOH,p}$: Molar concentration of the pulse of the strong base [moles L^{-1}].

A_i: Affinity of the i step reaction process [J $mole^{-1}$].

ε_i^*: Departure from the equilibrium of the i species. The superscript “*” is valid for a quantity which is not in equilibrium.

R: Ideal gas constant [mm Hg L $mole^{-1}$ K^{-1}].

a_{int}: Interfacial surface area per unit volume of the liquid phase.

$n_i^{(\alpha)}$: Mass of the i species present in phase α [moles of i].

$m_i^{(eq)}$: Molar concentration of the i species at equilibrium [moles of i L^{-1}].

x_i : Molar fraction of the i species.

$j_i^{(1\rightarrow 2)}$: Net mole flux density of the i species.

$L_{i,i}$: Onsager’s reciprocal coefficient of the i reaction step.

$P_{CO_2,g}^*$: Partial pressure of Carbon Dioxide during a transition to a new equilibrium state [mm Hg].

$P_{CO_2,g}^{(eq)}$: Partial pressure of Carbon Dioxide in an equilibrium state [mm Hg].

$\dot{\sigma}$: Rate of generation of internal Entropy [J $mole^{-1}$ K^{-1} min^{-1}].

r_i^*: Reaction rate of the i reaction occurring during the transition to a new equilibrium state [molar min^{-1}].

T: Temperature [° K].

k_i: Velocity constant of the forward i reaction.

k_{-i}:	Velocity constant the backward i reaction.
$V^{(1)}$:	Volume of the gaseous phase dissolved in the liquid phase [L].
$V^{(2)}$:	Volume of the liquid phase [L].
CO_2:	Carbon dioxide.
CO_3^{-2}:	Carbonate ion.
H^+:	Hydrogen ion.
H_2O:	Water.
$H_2PO_4^-$:	Dihydrogen phosphate ion.
H_3PO_4:	Phosphoric Acid.
HCO_3^-:	Bicarbonate ion.
HPO_4^{-2}:	Monohydrogen phosphate ion.
N_2:	Diatomic gaseous Nitrogen.
Na_2HPO_4:	Disodium monohydrogen phosphate.
NaH_2PO_4:	Sodium dihydrogen phosphate.
NaOH:	Sodium hydroxide.
O_2:	Diatomic gaseous Oxygen.
PO_4^{-3}:	Phosphate ion.

Chapter (2)

λ	wavelength [nm]
t	time [s]
θ	polar angle
φ	azimuth angle
μ	polar angle cosine θ, $\cos(\theta)$
N_λ	number of photons with wavelength λ [μmol]
n_λ	the radiation intensity of a photon beam with wavelength λ [μmol s^{-1} m^{-2} nm^{-1} sr^{-1}]
$\underline{\hat{\Omega}}$	unit vector describing the direction of motion
r	distance across surfaces that exchange radiant energy [m]
$\underline{r}$	position vector, describing the position of a particle
$\underline{\hat{n}}$	normal unit vector to a surface
c	the speed of light in vacuum [m s^{-1}]

h	Planck constant [Joule s]
$q_{\lambda,w}, q_{\lambda,f}$	spectral photon flux density [μmol s^{-1} m^{-2} nm^{-1}] or energy density [Joule s^{-1} m^{-2} nm^{-1}]
Q_{λ}	spectral photon flux [μmol s^{-1} nm^{-1}]
E_{θ}, E_{φ}	LED directional distribution function, in terms of the polar θ and azimuth φ angle
$E_{\lambda,w}(\lambda), E_{\lambda,f}(\lambda)$	LED spectral distribution function, in terms of energy or photons [nm^{-1}]
A_D	área of the detector (light sensor) [m^2]
$\underline{v}$	the position vector of a surface element over the light sensor
$\lvert\underline{v}\rvert$	vector modulus $\underline{v}$

Chapter (3)

t	time [s]
λ	wavelength [nm]
$\underline{\hat{\Omega}}$	unit vector describing the direction of motion
$\underline{r}$	position vector, describing the position of a particle
$\underline{\hat{n}}$	normal unit vector to a surface
θ	polar angle
φ	azimuth angle
μ	polar angle cosine, $\cos(\theta)$
N_{λ}	number of photons with wavelength λ [μmol]
n_{λ}	the radiation intensity of a photon beam with wavelength λ [μmol s^{-1} m^{-2} nm^{-1} sr^{-1}]
κ_{λ}	spectral absorption coefficient [mm^{-1}]
σ_{λ}	spectral scattering coefficient [mm^{-1}]
$B(\underline{\hat{\Omega}} \cdot \underline{\hat{\Omega}}')$	scattering phase function
$p_{\lambda,\underline{\hat{\Omega}}}(\underline{r}, \underline{\hat{\Omega}}, t)$	spectral local photon density of wavelength λ, and trajectory through the position $\underline{r}$ in the direction $\underline{\hat{\Omega}}$ [μmol m^{-3} nm^{-1} sr^{-1}]
$e_{\lambda}(\underline{r}, t)$	spectral local photon density of wavelength λ in the proximity of the position $\underline{r}$ [μmol m^{-3} nm^{-1}]

$r_\lambda(\underline{r},t)$	spectral local volumetric absorption rate of photons of wavelength λ [μmol s^{-1} m^{-3} nm^{-1}]
$n_\lambda(\underline{r},\underline{\hat{\Omega}},t)$	the radiation intensity of a photon beam with wavelength λ [μmol s^{-1} m^{-2} nm^{-1} sr^{-1}]
$q_\lambda(\underline{r},\underline{\hat{\Omega}},t)$	spectral photon flux density in the position $\underline{r}$ [μmol s^{-1} m^{-2} nm^{-1}]
δ	random number in the interval $0 \le \delta \le 1$
$E_{\lambda,f}(\lambda)$	LED spectral distribution function in terms of the number of photons [nm^{-1}]
$P(\theta), P(\varphi), P(\lambda)$	probabilities associated with the direction of the emitted photons and their wavelength λ
$\underline{\hat{e}}_i$	accessory unit vectors
n_i	the refraction index of the medium *i*
$\rho_{i,j}$	reflectivity in the interface between media *i* and *j*
$T_{i,j}$	transmissivity in the interface between media i and j
$P(A)$	probability of photon absorption
$P(D)$	probability of photon scattering
$P\ (NA, ND)$	probability of non-occurrence, either absorption or scattering
$S_{L,M}$	average free path
ΔS	photon step inside the suspension of microalgae

Chapters (4) and (5)

OP	optical/radiative property
r_{abs}:	local volumetric light absorption rate [μmol L^{-1} day^{-1}].
κ_λ:	absorption coefficient [mm^{-1}].
σ_λ:	scattering coefficient [mm^{-1}].
$\beta_{\theta,\lambda}$:	the scattering phase function.
$I'_\lambda\left(\underline{\hat{\Omega}}\right)$:	the spectral intensity [μmol s^{-1} nm^{-1} sr^{-1}].
$I'^{*}_\lambda\left(\underline{\hat{\Omega}}\right)$:	the spectral intensity of the sample [μmol s^{-1} nm^{-1} sr^{-1}].
$I^{R}_\lambda\left(\underline{\hat{\Omega}}\right)$:	the relative spectral intensity.

$I_\lambda^{R,*}\left(\underline{\hat{\Omega}}\right)$: the relative spectral intensity of the sample.

$\bar{I}_R\left(\underline{\hat{\Omega}}\right)$: the average spectral intensity in the PAR spectral range.

Q_λ: the total photon flux [μmol s^{-1}].

Q_λ^*: the total photon flux through the suspension [μmol s^{-1}].

$\left(Q_\lambda^*\right)_{GA}$: the total photon flux through the suspension (algorithm) [μmol s^{-1}].

$\left(Q_\lambda^*\right)_{EXP}$: the total photon flux through the suspension (experiment) [μmol s^{-1}].

$\left(\mu_n^*\right)_\lambda$: coefficient of the phase function [rad].

$\left(\overline{\mu}_n^*\right)_{PAR}$: averaged coefficient of the phase function in the PAR range [rad].

Abstract

Microalgae refer to distinct subsets of microscopic photosynthetic microorganisms that can grow autotrophically or heterotrophically. They are present in almost all bodies of water and many terrestrial environments, even in the most extreme ones. Due to their simple structure, they are more often than not highly efficient in fixing CO_2 and utilising solar energy for biomass production.

Biotechnology applied to microalgae cultivation is growing by leaps and bounds, as biomass composition can be adapted to specific purposes, most notably human food and energy supply, to ensure social security. Although microalgae are cultivated on an industrial scale, the yields and efficiencies achieved are far below the theoretical expectations and those obtained in the laboratory. Considering the extensive improvement achieved in the last two decades, numerous problems still need to be solved to achieve an efficient and cost-effective cultivation technology. Radiant energy is considered the most influential factor in the growth of photosynthetic organisms and is used as a parameter in the synthesis and scale-up stages of bioprocesses. In addition, given that CO_2 is the primary carbon source in autotrophic cultures of these microorganisms, it is of particular interest to understand the physicochemical processes involved in the trajectory of CO_2 molecules from the bubbles in contact with the growth medium to their fixation inside the cells.

In the present thesis, it has been proposed to study the effects of radiation's quality, quantity and distribution on the behaviour of microalgae suspensions in tubular photobioreactors. In particular, a commercial reactor for biomass production, which has a particular geometry, is analysed. Additionally, a method for analysing the mass transfer process of carbon dioxide is presented, flexible enough to be adapted to other media compositions or analogously designed media that resembles wastewater and other complex substrates. Special attention is devoted to the development of predictive tools, based on computational simulation and laboratory cultivation, of the performance of horizontal tubular geometry reactors since this technology is one of the most widely used for the cultivation of sensitive species or with applications for human food and pharmaceutical products

manufacturing. Possessing fast and accurate laboratory methodologies to estimate the productivity of microalgae strains in various reactors saves time and costs associated with the design, start-up and scale-up of bioprocesses.

Resumen

El termino microalgas nuclea a un conjunto de microorganismos microscópicos fotosintéticos que pueden crecer de manera autotrófica o heterotrófica. En general, debido a su estructura simple, son altamente eficientes en la fijación de CO_2 y la utilización de energía solar para la producción de biomasa. Se encuentran presente en todos los cuerpos de agua y en la mayoría de los ambientes terrestres, incluso en los más extremos.

La biotecnología aplicada al cultivo de microalgas crece a grandes pasos, producto de que la composición de la biomasa puede ser adaptada a fines específicos, entre los más destacados, alimentación humana y abastecimiento de energía para garantizar la seguridad social. Si bien se cultivan microalgas a escala industrial, las productividades y eficiencias alcanzadas se encuentran muy por debajo de las teóricas, y las obtenidas en laboratorio. Considerando el extenso desarrollo logrado en las últimas dos décadas, existen aún numerosos problemas cuya resolución es necesaria a fin de lograr una tecnología de cultivo eficiente y rentable. La energía radiante es considerada el factor más influyente en el crecimiento de organismos fotosintéticos, y es utilizada como parámetro en las etapas de síntesis y escalado de bioprocesos. Adicionalmente y dado que el CO_2 es la principal fuente de carbono en los cultivos autotróficos de estos microorganismos, es de especial interés profundizar en la forma de entender los procesos físico-químicos involucrados en la trayectoria de las moléculas de CO_2 desde las burbujas en contacto con el medio de crecimiento hasta su fijación en el interior de las células.

En la presente Tesis se propone estudiar los efectos de la calidad, la cantidad y la distribución de la radiación sobre la conducta de suspensiones de microalgas en fotobiorreactores. En particular, se analiza un reactor comercial de producción de biomasa, que cuenta con una geometría particular. Se dedica especial atención al desarrollo de herramientas predictivas, basadas en simulación computacional y cultivo en laboratorio, de la performance de reactores de geometría tubular horizontal, debido a que esta tecnología es una de las más ampliamente utilizadas para el cultivo de especies sensibles y/o con aplicaciones para la alimentación

humana y farmacéutica. Contar con metodologías de laboratorio rápidas y precisas, para estimar la productividad de cepas de microalgas en reactores varios, permite evitar gastos de tiempo y dinero asociados al diseño, puesta en funcionamiento y escalado de bioprocesos.

Zusammenfassung

Mikroalgen bezeichnen verschiedene Untergruppen mikroskopischer photosynthetischer Mikroorganismen, die autotroph oder heterotroph wachsen können. Sie kommen in fast allen Gewässern und vielen terrestrischen Umgebungen vor, sogar in den extremsten. Aufgrund ihrer einfachen Struktur sind sie in den meisten Fällen sehr effizient bei der CO2-Bindung und der Nutzung der Sonnenenergie für die Biomasseproduktion.

Die Biotechnologie, die bei der Kultivierung von Mikroalgen zum Einsatz kommt, entwickelt sich sprunghaft, da die Zusammensetzung der Biomasse an bestimmte Zwecke angepasst werden kann, vor allem an die menschliche Ernährung und die Energieversorgung, um die soziale Sicherheit zu gewährleisten. Obwohl Mikroalgen in industriellem Maßstab kultiviert werden, liegen die erzielten Erträge und Wirkungsgrade weit unter den theoretischen Erwartungen und den im Labor erzielten Werten. In Anbetracht der umfangreichen Verbesserungen, die in den letzten zwei Jahrzehnten erzielt wurden, müssen noch zahlreiche Probleme gelöst werden, um eine effiziente und kostengünstige Anbautechnologie zu entwickeln. Die Strahlungsenergie gilt als der einflussreichste Faktor für das Wachstum photosynthetischer Organismen und wird als Parameter in der Synthese- und Scale-up-Phase von Bioprozessen verwendet. Da CO2 die primäre Kohlenstoffquelle in autotrophen Kulturen dieser Mikroorganismen ist, ist es von besonderem Interesse, die physikalisch-chemischen Prozesse zu verstehen, die am Weg der CO2-Moleküle von den Blasen in Kontakt mit dem Wachstumsmedium bis zu ihrer Fixierung in den Zellen beteiligt sind.

In der vorliegenden Arbeit werden die Auswirkungen der Qualität, Quantität und Verteilung der Strahlung auf das Verhalten von Mikroalgensuspensionen in röhrenförmigen Photobioreaktoren untersucht. Insbesondere wird ein kommerzieller Reaktor für die Biomasseproduktion analysiert, der eine besondere Geometrie aufweist. Darüber hinaus wird eine Methode zur Analyse des Stofftransfers von Kohlendioxid vorgestellt, die so flexibel ist, dass sie an andere Medienzusammensetzungen oder analog gestaltete Medien angepasst werden kann, die Abwässern und anderen komplexen Substraten ähneln. Besonderes Augenmerk gilt der Entwicklung von Vorhersageinstrumenten für die Leistung

von Reaktoren mit horizontaler Röhrengeometrie auf der Grundlage von Computersimulationen und Laborkulturen. Diese Technologie ist eine der am häufigsten verwendeten für die Kultivierung empfindlicher Arten oder für die Herstellung von Lebensmitteln und pharmazeutischen Produkten. Schnelle und genaue Labormethoden zur Abschätzung der Produktivität von Mikroalgenstämmen in verschiedenen Reaktoren sparen Zeit und Kosten bei der Planung, Inbetriebnahme und dem Scale-up von Bioprozessen.

Introduction

(1). - “Algae”: Cyanobacteria and Microalgae

Algae are vital components of the marine environment and may significantly address worldwide strategical priorities. “Algae” is a common term used to address a group of photosynthetic micro- and macroorganisms composed mainly of three subsets: Cyanobacteria (prokaryotes), Micro- and Macroalgae (eukaryotes) [1]. Cyanobacteria, or the blue-green algae as they used to be referred to until 1974, are the oldest oxygenic photosynthesizers [2]. Further in time, with the appearance of the primitive eukaryotic microalgae via endosymbiosis of smaller photoautotrophs, they had a role in the creation of the earth’s oxidative atmosphere (enriched in O_2) in which we live. Cyanobacteria are the photosynthetic ancestors of plastids in Micro- and Macroalgae and plants [3]. About 50% of global primary photosynthetic productivity throughout their metabolism originates from algae. The latter corresponds to the yearly fixation of about 50 Gt of carbon dioxide (CO_2) into biomass and the release of about 80 Gt of O_2 in the atmosphere by these oxygenic beings [4]. In addition, many cyanobacteria can fix atmospheric N_2 into a biologically accessible form, thereby playing a pivotal role in the nitrogen cycle of the biosphere.

Macroalgae (or seaweeds) are also critical habitat-structuring species in coastal ecosystems, whereas microalgae, as phytoplankton, constitute the basis of the marine and aquatic food chain as the prime source of omega-3 fatty acids. From Phycology, various criteria are used for classifying these microorganisms related to their biochemical, cytological, ultrastructural and molecular characteristics. Nonetheless, there is no explicit agreement about to which of the three life domains the term “algae” belongs. Thus, it is accepted from ecology to interpret them as a functional group on the whole [5].

These photosynthetic microorganisms may be found, colonizing and spread in various locations, including fresh and salt water, rocks, deserts, and ice. The latter implies a remarkable adaptative capacity alongside the biosphere. Concerning their metabolism, they produce organic matter (biomass) from CO_2 (or other inorganic-carbon ionic forms), light, water and salts. Furthermore, they can be autotrophic or heterotrophic [6]. If they are autotrophic, they use inorganic compounds as their carbon source. Besides, they can be photoautotrophic if they use light as an energy source or chemoautotrophic when they oxidize inorganic compounds to obtain energy. Some photosynthetic algae can simultaneously use organic compounds supplied in the culture medium and light as an energy source, namely mixotrophic microorganisms.

The cultivation of photosynthetic microorganisms has represented an advance in basic science in numerous fields, such as evolution, genomics, physiology and diversity. An example of the latter is the recent developments in the study of photosystems' fluorescence [7]. In what to applied research concerns, the current trend topics point to the discovery and development of natural products from algae, with potential biotechnological and biomedical use [8]. Nevertheless, only a minor share of the naturally occurring algae species are exploited commercially [9].

From a global perspective, it has been argued that the rate of exploitation of new species is also hindered by administrative burdens, namely the need for any novel species to go through food regulation proceedings before it can be placed on the food market. The stakeholders from the algae industry claim that these procedures represent an expensive and time-consuming endeavour. Some of these species are already extensively cultivated at the industrial scale and have a well-established market.

The market value for these species at the moment is very much based on their potential as a source of high-value bioactive and functional compounds such as pigments (e.g., carotenoids such as β-carotene and fucoxanthin), anti-oxidants (e.g., astaxanthin, fucoxanthin), long-chain polyunsaturated omega-3 fatty-acids [e.g., docosahexaenoic acid (DHA), eicosapentaenoic acid (EPA)], phycobiliproteins (phycocyanin) and polysaccharides [10]. The most widely exploited species worldwide over the last decades for biotechnology applications in terms of the number of companies are *Chlorella spp.*, *Nannochloropsis spp.*, and *Haematococcus pluvialis* together with Spirulina (*Arthrospira*). Indeed, *Chlorella* and *Spirulina* are the most produced species in terms of dried algae volumes. Other species such as *Tetraselmis sp.*, *Tisochrysis lutea* (formerly *Isochrysis galbana*), *Dunaliella salina*, *Phaeodactylum tricornutum*, *Porphyridium sp.*, and *Scenedesmus sp.* are also among the top produced species.

The worth for microalgae biomass varies depending on several factors such as the production system, production costs (energy and workforce), geographical origin, certification schemes (e.g., organic production) and step of the value chain [e.g., Business to Business (B2B) or Business to Consumers (B2C)]. Based on consultation with algae producers, B2B values (on dry weight) for *Chlorella* sp. and

Spirulina (the two main species marketed for food and dietary supplements) vary between 25–50 € kg^{-1} and 30–70 € kg^{-1}, respectively [9]. In contrast, B2C values for both species range between 150 and 280 € kg^{-1} (higher values for small package sizes and finished products). For *Nannochloropsis* sp., the most relevant species for feed, B2B price values are in the range of 30–110 € kg$^{-1,}$ and B2C market value (as marine phytoplankton) can go up to 1000€ kg^{-1} [9]. Speciality algae, as well as algae used for the extraction of high-value products, are in a different price range. For example, *H. pluvialis* B2C price varies between 150 and 300 € kg^{-1} while the B2B price for astaxanthin oleoresin, based on pure astaxanthin, is in the range of 6.000–8.000 € kg^{-1} [11].

The emerging applications of microalgae biomass face an increasing market demand and still have room for a substantial increase in production volumes. Some of these will be covered at the end of this introductory part. However, further technological developments are needed to upscale the production volumes and reduce production costs, which can quickly turn biofuel production from microalgae biomass into a reality [12]. Over the past decade, algal biorefineries have been investigated as an approach to optimize the use of multiple feedstock components for different applications. In addition, if connected to other industrial infrastructures, the algae production plants can benefit from the associated resources (e.g., water, heat) and function as a source of additional services such as wastewater treatment [13]. This synergy is expected to reduce the costs and increase the environmental sustainability of microalgae production, but further research is needed on the optimization of such an approach.

Here, from an integral biotechnological perspective, it is possible to play a part in the generation of tools for designing, studying and improving the algae cultivation process. First and foremost, the following sections will present a brief summary of photosynthesis and carbon uptake, as these two essential processes are the pillars of the present thesis. Subsequently, an overview of the existing cultivation technology and potential uses for the produced biomass is also included. Last but not least, the objectives of the present work will be presented as an attempt to help bioprocess engineering in addressing some of the major concerns for cultivating cyanobacteria and microalgae in current times.

(2). - Oxygenic photosynthesis in prokaryotes and eukaryotes

Oxygenic photosynthesis started about 3 billion years ago when ancient cyanobacteria-like organisms evolved an apparatus capable of capturing and utilizing visible solar radiation (300–700 nm) [14]. By using electrons extracted from H_2O, the reduction of CO_2 to energy-rich carbohydrates with concomitant release of O_2 had become possible. It created an aerobic condition and the requisite background for developing and sustaining aerobic metabolism and more-advanced life forms [15].

Two membranes surround cyanobacterial cells: an outer one, which forms the cell wall (made of murein), and an inner one, the cytoplasmic membrane, which separates the cytoplasm from the periplasm. The latter also occurs for microalgal cells, although their major cell wall component is algaenan [16]. The light reaction of oxygenic photosynthesis takes place in the so-called thylakoid membranes that occur in pairs; the space between the pair is called the lumen, and the space between the two pairs is contiguous with the cytoplasm [17]. One of the major salient points between cyanobacteria and photosynthetic eukaryotes is that respiratory and photosynthetic redox-active protein complexes share a common thylakoid membrane in cyanobacteria. The thylakoid membrane in cyanobacteria does not form grana as it does in plants and algae. Contrarily, each process mentioned above in eukaryotic algae takes place within specialised organelles (plastids) like mitochondrion or chloroplasts.

Cyanobacteria show rapid growth in nature and under laboratory culture conditions; they owe a large part of their evolutionary success to their tremendous metabolic flexibility. The mechanism of oxygenic photosynthesis in cyanobacteria resembles that of oxygenic eukaryotes (algae and higher plants). This allows us to use cyanobacteria as a suitable model to study different aspects of oxygenic photosynthesis and its regulation, which is often challenging to study in higher plants or algae. Compared to the multicellular higher plant models, the simplicity of a single-cell system and relatively easy transformation techniques has also contributed to cyanobacteria becoming essential model systems to study responses to abiotic stress [18].

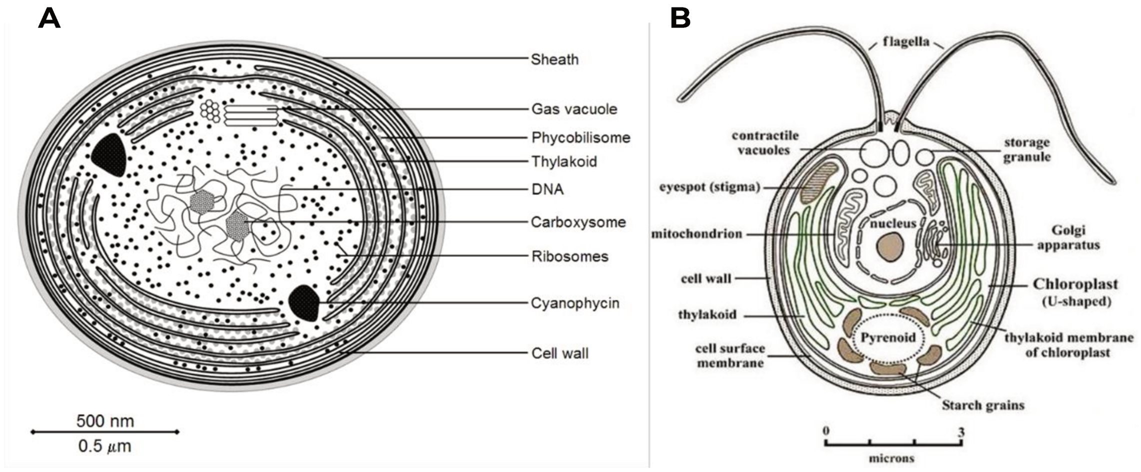

Figure (1.1). A] Simplified schematic of a cyanobacteria B] Simplified diagram of a eukaryotic microalga (redrawn from [4]).

Concerning the O_2-evolving apparatus and similar to all photosynthetic eukaryotic organisms, cyanobacteria share the use of three membrane-bound pigment-protein complexes acting as unique reaction centres (RCs): photosystems II (PS II), photosystem I (PS I), and the Cyt b6f complex [4]. Along with these pigment-protein complexes, the mobile electron carriers such as plastoquinone (PQ) and plastocyanin (PC) form the photosynthetic electron transport chain (PET), providing the required amount of energy to an ATP synthase complex. The latter implies light-induced electron transfer from H_2O to $NADP^+$ (the oxidized form of nicotinamide adenine dinucleotide phosphate); its reduced form, NADPH, is used to power the photophosphorylation of ADP to ATP and, ultimately, the synthesis of carbohydrates [19].

The photosynthetic process wholly depends on the interactive role of primary and accessory photosynthetic pigments (chromophores) present as accessory groups in proteins immersed in the thylakoid membranes and attached to the RCs, the so-called light-harvesting complexes (LHCs) [20]. LHCs are recognised as phycobiliproteins (PBPs) in cyanobacteria, red algae and cryptomonads, and antennae in the rest of the eukaryotic organisms. Independently of the microorganism type, these proteins alter the absorption properties of the chromophores (relative to their free state) and facilitate the transfer of the excitation energy of the absorbed photons (excitons) to a pigment complex of the CR, where the transformation of exciton energy into chemical energy takes place. The PBS/antennae act like a funnel, allowing a large surface area for photon collection in the service of the CR. The energy transport, called resonance excitation energy transfer (Förster), depends on the proximity of the pigments (10-100 Å), the orientation (dipole moments) and the excitation-emission levels of the donors and acceptors. Within the LHCs, the pigments that absorb higher energy photons (lower λ) are located in the most peripheral areas. This arrangement ensures that the energy transfer is unidirectional towards the CR. The average transfer time of an exciton to the CR is estimated to be of the order of 10^{-10} s, with an efficiency of 90%. Antenna pigments do not have the ability to release an e^- when absorbing a photon.

In cyanobacteria, three types of photosynthetic pigment content are present: First is chlorophyll *a* (major pigments); second is phycobiliproteins (PBPs: light-harvesting pigments); and third is the carotenoids (photoprotective nature) that protect the photosynthetic apparatus against adverse environmental factors [21]. Green eukaryotic algae and plants share similar chromophore families, except for the bilins. Among three photosynthetic pigments, chlorophyll is the leading light-harvesting pigment directly linked with photosynthetic organisms' healthiness and acts as a reaction centre and very sensitive pigment against adverse stress factors [22]. A decrease in the Chl content is directly linked with a reduction in the biomass content of photoautotrophs. Chlorophyll is an incredible photoreceptor because of its interconnecting single and double bonds, which allow the delocalization of electrons in their structure. This delocalization of electrons that permits polyene structures mediates light absorption from different bands of the visible spectrum of sunlight and initiates electron transport chain reaction.

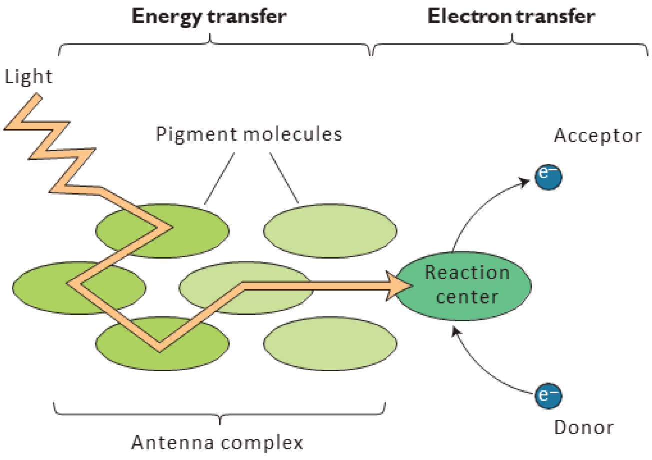

Figure (1.2). *Simplified diagram of the organisation of the photosynthetic apparatus of cyanobacteria and microalgae*. The light-harvesting complex act like a funnel, allowing a large surface area for photon collection in the service of the reaction centre (adapted from [23])

PBPs possess light-harvesting properties due to the presence of covalently attached chromophores called bilins, and these prosthetic groups mediate the absorption of light in the visible region where Chl *a* has minimal absorption. PBPs are classified into three significant categories: allophycocyanin (APC), phycocyanin (PC), and phycoerythrin (PE) [24], with characteristic spectra, referred to as blue-green (650–655 nm), blue (610–620 nm), and pink (540–570 nm), respectively. Among these three, Phycocyanin is the most common water-soluble protein with a hexameric conformation having a single chromophore named phycocyanobilin.

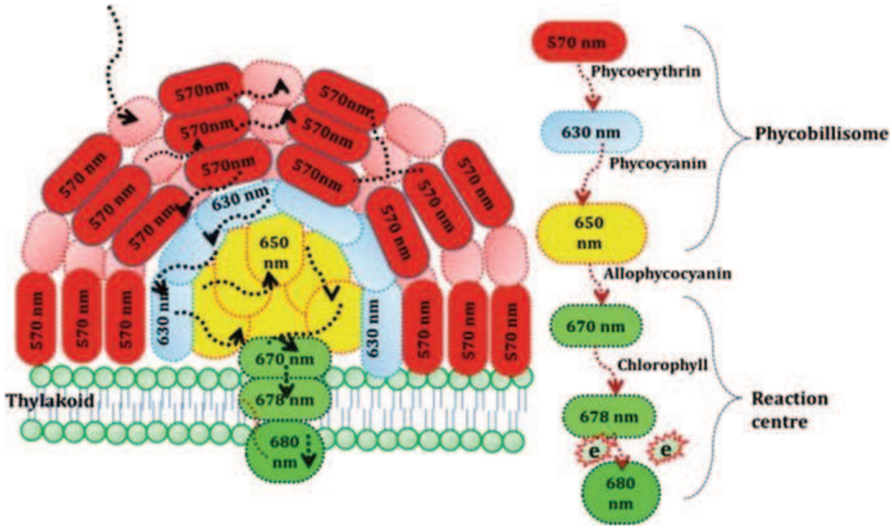

Figure (1.3). *Structural organization of the antenna system of PSII for red algae and cyanobacteria and energy transfer steps, including charge separation (photochemical reaction) at the PSII RC for cyanobacteria*. The energy of absorbed photons is passed through many antenna molecules [phycoerythrin (absent in most cyanobacteria) → phycocyanin → allophycocyanin] until it reaches the RC Chl *a* (P680). The excited P680 donates its electron, which is in the molecule's excited state, to an electron acceptor (A). The electron vacancy of the Chl *a* is filled by the electron from an electron donor (D). The wavelength numbers (nm) inside the circles represent pigments corresponding to these pigments' long-wavelength absorption maxima (redrawn from [25]).

To protect the photosynthetic apparatus, photosynthetic organisms have photoprotective pigments named carotenoids (Car). Car generally perform dual roles as they behave as accessory light-harvesting pigments and are also involved in photochemical quenching [25]. On the other hand, they have antioxidative properties and participate in minimizing oxidative stress by quenching singlet oxygen. In cyanobacteria, the orange carotenoid protein (OCP) is unique, which is water-soluble and carries out both photosensory and photoprotective functions. In the blue-green light spectrum, light absorption interchanged the stable form of OCPO into OCPR that binds to the primary light-harvesting antenna. Cyanobacteria, when exposed to high light irradiance, the activated OCPR participates in thermal energy dissipation and protects photosynthetic apparatus against damage and after completion of energy dissipation, the OCPR interchange into OCPO in the dark. Besides, OCP cyanobacteria also have different Cars, such as myxoxanthophyll, β-carotene, and its derivatives, echinenone and zeaxanthin. The same families of Cars were reported in green algae and plants, with fractions significantly enriched in lutein, violaxanthin and astaxanthin. A decrease in the Car content under adverse environmental factors proves severe toxicity in these microorganisms against particular stress conditions. Hence, the basal level of Car is necessary to maintain the photosynthetic apparatus's structure and functions [26].

(2.1). - Radiant energy-harvesting reactions

The initial event in photosynthetic light reactions of cyanobacteria and microalgae begins with the absorption of light (photons) by large antenna systems, PBSs, attached to the cytoplasmic surface of the photosynthetic membrane and the eukaryotic antennae present in the chloroplast, accordingly. Phycobilins deliver the energy of absorbed light to the large pigment-protein RC complexes, PSII and PSI. Cyanobacteria contain a relatively low amount of PSII complexes compared to PSI (the PSI/PSII ratio may vary from ~3 up to 5.8), and PBSs are primarily associated with PSII. In eukaryotic microalgae, this ratio tends to unity for normal growth conditions. Nonetheless, under certain conditions, PBSs are redistributed to PSI, thereby regulating the efficiency of excitation energy transfer between the two photosystems. Similarly, Chl *a*-/Chl *b*-containing membrane-integral light-harvesting complexes (LHCs) in plants show an energy equilibration between the photosystem complexes.

The conversion of solar energy into chemical energy forms results from the two photochemical RCs (PSII and PSI) acting in tandem. Delivery of excitation energy to the RC-Chl *a* molecules, referred to as P680 and P700, initiates the energy conversion process. Due to the redox-active cofactors embedded into a protein matrix of both photosystems, the photochemical steps within RCs involve fast, sequential electron transfers that result in stabilized charge separation, stepwise “extraction” of electrons from water and their transfer to $NADP^+$ (the so-called “Z-scheme”). The primary photochemical reaction in PSII involves the formation of the singlet excited state of P680, either upon excitation energy transfer from antenna molecules or upon absorption of a photon with a wavelength of <680 nm. The photochemistry-driving energy per photon absorbed by PSII equals the energy of a 680 nm photon. The latter results in a loss of 20-21% of the energy that light beams with shorter λ wavelengths contain [27].

Further, by the presence of pheophytin (Pheo), a radical is formed, which has one of the highest known oxidizing potentials in nature, capable of driving a sequential oxidation process of water molecules. Subsequently, the result of water oxidation is the evolution of molecular oxygen and the release of protons into the thylakoid lumen. Later, 50% of the free energy stored by PSII is transferred to plastoquinone (PQ).

PSI, which has some similarities to PSII, captures (up to) <700 nm light energy to drive the redox reactions of the electron transfer in that system. Even though the redox potential for the primary electron donor P700 in cyanobacteria and microalgae/plants is not high enough to extract electrons directly from water, it is enough to drive transmembrane electron transfer between the external electron donor, cytochrome c6 (Cyt c6) or plastocyanin (PC)) in the thylakoid lumen and acceptor (ferredoxin (Fd)) in the cytoplasm.

The integral membrane cytochrome b6f (Cyt b6f) complex is an essential player in noncyclic and cyclic electron flow, mediating the photo-induced electron transfer between the two photosystems and increasing the number of protons pumped across the membrane into the lumen. It is a large multi-subunit protein with several prosthetic groups, which has high structural and functional similarity between those from cyanobacteria and plants [25]. Unlike eukaryotic microalgae, cyanobacteria share the use of PQ pool, Cyt b6f complex, and PC/Cytc6 for both photosynthetic and respiratory electron transport pathways. Under certain conditions, cyclic electron flow occurs from the reducing side of PSI, through the PQ pool or Cyt b6f complex and back to PSI. This cyclic electron flow increases proton pumping into the lumen. Finally, the production of NADPH from NADP is catalysed by the membrane-associated flavoprotein ferredoxin-NADP+ reductase (FNR).

All in all, photosynthetic electron transfer establishes a proton electrochemical potential difference ($\Delta\psi$) across the thylakoid membrane (the cytoplasmic side being called the n (negative) side, and the luminal side being called the p (positive) side). The ATP synthase utilizes this proton motive force (PMF) to phosphorylate ADP to ATP. This last occurs when the protons return to the cytoplasm or chloroplast stroma through the protein complexes of the ATP synthase.

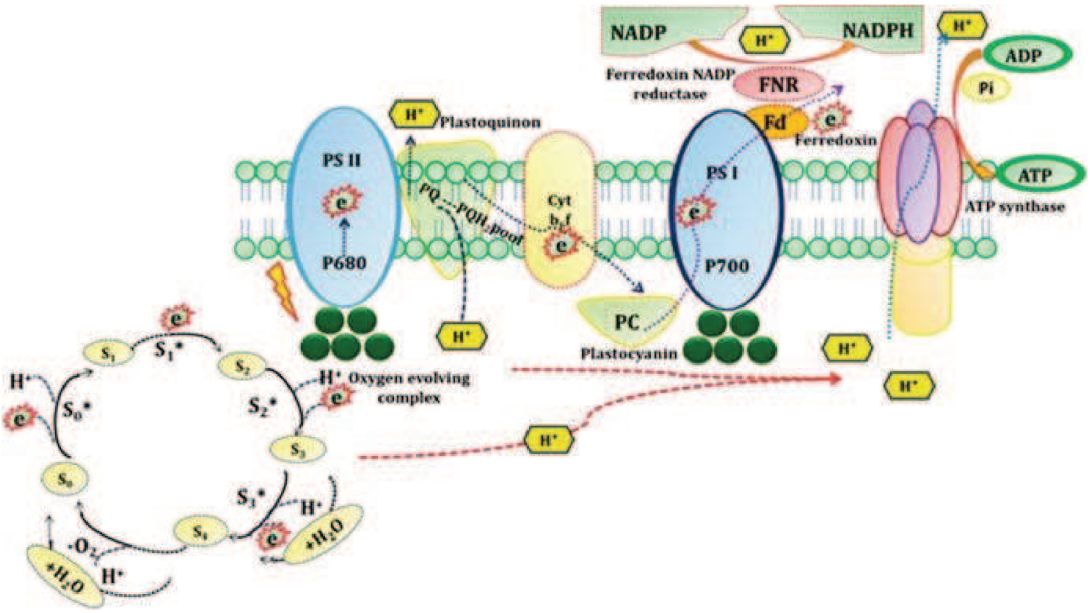

Figure (1.4). Schematic representation of electron flow (transfer of electron and proton) in the thylakoid membrane (adapted from [2]).

(2.2). - CO2-fixation reactions

Carbon dioxide (CO_2) exists in three forms in contact with water: dissolved CO_2, bicarbonate (HCO_3^-) and carbonate (CO_3^{-2}) ions [28]. The distinctive features of the same process carried out by bacteria or microalgae are mainly in which form of dissolved inorganic carbon (DIC) they prefer to uptake from the surrounding liquid media. In the case of prokaryotes, the preferred DIC form is bicarbonate ions (HCO_3^-) which are actively pumped into the cytosol[29]. However, CO_2 can be assimilated as well through passive transport. In the case of eukaryotic algae, the presence of peripheral carbonic anhydrases in the cell membrane is proven, which catalyses the conversion of CO_2 directly into HCO_3^- for trapping this carbon into the cytosol [19].

The CO_2-binding reaction on carbohydrates is catalysed by the enzyme Ribulose 1,5 bisphosphate carboxylase (RubisCO), located in the stroma of chloroplasts in eukaryotic algae and the carboxysomes in photosynthetic bacteria. The enzyme adds CO_2 to the five-carbon sugar ribulose 1,5 bisphosphate, resulting in two molecules of 3-phosphoglycerate. Because the reaction rate is slow, multiple copies of the enzyme are needed to fix sufficient CO_2. The fate of the 3-phosphoglycerate is complex, with some being converted to sucrose or starch and the remainder being used to regenerate the five-carbon starting sugar. The reactions involved in CO_2 fixation, and the generation and conversion of sugars, are often referred to as the "Calvin-Benson-Bassham cycle" [3]. ATP and NADPH, previously generated in the presence of radiant energy, are used for this process. Many of the enzymes in the cycle are regulated by the quality and quantity of light absorbed [4].

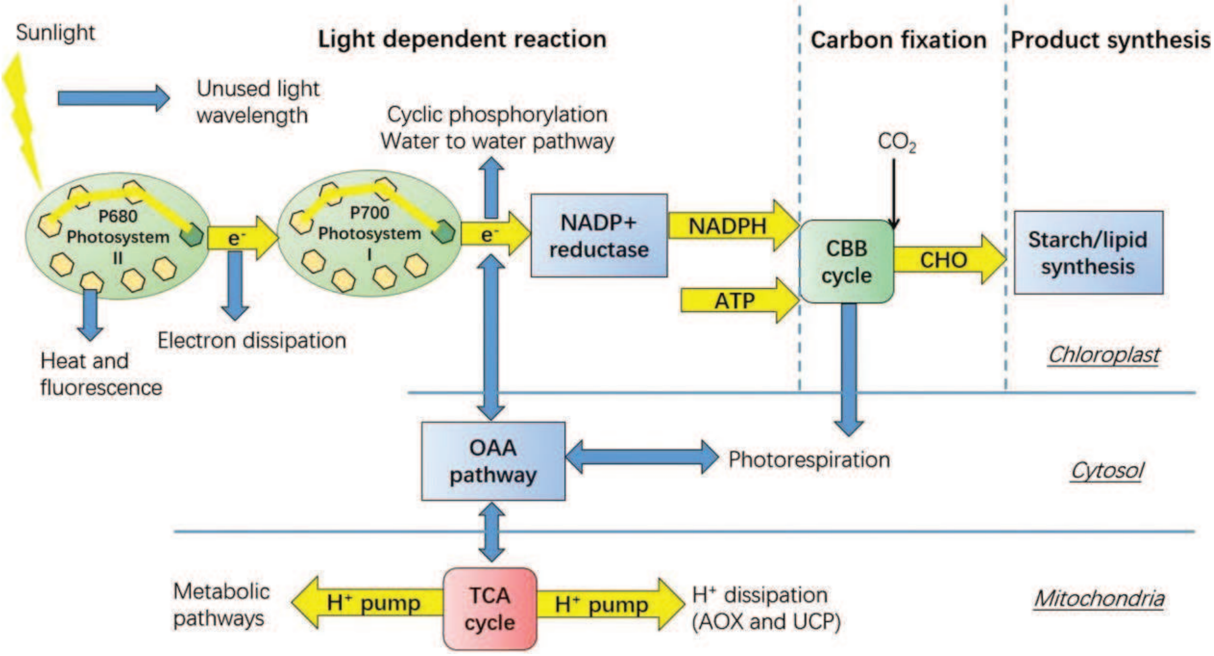

Figure (5). *Energy capture, delivery and dissipation in plants and microalgae*. When pigment molecules in Photosystem II absorb light, electrons are passed along an electron acceptor chain to $NADP^+$ reductase. The ATP and NADPH generated in the light reactions are used to fix CO_2. The Calvin-Benson-Bassham cycle (CBB) intermediates are then to participate in anabolism. The energy delivery in microalgae depends on various pathways like malate/oxaloacetate shuttle (OAA) and photorespiration. The energy dissipation depends on alternative pathways like water-to-water pathways, photorespiration and H^+ dissipation (TCA) (adapted from [30]).

In closing, it should be noted that the photosynthetic phenomenon can be accompanied by a process called photorespiration, in which a molecule of O_2 is bound to ribulose 1,5-bisphosphate, resulting in a molecule of 3-phosphoglycerate and a molecule of phosphoglycolate. Photorespiration may lead to a waste of energy, as it consumes ATP and O_2 and generates CO_2.

The overall equation of oxygenic photosynthesis turns out to be:

$$6CO_2 + 12NADPH + 18ATP + 12H^+ + 12H_2O \longrightarrow C_6(H_2O)_6 + 18ADP + 18P_i + 12NADP^+$$

(3). - Uses and applications of green microalgae and cyanobacteria

Given the vast diversity of algae and the high capacity to adapt to environmental conditions (e.g., through the production of metabolites), new social, biotechnological and industrial applications and uses have emerged. The most frequent ones are shown below, and the potential for developing new technologies based on their qualities is highlighted:

(3.1). - Animal and human food products

Large-scale microalgae cultivation began in the 1960s in Japan, where *Chlorella sp.* was used as a food additive, given the biomass composition (30-60% dry weight (dw) protein, 20-40% dw carbohydrate). In addition, this microalga can be enriched in selenium through changes in cultivation conditions, incorporating this mineral into individuals' nutrition in less toxic forms to the human body.

A blue-green alga of particular interest in human nutrition is Spirulina (*Limnospira*) since its biomass is characterised by a high protein content (60-70% dw), and it is also a source of vitamins (thiamine (B1), riboflavin (B2), cobalamin (B12)), essential amino acids, minerals, fatty acids (α-linolenic acid) and antioxidant pigments [31]. The food industry has also used *Dunaliella salina*, *Haematococcus pluvialis* and *Phaeodactylum tricornutum* to produce proteins.

Today's commercial presentations for human consumption are very diverse, including powders, flours, oils, capsules, tablets and liquids. The work of Camacho et al. contains a list of foods (cheeses, kinds of pasta, cakes and soups) prepared from microalgae containing functional metabolites. The main disadvantage of using microalgae in human food is the high content of nucleic acids, so processes must be developed that allow their removal without altering the properties of the rest of the components [32].

As far as animal feed is concerned, they can be incorporated into the diet of farm animals (pigs, ruminants, poultry), fish, and pets, and have the advantage that they can be produced throughout the year, unlike some traditional (seasonal) foods. In poultry, *Chlorella* sp. has been shown to increase microbial diversity in the digestive tract [33]. In aquaculture, strains should be minor in size and have loose cell walls that are easy to digest. Strains such as *Tretaselmis*, *Isochrysis*, *Pavlova*, *Nannochloropsis*, *Skeletonema, Phaeodactylum, and Chaetoceros* are mainly used.

(3.2). - CO_2 removal from industrial flue gases

Microalgae perform well at CO_2 concentrations of 10-20% (v/v%), irrespective of the source [34]. Flue gas contains 3-15% CO_2, depending on the fuel feedstock and type of operation, and 100 other components (SO_X, NO_X, HF, heavy metals, among others), some of which inhibit algal biomass growth. The cement industry is responsible for approx. 4-5% of global CO_2 emissions have made it a target for algal biotechnology.

In 1997 Yamaha Motor, in order to reduce the environmental impact of greenhouse gas emissions, began developing technologies for CO_2 fixation through algae photosynthesis. In 2006, it was the pioneer in establishing a new business model (life science business), initiating the sale of high-quality astaxanthin (see Section (3.4)) from indoor *Haematococcus pluvialis* cultures (20-ton dw/year), using its gaseous effluents, and a PBR based on advanced fluid control technology (Yamaha High-efficiency Bio Reactor) [35].

(3.3). - Environmental bioremediation and effluent treatment

Microalgae are able to consume nitrogen (N), phosphorus (P) and ammonium (NH_4^+), which are the leading causes of eutrophication of water bodies, and produce O_2, which allows the growth of heterotrophic bacteria.

Urban wastewater or wastewater from industries such as metallurgy and paper mills contain lead (Pb), chromium (Cr), cadmium (Cd), copper (Cu), mercury (Hg) and zinc (Zn) [36], which persist in the environment, undergo biotransformation, or accumulate in the food chain. Algae, especially strains of *Chlorella* and *Scenedesmus*, are used for biosorption of toxic and radioactive metal cations, as well as to recover gold (Au) and silver (Ag).

Rural water bodies contain high amounts and types of pesticides from agriculture. There is a history of microalgae removal of lindane, pentachlorobenzene, chlorpyrifos and alachlor [37].

Some pharmaceutically active chemicals are present in urban effluents, including anti-inflammatories, antibiotics, anti-depressants and anti-epileptics [38].

Microalgae are vital indicators for monitoring water quality and ecological toxicity due to these pollutants [39].

It has been observed that microalgae in consortium with bacteria are capable of removing contaminants from crude oil [40]. The technology is being developed in view of *in situ* remediation processes in seas and oceans.

(3.4). - Bio-active products

There are products extracted from microalgae that are biologically active and have high commercial value [41], among them:

- Astaxanthin: a keto-carotenoid responsible for the reddish-pink colour of trout and salmon and a super-antioxidant. *Haematococcus pluvialis* (Chlorophyta) is a species that has demonstrated its potential for its production.
- β-carotene: is the precursor of vitamin A and is accumulated in significant quantities by the microalgae *Dunaliella salina* (Chlorophyta).
- Lutein: a yellow pigment that belongs to the xanthophylls. Since animals do not produce lutein, it is included in food supplements as an antioxidant.
- Fucoxanthin: an epoxy-carotenol found in brown algae and diatoms. It is used in nutrition because it accelerates the burning of abdominal fat and brings glucose into the tissues [42].
- Phycocyanin: a water-soluble protein pigment extracted from blue-green algae (cyanobacteria) such as *A. maxima* and *L. platensis*. It is used as a dye in many industrial processes and as an antioxidant and wound-healing agent in the health field [43].
- Mycosporins (MAAs): amino acid compounds present in phytoplanktonic microalgae, generally secondary metabolites, with the potential to dissipate UV radiation [44].
- Docosahexaenoic acid (DHA, C22:6): plays a vital role in the development and function of the nervous system and the visual organ in the foetus and newborn. It is produced by the microalgae *Isochrysis galbana* [45].

Many of the components described here are incorporated in cosmetic industry products, such as creams (regenerative, anti-ageing, refreshing, UV-VIS sun protection, hair care), in the food and nutraceutical industry for the generation of functional foods (protein-cereal bars for high-impact sports, muscle recovery shakes, energisers), and in the pharmaceutical industry for the prevention and treatment of diseases (Parkinson's, Alzheimer's).

(3.5). – Bioenergy production

Microalgae are considered a promising feedstock for the production of third-generation (3G) biofuels, as they present some potential advantages compared to conventional plant crops, such as i) higher biomass and oil productivity (4-5 times) per unit area and time; ii) lack of competitiveness for land use or with the food market, as they can be grown on non-arable land; iii) better H_2O and nutrient economy, by recycling or reuse; iv) the possibility of using waste from industries as a source of cheap nutrients.

(3.5.1). - *Bio-oil*

Bio-oil is an organic liquid commonly black in colour, which has a calorific value of 31-39 MJ kg^{-1} and is mainly obtained by hydrothermal liquefaction (HTL) of algal biomass under sub-critical temperature and pressure conditions (280-380 °C, 7-30 MPa). It contains phenolic compounds, long-chain and organic fatty acids, esters, nitrogenates, polyaromatics, alkanes, alkenes, phytol and cholesterol derivatives, among other organic groups [46].

The HTL process is commonly carried out in stainless steel tanks operating in batch mode, with retention times of up to 1 h. The HTL product comprises a mixture of phenolic and organic compounds. The HTL product is composed of three phases, liquid, solid, and gas. The solid phase, recovered by filtration and dried for stabilisation, is called "biocarbon" and is used in agriculture as a fertiliser due to its high N content. The liquid phase can be extracted with an organic solvent (e.g., diethyl ether), yielding two phases: aqueous and non-aqueous. The non-aqueous phase is recovered, and the solvent is removed by evaporation, resulting in biocrude, which can be transformed into fuel.

H_2O, playing the role of catalyst and reagent, has several advantages over chemical solvents, as it is environmentally benign, non-toxic, cheap and readily available. The process does not require dry biomass, avoiding drying costs.

(3.5.2). - Biohydrogen (H_2)

H_2 is a clean fuel that generates only H_2O vapour in combustion and has the highest energy content per unit weight (122 KJ gr^{-1}) compared to other fuels. Among the main disadvantages are the difficulty of storage and distribution and the cost associated with its generation, which is currently unfeasible for commercialisation.

As far as algae are concerned, mainly *Chlamydomonas reinhardtii* is used, and there are two photosynthetic production routes:

i. **Direct biophotolysis / PSII-dependent pathway**

H_2 photoproduction is achieved by linear e^- transfer involving both PSs. Under anaerobic conditions and in the absence of CO_2, Ferredoxin can direct the e^- to hydrogenases. The reaction is combined with the photolysis of H_2O, as follows:

$$\begin{array}{c} 2H_2O + 4fot \rightarrow 4H^+ + 4e^- + O_2 \\ 2\left(2H^+ + 2e^- + 2fot \rightarrow H_2\right) \\ \hline 2H_2O + 8fot \rightarrow 2H_2 + O_2 \end{array}$$

Eight photons are used because both PSs are involved. Direct biophotolysis contributes around 90% of the total e^- flux. A relevant disadvantage is the incompatibility of the simultaneous production of H_2 and O_2, as O_2 mildly inhibits algal hydrogenases.

ii. **Indirect H_2 biophotolysis / PSII-independent pathway**

They consist of pathways using e^- from NADPH, which are transferred directly to the PQ pool, bypassing PSII, and is a process mediated by NDA2 (NADH dehydrogenase type II) enzymes. The most common source of reductants from the PQ pool is the glycolytic degradation of glucose or starch. The pathway allows the production of O_2 and H_2 to be separated, as it does not involve PSII activity. H_2 production rates are about ten times lower than those of the PSII-dependent pathway [47].

(3.5.3). - Biomethane (CH_4, biogas)

CH_4 production is effortless and does not require much infrastructure. It is carried out in an anaerobic digester containing microbial populations that convert the organic compounds of macro- and microalgae (lipids, proteins, carbohydrates) into CH_4 and CO_2 synergistically and concerted. Pre-treatment of the algal biomass is necessary to obtain high yields [48].

(3.5.4). – Bioethanol

Some microalgae accumulate starch and cellulose in amounts greater than 40% dw when subjected to stress (e.g., N limitation) [12]. These polymers are more easily converted to monosaccharides than plant materials due to the absence of lignin. The algal biomass is hydrolysed by chemical (acid or alkaline), physicochemical, or enzymatic treatments to release the monosaccharides, which are anaerobically fermented by yeasts (e.g., *Saccharomyces cerevisiae*, *S. bayanus, Kluyveromyces marxianus, Zymomonas mobilis*). Ethanol is recovered from the medium by distillation.

The cell walls of intact microalgae, or the remains of the wall from downstream processes, can be a potential raw material for the generation of fermentable sugars, as they are composed of a matrix of polysaccharides and glycoproteins (pectins, chitin agar, alginates, cellulose, hemicellulose, aliphatic polymers such as algaenan, among others) [49], [50].

(3.5.5). – Biodiesel

The transesterification of animal fats or vegetable oils results in biodiesel. Biodiesel derived from microalgae lipids has technical advantages over 1G biodiesel, including a higher calorific value (29-30 MJ kg^{-1}), lower viscosity and lower density [51]. Currently, no technologies are mature enough to be applied commercially.

Reported lipid contents of microalgae vary widely and are highly dependent on strain and culture conditions. The most extensively studied genera, such as *Chlorella, Dunaliella, Nannochloropsis, Scenedesmus, and Neochloris*, yield 20-50% dw [52]. Stress conditions such as Nitrogen, light, or CO_2 limitation trigger lipid biosynthesis but negatively affect biomass production and, thus, lipid productivity [53]. The main components of microalgal oils are neutral, polar lipids and some number of hydrocarbons, sterols, waxes and pigments [54].

(4). - Nutrient requirements and growing conditions

The main components of microalgae biomass are C (30-50% dw), O (30-50% dw), H (3-7% dw), N (4-9% dw), phosphorus (P) (3% dw), and minor amounts of sulphur (S), potassium (K), magnesium (Mg), calcium (Ca), sodium (Na), among traces of other elements. The latter results in a minimum formula close to $CO_{0.48}H_{1.83}N_{0.11}P_{0.01}$ [55]. In principle, a culture medium should be composed of the above primary elements, to which trace amounts of cobalt (Co), iron (Fe), Zn and Cu may be added. Metals tend to precipitate, so a chelating agent (e.g., EDTA) is usually considered. For demanding strains, it is necessary to add growth promoters (e.g., vitamins) to the medium. The components should be supplied in dissolved form, as microalgae grow in aqueous media.

Microalgae can be grown under photoautotrophic, heterotrophic and mixotrophic conditions using various C sources, such as CO2, methanol, acetate, glucose, glycerol or other organic compounds. Photoautotrophic growth is supported by inorganic C (e.g., CO2 or bicarbonates). N can be supplied as urea, NO_3^- or NH_4^+. Ammonium is thermodynamically more favourable than $NO3^-$, but it is possible to become toxic (< 100 mg L^{-1}) [56].

Optimum pH values are in the range of 7 - 10. The pH of the cultures varies as a result of the reactions involved in the consumption of C and N. pH values in the range 9 - 12 lead to the formation of hydroxides charged with Mg^{+2} or other metals (e.g., Fe, Aluminium (Al)), which neutralise the negative charges of the microalgae, leading to sedimentation of the cells or flocs [57]. The most commonly used method of pH control is CO_2 injection (1-5%), which can constitute up to 30% of the total microalgae production cost [58].

The optimum temperature for growth varies from 20-35 °C, and in a cultivation process, it can vary due to the absorbed radiation (solar or artificial), and in the case of outdoor systems, also due to daytime weather conditions.

Light is one of the most relevant factors in microalgae cultivation, and under typical operating conditions, it is the limiting "nutrient". It must be ensured that it is distributed in quantity (intensity) and quality (spectral distribution) in the suspension. Light can be supplied continuously or employing a photoperiod, defined as the hours during which a suspension is illuminated, on a 24-hour basis.

(5). - Photobioreactors for the production of photosynthetic microorganisms

There are currently two large-scale algae production systems, open and closed (photobioreactors (PBRs)). On the one hand, open systems are intended for commodities. Nonetheless, their use is restricted to a relatively small number of "robust" species, such as *Chlorella, Scenedesmus* and *Nannochloropsis*, which overgrow, or *Arthrospira* and *Dunaliella*, which propagate under very selective conditions (e.g., high salinity). On the other hand, closed systems are used to generate high-quality biomass (e.g., human consumption) and high commercial-value products accumulated by strains that do not tolerate the dynamics of (sensitive) environmental variables. A detailed description of the production systems, and distinctive designs of each type, can be found below.

(5.1). - Open systems

(5.1.1). - *Open y raceway ponds*

They consist of ponds exposed to the environment, built on compact soil covered with membranes, and a depth of 0.1-0.5 m. Most industrial-scale units (1000-5000 m^2) are based on the raceway pond design proposed by Oswald [59] (see Fig. (6A and 6D)), with 2 or 4 channels with curved ends. The length of each channel is proportional to the width of the channels, with ratios of 10-20. There are also ponds with circular designs (see Fig. (6E)). All share a relatively low illuminated area-to-volume (A/V) ratio of 5-10 m^{-1}, which requires large areas of land. The algal suspension is recirculated continuously at velocities of 0.1-0.3 $m\ s^{-1}$, which prevents sedimentation of the cell formations (microalgae are commonly flocculated). Recirculation is carried out via a paddle wheel, impeller, or rotating arm, with a reported power consumption of 0.5-1.2 $W\ m^{-2}$ [60]. CO_2 supply and O_2 removal are mainly performed in the regions where the liquid drive devices are located but can also be performed through sinks located along the channels. Benefits include low costs for construction (an order of magnitude lower than closed systems) [61], maintenance (e.g., cleaning) and operation, and ease of scale-up without design modifications [62]. Investment for a scale of 100 ha varies from 0.13 to 0.37 M€ ha^{-1}. Ponds may be strategically built near wastewater treatment plants or agricultural facilities to utilise the effluent's nutrients [63].

Among their main disadvantages are low yields and working biomass concentrations of 0.5 to 1 $g\ L^{-1}$, which make the downstream processes of harvesting and dewatering difficult and expensive. This is due to several aspects, including radiant energy transfer within the culture medium and gas-liquid matter transfer at the culture surface. As far as light on the pond surface is concerned, it is highly variable throughout the day, being limiting in the early morning or late afternoon and photoinhibitory at midday, depending on the geographical location. Within the culture itself, cells are exposed to different energy densities as they circulate from the surface to the depths of the culture (photoinhibitory and limiting). The frequency with which the algae circulate between the light and dark zones of the reactor, and the time spent in each, is regulated by the mixing rate. The light distribution depends on the reactor geometry, the cell density and the optical properties of the algae suspension. Ponds are characterised by having a significant fraction of the reactor volume in darkness.

Regarding gas-liquid transfer, O2 saturation values of 115-450% have been observed due to the fact that the stirring devices are sectored [64]. When CO_2 is bubbled into a shallow channel, the contact time between gas and liquid is shallow, and 80-90% of the injected CO_2 is lost to the atmosphere [65].

Other aspects that may reduce the chances of success in ponds are contamination by competing algae, culture collapse by insect herbivores, fungi, and pathogens of the microalgae of interest, dilution by weather events (e.g., rainfall), the presence of dust or airborne pollutants, among others [60].

More than 95% of microalgae production worldwide has been carried out using raceway ponds. Many algae biotechnology companies have started using raceway ponds for indoor cultivation processes (artificial LED or fluorescent light) of non-robust strains.

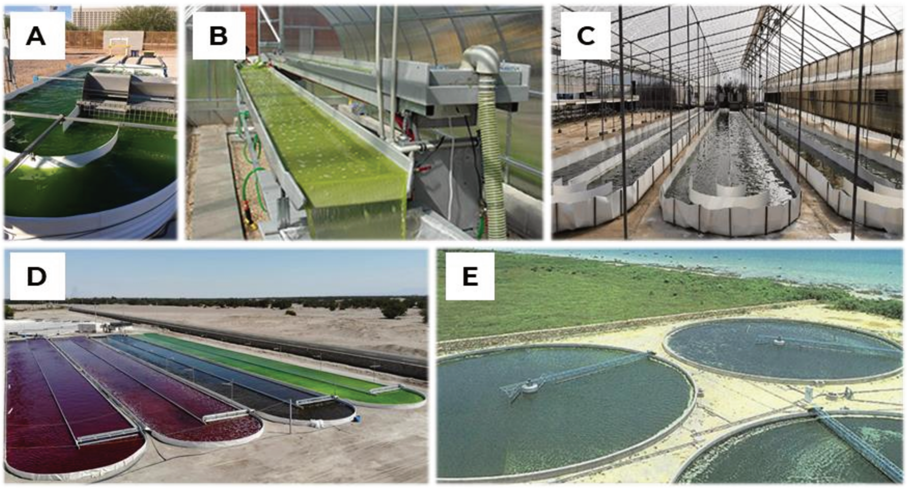

Figure (6). A] *raceway pond* in AlgaePARC, University of Wageningen, Wageningen, Netherlands, (reprinted from [66]); B] *thin layer cascade* reactor constructed at the Institute of Microbiology in Trebon, Czech Republic (redrawn from [67]); C] Indoor r*aceway pond* (adapted from [68]); D] *raceway pond* for two-stage cultivation process of *H. pluvialis* of Cellana LLC, (Kailua-Kona, Hawaii, USA) (reprinted from [67]); E] Rotating arm type recirculating circular pond at Yaeyama, Japan. (Reprinted from [69]).

(5.1.2). - *thin layer cascade photobioreactors*

They commonly consist of two sections: i) photosynthetic, consisting of stainless steel or plastic plates through which the culture is circulated (in layers of 0.06-4 cm) [70], under turbulent flow by pump drive (speed ≥0.5 m s^{-1}, required power 1-10 W m^{-2}). The reduced light passage and relatively high A/V ratios (25-180 m^{-1}) allow for decreasing the dark volume of the suspension (<10%), increasing the working biomass concentration (4-20 g L^{-1}), and maximising light utilisation efficiency. Platforms can be vertically adjustable, concerning the surface, at angles of 0.5-3°; ii) gas-liquid matter transfer, consisting of a tank or receptacle where the air is injected to desorb dissolved O_2. CO_2 is commonly supplied in pure form, separate from aeration, because it improves the efficiency of the transfer process. The mixing tank also houses the variable monitoring and control system.

The necessary dimensions vary according to the depth of the culture, with production facilities ranging from 400-900 m^2. Fig. (6B) illustrates a state-of-the-art display thin layer cascade reactor with a variable liquid thickness of 0.5-1.5 cm, an area of 90 m^2 and a variable volume of 500-1500 L.

(5.2). - closed systems: photobioreactors (PBRs)

PBRs may be defined as culture systems in which photons do not directly hit the photosynthetic microorganism suspension but must pass through the transparent walls of the reactor [71]. The isolation from the surrounding environment allows strict control of the operating conditions, such as temperature, pH, agitation (mechanical or pneumatic), aeration, feeding, dissolved O_2, along with others. The occurrence of contamination is significantly reduced, allowing longer cultivation times. PBRs are classified on the basis of their design/geometry, namely:

(5.2.1). – Tubular PBRs

Tubular PBRs are the most common design at the industrial scale [72]. The cost is significantly higher than open systems, with investment costs of 0.51 M€ ha^{-1} at a scale of 100 ha [61].

These reactors, like thin layer cascades, are composed of two main sections: i) photosynthetic, consisting of glass or plastic tubes with diameters of 0.03-0.1 m, in which the crop is circulated by pumps or airlifts, at speeds of 0.1-0.8 m s^{-1}. The power required ranges from 10-100 W m^{-2}. They have A/V ratios of up to 80 m^{-1}, which makes it possible to work with high crop densities. The tubes can be arranged vertically, horizontally and at an angle, depending on the amount of sunlight collected. There are designs in which black tapes are glued over the tubes, with a particular length and spacing, to create light-dark cycles suitable for the operating conditions of interest; ii) gas-liquid matter transfer, which consists of a tank or receptacle where the air is injected at rates of 0.01-0.1 vvm, in order to desorb dissolved O_2. The CO_2 is supplied in pure form elsewhere in the receptacle.

Typical methods for temperature maintenance, especially by cooling, are spraying water on the surface of the tube, shading (e.g., by overlapping the tubes), or immersing the system in a temperature-controlled water bath [73].

There are several types of tubular PBRs, namely:

- **(5.2.1.1). - serpentine tubular PBRs**

Fig. (7A) shows a vertical serpentine-type tubular PBR consisting of units formed by Plexiglas® tubes assembled through U-bends. Gas transfer and temperature control, commonly through a stainless-steel heat exchanger, are performed in the vertical bubbling column at the system's end. Harvesting is by overflow at the top of the vertical bubbler column.

In Fig. (7B) is possible to see a horizontal serpentine-type tubular PBR with an atypical diameter of 0.38 m, which is used for growing *H. pluvialis* in the vegetative stage. Temperature control of the culture is achieved by immersing the PBR in a pool of water.

- **(5.2.1.2). - *manifold* PBRs**

They consist of a series of parallel tubes, in vertical or horizontal arrangement (see Fig. (7C and 7D)), connected at the end by two manifolds, one for distribution and one for harvesting.

The main advantages over serpentine reactors are reduced head losses (avoiding U-bends) and lower dissolved O2 concentrations, two factors that facilitate scale-up [73].

(5.2.1.3). - Helical PBRs

It consists of small diameter (0.03 m) flexible tubes wrapped around a vertical cylinder, or cone, to provide support (see Fig. (8A)). The conical version has been suggested because it exposes a larger area to sunlight, thus increasing the

A/V ratio. The gas exchange system is located outside the reactor, as is the temperature control system. They have been tested at scales of 1000 L but have not been implemented at present due to the difficulty of cleaning and the hydrodynamic stress the microalgae suffered due to the operating conditions required to prevent the biomass from sticking to the walls.

(5.2.2). - *flat panel* PBRs

The basic design consists of two parallel panels of PVC, polycarbonate, polymethyl methacrylate, glass or polyethene, with a thin layer of microalgae suspension flowing between them [71] (see Fig. (7C)). They are characterised by A/V ratios of 16-80 m^{-1}, volumetric productivities of 2 $g\ L^{-1}\ d^{-1}$ and areal productivities of 5-15 $g\ m^{-2}\ d^{-1}$. A stream of compressed air (0.4-1 vvm) from the base through a porous diffuser can be carried out through suspension mixing and gaseous mass transfer. Other designs contemplate an external gas exchange system open to the atmosphere.

(5.2.3). - bubble columns, *airlift* y bag PBRs

Bubble columns consist of vertical cylinders with diameters (D) of 20-50 cm and heights (H) of 1.5-2.5 m (H>2D, commonly 4-8), constructed of rigid materials (e.g., acrylic, glass), and mixed through an air stream passing through a porous diffuser at the base (see Fig. (8B)). They have A/V ratios of 4-10 m^{-1}, which are considered low. While this could be a drawback for the cultivation of robust strains, it could be helpful for strains sensitive to lighting conditions (e.g., *H. pluvialis* in the mobile vegetative stage). Among its main advantages are the absence of internal parts (allowing better use of the volume of the device), the absence of moving parts and typical operating conditions that do not lead to shear stress, and high matter transfer. A bubbler column reactor can be transformed into an airlift system by adding an internal cylinder or baffle, resulting in the generation of two zones, a riser and a downcomer. This last allows the generation of a return current that interacts with the reactor walls (avoiding biomass deposition) and light-dark cycles.

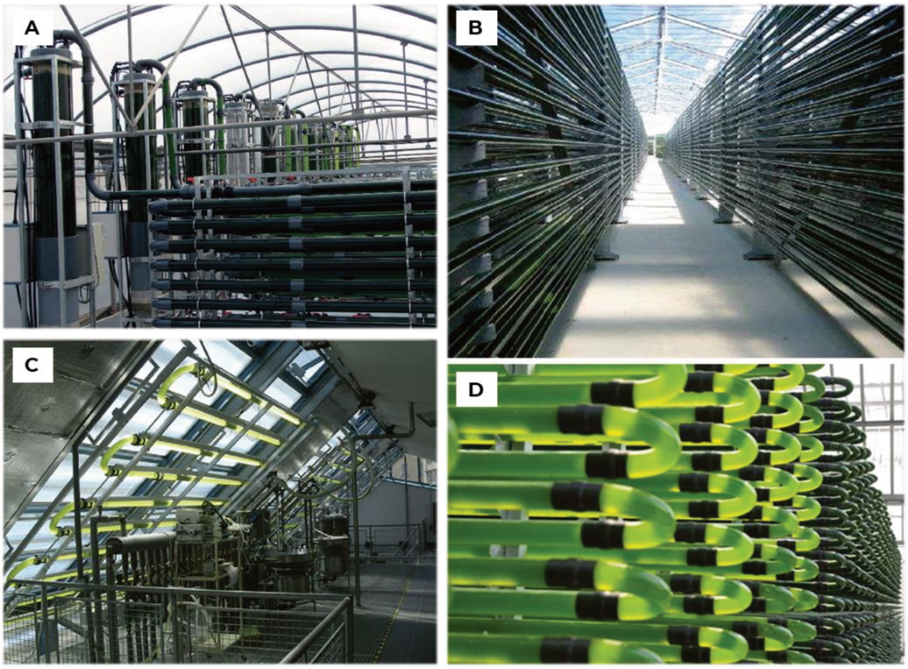

Figure (7). A] Vertical tubular serpentine photobioreactor installed at the Estación Experimental de Cajamar “Las Palmerillas” (Almeria, Spain) (reprinted from [67]); B] two-phase flow vertical serpentine designed by Microphyt SAS (Baillargues, France), (adapted from [74]); C] Reactor tubular *manifold* horizontal installed in Roquette & Klötze GmbH, (Klötze, Germany), (reprinted from [75]); D] Tubular manifold photobioreactors: a commercial plant with vertical reactors at A4F-Algae for Fuel, S.A Pataias (Portugal), (adapted from [67]).

The main disadvantages of both systems are the wear of the rigid vessel material due to cleaning (scratches and changes in colour) and their cost. This was the trigger for the search for reactors that mimic the operation of a bubbling column but are constructed of flexible materials associated with low cost (e.g., polyethene bags). In bag-type reactors (Fig. (8D), sometimes called "sleeves" for V-type geometries (see Fig. (8D)), the bags (50-500 L) are suspended from a frame or a hanger-type structure, and aeration is carried out from the base using a diffuser. The main advantage is the already mentioned low cost, allowing discarding and replacement, and the main disadvantage is the fouling of the biomass to the internal wall of the bag. Generally, these systems are used in indoor cultivation under artificial lighting.

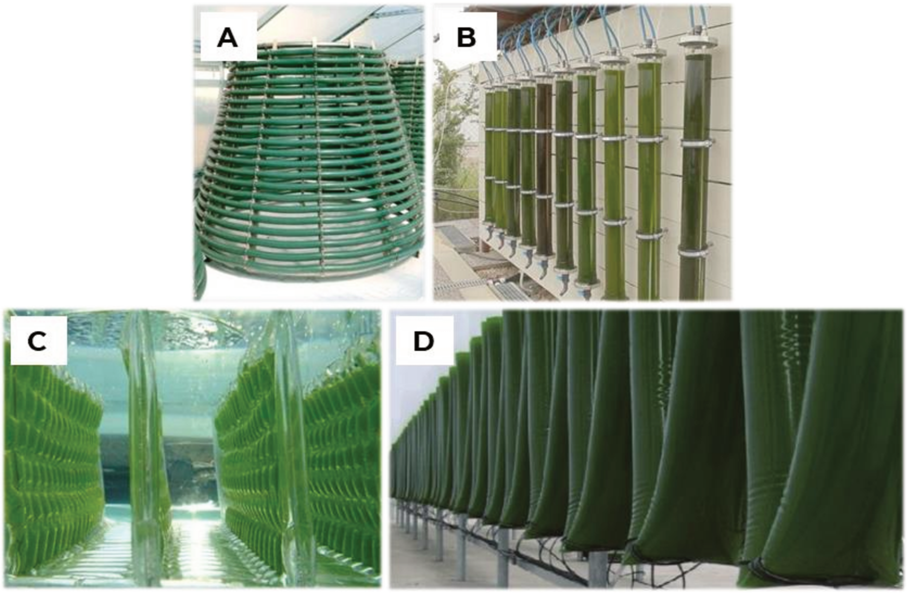

Figura (8). A] Helical photobioreactors designed by GICON (www.gicon.de) and tested at Anhalt University in Köthen, Germany (reprinted from [76]); B] Pilot installation of flat panel reactors at a thermoelectric power plant in Tocopilla (Chile), (adapted from [67]); C] Plastic flat panel photobioreactor designed in AlgaePARC Wageningen University, Wageningen, Netherlands, (adapted from [77]); D] Vertical plastic bag reactor, (reprinted from [67]);

Objectives

General objective

Contribute to the development of biotechnological processes to propagate microalgae destined to obtain metabolites of industrial interest in human health and animal aquaculture.

Specific objectives

- Evaluation of the biomass growth rate and pigments productivity of different microalgae strains and the variables that affect pigments production throughout an average industrial cultivation biotechnological process.
- Development of a methodology that allows efficient use of carbon dioxide, aiming to avoid CO_2-desorption from the liquid culture medium through analysing gas-liquid mass transfer processes within photobioreactors.
- Establishment of a methodology that allows assessing the radiative properties of phototrophic suspensions throughout the process duration.
- To obtain a model for the kinetics of pigment production that meets the condition of considering the radiant energy field (intensity and availability of radiant energy), CO_2 transfer phenomena and the mixing regime of tubular horizontal photobioreactors.
- To design a systematic scaling-up methodology that allows predicting the productivity (in terms of biomass and pigments) of large-scale photobioreactors (PBR) from tests in a 3L capacity laboratory-scale photobioreactor.

Additional information concerning the specific objectives: as it is possible to be checked in the Academic production list associated with this manuscript, there was academic articles published as a result of joint work with Dr Rodrigo Leonardi, a former PhD student of Prof. Heinrich. The first and last specific objectives listed above are not described in the present thesis, as they were covered during the experimental work associated with Dr Leonardi's thesis: "DISEÑO, CARACTERIZACIÓN, MODELADO Y OPTIMIZACIÓN DE FOTOBIORREACTORES DESTINADOS AL CULTIVO DE MICROALGAS Y LA PRODUCCIÓN DE METABOLITOS DE INTERÉS TECNOLÓGICO-BIOLÓGICO" published in the year 2020 in the UNL, Argentina. Further information concerning these topics is present in the academic work listed at the beginning of this manuscript.

Chapter (1)

A colourimetric method for the measuring of the mass transfer kinetics of CO_2 in aqueous media.

---

(1). – Summary

The measurement of the gas-liquid mass transfer coefficient of carbon dioxide in aqueous media is relevant in the field of phototrophic microorganism culture. Here, it is presented an approach that allowed the handling of a system composed of seven chemical reactions, in which the transfer process of carbon dioxide (CO_2) was one of them, pursuing the objective of quantifying the rate of dissolution of carbon dioxide in a designed liquid medium. A simple methodology involving the use of an acid-base indicator acting as a tracer was successfully employed. It was established that starting from a condition distant from its unique equilibrium, through the alteration of the initial pH value of a designed arbitrary state by adding onto it exact amounts of a strong base, the incorporation of CO_2 from an air current in contact with the perturbed liquid, occurred in order to restore a new balance. For each experiment achieved under the same operational conditions, it was possible to calculate nearly equal values of kinetic constants, which hold information about the behaviour of the system. Collectively the results presented here suggest that this methodology could be adapted to several different systems, enlightening easier ways of incorporating the transfer kinetics of this major carbon source on the existing growth kinetic models of phototrophic microorganisms. At the same time, it highlights the fact that probably the rate-controlling step is not the transfer reaction of gaseous CO_2 by itself, as the process of hydration of it is.

(2). – Introduction

It is thought that the quantity and quality of light are the major concerns in conducting properly any culture of phototrophic microorganisms [78]. Photosynthetic microalgae harbour enormous potential as light-driven green-cell factories for sustainable bioproduction of a range of natural and heterologous products [79]. In order to grow in an autotrophic way, light must be supplied to the cultures, plus a sufficient amount of dissolved carbon dioxide (CO_2), among other nutrients. One accepted criterion for culture techniques is managing to equalize the rate of transfer of CO_2 with the rate of fixation of it due to photosynthesis [80]. Even if light requirements are sufficient, mass transfer limitations could slow down the cell growth of microalgae [81], [82]. Therefore, several works have been carried out analysing different configurations of photobioreactors (PBR) whose characteristics allow a suitable area of contact between the aqueous growth medium with air, seeking for proper bubble sizing and mixing regimes, and also supplement CO_2 in the air stream [83], [84]. Even though this is feasible, the impact of the cost of providing CO_2 is estimated to be at least 27% of the total microalgal production system costs [85]. Moreover, carbon loss due to desorption is unavoidable and was recently proved, for raceways ponds, that variations in the CO_2 molar fraction of the air supplied or the gas flow rates did not modify biomass productivity but affected carbon loss through degassing, increasing it [80], [86].

Aiming to contribute from other perspectives, assumptions and models have been established in search of an answer on how important it could be to know the dynamics and the mechanism of the mass transfer process of CO_2 into aqueous media. At the time of modelling a biphasic system composed of an aqueous solution exchanging carbon dioxide with a gas phase dispersed in its interior, the majority of the absorption models published assume that a total mass of carbon is transferred through a prolonged steady-state process involving a quasi-constant mass flux of this gaseous species during the exchange, entirely dominated by slight changes in the concentration of CO_2 dissolved, in order to fulfil with Henry's law, assuming that it is a purely physical process [87], [88]. Such assumptions could be unquestionable if the dissolved molecules of CO_2 remain in that form, but it is known that a process of hydration also exists, with the consequent formation of three other ionic species: HCO_3^-, CO_3^{-2} and H^+. The integration of these chemical reactions to other models has been done [89]–[92], proposing to follow the evolution of the mass transfer process of CO_2 via the changes in the concentration of Hydronium ions, assuming Henry's law, and commuting pH shifts into carbonic acid shifts through the well-known acid-base dissociation constants, based on the fact that carbonic acid formation (hydration process) might be the controlling step of the whole process [93]. Nonetheless, even if the whole mass transfer process of CO_2 may be in a steady state, this does not imply that all the step reaction rates must be processes independent of time. Thus, it could be helpful to moot if there is no effect whatsoever of these acid-base reactions over the kinetics of the first step, the gaseous mass transfer process, or if a coupled relationship in which the hydronium ions formation (or its consumption in a desorption process) may have an effect on the exchanging of CO_2, should not be ignored.

Up to now, the development of methodologies that allow the measurement of the rate of dissolution of CO_2 implies the use of techniques that estimate the desired outcome via indirect data. Danckwerts and Gillham [87] proposed a technique that uses an alkaline treatment and, through the measurement of the oxygen mass transfer coefficient in the liquid (Kla_{O2}), estimated the Kla_{CO2} using a relationship which correlates both species with their respective diffusivities in water. The latter allows the calculation of the rate of these processes, making use of the two-film theory. Livansky (1990) [94] determined the rate of desorption of carbon dioxide from a stirred solution without bubbling using pH profiles. Dahod (1993) [95] allowed dissolved carbon dioxide to diffuse through silicone tubing into a nitrogen gas stream to measure steady-state dissolved carbon dioxide concentrations, but that method would be too slow to determine transient concentration changes. Hill (2006) [90] proposed the use of pH probes in order to follow the dissolution of CO_2 into freshwater from the air, and through a steady-state proposal, managed to calculate a Kla_{CO2} value with considerable time delay, neglecting the concentration of other ionic species present. Later, Kordac and Linec (2008) proposed the use of other models for the calculation of Kla_{CO2} in salty waters based on the analysis of Rixon (1948) [91] and recently Hindi (2017) [88] published Kla_{CO2} values for absorption and desorption models, following the same methodology.

Here, this study set forth a different insight that enabled a practical treatment of a system composed of at least seven chemical reactions, of which the mass transfer process of carbon dioxide was one of them. Departing from a designed perturbed state, which is far away from its unique equilibrium, while the dissolution of CO_2 from an air current in contact with an aqueous solution naturally occurred, we quantified the absorbance of an acid-base indicator in the liquid through time. Since the tracer reacted instantaneously with the hydronium ions formed via the hydration process of carbon dioxide, it allowed characterising the rate of incorporation of the only gas with the possibility to react upon entering into the liquid present in the gaseous phase. Because our proposal involved the treatment of a non-equilibrium system, the results obtained were combined with a model arising from a methodical perspective of irreversible thermodynamics. Altogether, these results allowed us to measure the rate of the mass transfer process of CO_2 as well as the rate of hydration of the same species. In addition, it was possible to infer a coupled relationship between the shift in the concentration of hydronium ion (during the transient state) and the driving force of the absorption process of CO_2 in the progression of the system towards the direction of its final thermodynamic equilibrium state.

(3). - Specific objectives

- To analyse CO_2 gas-liquid mass transfer processes within photobioreactors.

(4). - Materials and methods

(4.1). - Reactor and experimental conditions

The experiments were performed in a Labfors 3 bioreactor from INFORS HT. This commercial model has a working volume of 3 [L] and offers the possibility to control the most important operative variables. The liquid inside was mixed using two sets of Rushton turbines. In all the runs, the temperature (*T*) was set to 298 [°K], stirring speed of 300 [rpm] and aeration rate of filtered air (*Q*), equal to 1.2 [L min^{-1}], with a partial pressure of carbon dioxide in the feed stream ($P^{f}_{CO_{2},g}$) of the bioreactor equal to 0.27 [mmHg]. Regarding the composition of the liquid phase, mixtures of dihydrogen and monohydrogen phosphate, with Sodium chloride in a final volume of distilled water equal to 3 [L], were prepared. Maintaining constantly a total mass of phosphorus compounds equivalent to 2.0 10^{-3} [mole L^{-1}], three initial compositions were designed, taking the molar fraction of dihydrogen phosphate as a variable ($x_{H_2PO_4^-}$), with values: 0.2, 0.5 and 0.8. Each mixture was formulated by dissolving each required amount of mono and disodium salts, respectively ($m^{0}_{NaH_2PO_4}+m^{0}_{Na_2HPO_4}$). The concentration of Sodium chloride was the same for all the runs (m^{0}_{NaCl}), holding a value of 7.0 10^{-3} [mole L^{-1}]. To estimate the pH value of the mixtures, each proposed condition was simulated in MATLAB with the algorithm *fzero*, calculating the proton molar concentration from the electroneutrality condition. Each solution was treated as non-ideal, utilizing the extended law of Debye-Hückel, as well as the dissociation constants of every chemical equilibrium involved (Appendix – Table A-1). From this treatment, it has been selected three concentrations of NaOH ($m_{NaOH,p}$): 1.2 10^{-3} [mole L^{-1}], 1.5 10^{-3} [mole L^{-1}] and 1.8 10^{-3} [mole L^{-1}], which allowed the generation of nine non-equilibrium conditions. Then, these nine conditions were tested in the reactor and assessed through the presence of a defined amount of Cresol Red (m_{CR}), an acid-base indicator acting as a tracer. The absorbance at 573 [nm] from aliquots of 2 [mL] of each mixture, every 5 minutes, was registered, starting at zero time and following the progression of the system until no shift in the optical density of the samples was detected. After its measurement, every sample was thereupon restored to the vessel.

(4.2). - Preparation of Sodium Hydroxide

The solution of Sodium Hydroxide ($m_{NaOH,p}$) that was employed to perform the perturbations was prepared to dissolve 40 [g] of NaOH in a litre of distilled water. The unitary concentration of this solution (1 [mole L^{-1}]) was assessed through titration. The titrated solution was then stored until its use was required.

(4.3). - Preparation of Cresol Red

The acid-base indicator's solution, Cresol Red, was prepared to dissolve 9.0 10^{-4} [mole] of it in 100 [mL] of distilled water, plus 200 [µL] of NaOH, 5 [mole L^{-1}]. The later procedure reached a solution with a final concentration of 9.0 10^{-3} [mole L^{-1}]. In order to secure measurements of Absorbance at 573 [nm] in the linear range of a BOECO VIS S-20 spectrophotometer, it was calculated from Lambert – Beer's law, including the acid-base equilibria of Cresol Red into the electroneutrality condition of the system under study, that a concentration value equal to 1.5 10^{-5} [molal] was required (m_{CR}).

(4.4). - regression of intrinsic parameters

The correspondent optical density values registered through the time of each run performed at 573 [nm] were combined with the equations obtained by irreversible thermodynamics (Section 5 – eq. (21) and (22)), utilising the dissociation constant of Cresol Red in water, in combination with the lever rule. This last methodology involved measuring, before making the perturbation with NaOH, the value of the optical density of 10 [mL] of each mixture under a pH value equal to 5 (the total mass of Cresol Red present in an acidic form) and at pH value of 12 (the total mass of Cresol Red present in a basic form). Using this methodology, 18 runs (the nine conditions by duplicate) were regressed, employing the *lscqcurvefit + multistart* solver of MATLAB. The latter is a nonlinear least-squares solver that finds the coefficients necessary to minimize the difference between observed and input data. Every independent data series was adjusted utilizing the trust-region-reflective algorithm under a default step tolerance and function tolerance. Finally, the non-linear 90% confidence intervals of the kinetic constants of interest were calculated through the *nlparci* solver of MATLAB. This last required the Jacobian regression matrix of each experimental data series obtained.

(5). - Theoretical approach and mathematical model

(5.1). - *The absorption of CO_2 on $H_2O / H_2PO_4^- / HPO_4^{2-}$ mixtures: gas to liquid phase transfer and ensuing chemical reactions. The overall equilibrium state of the transfer process.*

Let us denote by $m_{HCO_3^-}$, $m_{CO_3^{2-}}$, $m_{H_2PO_4^-}$, $m_{HPO_4^{2-}}$, $m_{PO_4^{3-}}$, m_{HO^-}, m_{H^+} and m_{Na^+} the molal concentrations of the ionic species $HCO_3^-, CO_3^{2-}, H_2PO_4^-, HPO_4^{2-}, PO_4^{3-}, OH^-, H^+$ and Na^+, respectively.

The passive transport of CO_2 across the gas-liquid interface was modelled as a pseudo-chemical reaction. The equilibrium state is wholly characterised by T, P_{CO_2} and the species concentrations $m_{HCO_3^-}$, $m_{CO_3^{2-}}$, $m_{H_3PO_4}$, $m_{H_2PO_4^-}$, $m_{HPO_4^{2-}}$, $m_{PO_4^{3-}}$, m_{OH^-}, m_{H^+}, m_{Na^+} and $m_{CO_{2,dis}}$. Nevertheless, not all these state properties are independently variable at equilibrium. They are functionally related to each other by the following constraints:

- The species concentrations $m_{HCO_3^-}$, $m_{CO_3^{2-}}$, $m_{H_2PO_4^-}$, $m_{HPO_4^{2-}}$, $m_{PO_4^{3-}}$, m_{HO^-}, m_{H^+}, m_{Na^+} must satisfy the electro-neutrality condition:
  $m_{HCO_3^-} + 2\,m_{CO_3^{2-}} + m_{H_2PO_4^-} + 2m_{HPO_4^{2-}} + 3m_{PO_4^{3-}} + m_{HO^-} = m_{H^+} + m_{Na^+}$,

where $m_{Na^+} = m^0_{H_2PO_4^-} + 2m^0_{HPO_4^{2-}}$.

- By setting up a phosphorus atoms balance, we also have the constraint:
  $m_{H_3PO_4} + m_{H_2PO_4^-} + m_{HPO_4^{2-}} + m_{PO_4^{3-}} = m^0_{H_2PO_4^-} + m^0_{HPO_4^{2-}}$
- There are seven chemical equilibrium conditions between the chemical potentials of reactants or products, with one condition for each independent reaction.

Reaction pathway	***Reaction rate***	***Affinity***
$CO_{2,g} \xrightleftharpoons[k_{-1}]{k_1} CO_{2,d}$	r_1	$A_1 = \left[\mu_{CO_{2,g}} - \mu_{CO_{2,sol}}\right]$
$CO_{2,sol} + H_2O \xrightleftharpoons[k_{-2}]{k_2} HCO_3^- + H^+$	r_2	$A_2 = \left[\mu_{CO_{2,sol}} + \mu_{H_2O} - \mu_{HCO_3^-} - \mu_{H^+}\right]$
$HCO_3^- \xrightleftharpoons[k_{-3}]{k_3} CO_3^{2-} + H^+$	r_3	$A_3 = \left[\mu_{HCO_3^-} - \mu_{CO_3^{2-}} - \mu_{H^+}\right]$
$H_3PO_4 \xrightleftharpoons[k_{-4}]{k_4} H_2PO_4^- + H^+$	r_4	$A_4 = \left[\mu_{H_3PO_4} - \mu_{H_2PO_4^-} - \mu_{H^+}\right]$
$H_2PO_4^- \xrightleftharpoons[k_{-5}]{k_5} HPO_4^{2-} + H^+$	r_5	$A_5 = \left[\mu_{H_2PO_4^-} - \mu_{HPO_4^{2-}} - \mu_{H^+}\right]$
$HPO_4^{2-} \xrightleftharpoons[k_{-6}]{k_6} PO_4^{3-} + H^+$	r_6	$A_6 = \left[\mu_{HPO_4^{2-}} - \mu_{PO_4^{3-}} - \mu_{H^+}\right]$
$H_2O \xrightleftharpoons[k_{-7}]{k_7} HO^- + H^+$	r_7	$A_7 = \left[\mu_{H_2O} - \mu_{H^+} - \mu_{HO^-}\right]$

Table 1: *The process of* CO_2 *transfer from gas (*$_g$*) to liquid phase (*$_d$*) (aqueous phase).* k_i *and* k_{-i} *values are the correspondent velocity constants of the forward and backward reaction of each step from 1 to 7.*

Therefore, at the equilibrium state, we are left with only two properties which are independent variables. For convenience, we chose T and P_{CO_2} as the independent variables.

Altogether, the concentration of reactants, products and intermediate species must satisfy the step equilibrium constants:

$$K_1(T)=\frac{m^{(eq)}_{CO_2}}{P_{CO_2}}\ ;\ m^{(eq)}_{CO_2}=K_1(T)\,P_{CO_2} \tag{0.1-a}$$

$$K_2(T)=\frac{m^{(eq)}_{HCO_3^-}\,m^{(eq)}_{H^+}}{m^{(eq)}_{CO_2}};m^{(eq)}_{HCO_3^-}=K_2(T)\frac{m^{(eq)}_{CO_{2,dis}}}{m^{(eq)}_{H^+}}=K_1(T)\,K_2(T)\frac{P_{CO_2}}{m^{(eq)}_{H^+}} \tag{0.1-b}$$

$$K_3(T)=\frac{m^{(eq)}_{CO_3^{2-}}\,m^{(eq)}_{H^+}}{m^{(eq)}_{HCO_3^-}};m^{(eq)}_{CO_3^{2-}}=K_3(T)\frac{m^{(eq)}_{HCO_3^-}}{m^{(eq)}_{H^+}}=K_1(T)\,K_2(T)\,K_3(T)\frac{P_{CO_2}}{\left(m^{(eq)}_{H^+}\right)^2} \tag{0.1-c}$$

$$K_4(T)=\frac{m^{(eq)}_{H_2PO_4^-}\,m^{(eq)}_{H^+}}{m^{(eq)}_{H_3PO_4}};\quad m^{(eq)}_{H_2PO_4^-}=K_4(T)\frac{m^{(eq)}_{H_3PO_4}}{m^{(eq)}_{H^+}} \tag{0.1-d}$$

$$K_5(T)=\frac{m^{(eq)}_{HPO_4^{2-}}\,m^{(eq)}_{H^+}}{m^{(eq)}_{H_2PO_4^-}};m^{(eq)}_{HPO_4^{2-}}=K_5(T)\frac{m^{(eq)}_{H_2PO_4^-}}{m^{(eq)}_{H^+}}=K_4(T)\,K_5(T)\frac{m^{(eq)}_{H_3PO_4}}{\left(m^{(eq)}_{H^+}\right)^2} \tag{0.1-e}$$

$$K_6(T)=\frac{m^{(eq)}_{PO_4^{3-}}\,m^{(eq)}_{H^+}}{m^{(eq)}_{HPO_4^{2-}}};m^{(eq)}_{PO_4^{3-}}=K_6(T)\frac{m^{(eq)}_{HPO_4^{2-}}}{m^{(eq)}_{H^+}}=K_4(T)\,K_5(T)\,K_6(T)\frac{m^{(eq)}_{H_3PO_4}}{\left(m^{(eq)}_{H^+}\right)^3} \tag{0.1-f}$$

$$K_7(T)=m^{(eq)}_{H^+}\,m^{(eq)}_{HO^-}\quad;\quad m^{(eq)}_{HO^-}=\frac{K_7(T)}{m^{(eq)}_{H^+}} \tag{0.1-g}$$

together with the electro-neutrality condition,

$$m^{(eq)}_{HCO_3^-}+2\,m^{(eq)}_{CO_3^{2-}}+m^{(eq)}_{H_2PO_4^-}+2m^{(eq)}_{HPO_4^{2-}}+3m^{(eq)}_{PO_4^{3-}}+m^{(eq)}_{HO^-}=m^{(eq)}_{H^+}+m_{Na^+} \tag{0.1-h}$$

and the phosphorus atoms balance,

$$m^{(eq)}_{H_3PO_4}+m^{(eq)}_{H_2PO_4^-}+m^{(eq)}_{HPO_4^{2-}}+m^{(eq)}_{PO_4^{3-}}=m^{0}_{H_2PO_4^-}+m^{0}_{HPO_4^{2-}} \tag{0.1-i}$$

The equilibrium constants are correlated with temperature as follows,

$$pK_i=-log_{10}K_i=\frac{A_1^{(i)}}{T}-A_2^{(i)}+A_3^{(i)}\,T\quad;\ (i=1,2,3,4,5,6,7) \tag{0.2}$$

while their weak dependence on the solution pressure will be considered negligible. Because of the mild pressure conditions prevailing in our experiments, the departure from the ideal gas behaviour of the vapour phase at equilibrium with the electrolyte solution will be neglected. Substitution of $m^{(eq)}_{HCO_3^-}, m^{(eq)}_{CO_3^{2-}}, m^{(eq)}_{HO^-}, m^{(eq)}_{H_3PO_4}$, $m^{(eq)}_{H_2PO_4^-}, m^{(eq)}_{HPO_4^{2-}}, m^{(eq)}_{PO_4^{3-}}, m^{(eq)}_{H^+}$ from Equations (1-b, c, d, e, f, g) in Equations (1-h, i) gives

$$\begin{aligned}
&\left(m^{(eq)}_{H^+}\right)^4 + \\
&\left[m^0_{H_2PO_4^-} + 2m^0_{HPO_4^{2-}}\right]\left(m^{(eq)}_{H^+}\right)^3 - \\
&\left[K_1K_2P_{CO_2} + K_4m^{(eq)}_{H_3PO_4} + K_7\right]\left(m^{(eq)}_{H^+}\right)^2 - \\
&\left[2\,K_1K_2K_3P_{CO_2} + 2K_4K_5m^{(eq)}_{H_3PO_4}\right]\left(m^{(eq)}_{H^+}\right) - \\
&\left[3K_4K_5K_6m^{(eq)}_{H_3PO_4}\right] = 0
\end{aligned} \tag{0.3}$$

and

$$m^{(eq)}_{H_3PO_4} = \frac{\left[m^0_{H_2PO_4^-} + m^0_{HPO_4^{2-}}\right]\left(m^{(eq)}_{H^+}\right)^3}{\left[\left(m^{(eq)}_{H^+}\right)^3 + K_4\left(m^{(eq)}_{H^+}\right)^2 + K_4K_5\left(m^{(eq)}_{H^+}\right) + K_4K_5K_6\right]} \tag{0.4}$$

$pK_i = -log_{10}\,K_i$ $(Molality\ scale)$	$t = 25[°C]$	A_1^i	A_2^i	A_3^i
$pK_1 = -log_{10}\,K_1$	4.3496	377.445	1.791382	0.016351
$pK_2 = -log_{10}\,K_2$	6.352	3404.71	14.8435	0.032786
$pK_3 = -log_{10}\,K_3$	10.329	2902.39	6.4980	0.02379
$pK_4 = -log_{10}\,K_4$	2.148	799.31	4.5535	0.013486
$pK_5 = -log_{10}\,K_5$	7.201	1979.5	5.3541	0.01984
$pK_6 = -log_{10}\,K_6$	12.37	-.-	12.37	-.-

$pK_7 = -log_{10} K_7$	13.995	4470.99	6.0875	0.01706

Table 1.1: The parameters in Equations (20) for $(i = 2,3,5)$ were taken from [96].

Combining equations (3) y (4) results in a sixth-order polynomial in the unknown $m_{H^+}^{(eq)}$

$$\begin{aligned}
&\left(m_{H^+}^{(eq)}\right)^6 + \\
&\left[K_4 + m^0_{H_2PO_4^-} + 2\left(m^0_{H_2PO_4^-} + m^0_{HPO_4^{2-}}\right)\right]\left(m_{H^+}^{(eq)}\right)^5 + \\
&\left[K_4K_5 - K_1K_2P_{CO_2} - K_4m^0_{HPO_4^{2-}}\right]\left(m_{H^+}^{(eq)}\right)^4 + \\
&\left[K_4K_5K_6 - K_1K_2\left(K_4 + 2K_3\right)P_{CO_2} - K_4K_5\left(m^0_{H_2PO_4^-} + 2m^0_{HPO_4^{2-}}\right)\right]\left(m_{H^+}^{(eq)}\right)^3 + \qquad (0.5)\\
&K_4\left[K_5K_6m^0_{H_2PO_4^-} - K_1K_2\left(K_5P_{CO_2} + 2K_3\right)P_{CO_2} - 3K_5K_6\left(m^0_{H_2PO_4^-} + m^0_{HPO_4^{2-}}\right)\right]\left(m_{H^+}^{(eq)}\right)^2 - \\
&\left[K_1K_2K_4K_5\left(K_6 + 2K_3\right)P_{CO_2} + \frac{1}{K_7}\right]\left(m_{H^+}^{(eq)}\right) - \\
&2K_1K_2K_3K_4K_5K_6P_{CO_2} = 0
\end{aligned}$$

In a more compact notation, Equation (5) can be recast into the following expression

$$a_0 + a_1\left(m_{H^+}^{(eq)}\right) + a_2\left(m_{H^+}^{(eq)}\right)^2 + a_3\left(m_{H^+}^{(eq)}\right)^3 + a_4\left(m_{H^+}^{(eq)}\right)^4 + a_5\left(m_{H^+}^{(eq)}\right)^5 + a_6\left(m_{H^+}^{(eq)}\right)^6 = 0 \qquad (0.6)$$

where

$$a_6 = 1 \qquad (0.7\text{-a})$$

$$a_5 = \left[K_4 + m^0_{H_2PO_4^-} + 2m^0_{HPO_4^{2-}}\right] \qquad (0.7\text{-b})$$

$$a_4 = \left[K_4K_5 + m^0_{HPO_4^{2-}}K_4 - K_1K_2P_{CO_2} - \frac{1}{K_7}\right] \qquad (0.7\text{-c})$$

$$a_3 = \left[K_4K_5\left(K_6 - m^0_{H_2PO_4^-}\right) - K_1K_2\left(K_4 + 2K_3\right)P_{CO_2} - K_4\frac{1}{K_7}\right] \qquad (0.7\text{-d})$$

$$a_2 = -K_4\left[\left(2m^0_{H_2PO_4^-} + m^0_{HPO_4^{2-}}\right)K_5K_6 + K_1K_2\left(K_5 + 2K_3\right)P_{CO_2} + K_5\frac{1}{K_7}\right] \tag{0.7-e}$$

$$a_1 = -\left[K_4K_5\left(K_1K_2\left(K_6 + 2K_3\right)P_{CO_2} + K_6\frac{1}{K_7}\right)\right] \tag{0.7-f}$$

$$a_0 = -2\ K_1K_2K_3K_4K_5K_6P_{CO_2} \tag{0.7-g}$$

The coefficients of this polynomial are evaluated for each value of the partial pressure of CO_2 in the gas phase, P_{CO_2}, and by substitution of the values of the equilibrium constants obtained from the correlations listed in Table 1.1 for the temperature of the system at global equilibrium. Substitution of each root of this polynomial in Equations (1-a-g) allows obtaining the rest of the unknowns in a simple, hierarchical substitution procedure.

The results obtained for P_{CO_2} in the range $\left(0.05\ mmHg < P_{CO_2} < 1.5\ mmHg\right)$ and $T = 298.15\ K$ are presented in Figures (1.1) and (1.2 - a,b).

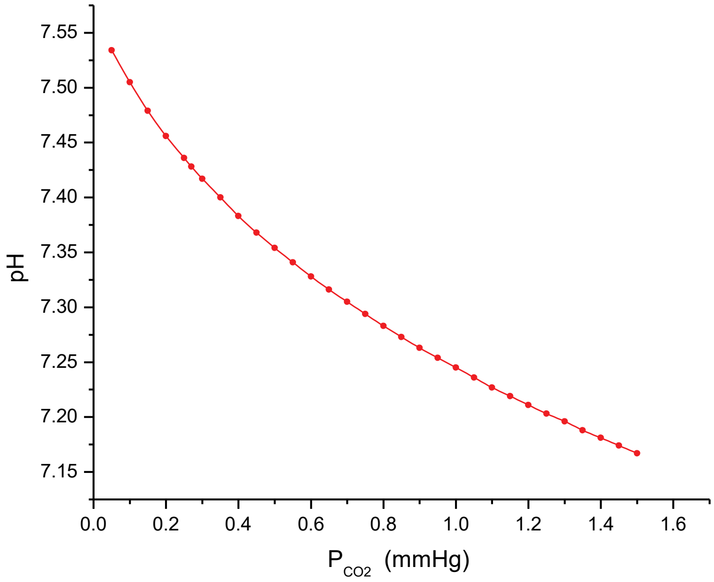

Figure 1.1: CO_2 absorption on $H_2O / H_2PO_4^- / HPO_4^{2-}$ mixtures. pH vs P_{CO_2} for $T = 298.15\ \ K$, $m^0_{H_2PO_4^-} = 0.6\ \ 10^{-3}\left(molal\right)$ and $m^0_{HPO_4^{2-}} = 1.4\ 10^{-3}\ \left(molal\right)$.

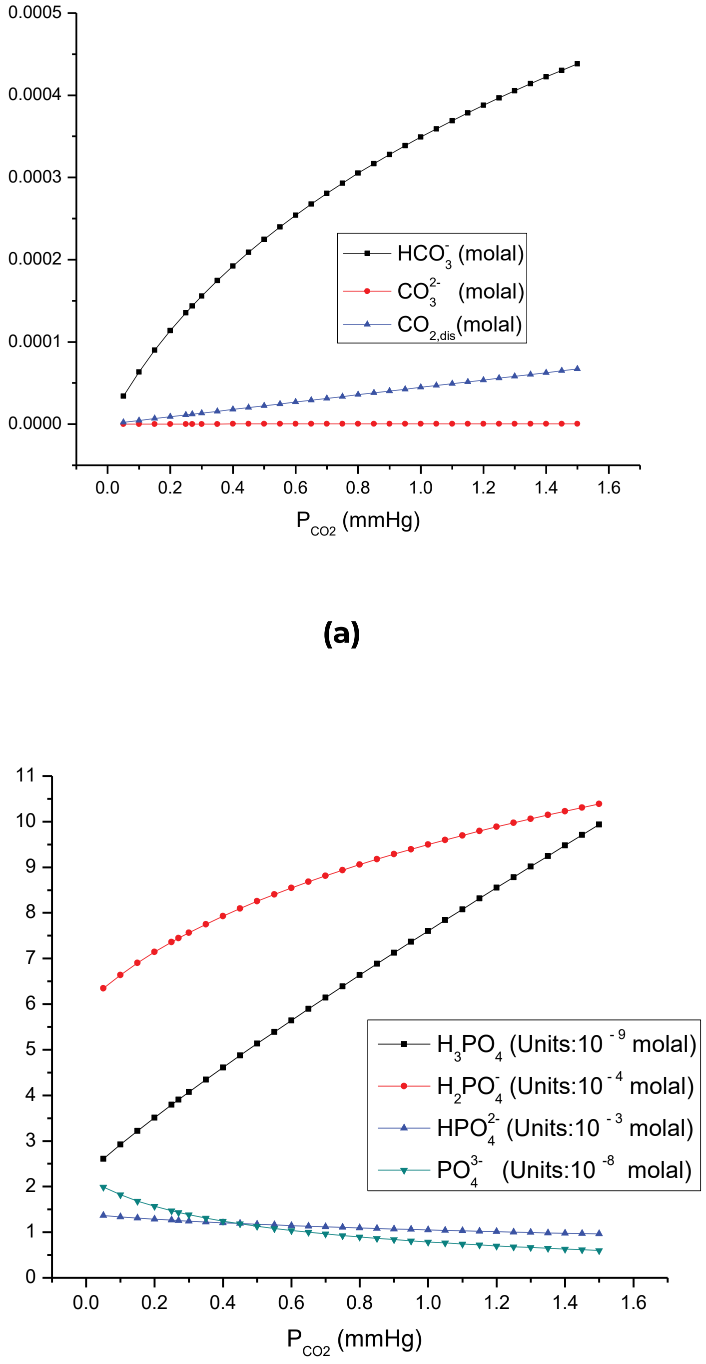

Figures 1.2 (a-b): CO_2 absorption on $H_2O / H_2PO_4^- / HPO_4^{2-}$ mixtures for $T = 298.15\ K$, $m^0_{H_2PO_4^-} = 0.6\ 10^{-3}\left(molal\right)$ and $m^0_{HPO_4^{2-}} = 1.4\ 10^{-3}\ \left(molal\right)$. Species concentrations have been expressed as multiples of the corresponding molal concentrations.

(5.2). - *The absorption of* CO_2 *on* $H_2O / H_2PO_4^- / HPO_4^{2-} / NaCl$ *mixtures in an open gas-liquid system. An irreversible thermodynamic approach.*

In order to correlate the observations in the changes of the absorbance of Cresol Red along with the experiments, we started considering an experiment in which an open, two-phase system (Fig. (1.3)) was initially at the state of overall equilibrium. This equilibrium state is wholly characterized by T, $P_{CO_2,g}^{(eq)}$ and the species concentrations $m_{HCO_3^-}, m_{CO_3^{2-}}, m_{H_3PO_{4,d}}, m_{H_2PO_4^-}, m_{HPO_4^{2-}}, m_{PO_4^{3-}}, m_{OH^-}, m_{H^+}$, m_{Na^+}, m_{Cl^-} and $m_{CO_{2,dis}}$. The gas phase in contact with the liquid (totally dispersed in it in bubbles form) occupies a volume that was denoted as $V^{(1)}$, in consequence, $V^{(2)}$ represents the volume of the liquid phase (Fig. (1.3)). Not all these state properties are independent variables at equilibrium. They are functionally related to each other by the following constraints:

- The species concentrations must satisfy the electro-neutrality condition: $\sum z_i \; m_i = 0$,

  where $m_{Na^+} = m^0_{NaH_2PO_4} + m^0_{Na_2HPO_4} + m^0_{NaCl}$ and $m_{Cl^-} = m^0_{NaCl}$.

- By setting up a phosphorus atoms balance, we also have the constraint: $m_{H_3PO_{4,dis}} + m_{H_2PO_4^-} + m_{HPO_4^{2-}} + m_{PO_4^{3-}} = m^0_{NaH_2PO_4} + m^0_{Na_2HPO_4}$

The two phases are simple and uniform subsystems separated from each other by a ***diathermal*** and ***permeable*** surface. The mass exchange between the two phases and chemical reactions in the liquid phase are not necessarily at equilibrium. Nonetheless, the non-uniform ***closed simple system*** as a whole is assumed at internal thermal equilibrium and also at thermal equilibrium with a bath at temperature T. The system is also at internal mechanical equilibrium and with atmospheric P. We considered the case in which the system, initially at balance, was suddenly perturbed by adding a pulse of a $NaOH$ solution ($m_{NaOH,p}$), with a negligible change in the liquid phase volume. The increase in the Na^+ concentration due to the addition of a pulse of the basic solution had a direct impact on the electro-neutrality condition. It was assumed that ionic dissociation reactions (i.e., reactions 3 to 7 of Table 1) rapidly reached their individual equilibrium, which was maintained as they evolved with time at the pace of the progress of the much slower reactions (i.e., reactions 1 and 2) [88]. Departing from the perturbed initial state, the system evolved to reach a new final equilibrium state. Under the conditions prevailing in our work, the effects of the exchange of H_2O between gas and liquid phases were negligible, and the N_2 present was considered an inert gas and insoluble in the liquid phase. *Moreover, no chemical reactions occurred in the gas phase*.

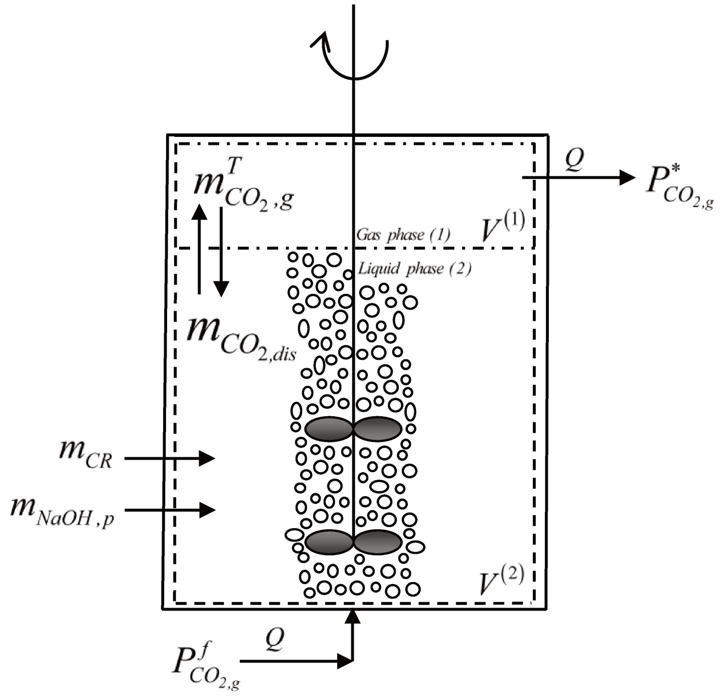

Figure 1.3: Schematics of the open gas-liquid system under study: a bioreactor vessel containing the perturbed liquid (liquid phase (2), continuously stirred by mechanical mixing and gas sparging) and the gaseous phase totally dispersed through bubbles (white circles) in its interior, exchanging $CO_{2\,(g)}$ from a feed current that goes out the liquid through the upper part. In fig. (1.3), $m^{T}_{CO_2,g}$ is the total mass of CO_2 that it is being exchanged between the phases and $m_{CO_{2,dis}}$ is the concentration of dissolved CO_2 in equilibrium with phase (1). $V^{(1)}$ represents the gas volume in contact with the liquid, as $V^{(2)}$ is the volume of the liquid phase. $P^{f}_{CO_{2,g}}$ is the partial pressure of carbon dioxide in the fed gas stream and, consequently, $P^{*}_{CO_{2,g}}$ is the partial pressure of CO_2 that flows out of the liquid. Both quantities flow through the liquid under a constant aeration rate (Q). $m_{NaOH,p}$ is the concentration of a strong base that effectively creates the perturbation and m_{CR} is the concentration of the acid-base indicator present.

For a system of these characteristics, the number of moles of species i in a phase α, $n_i^{(\alpha)}$, may change with time due to chemical reactions ("react") and mass exchange between phases ("exch"), and since we are modelling an open system, mass fluxes of feed or output of reactants (in/out the contactor) has also to be included. Thus, the following balance may be written:

$$\frac{dn_i^{(\alpha)}}{dt} = \left(\dot{n}_i^{(\alpha)} \right)_{feed} - \left(\dot{n}_i^{(\alpha)} \right)_{output} + \left(\frac{dn_i^{(\alpha)}}{dt} \right)_{react} + \left(\frac{dn_i^{(\alpha)}}{dt} \right)_{exch} \quad ; \quad \alpha = 1,2 \tag{1}$$

The application of equation (1) on the seven reactions from Table 1, for both phases containing the species mentioned above, fulfilling the conditions also mentioned earlier, gives:

$$\frac{dn_{CO_2}^{(1)}}{dt} = \underbrace{\left(\dot{n}_{CO_2}^{(1)} \right)}_{\substack{feed\ mass\ flux \\ of\ CO_{2,g}}} - \underbrace{\left(\dot{n}_{CO_2}^{(1)} \right)}_{\substack{output\ mass\ flux \\ of\ CO_{2,g}}} + \left(\frac{dn_{CO_{2,g}}^{(1)}}{dt} \right)_{exch} = \left(\dot{n}_{CO_{2,g}}^{(1)} \right)_{f} - \left(\dot{n}_{CO_{2,g}}^{(1)} \right)_{*} + \left(\frac{dn_{CO_{2,g}}^{(1\to 2)}}{dt} \right)_{exch} \tag{2}$$

$$\frac{dn_{CO_2}^{(2)}}{dt} = \left(\frac{dn_{CO_{2,dis}}^{(2)}}{dt} \right)_{react} + \left(\frac{dn_{CO_{2,dis}}^{(2)}}{dt} \right)_{exch} = -V^{(2)} r_2^* + \left(\frac{dn_{CO_{2,dis}}^{(2\to 1)}}{dt} \right)_{exch} \tag{3}$$

$$\frac{dn_{HCO_3^-}^{(2)}}{dt} = \left(\frac{dn_{HCO_3^-}^{(2)}}{dt} \right)_{react} = V^{(2)} \left(r_2^* - r_3^* \right) \tag{4}$$

$$\frac{dn_{CO_3^{2-}}^{(2)}}{dt} = \left(\frac{dn_{CO_3^{2-}}^{(2)}}{dt} \right)_{react} = V^{(2)} r_3^* \tag{5}$$

$$\frac{dn_{H_3PO_{4,dis}}^{(2)}}{dt} = \left(\frac{dn_{H_3PO_{4,dis}}^{(2)}}{dt} \right)_{react} = -V^{(2)} r_4^* \tag{6}$$

$$\frac{dn^{(2)}_{H_2PO_4^-}}{dt} = \left(\frac{dn^{(2)}_{H_2PO_4^-}}{dt}\right)_{react} = V^{(2)}\left(r_4^* - r_5^*\right) \tag{7}$$

$$\frac{dn^{(2)}_{HPO_4^{2-}}}{dt} = \left(\frac{dn^{(2)}_{HPO_4^{2-}}}{dt}\right)_{react} = V^{(2)}\left(r_5^* - r_6^*\right) \tag{8}$$

$$\frac{dn^{(2)}_{PO_4^{3-}}}{dt} = \left(\frac{dn^{(2)}_{PO_4^{3-}}}{dt}\right)_{react} = V^{(2)} r_6^* \tag{9}$$

$$\frac{dn^{(2)}_{OH^-}}{dt} = \left(\frac{dn^{(2)}_{OH^-}}{dt}\right)_{react} = V^{(2)} r_7^* \tag{10}$$

$$\frac{dn^{(2)}_{H^+}}{dt} = \left(\frac{dn^{(2)}_{H^+}}{dt}\right)_{react} = V^{(2)}\left(r_2^* + r_3^* + r_4^* + r_5^* + r_6^* + r_7^*\right) = V^{(2)} r_{H^+}^* \tag{11}$$

In eq. (2 - 11) above, it can be seen that departing from eq. (3) every single change in the quantity of dissolved carbon dioxide will have a direct impact on every balance under it, altogether linked by eq. (11). If we recall the definition of eq. (Appendix (A-12)) altogether with (Appendix (A-31)), eq. (11) may be written in the following useful form, where $\varepsilon_{H^+}^*$ is the departure from the equilibrium of the hydronium ions molar concentration:

$$\frac{d\varepsilon_{H^+}^*}{dt} = -\frac{V^{(2)}}{m_{H^+}^{(eq)}} r_{H^+}^* \; ; \quad \varepsilon_{H^+}^* = \left(\frac{m_{H^+}^{(eq)} - m_{H^+}^*}{m_{H^+}^{(eq)}}\right) \tag{12}$$

In order to obtain a different, more functional form of eq. (2), in combination with the definition (Appendix (A-39)), the changes in the molar concentration of carbon dioxide through time, in the gas phase, can be rearranged to:

$$\frac{d\varepsilon_{P_{CO_2,g}}^*}{dt} = -\frac{1}{\left(n_{CO_2,g}^{(1)}\right)_{eq}}\left[Q\left(\frac{P_{CO_2,g}^f}{RT}\right) - Q\left(\frac{P_{CO_2,g}^*}{RT}\right) \pm a_{int}\, j_{CO_2,g}^{(1\rightarrow 2)}\right] \tag{13}$$

In eq. (13), a_{int} is the interfacial surface area per unit volume of the liquid phase and $j_{CO_2,g}^{(1\rightarrow 2)}$ is the net mole flux density of $CO_{2,g}$ from phase (1) to phase (2). R is the

Ideal gas constant, and the temperature of the bubbling gas is assumed as T, equal value to the liquid medium.

In order to correlate the observations in the changes of the absorbance of the acid-base indicator along with the experiments, a relationship bestowed by the condition of the minimal rate of generation of internal entropy [97] has been used. The process involves writing each of the reactions shown in Table 1, based on their contribution to the generation of entropy ($\dot{\sigma}$) throughout the system, or in other words, to express every reaction as the combination of the Affinity (driving force) involved in each step, and the reaction rate of every step (thermodynamic flows – Appendix eq. (A-6)). In the linear irreversible regime, the rate of transfer of carbon dioxide and those of the ensuing chemical reactions could be expressed in terms of Onsager Coefficients and linearised affinities. From the latter perspective, the rate of the process of dissolution of gaseous carbon dioxide (reaction step 1) and the process of hydration (reaction step 2) may be expressed in the following form (Appendix – eq. (A-19) – eq. (A – 23)):

$$r_1^* = a_{int} k_1 P_{CO_2,g}^{(eq)} \left[\varepsilon_{m_{CO_2,dis}}^* - \varepsilon_{P_{CO_2,g}}^* \right] \tag{14}$$

$$r_2^* = k_2 K_1 P_{CO_2,g}^{(eq)} \left[\varepsilon_{HCO_3^-}^* + \varepsilon_{H^+}^* - \varepsilon_{m_{CO_2,dis}}^* \right] \tag{15}$$

In eq. (14) and eq. (15) $P_{CO_2,g}^{(eq)}$ is the partial pressure of carbon dioxide, whose value is invariant. K_1 is the reciprocal value of Henry's constant. k_1 and k_2 are the kinetic constants of each step, and $\varepsilon_{m_{CO_2,dis}}^*$, $\varepsilon_{P_{CO_2,g}}^*$, $\varepsilon_{HCO_3^-}^*$, $\varepsilon_{H^+}^*$ are the departure from the equilibrium of each species involved. The kinetics of reactions 3 to 6 were deduced using the same methodology (Appendix – Table A-2). It should be noted that the affinities A_i $i = 1,2$ are not independent thermodynamic properties since they were required to add up to a value $A_0 = A_1 + A_2$ ***prescribed as the boundary condition***. *This last implies that the system is at least at partial equilibrium, with the transfer from gas to the liquid phase in progress and the ensuing reactions.*

There are no restrictions imposed on the values of A_3, A_4, A_5, A_6 and A_7, except for the requirement that the concentration of the components involved must satisfy the electro-neutrality condition and the total phosphorus atom conservation.

In line with the latter, the least possible $\dot{\sigma}$ was founded, minimizing the eq. (Appendix (A-6)) with Lagrange Multipliers. A set of seven algebraic equations were obtained, allowing us to write, for every admissible value of A_0, the expressions of the unknowns: $\varepsilon^*_{m_{CO_2,dis}}$, $\varepsilon^*_{HCO_3^-}$, $\varepsilon^*_{CO_3^{2-}}$, $\varepsilon^*_{H_3PO_{4,dis}}$, $\varepsilon^*_{H_2PO_4^-}$, $\varepsilon^*_{HPO_4^{2-}}$, $\varepsilon^*_{PO_4^{3-}}$, $\varepsilon^*_{OH^-}$ in terms of the only two independent variables $\varepsilon^*_{P_{CO_2,g}}$ and $\varepsilon^*_{H^+}$ (Appendix – eq. (29 – (a,h))). At the same time, from eq. (Appendix – (25-a)), it could readily derive the following critical condition,

$$\frac{L_{1,1}}{T}A_1 = \frac{L_{2,2}}{T}A_2 = \left(\frac{1}{T}\right)\frac{1}{\left(\frac{1}{L_{1,1}}+\frac{1}{L_{2,2}}\right)}A_0 \tag{16}$$

In eq. (16), $L_{1,1}$ and $L_{2,2}$ are the Onsager Coefficients of the first and second steps of the reaction pathway shown in Table 1 (Appendix – Table A-2). Eq. (16) could be rearranged into the following form:

$$r_1^* = r_2^* = r^* = \left(\frac{1}{T}\right)\frac{1}{\left(\frac{1}{L_{1,1}}+\frac{1}{L_{2,2}}\right)}A_0; \quad r^*_{H^+} = r_2^*;\ r_3^* = r_4^* = r_5^* = r_6^* = r_7^* = 0 \tag{17}$$

The expressions of r_1^*, r_2^* are the same as eq. (14) and (15). As for r^* is as follows:

$$r^{*}=\frac{P_{CO_{2},g}^{(eq)}}{\left[\frac{1}{a_{int}k_{1}}+\frac{1}{k_{2}K_{1}}\right]}\left[\varepsilon_{HCO_{3}^{-}}^{*}+\varepsilon_{H^{+}}^{*}-\varepsilon_{P_{CO_{2},g}}^{*}\right] \tag{18}$$

Only two among the three reaction rate expressions (r_1^* , $r_2^* = r_{H^+}^*$ and r^*) are linearly independent. The restriction given in Equations (Appendix – (29 – (a,h))) between the reaction rates of the independent non-equilibrium steps in the absorption-reaction mechanism is a distinctive result derived from the condition of the minimal rate of internal generation of entropy, in the Linear Irreversible Regime. The affinities (driving forces) associated with all ***the non-zero reaction rates*** must adjust their values in order to satisfy the constraint that the corresponding reaction rates ***must remain equal to each other*** as the system moves from an initial partial equilibrium state to the final global equilibrium state***,*** along the trajectory of the minimum rate of internal generation of entropy. ***The most significant driving force corresponds to the rate-determining step***.

By a combination of Equations (12) and (13) with equation (18), and recalling the definition of κ_{H^+} (Appendix – Eq. (33)), the set of ***coupled ordinary differential equations*** describing the dynamics of the two-phase system in its way to overall equilibrium is,

$$\frac{d\varepsilon_{H^{+}}^{*}}{dt}=-\frac{P_{CO_{2},g}^{f}}{m_{H^{+}}^{(eq)}\left[\frac{1}{a_{int}k_{1}}+\frac{1}{k_{2}K_{1}}\right]}\kappa_{H^{+}}\,\varepsilon_{H^{+}}^{*}+\frac{P_{CO_{2},g}^{f}}{m_{H^{+}}^{(eq)}\left[\frac{1}{a_{int}k_{1}}+\frac{1}{k_{2}K_{1}}\right]}\varepsilon_{P_{CO_{2},g}}^{*} \tag{19}$$

$$\frac{d\varepsilon_{P_{CO_{2},g}}^{*}}{dt}=RT\left(\frac{V^{(2)}}{V^{(1)}}\right)\frac{\kappa_{H^{+}}}{\left[\frac{1}{a_{int}k_{1}}+\frac{1}{k_{2}K_{1}}\right]}\varepsilon_{H^{+}}^{*}-\left[RT\left(\frac{V^{(2)}}{V^{(1)}}\right)\frac{1}{\left[\frac{1}{a_{int}k_{1}}+\frac{1}{k_{2}K_{1}}\right]}+\left(\frac{Q}{V^{(1)}}\right)\right]\varepsilon_{P_{CO_{2},g}}^{*} \tag{20}$$

In the last step, eq. (19) and (20) were compacted into a matrix form, and by finding the eigenvalues and eigenvectors corresponding to them, it was possible to elucidate a set of two uncoupled algebraic equations. Thus, in the process of dissipation of the perturbation to the initial equilibrium state, $\varepsilon^{*}_{P_{CO_2,g}}$ and $\varepsilon^{*}_{H^+}$ tend to zero with t as the system approaches a new equilibrium, according to,

$$\varepsilon^{*}_{P_{CO_2,g}(t)} = \frac{\left(\varepsilon^{*}_{H^+}\right)_{t\to 0}}{\left(x_1^{(1)} - x_1^{(2)}\right)}\left[e^{\lambda^{(1)}(t-t_0)} - e^{\lambda^{(2)}(t-t_0)}\right] + \frac{\left(\varepsilon^{*}_{P_{CO_2,g}}\right)_{t\to 0}}{\left(x_1^{(1)} - x_1^{(2)}\right)}\left[x_1^{(1)}e^{\lambda^{(2)}(t-t_0)} - x_1^{(2)}e^{\lambda^{(1)}(t-t_0)}\right] \tag{21}$$

and

$$\varepsilon^{*}_{H^+(t)} = \frac{\left(\varepsilon^{*}_{H^+}\right)_{t\to 0}}{\left(x_1^{(1)} - x_1^{(2)}\right)}\left[x_1^{(1)}e^{\lambda^{(1)}(t-t_0)} - x_1^{(2)}e^{\lambda^{(2)}(t-t_0)}\right] - \frac{x_1^{(1)}x_1^{(2)}\left(\varepsilon^{*}_{P_{CO_2,g}}\right)_{t\to 0}}{\left(x_1^{(1)} - x_1^{(2)}\right)}\left[e^{\lambda^{(1)}(t-t_0)} - e^{\lambda^{(2)}(t-t_0)}\right] \tag{22}$$

respectively (Appendix – eq. (A-45-a,b). The terms $\left(\varepsilon^{*}_{H^+}\right)_{t\to 0}$ and $\left(\varepsilon^{*}_{P_{CO_2,g}}\right)_{t\to 0}$ are unknown values that represent the magnitude of each ε_i at the beginning of the perturbed condition. t_0 is a factor included in the analysis aiming to explore if it could be a time delay effect in the process of dissipation of the perturbation. $x_1^{(1)}, x_1^{(2)}, \lambda^{(1)}, \lambda^{(2)}$ are constants whose expressions can be seen in equations (23-30) that retain the same values as the initial set of coupled equations (19) and (20).

$$\lambda^{1} = \frac{1}{2}\left[\; a_{11} + a_{22} \; - \sqrt{\; a_{11} - a_{22} \;{}^{2} + 4a_{12}a_{21}}\;\right] < 0 \tag{23}$$

$$\lambda^{2} = \frac{1}{2}\left[\; a_{11} + a_{22} \; + \sqrt{\; a_{11} - a_{22} \;{}^{2} + 4a_{12}a_{21}}\;\right] \tag{24}$$

$$x_1^{(1)} = \frac{\left[\left(a_{11} - a_{22}\right) - \sqrt{\left(a_{11} - a_{22}\right)^2 + 4a_{12}a_{21}} \right]}{2a_{21}} \tag{25}$$

$$x_1^{(2)} = \frac{\left[\left(a_{11} - a_{22}\right) + \sqrt{\left(a_{11} - a_{22}\right)^2 + 4a_{12}a_{21}} \right]}{2a_{21}} \tag{26}$$

$$a_{11} = -\frac{P_{CO_2}^f}{m_{H^+}^{eq}\left[\dfrac{1}{a_{\mathrm{int}}k_1} + \dfrac{1}{k_2K_1}\right]}\kappa_{H^+} < 0 \tag{27}$$

$$a_{12} = \frac{P_{CO_2}^f}{m_{H^+}^{eq}\left[\dfrac{1}{a_{\mathrm{int}}k_1} + \dfrac{1}{k_2K_1}\right]} > 0 \tag{28}$$

$$a_{21} = RT\left(\frac{V^2}{V^1}\right)\frac{\kappa_{H^+}}{\left[\dfrac{1}{a_{\mathrm{int}}k_1} + \dfrac{1}{k_2K_1}\right]} > 0 \tag{29}$$

$$a_{22} = -\left[RT\left(\frac{V^2}{V^1}\right)\frac{1}{\left[\dfrac{1}{a_{\mathrm{int}}k_1} + \dfrac{1}{k_2K_1}\right]} + \left(\frac{Q}{V^1}\right)\right] < 0 \tag{30}$$

(6). - Results and discussion

Eukaryotic green microalgae hold potential as green-cell factory biocatalysts for sustainable light-driven production of heterologous products making use of carbon dioxide as a carbon source [98]–[101]. The study of CO_2 transfer in photobioreactors is often neglected in favour of light transfer because photo-limitation is difficult to avoid. Ensuring efficient CO_2 transfer is nevertheless of high interest; in fact, CO_2 is often used in excess to avoid limitation, but in this case, carbon loss due to degassing can be high and may represent significant production costs [80]. In order to find better strategies for inorganic carbon intake to photosynthetic microorganisms' cultures, a better understanding of the kinetics of the CO_2 dissolution process and the reactions that follow is required.

A dissimilar perspective was used here, attempting to contribute to understanding the kinetics of the process of incorporation of CO_2 from the gaseous phase. Up to date, different assumptions consider the occurrence of a heterogeneous reaction of absorption of CO_2 from the gaseous phase into an aqueous medium and its consequential hydration occurring naturally after the incorporation as partially independent processes, thus remaining unclear if there is no effect whatsoever in the shifts of hydronium ions over the kinetics of dissolution of CO_2 molecules, or if an associated relationship is possible to take into account. Here, it was sought to investigate whether it was possible to measure the overall process of incorporation of the desired greenhouse gas, following the concentration of hydronium ions produced in the transition from a perturbed state while it goes over its trajectory to a final equilibrium state, totally characterized by the temperature, the atmospheric pressure, the volume, and the composition of that particular condition. A common problem highlighted in similar approaches is the presence of a significant time delay linked to the procedures used to measure the Kla_{CO2}. To overcome the latter, an acid-base indicator in the liquid (Cresol Red) was added, selected for having an instantaneous capacity to react in front of proton ion shifts. In order to correlate the data obtained with the desired kinetics, we made use of a model constructed with a perspective bestowed by irreversible thermodynamics. This approach allowed us to infer the reaction rates of the step reactions involved, as well as the energy involved among them and the overall dissipation of the entropy towards the direction of a minimum state of energy corresponding to balance.

(6.1). - The time evolution of the absorbance of Cresol Red during the process of transfer of CO_2 in an open system.

Previous reports highlighted the fact that the hydration process is the major limiting step of the whole process [93]. Here it has been presented a proposal founded on the idea that the driving force of two processes: a heterogeneous reaction of the mass transfer process of carbon dioxide dissolved from a gas phase scattered in a liquid medium, and the hydration of that dissolved molecules, are bounded through the condition that the reaction rate of both processes have to remain equal as long as the system follows its trajectory toward its unique equilibrium. This approach has enabled the possibility to follow the progression of 9 perturbed states, utilizing an acid-base dye and following the shifts of its absorbance during the transitions from its basic to acid form, offering the possibility to estimate the value of the departure from the equilibrium for the hydronium ions present in the liquid ($\varepsilon^{*}_{H^{+}}$), as well as the value of these dimensionless changes in the partial pressure of carbon dioxide ($\varepsilon^{*}_{P_{CO_2,g}}$), present in the feed gas stream. Figure (2-3-4) shows the progression of the absorbance values measured at 573 nm as long as the transition state lasted. The results presented were analysed, taking into account the final 60 minutes for each run.

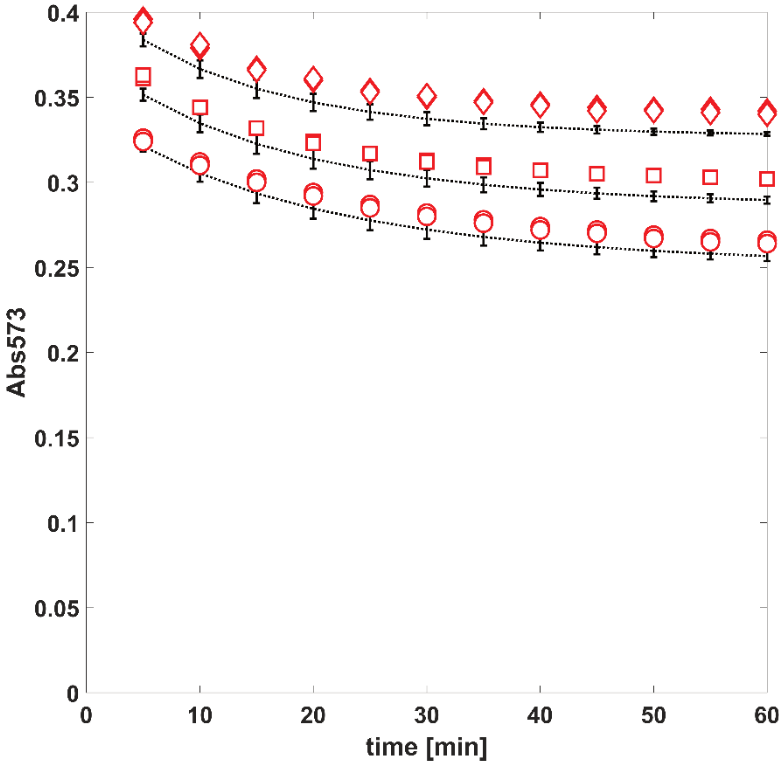

(2)

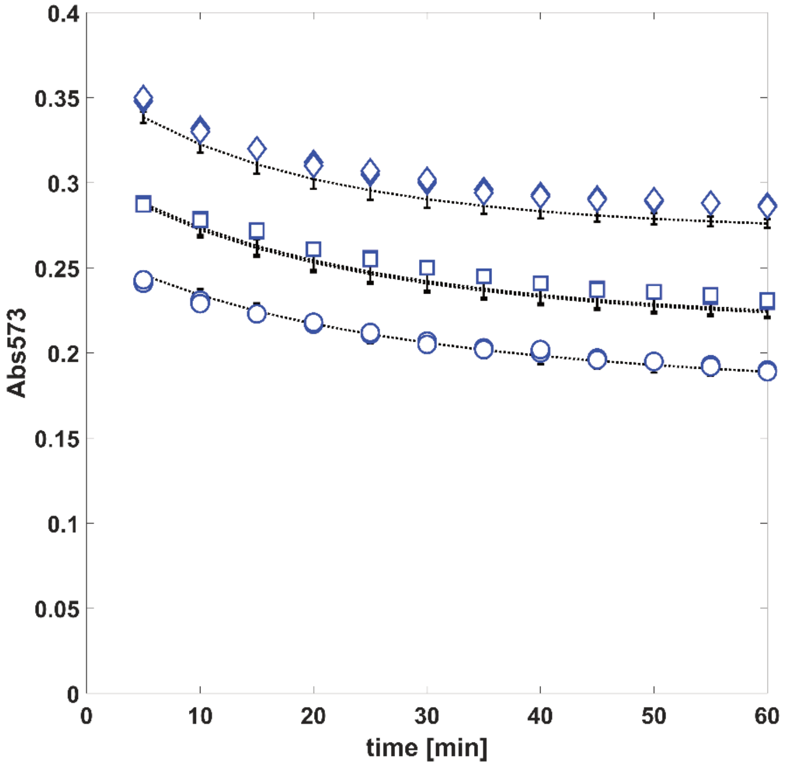
0.4
0.35
0.3
0.25
0.2
0.15
0.1
0.05
0
Abs573
0
10
20
30
40
50
60
time [min]

(3)

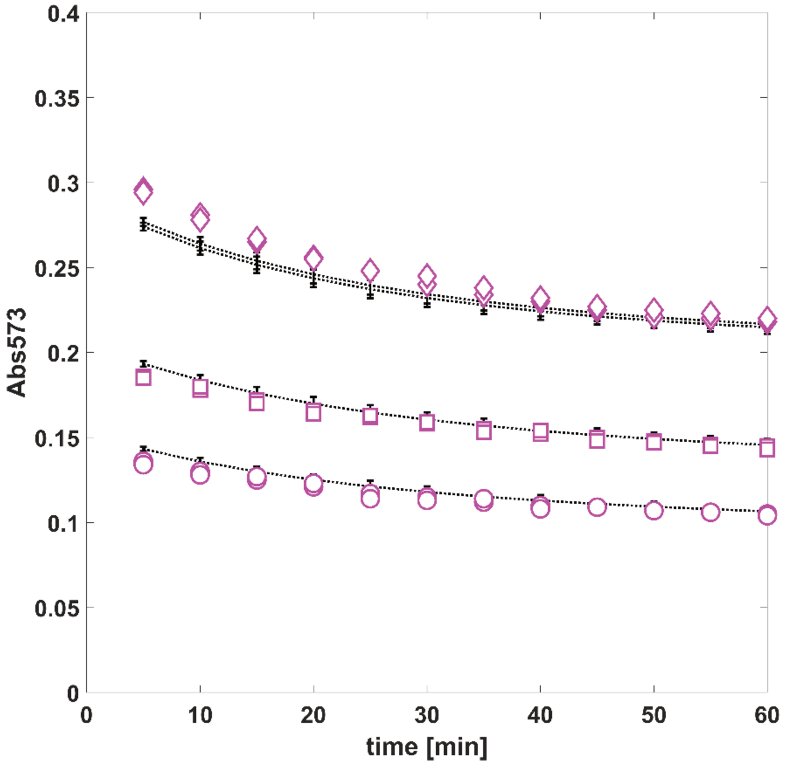
0.4
0.35
0.3
0.25
0.2
0.15
0.1
0.05
0
Abs573
0
10
20
30
40
50
60
time [min]

(4)

Figures (2-3-4): *corresponding Absorbance (λ = 573 nm) values of Red Cresol during the last 60 minutes of every experiment performed. The values highlighted as (○) represent the evolution of an altered condition obtained after disturbing its initial balanced state with a perturbation equal to 1.2 10^{-3} [molar] of NaOH. The (▫) values and (◊) are correspondent with the evolutions obtained from 1.5 10^{-3} [molar] and 1.8 10^{-3} [molar], respectively. The red coloured markers (Fig. 2) are the corresponding values of three experiments performed departing from the same $x_{H_2PO_4^-}$ value, equal to 0.2. Blue values (Fig. 3) are the dependences corresponding to $x_{H_2PO_4^-}$ equal to 0.5 and 0.8 for magenta markers (Fig. 4). The dotted black lines highlight the theoretical values regressed for each run, calculated from equations (21 - 22).*

Making use of equations (21 - 22) and relating the latter with the absorbance of the tracer through its acid-base constant expression and Lambert-Beer law, a multiparametric adjustment has successfully been applied. Regarding the fact that each of the runs explored was made under the same conditions of temperature, pressure, aeration rate and agitation on a well-mixed reactor, four parameters were regressed ($k_1a_{int}, k_2, \left(\varepsilon^*_{H^+}\right)_{t\to 0}$ and V^1). Firstly, the parameter t_0 resulted tended to zero in all the conditions performed, which allowed the dismissal of a possible effect of time delay among the measurements and also the consideration of mixing delay of the pulse-perturbation at the starting point inside the liquid. Kordac and Linek (2008) stated that ideal mixing and lower mass transfer resistance in the gas phase could be assumed for conditions with lower Kla_{CO2} values. Hindi (2017) [92] published a Kla_{CO2} equal to 0.606 [min^{-1}] under an aeration rate of 5.0 [L min^{-1}] and 200 [rpm] of stirring speed, with an aqueous media composition equal to this work, considering ideal mixing, whereas we assessed experiments under 1.2 [L min^{-1}] and 300 [rpm]. In addition, microalgae cultures require less stirring speed. Thus, assuming ideal mixing, it is possible for the conditions prevailing in our work [102], [103].

In the second place, the establishment of a model which is based on the assumption that any pseudo-equilibrium possible to analyse at each transition step must comply with Henry's law implies assuming that the corresponding value of the extent of reaction of the partial pressure of CO_2 for an initial point in the transition $\left(\varepsilon^*_{P_{CO_2,g}}\right)_{t\to 0}$, and the values as long as the transient state lasts, should be slight in contrast with $\varepsilon^*_{H^+}$ (Appendix – eq. (A-(14))). Figures (5 - 6) illustrate the results of the evolution of each condition evaluated. The order of magnitude of

$\varepsilon^{*}_{P_{CO_2,g}}$ is four times lesser than $\varepsilon^{*}_{H^+}$ it can be reckoned that the assumptions and the original calculations were not wide of the mark, allowing us to conclude that whereas broader changes in the concentration of $H^{+}_{(aq)}$ occurs in the solution, these shifts are not reflected in a relevant way on the constantly renewed air current bubbling in the interior of the liquid, as would be expected.

Finally, the kinetic constant of the first occurring reaction (k_1a_{int}) and the kinetic constant of the reaction of hydration were evaluated (k_2), taking values of 0.310 ± 0.023 [min^{-1}] and 2.09 10^{-5} ± 0.27 10^{-5} [min^{-1}] respectively. In addition, it was possible to infer that the gas hold-up's value was 65 ± 5 [cm^3]. Comparing the experimental and predicted absorbance data obtained from the model with these parameters brought values whose percentage relative error was 7 % at maximum. Although the approach presented in this work is based on a model that allows the calculation of two different kinetic constants, the value of (k_1a_{int}) was found to be in agreement with previously published data [88].

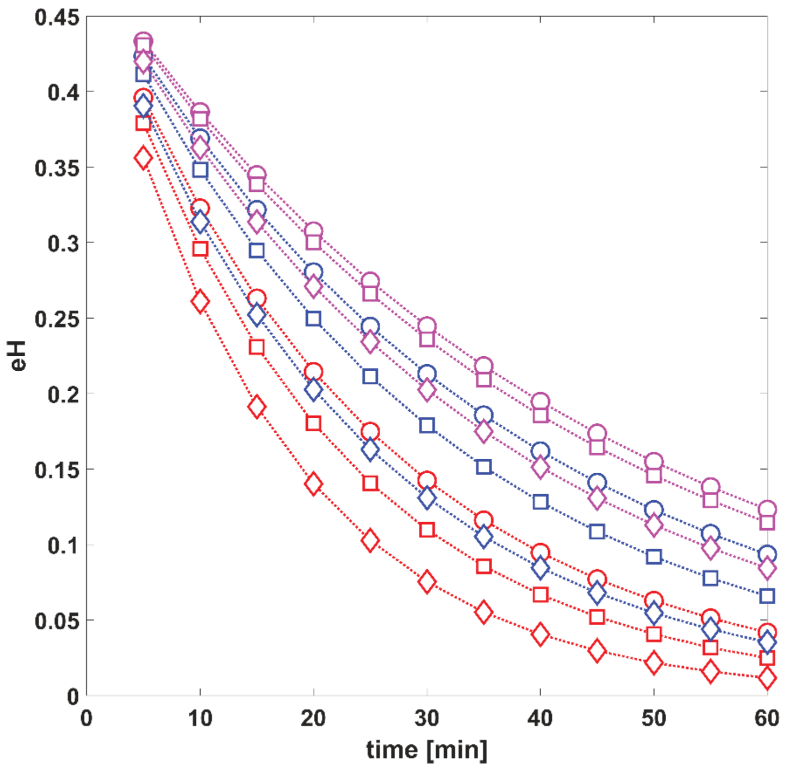

(5)

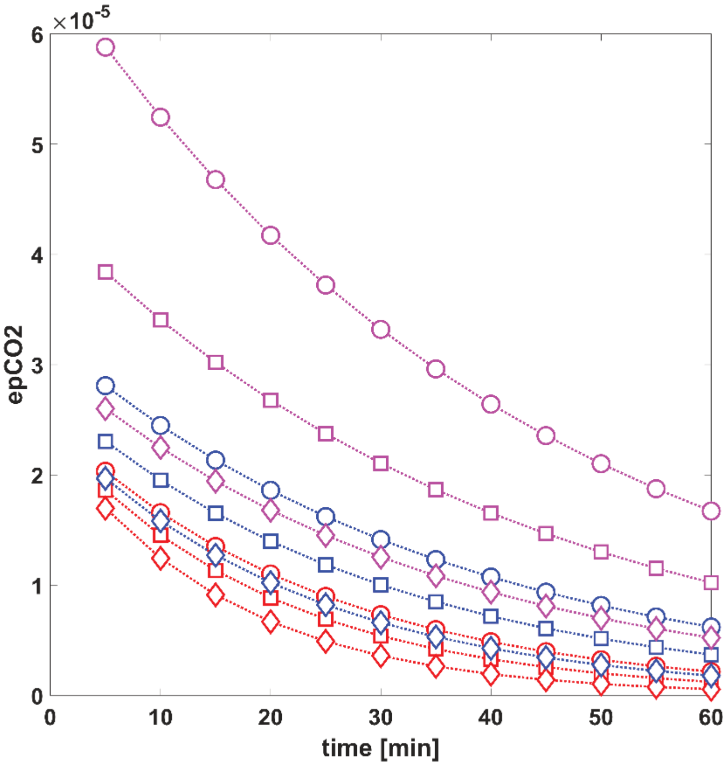

(6)

Figures (5 - 6): *Evolution of $\varepsilon^{*}_{H^{+}}$ (Fig. (5)) and $\varepsilon^{*}_{P_{CO_2,g}}$ (Fig. (6)) correspondent to every assessed condition during the last 60 minutes of each run performed. The markers and colours respect the same references explained in Fig. (2-b-d).*

(6.2). - The time evolution of $m_{CO_{2,dis}}$, $m_{HCO_3^-}$, $m_{CO_3^{2-}}$ and $m^{T}_{CO_2,g}$

The exploration of the shifts in the carbon species flux reveals that, as was expected, the total concentration of carbon species in the solution ($m^{T}_{CO_2,g}$) increases its value as long as the balance is restored (Table 2). Nine different initial compositions and perturbed states were tested, all selected under the criteria that $m^{T}_{CO_2,g}$ must reach at least three times its initial value or more at the deadline of each run. Our results illustrate that the contribution of $m_{CO_3^{2-}}$ over $m^{T}_{CO_2,g}$ represents a maximum of 2 % in the final state of the system, and the CO_2 incorporated is mainly as bicarbonate ions [84], [86]. Regarding the fact that these results are influenced by the current pH value of the solution, it is noteworthy that the value $m^{T}_{CO_2,g}$ at the final state of each perturbation, tested under the same operational conditions, resulted in different values, although each experiment has to respond to the same kinetic constants. The latter is a specific outcome that brings the possibility to rethink the design of new methodologies of cultivation based on the composition and behaviour of the culture medium, since considering that shifts in hydronium ions concentration (being influenced by the buffer capacity of some species like the ones that were included in the mixtures) has no whatsoever effect on the total carbon flux, is not correct at all. Moreover, it was recently concluded that the presence of Carbonic Anhydrase in some microalgae strains is influenced by the value of $m^{T}_{CO_2,g}$ [82].

Under the same operative conditions tested, it can be seen (Table 2) that as far as the difference between initially perturbed and balanced pH values results as more expansive, as significant the increment in the total concentration of carbon species will be (or vice versa).

Table 2: Total dissolved carbon dioxide ($m^{T}_{CO_2,g}$) and starting and final pH values for each condition assessed. Every concentration value is expressed in mol L^{-1}.

			$x_{H_2PO_4^-}$					
			0.2		**0.5**		**0.8**	
			pH	$m^{T}_{CO_2,g}$	**pH**	$m^{T}_{CO_2,g}$	**pH**	$m^{T}_{CO_2,g}$
$m_{NaOH,p}$	**$1.2\ 10^{-3}$**	*before the perturbation*	7.51	$2.11\ 10^{-04}$	7.08	$8.56\ 10^{-05}$	6.51	$3.21\ 10^{-05}$
		starting point	10.55	$2.11\ 10^{-04}$	9.87	$8.56\ 10^{-05}$	7.70	$3.21\ 10^{-05}$
		at balance	8.18	$9.67\ 10^{-04}$	7.90	$5.05\ 10^{-04}$	7.51	$2.11\ 10^{-04}$
	$1.5\ 10^{-3}$	*before the perturbation*	7.51	$2.11\ 10^{-04}$	7.08	$8.56\ 10^{-05}$	6.51	$3.21\ 10^{-05}$
		starting point	10.76	$2.11\ 10^{-04}$	10.46	$8.56\ 10^{-05}$	8.28	$3.21\ 10^{-05}$

		at balance	8.29	$1.23\ 10^{-03}$	8.06	$7.22\ 10^{-04}$	7.72	$3.32\ 10^{-04}$
	$1.8\ 10^{-3}$	*before the perturbation*	7.51	$2.11\ 10^{-04}$	7.08	$8.56\ 10^{-05}$	6.51	$3.21\ 10^{-05}$
		starting point	10.94	$2.11\ 10^{-04}$	10.77	$8{,}56\ 10^{-05}$	10.30	$3.21\ 10^{-05}$
		at balance	8.40	$1.59\ 10^{-03}$	8.22	$1.05\ 10^{-03}$	7.96	$5.73\ 10^{-04}$

In this work, the composition used for the assessment of each run was prepared by taking into account the composition of the most common salty mediums employed to culture microalgae. In every one of these environments, and especially the ones with Nitrate ions as the only source of Nitrogen being present, the phosphorous species could be taken as the ones that exert the primary buffer capacity over the rest of the micronutrients and trace metals (regarding the concentration of all nutrients and its chemical behaviour). Any modification in the composition will impact the ionic strength of the medium, and this change will be reflected in variations over the activity coefficients of every species present. Since the objective has been to study the absorption of CO_2 separated from other interferences, these results can now be extended to complex compositions to make a proper combination with other phenomena, such as light absorption.

(6.3). - Analysis of the driving forces and the ensuing reaction rate.

In this work, we sought to investigate whether it was possible to measure the kinetics of the mass transfer of CO_2 following the concentration of $H^{+}_{(aq)}$, meanwhile, the system evolves from a perturbed state to a new equilibrium state. The trajectory of this evolution must be such that every pseudo-equilibrium state, which can be analysed, must have associated a minimum generation rate of internal entropy toward its evolution to zero. In the linear irreversible regime, the latter condition is fulfilled throughout the rearrangement of the correspondent affinities bounded to the restriction that the reaction rates of the non-fast reactions must remain equal to each other. Figure (7) pictures the values of the Affinities of reactions 1 and 2 and their evolution to a minimum. It can be seen that the correspondent driving force of the second reaction (hydration) is eight orders of magnitude wider than the affinity of the first step reaction. This result infers that the second step might be taken as the controlling rate step. It is essential to highlight that this assumption is not based on the comparison of reactions rates, as it relays on the relation between the related affinities necessary to maintain the condition of equality of both reaction rates (Fig. (8)). At the same time, Figure (7) demonstrates that if each value of A_1 and A_2 correspondent to every pseudo-equilibrium state, are divided among themselves, they are bounded to a constant linear relationship. If eq. (16) is recalled, a simple rearrangement allows to obtain,

$$\frac{L_{2,2}}{L_{1,1}} = \frac{A_1}{A_2} \tag{31}$$

The replacement of eq. (Appendix – (A-(17))) and (Appendix – (A-(21))) in (16), after a simplification, shows the linear relationship that can be observed in Fig. (7),

$$\frac{L_{2,2}}{L_{1,1}} = \frac{\frac{k_2 K_1 P_{CO_2}^{(eq)}}{R}}{\frac{k_1 a_{int} P_{CO_2}^{(eq)}}{R}} = \frac{k_2 K_1}{k_1 a_{int}} = \frac{A_1}{A_2} \tag{32}$$

This noteworthy result reinforced our initial hypothesis, as well as the estimated reaction rates that resulted identically to each other for every step of the transition state of whichever condition was tested. Under the same operative conditions, nine different chemical paths reached their balance in such a way that eq. (17) was fulfilled; both overall reaction rates resulted equal to each other as long as the respective affinities rearranged their values during the transition.

In eq. (32), it is possible to notice that the energy involved in this two-coupled reaction cannot be affected by increasing the partial pressure of CO_2. Indeed, the latter will have an impact on eq. (18), changing the duration in time of the transition towards a new equilibrium state. Changes in the Temperature of the system could exert an impact on the ratio A_1/A_2 as it can affect the viscosity of the liquid (and so the interfacial area) and both kinetic constants values. Increasing mixing speed or gas flow definitively will affect the interfacial area, but since A_1 is subdued to A_2, it is possible that these changes have no effect whatsoever on the reaction rates (Fig. (7)). The presence of microalgae cells can affect all the variables since carbonic anhydrase acts directly over the value of A_2. Besides, all metabolic reactions may alter the composition of the liquid medium, affecting every one of the aforementioned variables. Thus, the study of the absorption of CO_2 in a simplified system like this, and the inclusion of this information in complex environments, might produce interesting results.

Another exciting aspect of eq. (21 – 22) is that if it is chosen, an acidic condition that turns the value of $\left(\varepsilon^{*}_{H^{+}}\right)_{t\to 0}$ in negative by means of the same kinetic constants, it is possible to follow the progression of the desorption process of carbon dioxide in the transition to a new balance, which in the end, will hold less quantity of $m^{T}_{CO_2,g}$. This last new balanced condition is bounded as well by eq. (32), with the only difference that the correspondent Affinities will approximate zero from the left, following a chemical path led by the condition of the minimal rate of internal generation of entropy.

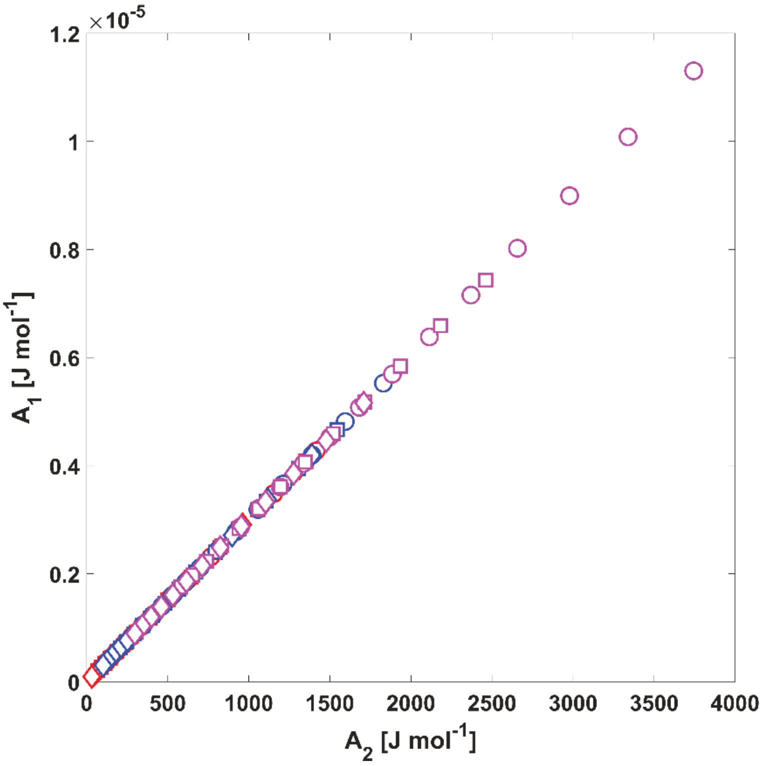
×10^-5
1.2
1
0.8
0.6
0.4
0.2
0
A_1 [J mol^-1]
0
500
1000
1500
2000
2500
3000
3500
4000
A_2 [J mol^-1]

(7)

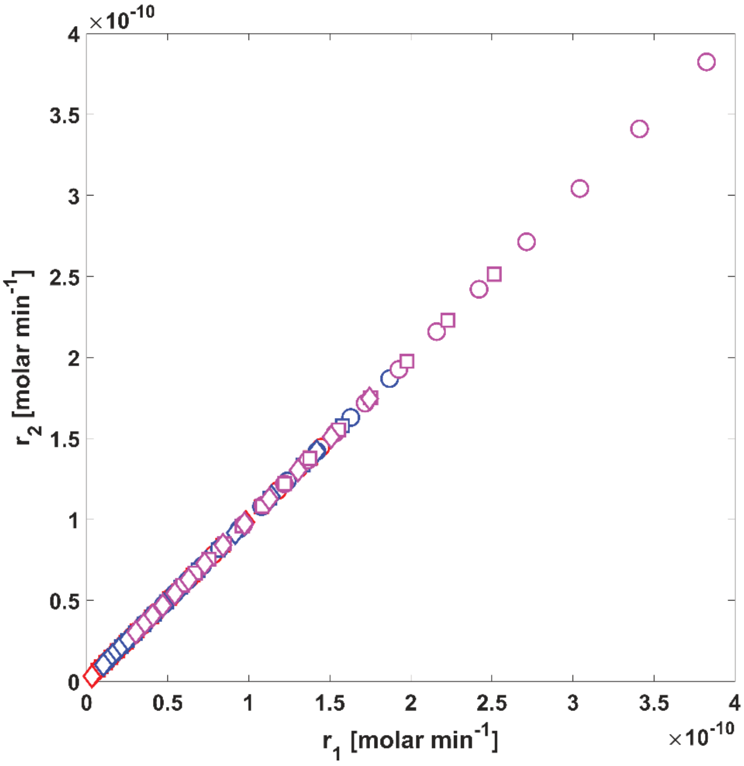
×10^-10
4
3.5
3
2.5
2
1.5
1
0.5
0
r_2 [molar min^-1]
0
0.5
1
1.5
2
2.5
3
3.5
4
r_1 [molar min^-1]
×10^-10

(8)

Figure (7 - 8): *(Fig. (7)) corresponding values of the driving forces of the first and second reaction step for every evolution evaluated in the direction of its own unique balance, showed altogether. It is noteworthy that, regarding the differences in the order of magnitude of each A_1 or A_2 value, they retain a linear relationship among them in the direction of zero in order to fulfil the eq. (32). In Fig. (8), it is shown the relationship among the values of the reaction rates of the first and second steps for every experiment. The slope of the relationship is the same, and it is equal to one, fulfilling with eq. (17). The markers and colours respect the same references explained in Fig. (2-4).*

(7). - Conclusion

In this chapter, a colourimetric method has been employed in order to assess the mass transfer coefficient of CO_2 through a gas-liquid interface and its dependence on time for a commercial bioreactor that contained a liquid medium, initially not at equilibrium, reaching a new balanced condition through exchanging CO_2 with an air current bubbling in its interior. The perspective granted by irreversible thermodynamics acts as a valuable tool for quantifying some phenomena and opens a new field of possibilities for continuing the optimization of culture techniques. The condition of the minimum generation of internal entropy enlightens a way in which, via following the changes in the concentration of H^+ across the duration of a perturbed state, the whole composition of the system can be characterised. In addition, the affinities associated with all the non-zero reaction rates must adjust their values to satisfy the constraint that the corresponding reaction rates must remain equal to each other as long as the transition state lasts. While this technique has been used in a CO_2 study, the extension to its use in O_2 removal could also be useful.

(8). – *Appendix of chapter 1*

8.1 The absorption of CO_2 on $H_2O/H_2PO_4^-/HPO_4^{2-}/NaCl$ mixtures: The perspective of irreversible thermodynamics.

8.1.1 The internal generation of Entropy in terms of reaction rates and driving forces

Reaction pathway	Reaction rate [molar min^{-1}]	Affinity (Driving Force: [J mol^{-1}])
$CO_{2,g} \xrightleftharpoons[k_{-1}]{k_1} CO_{2,d}$	r_1	$A_1 = \left[\mu_{CO_{2,g}} - \mu_{CO_{2,sol}}\right]$
$CO_{2,sol} + H_2O \xrightleftharpoons[k_{-2}]{k_2} HCO_3^- + H^+$	r_2	$A_2 = \left[\mu_{CO_{2,sol}} + \mu_{H_2O} - \mu_{HCO_3^-} - \mu_{H^+}\right]$
$HCO_3^- \xrightleftharpoons[k_{-3}]{k_3} CO_3^{2-} + H^+$	r_3	$A_3 = \left[\mu_{HCO_3^-} - \mu_{CO_3^{2-}} - \mu_{H^+}\right]$
$H_3PO_4 \xrightleftharpoons[k_{-4}]{k_4} H_2PO_4^- + H^+$	r_4	$A_4 = \left[\mu_{H_3PO_4} - \mu_{H_2PO_4^-} - \mu_{H^+}\right]$
$H_2PO_4^- \xrightleftharpoons[k_{-5}]{k_5} HPO_4^{2-} + H^+$	r_5	$A_5 = \left[\mu_{H_2PO_4^-} - \mu_{HPO_4^{2-}} - \mu_{H^+}\right]$
$HPO_4^{2-} \xrightleftharpoons[k_{-6}]{k_6} PO_4^{3-} + H^+$	r_6	$A_6 = \left[\mu_{HPO_4^{2-}} - \mu_{PO_4^{3-}} - \mu_{H^+}\right]$
$H_2O \xrightleftharpoons[k_{-7}]{k_7} HO^- + H^+$	r_7	$A_7 = \left[\mu_{H_2O} - \mu_{H^+} - \mu_{HO^-}\right]$

Table A-1: The process of CO_2 transfer from gas (${}_g$) to liquid phase (${}_d$) (aqueous phase). k_i and k_{-i} values are the correspondent velocity constants of the forward and backward reaction of each step from 1 to 7.

In order to correlate the observations in the changes of the absorbance of Cresol Red along the experiments, we employed a relationship bestowed by the condition of the minimal rate of generation of internal entropy (Kondepudi, 1998). We started considering an experiment in which an open, two-phase system (gas phase: (1); aqueous phase: (2)) was initially at the state of overall equilibrium. This equilibrium state is completely characterized by T, P_{CO_2} and the species concentrations $m_{HCO_3^-}$, $m_{CO_3^{2-}}$, $m_{H_3PO_4}$, $m_{H_2PO_4^-}$, $m_{HPO_4^{2-}}$, $m_{PO_4^{3-}}$, m_{HO^-}, m_{H^+}, m_{Na^+}, m_{Cl^-} and $m_{CO_{2,dis}}$. The gas phase in contact with the liquid occupies a volume that was denoted as $V^{(1)}$, in consequence, $V^{(2)}$ represents the volume in the liquid phase. Not all these state properties are independently variable at equilibrium. They are functionally related to each other by the following constraints:

The species concentrations must satisfy the electro-neutrality condition: $m_{HCO_3^-}+2m_{CO_3^{2-}}+m_{H_2PO_4^-}+2m_{HPO_4^{2-}}+3m_{PO_4^{3-}}+m_{Cl^-}+m_{HO^-}=m_{H^+}+m_{Na^+}$,

where $m_{Na^+}=m^0_{H_2PO_4^-}+2m^0_{HPO_4^{2-}}+m^0_{NaCl}$ and $m_{Cl^-}=m^0_{NaCl}$.

By setting up a phosphorus atoms balance, we also have the constraint: $m_{H_3PO_4}+m_{H_2PO_4^-}+m_{HPO_4^{2-}}+m_{PO_4^{3-}}=m^0_{H_2PO_4^-}+m^0_{HPO_4^{2-}}$

The two phases, are simple and uniform subsystems separated from each other by a **diathermal** and **permeable** surface. Mass exchange between the two phases and chemical reactions in the liquid phase are not necessarily at equilibrium. Nonetheless, the non-uniform **closed simple system** as a whole is assumed at internal thermal equilibrium, and also at thermal equilibrium with a bath at temperature T. The system is also at internal mechanical equilibrium, and with atmospheric P. We considered the case in which the system, initially at balance, was suddenly perturbed by adding a pulse of a $NaOH$ solution ($m_{NaOH,p}$), with negligible change of the liquid phase volume. The increase in the Na^+ concentration due to the addition of a pulse of the basic solution had a direct impact on the electro-neutrality condition. It was assumed that ionic dissociation reactions (i.e., reactions 3 to 7 of Table A-1), rapidly reached their individual equilibrium, which was maintained as they evolved with time at the pace of the progress of the much slower reactions (i.e., reactions 1 and 2). Departing from the perturbed initial state, the system evolved to reach a new final equilibrium state. Under the conditions prevailing in our work, the effects of the exchange of H_2O

between gas and liquid phases were negligible, and the N_2 present was considered an inert gas as well as O_2, insoluble in the liquid phase. Moreover, no chemical reactions occurred in the gas phase.

For a system of these characteristics, it was possible to assume that the changes of the free energy in each phase could be modelled by:

$$\frac{d\left(\underline{G}^{(1)}+\underline{G}^{(2)}\right)}{dt}=-T\underline{\dot{\sigma}} \qquad \text{(A-1)}$$

In which $\frac{d\left(\underline{G}^{\alpha}\right)}{dt}$ is the variation in free energy associated to each phase $\left(\alpha=1,2\right)$, occurring at the same value of T. $\underline{\dot{\sigma}}$ is the internal generation of Entropy. Applying the Euler's theorem and making use of the Gibbs – Duhem equation, for each phase we obtained:

$$\frac{d\left(\underline{G}^{(1)}+\underline{G}^{(2)}\right)}{dt}=\sum_{i=1}^{c}\mu_i^{(1)}\frac{dn_i^{(1)}}{dt}+\sum_{i=1}^{c}\mu_i^{(2)}\frac{dn_i^{(2)}}{dt}=-T\underline{\dot{\sigma}} \qquad \text{(A-2)}$$

In equation (2) $\frac{dn_i^{(\alpha)}}{dt}$ reflects the changes through time in the number of moles of species i in each phase α, and $\mu_i^{(\alpha)}$ is the chemical potential of each reactant. Whichever change that might occur, it is possible to acknowledge that a total mass of $n_i^{(\alpha)}$ may participate in mass transfer processes between the two phases or may react with other species (only in phase 2):

$$\frac{dn_i^{(\alpha)}}{dt}=\left(\frac{dn_i^{(\alpha)}}{dt}\right)_{react}+\left(\frac{dn_i^{(\alpha)}}{dt}\right)_{exch} \qquad \text{(A-3)}$$

The application of equation (A-3) in (A-2), for each specie present in the system, with the conditions mentioned above, allowed us to write the following:

$$\left[\mu^{(2)}_{CO_2}\left(\frac{dn^{(2)}_{CO_2}}{dt}\right)_{rxn} + \mu^{(2)}_{HCO_3^-}\left(\frac{dn^{(2)}_{HCO_3^-}}{dt}\right)_{rxn} + \mu^{(2)}_{CO_3^{2-}}\left(\frac{dn^{(2)}_{CO_3^{2-}}}{dt}\right)_{rxn}\right]_{P,T} +$$
$$\left[\mu^{(2)}_{H_3PO_4}\left(\frac{dn^{(2)}_{H_3PO_4}}{dt}\right)_{rxn} + \mu^{(2)}_{H_2PO_4^-}\left(\frac{dn^{(2)}_{H_2PO_4^-}}{dt}\right)_{rxn} + \mu^{(2)}_{HPO_4^{2-}}\left(\frac{dn^{(2)}_{HPO_4^{2-}}}{dt}\right)_{rxn} + \mu^{(2)}_{PO_4^{3-}}\left(\frac{dn^{(2)}_{PO_4^{3-}}}{dt}\right)_{rxn}\right]_{P,T} + \quad \text{(A-4)}$$
$$\left[\mu^{(2)}_{HO^-}\left(\frac{dn^{(2)}_{HO^-}}{dt}\right)_{rxn} + \mu^{(2)}_{H^+}\left(\frac{dn^{(2)}_{H^+}}{dt}\right)_{rxn}\right]_{P,T} + \left(\frac{dn^{(2)}_{CO_2}}{dt}\right)_{exch}\left(\mu^{(2)}_{CO_2} - \mu^{(1)}_{CO_2}\right) = -T\underline{\dot{\sigma}}$$

From Table A-1, for the liquid phase $(\alpha = 2)$, it was possible to assume: $\left(\frac{dn_i^{(\alpha)}}{dt}\right)_{rxn} = -V^{(2)} r_i$, for each net reaction rate of the i^{th} stage in terms of moles per unit time per unit volume (r_i). At the same time, the exchanging in the CO_2 through time could be written as: $\left(\frac{dn^{(2)}_{CO_2}}{dt}\right)_{exch} = A_{int}\, j^{(1\to 2)}_{CO_2}$ where $j^{(1\to 2)}_{CO_2}$ is the net mole flux density of CO_2 from phase 1 to phase 2 and A_{int} is the total gas-liquid interfacial area. The replacement of these equalities in equation (A-4) and further rearrangement produced:

$$\underbrace{\frac{1}{V^{(2)}} A_{int}\, j^{(1\to 2)}_{CO_2}}_{r_1} \underbrace{\left(\mu^{(1)}_{CO_2} - \mu^{(2)}_{CO_2}\right)}_{A_1} + r_2 \underbrace{\left(\mu^{(2)}_{CO_2} - \mu^{(2)}_{HCO_3^-} - \mu^{(2)}_{H^+}\right)}_{A_2} + r_3 \underbrace{\left(\mu^{(2)}_{HCO_3^-} - \mu^{(2)}_{CO_3^{2-}} - \mu^{(2)}_{H^+}\right)}_{A_3} +$$
$$r_4 \underbrace{\left(\mu^{(2)}_{H_3PO_4} - \mu^{(2)}_{H_2PO_4^-} - \mu^{(2)}_{H^+}\right)}_{A_4} + r_5 \underbrace{\left(\mu^{(2)}_{H_2PO_4^-} - \mu^{(2)}_{HPO_4^{2-}} - \mu^{(2)}_{H^+}\right)}_{A_5} + r_6 \underbrace{\left(\mu^{(2)}_{HPO_4^{2-}} - \mu^{(2)}_{PO_4^{3-}} - \mu^{(2)}_{H^+}\right)}_{A_6} + \quad \text{(A-5)}$$
$$r_7 \underbrace{\left(\mu^{(2)}_{H_2O} - \mu^{(2)}_{HO^-} - \mu^{(2)}_{H^+}\right)}_{A_7} = T\left(\frac{\underline{\dot{\sigma}}^{(1)} + \underline{\dot{\sigma}}^{(2)}}{V^{(2)}}\right) = T\dot{\sigma} > 0$$

$$r_1A_1 + r_2A_2 + r_3A_3 + r_4A_4 + r_5A_5 + r_6A_6 + r_7A_7 = T\dot{\sigma} > 0 \qquad \text{(A-6)}$$

Equation (A-5) expressed in the form of (A-6) allows the measurement of the specific rate of internal generation of Entropy ($\dot{\sigma}$), in terms of the reaction rate of each step reaction in the system proposed, as well as the Affinities (driving force) involved.

3.1.2 The expression of the gas-to-liquid transfer rate and those of the ensuing chemical reactions in the liquid phase, in terms of Onsager coefficients and linearized affinities.

The net rate of the i^{th} reaction in the reaction pathway is:

$$r_i = \left(r_{i,f} - r_{i,b}\right) \tag{A-7}$$

where $r_{i,f}$ and $r_{i,b}$ are the forward and backward reaction rates of the i^{th} **elementary step** in the reaction pathway. The corresponding affinity is:

$$A_i = RT\, ln\left(\frac{r_{i,f}}{r_{i,b}}\right) \tag{A-8}$$

Equation (A-8) can be rearranged into the following form:

$$r_{i,b} = r_{i,f}\, exp\left(-\frac{A_i}{RT}\right) \tag{A-9}$$

Substitution of the backward reaction rate $r_{i,b}$ from Equation (A-9) in Equation (A-7), gives:

$$r_i = r_{i,f} - r_{i,b} = r_{i,f}\left[1 - exp\left(-\frac{A_i}{RT}\right)\right] \tag{A-10}$$

which can be approximated about the equilibrium with a Taylor series, as follows:

$$\begin{gathered} r_i = r_{i,f}\left[1 - exp\left(-\frac{A_i}{RT}\right)\right] = \left[r_{i,f}^{(eq)} + \left(r_{i,f} - r_{i,f}^{(eq)}\right)\right]\left[1 - exp\left(-\frac{A_i}{RT}\right)\right] = \\ r_{i,f}^{(eq)}\left[1 + \frac{\left(r_{i,f} - r_{i,f}^{(eq)}\right)}{r_{i,f}^{(eq)}}\right]\left\{\left[1 - exp\left(-\frac{A_i}{RT}\right)\right]^{(eq)} + \left[\frac{1}{RT} exp\left(-\frac{A_i}{RT}\right)\right]^{(eq)}\left(A_i - A_i^{(eq)}\right) + \cdots\right\} \end{gathered} \tag{A-11}$$

Let’s suppose that the departure from chemical equilibrium of every elementary reaction (ε_i) in the mechanism is not so large, so that the inequalities:

$$\left(\frac{A_i}{RT}\right)^2 << 1; \qquad \varepsilon_i = \left|\frac{\left(r_{i,f} - r_{i,f}^{(eq)}\right)}{r_{i,f}^{(eq)}}\right| << 1 \qquad ; r_{i,f}^{(eq)} = r_{i,b}^{(eq)} \tag{A-12}$$

hold for $\left(A_i/RT\right)$ and for ε_i, respectively. Then, by only keeping linear terms on these small departures from equilibrium, we can write:

$$r_i = \frac{1}{T}\left(\frac{r_{i,f}^{(eq)}}{R}\right)A_i = \frac{1}{T}\left(\frac{r_{i,b}^{(eq)}}{R}\right)A_i = \frac{1}{T}L_{i,i}A_i \quad ; \quad L_{i,i} = \left(\frac{r_{i,f}^{(eq)}}{R}\right) = \left(\frac{r_{i,b}^{(eq)}}{R}\right) > 0 \qquad \text{(A-13)}$$

In Equation (A-13), $L_{i,i}$ is the Onsager's coefficient for the i^{th} independent reaction in the pathway. In a uniform system like the liquid phase, at internal thermal equilibrium (i.e., at uniform temperature, T) and at internal mechanical equilibrium (i.e., at uniform atmospheric pressure, P), chemical reactions coupled through common reactants or products can proceed as long as Equation (A-6) is satisfied. The replacement of (A-13) relations gives:

$$L_{1,1}A_1A_1 + L_{2,2}A_2A_2 + L_{3,3}A_3A_3 + L_{4,4}A_4A_4 + L_{5,5}A_5A_5 + L_{6,6}A_6A_6 + L_{7,7}A_7A_7 = T^2\dot{\sigma} \qquad \text{(A-14)}$$

Giving a useful quadratic form that is positive definite, meaning by this that the sum of all terms on the left will always be positive for physically admissible values of the affinities, either they be positive or negative.

We should note that the affinities $A_i \;, i = 1,2$, are not independent thermodynamic properties since we require that they add up to a value $A_0 = A_1 + A_2$ **prescribed as boundary condition**. This implies that the system is, at least, at partial equilibrium, with the CO_2 transfer from gas to liquid phase in progress, as well as the ensuing reactions. There are no restrictions imposed on the values of A_3, A_4, A_5, A_6 and A_7, except for the requirement that the concentration of the components involved must satisfy the electro-neutrality condition and the total phosphorus conservation.

In order to elucidate the expression of the Onsager coefficient and linearized affinity of the transfer Rate of CO_2 across the interfacial layer, from the information presented in Table A-1 for this "heterogeneous" reaction, and with the definitions presented for r_i (section 3.2.1-2), we could write:

$$\frac{1}{V^{(2)}}A_{int}j_{CO_2}^{(1\rightarrow 2)}=a_{int}j_{CO_2}^{(1\rightarrow 2)}=r_1=\left(r_{1,f}-r_{1,b}\right)=a_{int}k_1P_{CO_2}-a_{int}k_{-1}m_{CO_2}=$$
$$a_{int}k_1\left[P_{CO_2}-\frac{k_{-1}}{k_1}m_{CO_2}\right]=a_{int}k_1\left[P_{CO_2}-\frac{1}{K_1}m_{CO_2}\right] \tag{A-15}$$

where a_{int} is the interfacial surface area per unit volume of liquid phase. At **overall equilibrium**, this stage 1 is also at equilibrium:

$$r_1^{(eq)}=\left(r_{1,f}^{(eq)}-r_{1,b}^{(eq)}\right)=a_{int}k_1\left[P_{CO_2}^{(eq)}-\frac{k_{-1}}{k_1}m_{CO_2}^{(eq)}\right]=a_{int}k_1\left[P_{CO_2}^{(eq)}-\frac{1}{K_1}m_{CO_2}^{(eq)}\right]=0 \tag{A-16}$$

From Equations (13) and (16), we get:

$$L_{1,1}=\frac{r_{1,f}^{(eq)}}{R}=\frac{r_{1,b}^{(eq)}}{R}=a_{int}\left(\frac{k_1}{R}P_{CO_2}^{(eq)}\right)=a_{int}\left(\frac{k_{-1}}{R}m_{CO_2}^{(eq)}\right) \tag{A-17}$$

The corresponding linearized affinity, obtained by only retaining linear terms of its Taylor expansion, is

$$A_1=RT\left[\frac{\left(m_{CO_2}^{(eq)}-m_{CO_2}\right)}{m_{CO_2}^{(eq)}}-\frac{\left(P_{CO_2}^{(eq)}-P_{CO_2}\right)}{P_{CO_2}^{(eq)}}\right];\ \varepsilon_{P_{CO_2}}=\left(\frac{P_{CO_2}^{(eq)}-P_{CO_2}}{P_{CO_2}^{(eq)}}\right);\varepsilon_{m_{CO_2}}=\left(\frac{m_{CO_2}^{(eq)}-m_{CO_2}}{m_{CO_2}^{(eq)}}\right) \tag{A-18}$$

In the linear irreversible regime, the net rate of the elementary reaction, could be expressed as follows:

$$r_1=\frac{1}{T}L_{1,1}A_1=\frac{1}{T}a_{int}\left(\frac{k_1}{R}P_{CO_2}^{(eq)}\right)RT\left[\varepsilon_{m_{CO_2}}-\varepsilon_{P_{CO_2}}\right]=$$
$$a_{int}k_1P_{CO_2}^{(eq)}\left[\varepsilon_{m_{CO_2}}-\varepsilon_{P_{CO_2}}\right]=a_{int}k_1\left(P_{CO_2}-\frac{1}{K_1}m_{CO_2}\right) \tag{A-19}$$

A similar procedure has been applied to the secondary step reaction:

$$r_2=\left(r_{2,f}-r_{2,b}\right)=k_2\,m_{CO_2}-k_{-2}\,m_{HCO_3^-}m_{H^+}=$$
$$k_2\left[m_{CO_2}-\frac{k_{-2}}{k_2}m_{HCO_3^-}m_{H^+}\right]=k_2\left[m_{CO_2}-\frac{1}{K_2}m_{HCO_3^-}m_{H^+}\right] \tag{A-20}$$

The Onsager coefficient is:

$$L_{2,2} = \frac{r_{2,f}^{(eq)}}{R} = \frac{k_2}{R} m_{CO_2}^{(eq)} = \frac{k_2}{R} K_1 P_{CO_2}^{(eq)} \tag{A-21}$$

and, in the irreversible linear regime:

$$A_2 = RT\left[\frac{\left(m_{HCO_3^-}^{(eq)} - m_{HCO_3^-}\right)}{m_{HCO_3^-}^{(eq)}} + \frac{\left(m_{H^+}^{(eq)} - m_{H^+}\right)}{m_{H^+}^{(eq)}} - \frac{\left(m_{CO_2}^{(eq)} - m_{CO_2}\right)}{m_{CO_2}^{(eq)}}\right] \tag{A-22}$$

and $\varepsilon_{HCO_3^-} = \left(\frac{m_{HCO_3^-}^{(eq)} - m_{HCO_3^-}}{m_{HCO_3^-}^{(eq)}}\right); \varepsilon_{H^+} = \left(\frac{m_{H^+}^{(eq)} - m_{H^+}}{m_{H^+}^{(eq)}}\right)$ have made possible to express the linearized value of r_2 as:

$$r_2 = \frac{1}{T} L_{2,2} A_2 = k_2 m_{CO_2}^{(eq)}\left[\varepsilon_{HCO_3^-} + \varepsilon_{H^+} - \varepsilon_{m_{CO_2}}\right] = k_2 K_1 P_{CO_2}^{(eq)}\left[\varepsilon_{HCO_3^-} + \varepsilon_{H^+} - \varepsilon_{m_{CO_2}}\right] \tag{A-23}$$

where $\varepsilon_{HCO_3^-}$ and ε_{H^+} are a measure of the departure of $m_{HCO_3^-}$ and m_{H^+} from the values $m_{HCO_3^-}^{(eq)}$ and $m_{H^+}^{(eq)}$, respectively, corresponding to the system at global (overall) equilibrium.

Summing up all these results for the second reaction step in the pathway, in the irreversible linear regime we can express r_2 in the following form, in which the bilinear term $\left(m_{HCO_3^-} m_{H^+}\right)$ has been approximated with the linearized form $\left(m_{HCO_3^-} m_{H^+}^{(eq)} + m_{H^+} m_{HCO_3^-}^{(eq)} - m_{HCO_3^-}^{(eq)} m_{H^+}^{(eq)}\right)$.

$$r_2 = \frac{1}{T} L_{2,2} A_2 = k_2\left[m_{CO_2} - \frac{1}{K_2}\left(m_{HCO_3^-} m_{H^+}^{(eq)} + m_{H^+} m_{HCO_3^-}^{(eq)} - m_{HCO_3^-}^{(eq)} m_{H^+}^{(eq)}\right)\right] \tag{A-24}$$

Table A-2 offers the relationships founded for each reaction pathway, after the application of the same procedure for the following steps:

Reaction pathway	**Onsager Coefficients**	**Linearized Affinity (Driving Force: [J mol^{-1}])**
$CO_{2,g} \underset{k_{-1}}{\overset{k_1}{\rightleftarrows}} CO_{2,d}$	$L_{1,1} = \left(a_{int} \frac{k_1}{R} P_{CO_2}^{(eq)} \right)$	$A_1 \approx RT\left[\frac{\left(m_{CO_2}^{(eq)} - m_{CO_2} \right)}{m_{CO_2}^{(eq)}} - \frac{\left(P_{CO_2}^{(eq)} - P_{CO_2} \right)}{P_{CO_2}^{(eq)}} \right]$
$CO_{2,sol} + H_2O \underset{k_{-2}}{\overset{k_2}{\rightleftarrows}} HCO_3^- + H^+$	$L_{2,2} = \frac{k_2}{R} m_{CO_2}^{(eq)} = \frac{k_2 K_1}{R} P_{CO_2}^{(eq)}$	$A_2 \approx RT\left[\frac{\left(m_{HCO_3^-}^{(eq)} - m_{HCO_3^-} \right)}{m_{HCO_3^-}^{(eq)}} + \frac{\left(m_{H^+}^{(eq)} - m_{H^+} \right)}{m_{H^+}^{(eq)}} - \frac{\left(m_{CO_2}^{(eq)} - m_{CO_2} \right)}{m_{CO_2}^{(eq)}} \right]$
$HCO_3^- \underset{k_{-3}}{\overset{k_3}{\rightleftarrows}} CO_3^{2-} + H^+$	$L_{3,3} = \frac{k_3}{R} m_{HCO_3^-}^{(eq)} = \frac{k_3 K_2 K_1}{R} P_{CO_2}^{(eq)}$	$A_3 \approx RT\left[\frac{\left(m_{CO_3^{2-}}^{(eq)} - m_{CO_3^{2-}} \right)}{m_{CO_3^{2-}}^{(eq)}} + \frac{\left(m_{H^+}^{(eq)} - m_{H^+} \right)}{m_{H^+}^{(eq)}} - \frac{\left(m_{HCO_3^-}^{(eq)} - m_{HCO_3^-} \right)}{m_{HCO_3^-}^{(eq)}} \right]$
$H_3PO_4 \underset{k_{-4}}{\overset{k_4}{\rightleftarrows}} H_2PO_4^- + H^+$	$L_{4,4} = \frac{k_4}{R} m_{H_3PO_4}^{(eq)}$	$A_4 \approx RT\left[\frac{\left(m_{H_2PO_4^-}^{(eq)} - m_{H_2PO_4^-} \right)}{m_{H_2PO_4^-}^{(eq)}} + \frac{\left(m_{H^+}^{(eq)} - m_{H^+} \right)}{m_{H^+}^{(eq)}} - \frac{\left(m_{H_3PO_4}^{(eq)} - m_{H_3PO_4} \right)}{m_{H_3PO_4}^{(eq)}} \right]$
$H_2PO_4^- \underset{k_{-5}}{\overset{k_5}{\rightleftarrows}} HPO_4^{2-} + H^+$	$L_{5,5} = \frac{k_5}{R} m_{H_2PO_4^-}^{(eq)} = \frac{k_5 K_4}{R} \frac{m_{H_3PO_4}^{(eq)}}{m_{H^+}^{(eq)}}$	$A_5 \approx RT\left[\frac{\left(m_{HPO_4^{2-}}^{(eq)} - m_{HPO_4^{2-}} \right)}{m_{HPO_4^{2-}}^{(eq)}} + \frac{\left(m_{H^+}^{(eq)} - m_{H^+} \right)}{m_{H^+}^{(eq)}} - \frac{\left(m_{H_2PO_4^-}^{(eq)} - m_{H_2PO_4^-} \right)}{m_{H_2PO_4^-}^{(eq)}} \right]$
$HPO_4^{2-} \underset{k_{-6}}{\overset{k_6}{\rightleftarrows}} PO_4^{3-} + H^+$	$L_{6,6} = \frac{k_6}{R} m_{HPO_4^{2-}}^{(eq)} = \frac{k_6 K_4 K_5}{R} \frac{m_{H_3PO_4}^{(eq)}}{\left(m_{H^+}^{(eq)} \right)^2}$	$A_6 \approx RT\left[\frac{\left(m_{PO_4^{3-}}^{(eq)} - m_{PO_4^{3-}} \right)}{m_{PO_4^{3-}}^{(eq)}} + \frac{\left(m_{H^+}^{(eq)} - m_{H^+} \right)}{m_{H^+}^{(eq)}} - \frac{\left(m_{HPO_4^{2-}}^{(eq)} - m_{HPO_4^{2-}} \right)}{m_{HPO_4^{2-}}^{(eq)}} \right]$

Table A-2: The Onsager coefficients and linearized affinities correspondent to each step from 1 to 6.

Reaction pathway **(Detailed balance)**	**Linearized Kinetics**
$CO_{2,g} \underset{k_{-1}}{\overset{k_1}{\rightleftarrows}} CO_{2,d}$	$a_{int} j_{CO_2}^{(1\rightarrow 2)} = \frac{1}{T} L_{1,1} A_1 = k_1 \left(P_{CO_2} - \frac{1}{K_1} m_{CO_2} \right)$
$CO_{2,sol} + H_2O \underset{k_{-2}}{\overset{k_2}{\rightleftarrows}} HCO_3^- + H^+$	$r_2 = \frac{1}{T} L_{2,2} A_2 = k_2 \left[m_{CO_2} - \frac{1}{K_2} \left(m_{HCO_3^-} m_{H^+}^{(eq)} + m_{H^+} m_{HCO_3^-}^{(eq)} - m_{HCO_3^-}^{(eq)} m_{H^+}^{(eq)} \right) \right]$
$HCO_3^- \underset{k_{-3}}{\overset{k_3}{\rightleftarrows}} CO_3^{2-} + H^+$	$r_3 = \frac{1}{T} L_{3,3} A_3 = k_3 \left[m_{HCO_3^-} - \frac{1}{K_3} \left(m_{CO_3^{2-}} m_{H^+}^{(eq)} + m_{CO_3^{2-}}^{(eq)} m_{H^+} - m_{CO_3^{2-}}^{(eq)} m_{H^+}^{(eq)} \right) \right]$
$H_3PO_4 \underset{k_{-4}}{\overset{k_4}{\rightleftarrows}} H_2PO_4^- + H^+$	$r_4 = \frac{1}{T} L_{4,4} A_4 = k_4 \left[m_{H_3PO_4} - \frac{1}{K_4} \left(m_{H_2PO_4^-} m_{H^+}^{(eq)} + m_{H_2PO_4^-}^{(eq)} m_{H^+} - m_{H_2PO_4^-}^{(eq)} m_{H^+}^{(eq)} \right) \right]$
$H_2PO_4^- \underset{k_{-5}}{\overset{k_5}{\rightleftarrows}} HPO_4^{2-} + H^+$	$r_5 = \frac{1}{T} L_{5,5} A_5 = k_5 \left[m_{H_2PO_4^-} - \frac{1}{K_5} \left(m_{HPO_4^{2-}} m_{H^+}^{(eq)} + m_{HPO_4^{2-}}^{(eq)} m_{H^+} - m_{HPO_4^{2-}}^{(eq)} m_{H^+}^{(eq)} \right) \right]$
$HPO_4^{2-} \underset{k_{-6}}{\overset{k_6}{\rightleftarrows}} PO_4^{3-} + H^+$	$r_6 = \frac{1}{T} L_{6,6} A_6 = k_6 \left[m_{HPO_4^{2-}} - \frac{1}{K_6} \left(m_{PO_4^{3-}} m_{H^+}^{(eq)} + m_{PO_4^{3-}}^{(eq)} m_{H^+} - m_{PO_4^{3-}}^{(eq)} m_{H^+}^{(eq)} \right) \right]$

Table A-3: The process of CO_2 transfer from gas to liquid phase (aqueous phase). Linearized stage kinetics.

8.1.2 The condition of minimal rate of internal generation of entropy.

We are going to look for the set of unknowns $\varepsilon^*_{P_{CO_2}}$, $\varepsilon^*_{m_{CO_2}}$, $\varepsilon^*_{HCO_3^-}$, $\varepsilon^*_{CO_3^{2-}}$, $\varepsilon^*_{H_3PO_4}$, $\varepsilon^*_{H_2PO_4^-}$, $\varepsilon^*_{HPO_4^{2-}}$, $\varepsilon^*_{PO_4^{3-}}$, $\varepsilon^*_{HO^-}$, $\varepsilon^*_{H^+}$ that minimize $\dot{\sigma}$, constrained so that

$$A_1^* + A_2^* = A_0 \qquad \text{(A-24.1)}$$

where

$$A_1^* = RT \left[\varepsilon^*_{m_{CO_2}} - \varepsilon^*_{P_{CO_2}} \right] \qquad \text{(A-24.2)}$$

$$A_2^* = RT\left[\varepsilon^*_{HCO_3^-} + \varepsilon^*_{H^+} - \varepsilon^*_{m_{CO_2}}\right] \qquad \text{(A-24.3)}$$

for every admissible value A_0;and also satisfies the electroneutrality condition

$$m^{(eq)}_{HCO_3^-}\varepsilon_{HCO_3^-} + 2m^{(eq)}_{CO_3^{2-}}\varepsilon_{CO_3^{2-}} + m^{(eq)}_{H_2PO_4^-}\varepsilon_{H_2PO_4^-} + 2m^{(eq)}_{HPO_4^{2-}}\varepsilon_{HPO_4^{2-}} + 3m^{(eq)}_{PO_4^{3-}}\varepsilon_{PO_4^{3-}} + m^{(eq)}_{HO^-}\varepsilon_{HO^-} - m^{(eq)}_{H^+}\varepsilon_{H^+} = 0 \qquad \text{(A-24.4)}$$

as well as the phosphorus atoms conservation

$$m^{(eq)}_{H_3PO_4}\varepsilon^*_{H_3PO_4} + m^{(eq)}_{H_2PO_4^-}\varepsilon^*_{H_2PO_4^-} + m^{(eq)}_{HPO_4^{2-}}\varepsilon^*_{HPO_4^{2-}} + m^{(eq)}_{PO_4^{3-}}\varepsilon^*_{PO_4^{3-}} = 0 \qquad \text{(A-24.5)}$$

Searching for a minimum of $T^2\dot{\sigma}$ is equivalent to searching for a minimum of the combined function

$$\begin{aligned}
&T^2\dot{\sigma}\left(\varepsilon_{P_{CO_2}}, \varepsilon_{m_{CO_2}}, \varepsilon_{HCO_3^-}, \varepsilon_{CO_3^{2-}}, \varepsilon_{H_3PO_4}, \varepsilon_{H_2PO_4^-}, \varepsilon_{HPO_4^{2-}}, \varepsilon_{PO_4^{3-}}, \varepsilon_{HO^-}, \varepsilon_{H^+}\right) + \\
&\lambda_1\left(m^{(eq)}_{HCO_3^-}\varepsilon_{HCO_3^-} + 2m^{(eq)}_{CO_3^{2-}}\varepsilon_{CO_3^{2-}} + m^{(eq)}_{H_2PO_4^-}\varepsilon_{H_2PO_4^-} + 2m^{(eq)}_{HPO_4^{2-}}\varepsilon_{HPO_4^{2-}} + 3m^{(eq)}_{PO_4^{3-}}\varepsilon_{PO_4^{3-}} + m^{(eq)}_{HO^-}\varepsilon_{HO^-} - m^{(eq)}_{H^+}\varepsilon_{H^+}\right) + \qquad \text{(A-24.6)} \\
&\lambda_2\left(m^{(eq)}_{H_3PO_4}\varepsilon_{H_3PO_4} + m^{(eq)}_{H_2PO_4^-}\varepsilon_{H_2PO_4^-} + m^{(eq)}_{HPO_4^{2-}}\varepsilon_{HPO_4^{2-}} + m^{(eq)}_{PO_4^{3-}}\varepsilon_{PO_4^{3-}}\right)
\end{aligned}$$

inasmuch as the expressions within brackets equal zero. The parameters λ_1 and λ_2 (Lagrange multipliers) have yet to be determined.

$$\frac{r_1A_1 + r_2A_2 + r_3A_3 + r_4A_4 + r_5A_5 + r_6A_6 + r_7A_7}{T} = \dot{\sigma}$$

The necessary condition for a minimum of the combined function (118) is that its first derivative with respect to the independent variables must equal zero. From this condition we derive the following algebraic linear equations

$$T^2\frac{\partial\dot{\sigma}}{\partial\varepsilon^*_{P_{CO_2}}} = -2L_{1,1}\left(RT\right)^2\left(\varepsilon^*_{m_{CO_2}} - \varepsilon^*_{P_{CO_2}}\right) + 2L_{2,2}RT\left(A_0 - RT\left(\varepsilon^*_{m_{CO_2}} - \varepsilon^*_{P_{CO_2}}\right)\right) = 0 \qquad \text{(A-24.7)}$$

$$T^2\frac{\partial\dot{\sigma}}{\partial\varepsilon^*_{m_{CO_2}}} = 2L_{1,1}\left(RT\right)^2\left(\varepsilon^*_{m_{CO_2}} - \varepsilon^*_{P_{CO_2}}\right) - 2L_{2,2}RT\left(A_0 - RT\left(\varepsilon^*_{m_{CO_2}} - \varepsilon^*_{P_{CO_2}}\right)\right) = 0 \qquad \text{(A-24.8)}$$

$$T^2\frac{\partial\dot{\sigma}}{\partial\varepsilon^*_{HCO_3^-}} = -2L_{3,3}\left(RT\right)^2\left(\varepsilon^*_{CO_3^{2-}} + \varepsilon^*_{H^+} - \varepsilon^*_{HCO_3^-}\right) + \lambda_1 m^{(eq)}_{HCO_3^-} = 0 \qquad \text{(A-24.9)}$$

$$T^2\frac{\partial\dot{\sigma}}{\partial\varepsilon^*_{CO_3^{2-}}} = 2L_{3,3}\left(RT\right)^2\left(\varepsilon^*_{CO_3^{2-}} + \varepsilon^*_{H^+} - \varepsilon^*_{HCO_3^-}\right) + 2\lambda_1 m^{(eq)}_{CO_3^{2-}} = 0 \qquad \text{(A-24.10)}$$

$$T^2 \frac{\partial \dot{\sigma}}{\partial \varepsilon^*_{H_3PO_4}} = -2L_{4,4}\left(RT\right)^2\left(\varepsilon^*_{H_2PO_4^-} + \varepsilon^*_{H^+} - \varepsilon^*_{H_3PO_4}\right) + \lambda_2\, m^{(eq)}_{H_3PO_4} = 0 \tag{A-24.11}$$

$$\begin{aligned} T^2 \frac{\partial \dot{\sigma}}{\partial \varepsilon^*_{H_2PO_4^-}} &= 2L_{4,4}\left(RT\right)^2\left(\varepsilon^*_{H_2PO_4^-} + \varepsilon^*_{H^+} - \varepsilon^*_{H_3PO_4}\right) - \\ &\quad 2L_{5,5}\left(RT\right)^2\left(\varepsilon^*_{HPO_4^{2-}} + \varepsilon^*_{H^+} - \varepsilon^*_{H_2PO_4^-}\right) + \left(\lambda_1 + \lambda_2\right) m^{(eq)}_{H_2PO_4^-} = 0 \end{aligned} \tag{A-24.12}$$

$$\begin{aligned} T^2 \frac{\partial \dot{\sigma}}{\partial \varepsilon^*_{HPO_4^{2-}}} &= 2L_{5,5}\left(RT\right)^2\left(\varepsilon^*_{HPO_4^{2-}} + \varepsilon^*_{H^+} - \varepsilon^*_{H_2PO_4^-}\right) - \\ &\quad 2L_{6,6}\left(RT\right)^2\left(\varepsilon^*_{PO_4^{3-}} + \varepsilon^*_{H^+} - \varepsilon^*_{HPO_4^{2-}}\right) + \left(2\lambda_1 + \lambda_2\right) m^{(eq)}_{HPO_4^{2-}} = 0 \end{aligned} \tag{A-24.13}$$

$$T^2 \frac{\partial \dot{\sigma}}{\partial \varepsilon^*_{PO_4^{3-}}} = 2L_{6,6}\left(RT\right)^2\left(\varepsilon^*_{PO_4^{3-}} + \varepsilon^*_{H^+} - \varepsilon^*_{HPO_4^{2-}}\right) + \left(3\lambda_1 + \lambda_2\right) m^{(eq)}_{PO_4^{3-}} = 0 \tag{A-24.14}$$

$$T^2 \frac{\partial \dot{\sigma}}{\partial \varepsilon^*_{HO^-}} = 2L_{7,7}\left(RT\right)^2\left(\varepsilon^*_{H^+} + \varepsilon^*_{HO^-}\right) + \lambda_1 m^{(eq)}_{HO^-} = 0 \tag{A-24.15}$$

$$\begin{aligned} T^2 \frac{\partial \dot{\sigma}}{\partial \varepsilon^*_{H^+}} &= 2L_{3,3}\left(RT\right)^2\left(\varepsilon^*_{CO_3^{2-}} + \varepsilon^*_{H^+} - \varepsilon^*_{HCO_3^-}\right) + 2L_{4,4}\left(RT\right)^2\left(\varepsilon^*_{H_2PO_4^-} + \varepsilon^*_{H^+} - \varepsilon^*_{H_3PO_4}\right) + \\ &\quad 2L_{5,5}\left(RT\right)^2\left(\varepsilon^*_{HPO_4^{2-}} + \varepsilon^*_{H^+} - \varepsilon^*_{H_2PO_4^-}\right) + 2L_{6,6}\left(RT\right)^2\left(\varepsilon^*_{PO_4^{3-}} + \varepsilon^*_{H^+} - \varepsilon^*_{HPO_4^{2-}}\right) + \\ &\quad 2L_{7,7}\left(RT\right)^2\left(\varepsilon^*_{H^+} + \varepsilon^*_{HO^-}\right) - \lambda_1 m^{(eq)}_{H^+} = 0 \end{aligned} \tag{A-24.16}$$

From Equations (119-c, d), we conclude

$$\lambda_1\left(m^{(eq)}_{HCO_3^-} + 2\,m^{(eq)}_{CO_3^{2-}}\right) = 0 \ ; \qquad \lambda_1 = 0 \tag{A-24.17}$$

Moreover, from Equations (119-i) and (120), we get

$$2L_{7,7}\left(\varepsilon^*_{H^+} + \varepsilon^*_{HO^-}\right) = 0 \qquad ; \qquad \varepsilon^*_{HO^-} = -\varepsilon^*_{H^+} \tag{A-24.18}$$

Substitution of these results in Equations (119), and keeping only the linearly independent equations thus obtained, we are left with the following set of linear algebraic equations:

$$A_1 = RT\left(\varepsilon^*_{m_{CO_2}} - \varepsilon^*_{P_{CO_2}}\right) = \frac{L_{2,2}}{\left(L_{1,1}+L_{2,2}\right)}A_0 = \frac{1}{L_{1,1}}\frac{1}{\left(\dfrac{1}{L_{1,1}}+\dfrac{1}{L_{2,2}}\right)}A_0 \qquad \text{(A-24.19-a)}$$

$$A_2 = RT\left(\varepsilon^*_{HCO_3^-} + \varepsilon^*_{H^+} - \varepsilon^*_{m_{CO_2}}\right) = A_0 - A_1 = A_0 - \frac{L_{2,2}}{\left(L_{1,1}+L_{2,2}\right)}A_0 = \frac{1}{L_{2,2}}\frac{1}{\left(\dfrac{1}{L_{1,1}}+\dfrac{1}{L_{2,2}}\right)}A_0 \qquad \text{(A-24.19-b)}$$

$$A_3 = RT\left(\varepsilon^*_{CO_3^{2-}} + \varepsilon^*_{H^+} - \varepsilon^*_{HCO_3^-}\right) = 0 \qquad \text{(A-24.20)}$$

$$2L_{4,4}\left(RT\right)A_4 = 2L_{4,4}\left(RT\right)^2\left(\varepsilon^*_{H_2PO_4^-} + \varepsilon^*_{H^+} - \varepsilon^*_{H_3PO_4}\right) = \lambda_2\, m^{(eq)}_{H_3PO_4} \qquad \text{(A-24.21)}$$

$$\begin{aligned} &2L_{4,4}\left(RT\right)^2\left(\varepsilon^*_{H_2PO_4^-} + \varepsilon^*_{H^+} - \varepsilon^*_{H_3PO_4}\right) - \\ &\qquad 2L_{5,5}\left(RT\right)^2\left(\varepsilon^*_{HPO_4^{2-}} + \varepsilon^*_{H^+} - \varepsilon^*_{H_2PO_4^-}\right) + \lambda_2\, m^{(eq)}_{H_2PO_4^-} = 0 \end{aligned} \qquad \text{(A-24.22)}$$

$$\begin{aligned} &2L_{5,5}\left(RT\right)^2\left(\varepsilon^*_{HPO_4^{2-}} + \varepsilon^*_{H^+} - \varepsilon^*_{H_2PO_4^-}\right) - \\ &\qquad 2L_{6,6}\left(RT\right)^2\left(\varepsilon^*_{PO_4^{3-}} + \varepsilon^*_{H^+} - \varepsilon^*_{HPO_4^{2-}}\right) + \lambda_2 m^{(eq)}_{HPO_4^{2-}} = 0 \end{aligned} \qquad \text{(A-24.23)}$$

$$2L_{6,6}\left(RT\right)^2\left(\varepsilon^*_{PO_4^{3-}} + \varepsilon^*_{H^+} - \varepsilon^*_{HPO_4^{2-}}\right) = -\lambda_2\, m^{(eq)}_{PO_4^{3-}} \qquad \text{(A-24.24)}$$

$$\begin{aligned} &2L_{4,4}\left(RT\right)^2\left(\varepsilon^*_{H_2PO_4^-} + \varepsilon^*_{H^+} - \varepsilon^*_{H_3PO_4}\right) + \\ &\qquad 2L_{5,5}\left(RT\right)^2\left(\varepsilon^*_{HPO_4^{2-}} + \varepsilon^*_{H^+} - \varepsilon^*_{H_2PO_4^-}\right) + 2L_{6,6}\left(RT\right)^2\left(\varepsilon^*_{PO_4^{3-}} + \varepsilon^*_{H^+} - \varepsilon^*_{HPO_4^{2-}}\right) = 0 \end{aligned} \qquad \text{(A-24.25)}$$

Combination of Equations (122-d, e, f), gives

$$2L_{4,4}\left(RT\right)A_4 = 2L_{4,4}\left(RT\right)^2\left(\varepsilon^*_{H_2PO_4^-} + \varepsilon^*_{H^+} - \varepsilon^*_{H_3PO_4}\right) = \lambda_2\, m^{(eq)}_{H_3PO_4} \qquad \text{(A-24.26)}$$

$$2L_{5,5}\left(RT\right)^2\left(\varepsilon^*_{HPO_4^{2-}} + \varepsilon^*_{H^+} - \varepsilon^*_{H_2PO_4^-}\right) = \lambda_2\left(m^{(eq)}_{H_3PO_4} + m^{(eq)}_{H_2PO_4^-}\right) \qquad \text{(A-24.27)}$$

$$2L_{6,6}\left(RT\right)^2\left(\varepsilon^*_{PO_4^{3-}} + \varepsilon^*_{H^+} - \varepsilon^*_{HPO_4^{2-}}\right) = \lambda_2\left(m^{(eq)}_{H_3PO_4} + m^{(eq)}_{H_2PO_4^-} + m^{(eq)}_{HPO_4^{2-}}\right) = 0 \qquad \text{(A-24.28)}$$

$$2L_{6,6}\left(RT\right)^2\left(\varepsilon^*_{PO_4^{3-}} + \varepsilon^*_{H^+} - \varepsilon^*_{HPO_4^{2-}}\right) = -\lambda_2\, m^{(eq)}_{PO_4^{3-}} \qquad \text{(A-24.29)}$$

By comparing the last two equations, we conclude that $\lambda_2 = 0$.

Thus, seven algebraic relationships reflected the least possible $\dot{\sigma}$:

$$\left(\varepsilon^{*}_{m_{CO_2}} - \varepsilon^{*}_{P_{CO_2}}\right) = \frac{L_{2,2}}{\left(L_{1,1} + L_{2,2}\right)}\left(\varepsilon^{*}_{HCO_3^-} + \varepsilon^{*}_{H^+} - \varepsilon^{*}_{P_{CO_2}}\right) \qquad \text{(A-25-a)}$$

$$\left(\varepsilon^{*}_{CO_3^{2-}} + \varepsilon^{*}_{H^+} - \varepsilon^{*}_{HCO_3^-}\right) = 0 \quad ; \quad \left(\varepsilon^{*}_{HCO_3^-} - \varepsilon^{*}_{CO_3^{2-}}\right) = \varepsilon^{*}_{H^+} \qquad \text{(A-25-b)}$$

$$\left(\varepsilon^{*}_{H_2PO_4^-} + \varepsilon^{*}_{H^+} - \varepsilon^{*}_{H_3PO_4}\right) = 0 \quad ; \quad \left(\varepsilon^{*}_{H_3PO_4} - \varepsilon^{*}_{H_2PO_4^-}\right) = \varepsilon^{*}_{H^+} \qquad \text{(A-25-c)}$$

$$\left(\varepsilon^{*}_{HPO_4^{2-}} + \varepsilon^{*}_{H^+} - \varepsilon^{*}_{H_2PO_4^-}\right) = 0 \quad ; \quad \left(\varepsilon^{*}_{H_2PO_4^-} - \varepsilon^{*}_{HPO_4^{2-}}\right) = \varepsilon^{*}_{H^+} \qquad \text{(A-25-d)}$$

$$\left(\varepsilon^{*}_{PO_4^{3-}} + \varepsilon^{*}_{H^+} - \varepsilon^{*}_{HPO_4^{2-}}\right) = 0 \quad ; \quad \left(\varepsilon^{*}_{HPO_4^{2-}} - \varepsilon^{*}_{PO_4^{3-}}\right) = \varepsilon^{*}_{H^+} \qquad \text{(A-25-e)}$$

$$m^{(eq)}_{HCO_3^-}\varepsilon^{*}_{HCO_3^-} + 2\,m^{(eq)}_{CO_3^{2-}}\varepsilon^{*}_{CO_3^{2-}} + m^{(eq)}_{H_2PO_4^-}\varepsilon^{*}_{H_2PO_4^-} + 2m^{(eq)}_{HPO_4^{2-}}\varepsilon^{*}_{HPO_4^{2-}} + 3m^{(eq)}_{PO_4^{3-}}\varepsilon^{*}_{PO_4^{3-}} = \left(\frac{K_7}{m^{(eq)}_{H^+}} + m^{(eq)}_{H^+}\right)\varepsilon^{*}_{H^+} \qquad \text{(A-25-f)}$$

$$m^{(eq)}_{H_3PO_4}\varepsilon^{*}_{H_3PO_4} + m^{(eq)}_{H_2PO_4^-}\varepsilon^{*}_{H_2PO_4^-} + m^{(eq)}_{HPO_4^{2-}}\varepsilon^{*}_{HPO_4^{2-}} + m^{(eq)}_{PO_4^{3-}}\varepsilon^{*}_{PO_4^{3-}} = 0 \qquad \text{(A-25-g)}$$

From Equation (A-25-a), we could readily derive the following, very important condition,

$$\frac{L_{1,1}}{T}A_1^{*} = \frac{L_{2,2}}{T}A_2^{*} = \left(\frac{1}{T}\right)\frac{1}{\left(\dfrac{1}{L_{1,1}} + \dfrac{1}{L_{2,2}}\right)}A_0 \qquad \text{(A-26)}$$

From Equation (A-13), we could assume that the results shown in Equations (A-25a-g) are equivalent to the following:

$$r_1^{*} = r_2^{*} = r^{*} = \left(\frac{1}{T}\right)\frac{1}{\left(\dfrac{1}{L_{1,1}} + \dfrac{1}{L_{2,2}}\right)}A_0 \quad ; \quad r_3^{*} = r_4^{*} = r_5^{*} = r_6^{*} = r_7^{*} = 0 \qquad \text{(A-27)}$$

where the expressions of the Onsager coefficients were given in Table A-2.

The expressions of r_1^{*}, r_2^{*} and r^{*} are as follows:

$$r_1^{*} = a_{int}k_1P^{(eq)}_{CO_2}\left[\varepsilon^{*}_{m_{CO_2}} - \varepsilon^{*}_{P_{CO_2}}\right] \qquad \text{(A-28-a)}$$

$$r_2^* = k_2 K_1 P_{CO_2}^{(eq)} \left[\varepsilon_{HCO_3^-}^* + \varepsilon_{H^+}^* - \varepsilon_{m_{CO_2}}^* \right] \qquad \text{(A-28-b)}$$

$$r^* = \frac{P_{CO_2}^{(eq)}}{\left[\dfrac{1}{a_{int} k_1} + \dfrac{1}{k_2 K_1} \right]} \left[\varepsilon_{HCO_3^-}^* + \varepsilon_{H^+}^* - \varepsilon_{P_{CO_2}}^* \right] \qquad \text{(A-28-c)}$$

Only two among the three reaction rate expressions of Equations (A-28-a,b,c) are linearly independent. The restriction given in Equations (A-25a-g) between the reaction rates of the independent non-equilibrium steps in the absorption-reaction mechanism is a distinctive result derived from the condition of minimal rate of internal generation of entropy, in the Linear Irreversible Regime. The affinities (driving forces) associated to all **the non-zero reaction rates** must adjust their values in order to satisfy the constraint that the corresponding reaction rates **must remain equal to each other** as the system moves from an initial partial equilibrium state to the final global equilibrium state**,** along the trajectory of minimum rate of internal generation of entropy. **The largest driving force corresponds to the rate determining step**.

Regarding the other unknowns, the solution of the system of Equations (A-25a-g), in terms of the independent variables $\varepsilon_{H^+}^*$ and $\varepsilon_{P_{CO_2}}^*$ is:

$$\varepsilon_{H_3PO_4}^* = \frac{\left(m_{H_2PO_4^-}^{(eq)} + 2m_{HPO_4^{2-}}^{(eq)} + 3m_{PO_4^{3-}}^{(eq)} \right)}{\left(m_{H_2PO_4^-}^0 + m_{HPO_4^{2-}}^0 \right)} \varepsilon_{H^+}^* \qquad \text{(A-29-a)}$$

$$\varepsilon_{H_2PO_4^-}^* = -\frac{\left(m_{H_3PO_4}^{(eq)} - m_{HPO_4^{2-}}^{(eq)} - 2m_{PO_4^{3-}}^{(eq)} \right)}{\left(m_{H_2PO_4^-}^0 + m_{HPO_4^{2-}}^0 \right)} \varepsilon_{H^+}^* \qquad \text{(A-29-b)}$$

$$\varepsilon_{HPO_4^{2-}}^* = -\frac{\left(2m_{H_3PO_4}^{(eq)} + m_{H_2PO_4^-}^{(eq)} - m_{PO_4^{3-}}^{(eq)} \right)}{\left(m_{H_2PO_4^-}^0 + m_{HPO_4^{2-}}^0 \right)} \varepsilon_{H^+}^* \qquad \text{(A-29-c)}$$

$$\varepsilon_{PO_4^{3-}}^* = -\frac{\left(3m_{H_3PO_4}^{(eq)} + 2m_{H_2PO_4^-}^{(eq)} + m_{HPO_4^{2-}}^{(eq)} \right)}{\left(m_{H_2PO_4^-}^0 + m_{HPO_4^{2-}}^0 \right)} \varepsilon_{H^+}^* \qquad \text{(A-29-d)}$$

$$\varepsilon^{*}_{m_{CO_2}} = \frac{k_2K_1}{\left(a_{int}k_1 + 2k_2K_1\right)} \times$$

$$\Bigg(\; 1 + \frac{1}{\left(m^{0}_{H_2PO_4^-} + m^{0}_{HPO_4^{2-}}\right)\left(m^{(eq)}_{HCO_3^-} + 2m^{(eq)}_{CO_3^{2-}}\right)m^{(eq)}_{H^+}} \times$$

$$\Bigg(K_7\left(m^{0}_{H_2PO_4^-} + m^{0}_{HPO_4^{2-}}\right) + \Big(m^{(eq)}_{H_3PO_4}m^{(eq)}_{H_2PO_4^-} + 4m^{(eq)}_{H_3PO_4}m^{(eq)}_{HPO_4^{2-}} + m^{(eq)}_{H_2PO_4^-}m^{(eq)}_{HPO_4^{2-}} +$$

$$\left(9m^{(eq)}_{H_3PO_4} + 4m^{(eq)}_{H_2PO_4^-} + m^{(eq)}_{HPO_4^{2-}}\right)m^{(eq)}_{PO_4^{3-}} + \qquad \text{(A-29-f)}$$

$$2\Big(\left(m^{0}_{H_2PO_4^-} + m^{0}_{HPO_4^{2-}}\right)m^{(eq)}_{CO_3^{2-}}\Big)m^{(eq)}_{H^+} + \left(m^{0}_{H_2PO_4^-} + m^{0}_{HPO_4^{2-}}\right)\left(\left(m^{(eq)}_{H^+}\right)^2\right) \Bigg)\varepsilon^{*}_{H^+} +$$

$$\left(\frac{\left(a_{int}k_1 + k_2K_1\right)}{\left(a_{int}k_1 + 2k_2K_1\right)}\right)\varepsilon^{*}_{P_{CO_2}}$$

$$\varepsilon^{*}_{HCO_3^-} = \frac{1}{\left(m^{0}_{H_2PO_4^-} + m^{0}_{HPO_4^{2-}}\right)\left(m^{(eq)}_{HCO_3^-} + 2m^{(eq)}_{CO_3^{2-}}\right)m^{(eq)}_{H^+}} \times$$

$$\Bigg(\; K_7\left(m^{0}_{H_2PO_4^-} + m^{0}_{HPO_4^{2-}}\right) + \Big(m^{(eq)}_{H_3PO_4}m^{(eq)}_{H_2PO_4^-} + 4m^{(eq)}_{H_3PO_4}m^{(eq)}_{HPO_4^{2-}} + m^{(eq)}_{H_2PO_4^-}m^{(eq)}_{HPO_4^{2-}} + \qquad \text{(A-29-g)}$$

$$\left(9m^{(eq)}_{H_3PO_4} + 4m^{(eq)}_{H_2PO_4^-} + m^{(eq)}_{HPO_4^{2-}}\right)m^{(eq)}_{PO_4^{3-}} + 2\Big(\left(m^{0}_{H_2PO_4^-} + m^{0}_{HPO_4^{2-}}\right)m^{(eq)}_{CO_3^{2-}}\Big)m^{(eq)}_{H^+} +$$

$$\left(m^{0}_{H_2PO_4^-} + m^{0}_{HPO_4^{2-}}\right)\left(m^{(eq)}_{H^+}\right)^2 \quad \Bigg)\varepsilon^{*}_{H^+}$$

$$\varepsilon^{*}_{CO_3^{2-}} = \frac{1}{\left(m^{0}_{H_2PO_4^-} + m^{0}_{HPO_4^{2-}}\right)\left(m^{(eq)}_{HCO_3^-} + 2m^{(eq)}_{CO_3^{2-}}\right)m^{(eq)}_{H^+}} \times$$

$$\Bigg(\; K_7\left(m^{0}_{H_2PO_4^-} + m^{0}_{HPO_4^{2-}}\right) + \Big(\; m^{(eq)}_{H_3PO_4}m^{(eq)}_{H_2PO_4^-} + 4m^{(eq)}_{H_3PO_4}m^{(eq)}_{HPO_4^{2-}} + m^{(eq)}_{H_2PO_4^-}m^{(eq)}_{HPO_4^{2-}} + \qquad \text{(A-29-h)}$$

$$\left(9m^{(eq)}_{H_3PO_4} + 4m^{(eq)}_{H_2PO_4^-} + m^{(eq)}_{HPO_4^{2-}}\right)m^{(eq)}_{PO_4^{3-}} - \Big(\left(m^{0}_{H_2PO_4^-} + m^{0}_{HPO_4^{2-}}\right)m^{(eq)}_{HCO_3^-}\Big)m^{(eq)}_{H^+} +$$

$$\left(m^{0}_{H_2PO_4^-} + m^{0}_{HPO_4^{2-}}\right)\left(m^{(eq)}_{H^+}\right)^2 \quad \Bigg)\varepsilon^{*}_{H^+}$$

8.1.3 The time evolution of $\varepsilon^{*}_{H^+}$ and $\varepsilon^{*}_{P_{CO_2}}$ in the Linear Irreversible Regime for an open gas-liquid system.

From Equation (A-5), we were able to conclude that the rate of change of the proton molal concentration at any instant during the time interval that takes the system to go from the initial, perturbed state to the final, equilibrium state, in a well-mixed aqueous phase that is in contact just with a gas phase dispersed in its interior (simile to a batch process) is:

$$\frac{dm^*_{H^+}}{dt} = r^*_{H^+} = r^*_2 + r^*_3 + r^*_4 + r^*_5 + r^*_6 + r^*_7 = r^*_2 \qquad \text{(A-30)}$$

If we recall the definition:

$$\varepsilon^*_{H^+} = \left(\frac{m^{(eq)}_{H^+} - m^*_{H^+}}{m^{(eq)}_{H^+}} \right) \quad ; \qquad m^*_{H^+} = m^{(eq)}_{H^+}\left(1 - \varepsilon^*_{H^+}\right) \;\; ; \;\; -m^{(eq)}_{H^+}\frac{d\varepsilon^*_{H^+}}{dt} = r^*_2 \qquad \text{(A-31)}$$

The combination of Equations (A-31) with Equation (A-28-b) gives:

$$-m^{(eq)}_{H^+}\frac{d\varepsilon^*_{H^+}}{dt} = \frac{P^{(eq)}_{CO_2}}{\left[\dfrac{1}{a_{int}k_1} + \dfrac{1}{k_2K_1}\right]}\left[\varepsilon^*_{HCO_3^-} + \varepsilon^*_{H^+} - \varepsilon^*_{P_{CO_2}}\right] \qquad \text{(A-32)}$$

With the definition:

$$\begin{aligned}
\kappa_{H^+} = \Bigg[\; 1 + &\frac{1}{\left(m^0_{H_2PO_4^-} + m^0_{HPO_4^{2-}}\right)\left(m^{(eq)}_{HCO_3^-} + 2m^{(eq)}_{CO_3^{2-}}\right)m^{(eq)}_{H^+}} \times \\
&\Bigg(K_7\left(m^0_{H_2PO_4^-} + m^0_{HPO_4^{2-}}\right) + \left(m^{(eq)}_{H_3PO_4}m^{(eq)}_{H_2PO_4^-} + 4m^{(eq)}_{H_3PO_4}m^{(eq)}_{HPO_4^{2-}} + m^{(eq)}_{H_2PO_4^-}m^{(eq)}_{HPO_4^{2-}} + \right. \\
&\left(9m^{(eq)}_{H_3PO_4} + 4m^{(eq)}_{H_2PO_4^-} + m^{(eq)}_{HPO_4^{2-}}\right)m^{(eq)}_{PO_4^{3-}} + 2\left(m^0_{H_2PO_4^-} + m^0_{HPO_4^{2-}}\right)m^{(eq)}_{CO_3^{2-}}\Big)m^{(eq)}_{H^+} + \\
&\left(m^0_{H_2PO_4^-} + m^0_{HPO_4^{2-}}\right)\left(m^{(eq)}_{H^+}\right)^2 \Bigg) \Bigg] > 1
\end{aligned} \qquad \text{(A-33)}$$

Equations (A-32), could be written in the following, more compact way:

$$\left[\varepsilon^*_{HCO_3^-} + \varepsilon^*_{H^+} - \varepsilon^*_{P_{CO_2}}\right] = \kappa_{H^+}\,\varepsilon^*_{H^+} - \varepsilon^*_{P_{CO_2}} \qquad \text{(A-34)}$$

Substitution in Equations (A-31) and (A-34), gives

$$\frac{d\varepsilon^*_{H^+}}{dt} = -\frac{P^{(eq)}_{CO_2}}{m^{(eq)}_{H^+}\left[\dfrac{1}{a_{int}k_1} + \dfrac{1}{k_2K_1}\right]}\left[\kappa_{H^+}\,\varepsilon^*_{H^+} - \varepsilon^*_{P_{CO_2}}\right] \qquad \text{(A-35)}$$

In order to obtain an equation for the time dependence of $\varepsilon^{*}_{P_{CO_2}}$ in an **open system**, we started by setting up a CO_2 balance in the gas phase (1), bubbling in the interior of the aqueous phase (2), with a defined, constant, gas flow (Q) and a defined constant partial pressure of CO_2 in the feed gas stream ($P^{f}_{CO_2}$):

$$\begin{aligned}\frac{dn^{(1)}_{CO_2}}{dt} &= -V^{(2)}a_{int}\,j^{(1\rightarrow 2)}_{CO_2} + Q\left(\frac{P^{f}_{CO_2}}{RT}\right) - Q\left(\frac{P^{*}_{CO_2}}{RT}\right) \\ &= -V^{(2)}a_{int}\,j^{(1\rightarrow 2)}_{CO_2} + Q\left(\frac{P^{(eq)}_{CO_2}}{RT}\right)\left[\left(\frac{P^{f}_{CO_2} - P^{(eq)}_{CO_2}}{P^{(eq)}_{CO_2}}\right) - \left(\frac{P^{*}_{CO_2} - P^{(eq)}_{CO_2}}{P^{(eq)}_{CO_2}}\right)\right]\end{aligned} \qquad \text{(A-36)}$$

Therefore, in the final equilibrium state, $P^{(eq)}_{CO_2} = P^{f}_{CO_2}$ and Equation (36) can be simplified into the following

$$\frac{dn^{(1)}_{CO_2}}{dt} = -V^{(2)}a_{int}\,j^{(1\rightarrow 2)}_{CO_2} + Q\left(\frac{P^{f}_{CO_2}}{RT}\right)\left(\frac{P^{f}_{CO_2} - P^{*}_{CO_2}}{P^{f}_{CO_2}}\right) = -V^{(2)}a_{int}\,j^{(1\rightarrow 2)}_{CO_2} + Q\left(\frac{P^{f}_{CO_2}}{RT}\right)\varepsilon^{*}_{P_{CO_2}} \qquad \text{(A-37)}$$

If we consider the following identity,

$$n^{(1)}_{CO_2} = \left(n^{(1)}_{CO_2}\right)_{eq}\left(1 - \varepsilon^{*}_{P_{CO_2}}\right) \qquad \text{(A-38)}$$

Differentiation of Equation (A-38) with respect to time, gives,

$$\frac{dn^{(1)}_{CO_2}}{dt} = -\left(n^{(1)}_{CO_2}\right)_{eq}\frac{d\varepsilon^{*}_{P_{CO_2}}}{dt} \qquad \text{(A-39)}$$

By substitution in Equation (A-37), making use of equation (A-28-c), and after a rearrangement we have,

$$\frac{d\varepsilon^{*}_{P_{CO_2}}}{dt} = \frac{P^{f}_{CO_2}V^{(2)}}{\left(n^{(1)}_{CO_2}\right)_{eq}}\frac{1}{\left[\dfrac{1}{a_{int}k_1} + \dfrac{1}{k_2K_1}\right]}\left[\varepsilon^{*}_{HCO_3^-} + \varepsilon^{*}_{H^+} - \varepsilon^{*}_{P_{CO_2}}\right] - Q\left(\frac{P^{f}_{CO_2}}{\left(n^{(1)}_{CO_2}\right)_{eq}RT}\right)\varepsilon^{*}_{P_{CO_2}} \qquad \text{(A-40)}$$

Because the gas phase was assumed ideal, $\left(\dfrac{P^{f}_{CO_2}}{\left(n^{(1)}_{CO_2}\right)_{eq} RT}\right) = \dfrac{1}{V^{(1)}_{eq}}$ where $V^{(1)}_{eq}$ is the volume of the dispersed gas (i.e., the “resident” gas volume or “gas hold-up”) at the final, $t \rightarrow \infty$, CO_2 transfer equilibrium. In most cases of our interest, the partial pressure of CO_2 in the gas phase is very small compared with that of the inert, less soluble gases. Whenever this simplifying assumption holds, we can make the following approximation,

$$V^{(1)}_{eq} \approx V^{(1)} \approx constant \tag{A-41}$$

Then, we have,

$$\frac{d\varepsilon^{*}_{P_{CO_2}}}{dt} = \frac{V^{(2)}}{V^{(1)}} \frac{RT}{\left[\dfrac{1}{a_{int}k_1} + \dfrac{1}{k_2 K_1}\right]} \left[\varepsilon^{*}_{HCO_3^-} + \varepsilon^{*}_{H^+} - \varepsilon^{*}_{P_{CO_2}}\right] - \left(\frac{Q}{V^{(1)}}\right) \varepsilon^{*}_{P_{CO_2}} \tag{A-42}$$

After recalling the relationship (A-34), Equation (A-42) may be reorganized as follows,

$$\frac{d\varepsilon^{*}_{P_{CO_2}}}{dt} = RT\left(\frac{V^{(2)}}{V^{(1)}}\right) \frac{\kappa_{H^+}}{\left[\dfrac{1}{a_{int}k_1} + \dfrac{1}{k_2 K_1}\right]} \varepsilon^{*}_{H^+} - \left[RT\left(\frac{V^{(2)}}{V^{(1)}}\right) \frac{1}{\left[\dfrac{1}{a_{int}k_1} + \dfrac{1}{k_2 K_1}\right]} + \left(\frac{Q}{V^{(1)}}\right)\right] \varepsilon^{*}_{P_{CO_2}} \tag{A-43}$$

The set of **coupled ordinary differential equations** describing the dynamics of the two phase system in its way to overall equilibrium is,

$$\frac{d\varepsilon^{*}_{H^+}}{dt} = -\frac{P^{f}_{CO_2}}{m^{(eq)}_{H^+}\left[\dfrac{1}{a_{int}k_1} + \dfrac{1}{k_2 K_1}\right]} \kappa_{H^+}\, \varepsilon^{*}_{H^+} + \frac{P^{f}_{CO_2}}{m^{(eq)}_{H^+}\left[\dfrac{1}{a_{int}k_1} + \dfrac{1}{k_2 K_1}\right]} \varepsilon^{*}_{P_{CO_2}} \tag{A-44-a}$$

$$\frac{d\varepsilon^{*}_{P_{CO_2}}}{dt} = RT\left(\frac{V^{(2)}}{V^{(1)}}\right) \frac{\kappa_{H^+}}{\left[\dfrac{1}{a_{int}k_1} + \dfrac{1}{k_2 K_1}\right]} \varepsilon^{*}_{H^+} - \left[RT\left(\frac{V^{(2)}}{V^{(1)}}\right) \frac{1}{\left[\dfrac{1}{a_{int}k_1} + \dfrac{1}{k_2 K_1}\right]} + \left(\frac{Q}{V^{(1)}}\right)\right] \varepsilon^{*}_{P_{CO_2}} \tag{A-44-b}$$

This system of ordinary differential equations can be compacted into the following matrix form

$$\frac{d\,\underline{y}}{dt} = \underline{\underline{A}}\,\underline{y} \qquad \text{(A-44-c)}$$

where

$$\underline{y} = \begin{pmatrix} \varepsilon^{*}_{H^{+}} \\ \varepsilon^{*}_{P_{CO_2}} \end{pmatrix}$$

$$\frac{d\,\underline{y}}{dt} = \frac{d}{dt}\begin{pmatrix} \varepsilon^{*}_{H^{+}} \\ \varepsilon^{*}_{P_{CO_2}} \end{pmatrix}$$

$$\underline{\underline{A}} = \begin{pmatrix} a_{11} & a_{12} \\ a_{21} & a_{22} \end{pmatrix}$$

$$a_{11} = -\frac{P^{f}_{CO_2}}{m^{eq}_{H^{+}}\left[\dfrac{1}{a_{\text{int}}k_1} + \dfrac{1}{k_2K_1}\right]}\kappa_{H^{+}} < 0 \qquad \text{(A-44-d)}$$

$$a_{12} = \frac{P^{f}_{CO_2}}{m^{eq}_{H^{+}}\left[\dfrac{1}{a_{\text{int}}k_1} + \dfrac{1}{k_2K_1}\right]} > 0 \qquad \text{(A-44-e)}$$

$$a_{21} = RT\left(\frac{V^{2}}{V^{1}}\right)\frac{\kappa_{H^{+}}}{\left[\dfrac{1}{a_{\text{int}}k_1} + \dfrac{1}{k_2K_1}\right]} > 0 \qquad \text{(A-44-f)}$$

$$a_{22} = -\left[RT\left(\frac{V^{2}}{V^{1}}\right)\frac{1}{\left[\dfrac{1}{a_{\text{int}}k_1} + \dfrac{1}{k_2K_1}\right]} + \left(\frac{Q}{V^{1}}\right)\right] < 0 \qquad \text{(A-44-h)}$$

We want to look for an equivalent set of differential equations but where the equations have been uncoupled.

Let us start by considering the eigenvalue problem

$$\underline{\underline{A}}\,\underline{x}^{(i)} = \lambda_i \underline{x}^{(i)} \qquad ; \qquad i = 1,2$$

where

$$\underline{\underline{A}}\underline{x}^{(i)} = \begin{pmatrix} a_{11} & a_{12} \\ a_{21} & a_{22} \end{pmatrix} \begin{pmatrix} x_1^{(i)} \\ x_2^{(i)} \end{pmatrix} = \lambda^{(i)} \begin{pmatrix} x_1^{(i)} \\ x_2^{(i)} \end{pmatrix} = \lambda^{(i)} \underline{x}^{(i)} \qquad \text{(A-44-i)}$$

Rather obvious manipulation of equations (A-45-i) gives

$$a_{11}x_1^{(i)} + a_{12}x_2^{(i)} = \lambda^{(i)}x_1^{(i)} \qquad ; \qquad \left(a_{11} - \lambda^{(i)}\right)x_1^{(i)} + a_{12}x_2^{(i)} = 0$$

$$a_{21}x_1^{(i)} + a_{22}x_2^{(i)} = \lambda^{(i)}x_2^{(i)} \qquad ; \qquad a_{21}x_1^{(i)} + \left(a_{22} - \lambda^{(i)}\right)x_2^{(i)} = 0$$

For this set of algebraic equations to have a nontrivial solution, we set the following condition on $\lambda^{(i)}$:

$$\begin{vmatrix} a_{11} - \lambda^{i} & a_{12} \\ a_{21} & a_{22} - \lambda^{i} \end{vmatrix} =$$

$$a_{11} - \lambda^{i} \quad a_{22} - \lambda^{i} \quad - a_{12}a_{21} = a_{11}a_{22} - a_{12}a_{21} - \ a_{11} + a_{22} \ \lambda^{i} + \ \lambda^{i} \ ^{2} = 0$$

The solution of the canonical equation is

$$\lambda^{1} = \frac{1}{2}\left[\ a_{11} + a_{22} \ - \sqrt{\ a_{11} - a_{22} \ ^{2} + 4a_{12}a_{21}} \right]$$

$$\lambda^{2} = \frac{1}{2}\left[\ a_{11} + a_{22} \ + \sqrt{\ a_{11} - a_{22} \ ^{2} + 4a_{12}a_{21}} \right]$$

Equations (A-45-f) can be solved for $x_1^{(1)}$ and $x_1^{(2)}$, if we arbitrarily (although lawfully) choose $x_2^{(1)} = x_2^{(2)} = 1$:

$$x_1^{(1)} = -\frac{a_{12}}{\left(a_{11} - \lambda^{(1)}\right)} = \frac{\left[\left(a_{11} - a_{22}\right) - \sqrt{\left(a_{11} - a_{22}\right)^2 + 4a_{12}a_{21}}\right]}{2a_{21}}$$

$$x_1^{(2)} = -\frac{\left(a_{22}-\lambda^{(2)}\right)}{a_{21}} = \frac{\left[\left(a_{11}-a_{22}\right)+\sqrt{\left(a_{11}-a_{22}\right)^2+4a_{12}a_{21}}\right]}{2a_{21}}$$

Therefore, the eigenvectors of $\underline{\underline{A}}$ are

$$\underline{x}^{(1)} = \begin{pmatrix} x_1^{(1)} \\ 1 \end{pmatrix} = \begin{pmatrix} \frac{1}{2a_{21}}\left[\left(a_{11}-a_{22}\right)-\sqrt{\left(a_{11}-a_{22}\right)^2+4a_{12}a_{21}}\right] \\ 1 \end{pmatrix}$$

$$\underline{x}^{(2)} = \begin{pmatrix} x_1^{(2)} \\ 1 \end{pmatrix} = \begin{pmatrix} \frac{1}{2a_{21}}\left[\left(a_{11}-a_{22}\right)+\sqrt{\left(a_{11}-a_{22}\right)^2+4a_{12}a_{21}}\right] \\ 1 \end{pmatrix}$$

Let us define the matrix $\underline{\underline{B}}$, whose columns are the eigenvectors of $\underline{\underline{A}}$; i.e.

$$\underline{\underline{B}} = \left(\underline{x}^{(2)} \quad ; \quad \underline{x}^{(2)}\right) = \begin{pmatrix} x_1^{(1)} & x_1^{(2)} \\ 1 & 1 \end{pmatrix}; \underline{\underline{B}}^{-1} = \frac{1}{\left(x_1^{(1)}-x_1^{(2)}\right)}\begin{pmatrix} 1 & -x_1^{(2)} \\ -1 & x_1^{(1)} \end{pmatrix}$$

and form the product

$$\underline{\underline{A}}\,\underline{\underline{B}} = \begin{pmatrix} a_{11} & a_{12} \\ a_{21} & a_{22} \end{pmatrix}\begin{pmatrix} x_1^{(1)} & x_1^{(2)} \\ 1 & 1 \end{pmatrix} = \begin{pmatrix} a_{11}x_1^{(1)}+a_{12} & a_{11}x_1^{(2)}+a_{12} \\ a_{21}x_1^{(1)}+a_{22} & a_{21}x_1^{(2)}+a_{22} \end{pmatrix}$$

where

$$a_{11}x_1^{(1)}+a_{12} = \lambda^{(1)}x_1^{(1)} \qquad ; \qquad a_{21}x_1^{(1)}+a_{22} = \lambda^{(1)} \qquad \text{(A-44-j)}$$

$$a_{11}x_1^{(2)}+a_{12} = \lambda^{(2)}x_1^{(2)} \qquad ; \qquad a_{21}x_1^{(2)}+a_{22} = \lambda^{(2)} \qquad \text{(A-44-k)}$$

From Equations (A-45-g) and (A-45-h), we can easily conclude

$$\underline{\underline{A}}\,\underline{\underline{B}} = \begin{pmatrix} a_{11}x_1^{(1)}+a_{12} & a_{11}x_1^{(2)}+a_{12} \\ a_{21}x_1^{(1)}+a_{22} & a_{21}x_1^{(2)}+a_{22} \end{pmatrix} = \begin{pmatrix} \lambda^{(1)}x_1^{(1)} & \lambda^{(2)}x_1^{(2)} \\ \lambda^{(1)} & \lambda^{(2)} \end{pmatrix} =$$

$$\begin{pmatrix} x_1^{(1)} & x_1^{(2)} \\ 1 & 1 \end{pmatrix}\begin{pmatrix} \lambda^{(1)} & 0 \\ 0 & \lambda^{(2)} \end{pmatrix} = \underline{\underline{B}}\,\underline{\underline{\Lambda}}$$

or simply

$$\underline{\underline{A}}\,\underline{\underline{B}} = \underline{\underline{B}}\,\underline{\underline{\Lambda}} \qquad ; \qquad \underline{\underline{\Lambda}} = \begin{pmatrix} \lambda^{(1)} & 0 \\ 0 & \lambda^{(2)} \end{pmatrix}$$

At this point, it is helpful to recognise the product

$$\underline{\underline{B}}^{-1}\,\underline{\underline{A}}\,\underline{\underline{B}} = \left(\underline{\underline{B}}^{-1}\,\underline{\underline{B}}\right)\underline{\underline{\Lambda}} = \underline{\underline{\Lambda}} \tag{A-44-l}$$

The set of ODE's in matrix notation

$$\frac{d\,\underline{y}}{dt} = \underline{\underline{A}}\,\underline{y} \tag{A-44-m}$$

may also be written as follows

$$\frac{d\,\underline{y}}{dt} = \underline{\underline{A}}\,\underline{\underline{I}}\,\underline{y} = \underline{\underline{A}}\,\underline{\underline{B}}\,\underline{\underline{B}}^{-1}\,\underline{y} \tag{A-44-n}$$

By matrix multiplication of Equation (A-45-k) by $\underline{\underline{B}}^{-1}$ from the left, we get

$$\frac{d}{dt}\left(\underline{\underline{B}}^{-1}\,\underline{y}\right) = \left(\underline{\underline{B}}^{-1}\,\underline{\underline{A}}\,\underline{\underline{B}}\right)\left(\underline{\underline{B}}^{-1}\,\underline{y}\right) \tag{A-44-o}$$

From Equations (A-45-i) and (A-45-l),

$$\frac{d}{dt}\left(\underline{\underline{B}}^{-1}\,\underline{y}\right) = \underline{\underline{\Lambda}}\left(\underline{\underline{B}}^{-1}\,\underline{y}\right) \tag{A-44-p}$$

In Equation (A-45-m),

$$\left(\underline{\underline{B}}^{-1}\,\underline{y}\right) = \frac{1}{\left(x_1^{(1)} - x_1^{(2)}\right)} \begin{pmatrix} 1 & -x_1^{(2)} \\ -1 & x_1^{(1)} \end{pmatrix} \begin{pmatrix} \varepsilon^*_{H^+} \\ \varepsilon^*_{P_{CO_2}} \end{pmatrix} = \frac{1}{\left(x_1^{(1)} - x_1^{(2)}\right)} \begin{pmatrix} \varepsilon^*_{H^+} - x_1^{(2)}\varepsilon^*_{P_{CO_2}} \\ -\varepsilon^*_{H^+} + x_1^{(1)}\varepsilon^*_{P_{CO_2}} \end{pmatrix} \tag{A-44-q}$$

$$\underline{\underline{\Lambda}} = \begin{pmatrix} \lambda^{(1)} & 0 \\ 0 & \lambda^{(2)} \end{pmatrix} \tag{A-44-r}$$

It is apparent that Equation (A-44-i) is equivalent to the following set of uncoupled differential equations

$$\frac{d}{dt}\left(\varepsilon^*_{H^+} - x_1^{(2)}\varepsilon^*_{P_{CO_2}}\right) = \lambda^{(1)}\left(\varepsilon^*_{H^+} - x_1^{(2)}\varepsilon^*_{P_{CO_2}}\right)$$

$$\frac{d}{dt}\left(\varepsilon^*_{H^+} - x_1^{(1)}\varepsilon^*_{P_{CO_2}}\right) = \lambda^{(2)}\left(\varepsilon^*_{H^+} - x_1^{(1)}\varepsilon^*_{P_{CO_2}}\right)$$

$$\left(\varepsilon^*_{H^+} - x_1^{(2)}\varepsilon^*_{P_{CO_2}}\right) = \left(\varepsilon^*_{H^+} - x_1^{(2)}\varepsilon^*_{P_{CO_2}}\right)_{t\to 0} e^{\lambda^{(1)}(t-t_0)}$$

$$\left(\varepsilon^*_{H^+} - x_1^{(1)}\varepsilon^*_{P_{CO_2}}\right) = \left(\varepsilon^*_{H^+} - x_1^{(1)}\varepsilon^*_{P_{CO_2}}\right)_{t\to 0} e^{\lambda^{(2)}(t-t_0)}$$

$$\left(x_1^{(1)} - x_1^{(2)}\right)\varepsilon^*_{P_{CO_2}} = \left(\varepsilon^*_{H^+} - x_1^{(2)}\varepsilon^*_{P_{CO_2}}\right)_{t\to 0} e^{\lambda^{(1)}(t-t_0)} - \left(\varepsilon^*_{H^+} - x_1^{(1)}\varepsilon^*_{P_{CO_2}}\right)_{t\to 0} e^{\lambda^{(2)}(t-t_0)}$$

$$\left(x_1^{(1)} - x_1^{(2)}\right)\varepsilon^*_{H^+} = \left(x_1^{(1)}\varepsilon^*_{H^+} - x_1^{(1)}x_1^{(2)}\varepsilon^*_{P_{CO_2}}\right)_{t\to 0} e^{\lambda^{(1)}(t-t_0)} - \left(x_1^{(2)}\varepsilon^*_{H^+} - x_1^{(1)}x_1^{(2)}\varepsilon^*_{P_{CO_2}}\right)_{t\to 0} e^{\lambda^{(2)}(t-t_0)}$$

$$\left(x_1^{(1)} - x_1^{(2)}\right)\varepsilon^*_{P_{CO_2}} = \left(\varepsilon^*_{H^+}\right)_{t\to 0} e^{\lambda^{(1)}(t-t_0)} - x_1^{(2)}\left(\varepsilon^*_{P_{CO_2}}\right)_{t\to 0} e^{\lambda^{(1)}(t-t_0)} - \left(\varepsilon^*_{H^+}\right)_{t\to 0} e^{\lambda^{(2)}(t-t_0)} + x_1^{(1)}\left(\varepsilon^*_{P_{CO_2}}\right)_{t\to 0} e^{\lambda^{(2)}(t-t_0)}$$

$$\left(x_1^{(1)} - x_1^{(2)}\right)\varepsilon^*_{H^+} =$$
$$x_1^{(1)}\left(\varepsilon^*_{H^+}\right)_{t\to 0} e^{\lambda^{(1)}(t-t_0)} - x_1^{(1)}x_1^{(2)}\left(\varepsilon^*_{P_{CO_2}}\right)_{t\to 0} e^{\lambda^{(1)}(t-t_0)} - x_1^{(2)}\left(\varepsilon^*_{H^+}\right)_{t\to 0} e^{\lambda^{(2)}(t-t_0)} + x_1^{(1)}x_1^{(2)}\left(\varepsilon^*_{P_{CO_2}}\right)_{t\to 0} e^{\lambda^{(2)}(t-t_0)}$$

Thus, in the process of dissipation of the perturbation to the initial equilibrium state, $\varepsilon^*_{P_{CO_2}}$ and $\varepsilon^*_{H^+}$ tend to zero with t as the system approaches a new equilibrium, according to,

$$\varepsilon^*_{P_{CO_2}(t)} = \frac{\left(\varepsilon^*_{H^+}\right)_{t\to 0}}{\left(x_1^{(1)} - x_1^{(2)}\right)}\left[e^{\lambda^{(1)}(t-t_0)} - e^{\lambda^{(2)}(t-t_0)}\right] + \frac{\left(\varepsilon^*_{P_{CO_2}}\right)_{t\to 0}}{\left(x_1^{(1)} - x_1^{(2)}\right)}\left[x_1^{(1)}e^{\lambda^{(2)}(t-t_0)} - x_1^{(2)}e^{\lambda^{(1)}(t-t_0)}\right] \qquad \text{(A-45-a)}$$

and

$$\varepsilon^*_{H^+(t)} = \frac{\left(\varepsilon^*_{H^+}\right)_{t\to 0}}{\left(x_1^{(1)} - x_1^{(2)}\right)}\left[x_1^{(1)}e^{\lambda^{(1)}(t-t_0)} - x_1^{(2)}e^{\lambda^{(2)}(t-t_0)}\right] - \frac{x_1^{(1)}x_1^{(2)}\left(\varepsilon^*_{P_{CO_2}}\right)_{t\to 0}}{\left(x_1^{(1)} - x_1^{(2)}\right)}\left[e^{\lambda^{(1)}(t-t_0)} - e^{\lambda^{(2)}(t-t_0)}\right] \qquad \text{(A-45-b)}$$

respectively. The terms $\left(\varepsilon^*_{H^+}\right)_{t\to 0}$ and $\left(\varepsilon^*_{P_{CO_2}}\right)_{t\to 0}$ are unknown values that represents the magnitude of each ε_i at the beginning of the perturbed condition. t_0 is a factor included in the analysis aiming to explore if could be a time delay effect in the process of dissipation of the perturbation. $x_1^{(1)}, x_1^{(2)}, \lambda^{(1)}, \lambda^{(2)}$ are constants whose expressions can be seen in equations (A-46-a,h), that retain the same values as the initial set of coupled equations (A-44-a,b).

$$\lambda^{1} = \frac{1}{2}\left[\ a_{11} + a_{22}\ - \sqrt{\ a_{11} - a_{22}\ {}^{2} + 4a_{12}a_{21}}\right] < 0 \tag{A-46-a}$$

$$\lambda^{2} = \frac{1}{2}\left[\ a_{11} + a_{22}\ + \sqrt{\ a_{11} - a_{22}\ {}^{2} + 4a_{12}a_{21}}\right] \tag{A-46-b}$$

$$x_{1}^{(1)} = \frac{\left[\left(a_{11} - a_{22}\right) - \sqrt{\left(a_{11} - a_{22}\right)^{2} + 4a_{12}a_{21}}\right]}{2a_{21}} \tag{A-46-c}$$

$$x_{1}^{(2)} = \frac{\left[\left(a_{11} - a_{22}\right) + \sqrt{\left(a_{11} - a_{22}\right)^{2} + 4a_{12}a_{21}}\right]}{2a_{21}} \tag{A-46-d}$$

$$a_{11} = -\frac{P_{CO_2}^{f}}{m_{H^+}^{eq}\left[\dfrac{1}{a_{\text{int}}k_{1}} + \dfrac{1}{k_{2}K_{1}}\right]}\kappa_{H^+} < 0 \tag{A-46-e}$$

$$a_{12} = \frac{P_{CO_2}^{f}}{m_{H^+}^{eq}\left[\dfrac{1}{a_{\text{int}}k_{1}} + \dfrac{1}{k_{2}K_{1}}\right]} > 0 \tag{A-46-f}$$

$$a_{21} = RT\left(\frac{V^{2}}{V^{1}}\right)\frac{\kappa_{H^+}}{\left[\dfrac{1}{a_{\text{int}}k_{1}} + \dfrac{1}{k_{2}K_{1}}\right]} > 0 \tag{A-46-g}$$

$$a_{22} = -\left[RT\left(\frac{V^{2}}{V^{1}}\right)\frac{1}{\left[\dfrac{1}{a_{\text{int}}k_{1}} + \dfrac{1}{k_{2}K_{1}}\right]} + \left(\frac{Q}{V^{1}}\right)\right] < 0 \tag{A-46-h}$$

8.1.4 – Special case: the absorption of CO_2 on $H_2O / H_2PO_4^- / HPO_4^{2-}$ mixtures in a closed gas-liquid contactor. The time evolution of $\varepsilon^*_{H^+}$ and $\varepsilon^*_{P_{CO_2}}$ in the Linear Irreversible Regime.

In section 8.1.3, the equation (A-35) has been presented, for modelling the variations in time of $\varepsilon^*_{H^+}$:

$$\frac{d\varepsilon^*_{H^+}}{dt} = -\frac{P^{(eq)}_{CO_2}}{m^{(eq)}_{H^+}\left[\dfrac{1}{a_{int}k_1} + \dfrac{1}{k_2 K_1}\right]}\left[\kappa_{H^+}\,\varepsilon^*_{H^+} - \varepsilon^*_{P_{CO_2}}\right]$$

In order to set up an equation for the time dependence of $\varepsilon^*_{P_{CO_2}}$ **for an overall closed system,** we start by recalling Equation (A-36):

$$\frac{1}{V^{(2)}}\left(\frac{dn^{(2)}_{CO_2}}{dt}\right)_{exch} = \frac{A_{int}}{V^{(2)}}\,j^{(1\to2)}_{CO_2} = a_{int}\,j^{(1\to2)}_{CO_2} \qquad \text{(A-47-a)}$$

together with the conditions

$$\left(\frac{dn^{(1)}_{CO_2}}{dt}\right)_{exch} = -\left(\frac{dn^{(2)}_{CO_2}}{dt}\right)_{exch} \;;\; \left(\frac{dn^{(1)}_{i}}{dt}\right)_{react} = 0 \qquad \text{(A-47-b)}$$

Substitution in Equation (A-47-a), gives

$$\frac{1}{V^{(2)}}\frac{dn^{(1)}_{CO_2}}{dt} = -\frac{A_{int}}{V^{(2)}}\,j^{(1\to2)}_{CO_2} = -a_{int}\,j^{(1\to2)}_{CO_2} \qquad \text{(A-47-c)}$$

If the gas phase is assumed ideal

$$P_{CO_2} = RT\,\frac{n^{(1)}_{CO_2}}{V^{(1)}} \qquad \text{(A-47-d)}$$

A Taylor series expansion of P_{CO_2} around the equilibrium value $P^{(eq)}_{CO_2}$, keeping up to first order terms, gives the following linear expression

$$P_{CO_2}\left(n^{(1)}_{CO_2},V^{(1)};T\right)\approx P^{(eq)}_{CO_2}+\left(\frac{RT}{V^{(1)}}\right)_{eq}\left(n^{(1)}_{CO_2}-\left(n^{(1)}_{CO_2}\right)_{eq}\right)-\left(\frac{n^{(1)}_{CO_2}RT}{\left(V^{(1)}\right)^2}\right)_{eq}\left(V^{(1)}-V^{(1)}_{eq}\right)=$$

$$P^{(eq)}_{CO_2}\left[1+\left(\frac{n^{(1)}_{CO_2}-\left(n^{(1)}_{CO_2}\right)_{eq}}{\left(n^{(1)}_{CO_2}\right)_{eq}}\right)-\left(\frac{V^{(1)}-V^{(1)}_{eq}}{V^{(1)}_{eq}}\right)\right] \tag{A-47-e}$$

In Equation (143), $V^{(1)}$ is the volume of the gas phase dispersed in the liquid phase (the “resident” gas volume or “gas hold-up”), and $V^{(1)}_{eq}$ is the value of that volume at the CO_2 transfer equilibrium. In most cases of our interest, the partial pressure of CO_2 in the gas phase is very small compared with that of the inert, less soluble gases. Whenever this simplifying assumption holds, we can make the following approximation:

$$\left(\frac{V^{(1)}-V^{(1)}_{eq}}{V^{(1)}_{eq}}\right)\approx 0 \tag{A-47-f}$$

and Equation (A-47-f) simplifies into the following

$$\varepsilon^{*}_{P_{CO_2}}\approx\left(\frac{\left(n^{(1)}_{CO_2}\right)_{eq}-n^{(1)}_{CO_2}}{\left(n^{(1)}_{CO_2}\right)_{eq}}\right) \tag{A-47-g}$$

Differentiation of Equation (A-47-g) with respect to time, gives

$$\frac{dn^{(1)}_{CO_2}}{dt}\approx-\left(n^{(1)}_{CO_2}\right)_{eq}\frac{d}{dt}\varepsilon^{*}_{P_{CO_2}} \tag{A-47-h}$$

Substitution in Equation (A-47-c), gives

$$\frac{1}{V^{(2)}}\left(n^{(1)}_{CO_2}\right)_{eq}\frac{d\varepsilon^{*}_{P_{CO_2}}}{dt}=\frac{A_{int}}{V^{(2)}}\,j^{(1\to2)}_{CO_2}=\underbrace{a_{int}\,j^{(1\to2)}_{CO_2}}_{r_1}=\underbrace{a_{int}k_1P^{(eq)}_{CO_2}\left[\varepsilon^{*}_{m_{CO_2}}-\varepsilon^{*}_{P_{CO_2}}\right]}_{r_1}=$$

$$\frac{P^{(eq)}_{CO_2}}{\left[\dfrac{1}{a_{int}k_1}+\dfrac{1}{k_2K_1}\right]}\left[\varepsilon^{*}_{HCO_3^-}+\varepsilon^{*}_{H^+}-\varepsilon^{*}_{P_{CO_2}}\right] \tag{A-47-i}$$

or, after obvious simplifications

$$\frac{d\varepsilon^*_{P_{CO_2}}}{dt} = \frac{RT}{\left[\frac{1}{a_{int}k_1} + \frac{1}{k_2K_1}\right]}\left(\frac{V^{(2)}}{V^{(1)}}\right)\left[\varepsilon^*_{HCO_3^-} + \varepsilon^*_{H^+} - \varepsilon^*_{P_{CO_2}}\right] \tag{A-47-j}$$

In Equation (A-47-j)

$$\left[\varepsilon^*_{HCO_3^-} + \varepsilon^*_{H^+} - \varepsilon^*_{P_{CO_2}}\right] = \kappa_{H^+}\,\varepsilon^*_{H^+} - \varepsilon^*_{P_{CO_2}} \tag{A-47-k}$$

Therefore, we have:

$$\frac{d\varepsilon^*_{P_{CO_2}}}{dt} = RT\left(\frac{V^{(2)}}{V^{(1)}}\right)\frac{1}{\left[\frac{1}{a_{int}k_1} + \frac{1}{k_2K_1}\right]} \times \left[\kappa_{H^+}\varepsilon^*_{H^+} - \varepsilon^*_{P_{CO_2}}\right] \tag{A-47-l}$$

From equations (A-35) and (A-47-l), we conclude that for the **closed system** to approach spontaneously the final equilibrium state, the following condition must be satisfied in the Linear Irreversible Regime:

$$\frac{d\varepsilon^*_{P_{CO_2}}}{d\varepsilon^*_{H^+}} = -RT\left(\frac{V^{(2)}}{V^{(1)}}\right)\frac{m^{(eq)}_{H^+}}{P^{(eq)}_{CO_2}} < 0 \tag{A-47-m}$$

The integral analogue to Equation (A-47-m), is

$$\varepsilon^*_{P_{CO_2}} = -RT\left(\frac{V^{(2)}}{V^{(1)}}\right)\frac{m^{(eq)}_{H^+}}{P^{(eq)}_{CO_2}}\varepsilon^*_{H^+} + C \tag{A-47-n}$$

At the final, overall equilibrium state, $\varepsilon^*_{P_{CO_2}} = 0$ and $\varepsilon^*_{H^+} = 0$. Therefore, in Equation (A-47-n), $C = 0$:

$$\varepsilon^*_{P_{CO_2}} = -RT\left(\frac{V^{(2)}}{V^{(1)}}\right)\frac{m^{(eq)}_{H^+}}{P^{(eq)}_{CO_2}}\varepsilon^*_{H^+} = -\kappa_{P_{CO_2}}\varepsilon^*_{H^+} \quad ; \quad \kappa_{P_{CO_2}} = RT\left(\frac{V^{(2)}}{V^{(1)}}\right)\frac{m^{(eq)}_{H^+}}{P^{(eq)}_{CO_2}} > 0 \tag{A-47-o}$$

Substitution in Equation (138), gives

$$\frac{d\varepsilon^*_{H^+}}{dt} = -\frac{P^{(eq)}_{CO_2}}{m^{(eq)}_{H^+}\left[\frac{1}{a_{int}k_1} + \frac{1}{k_2K_1}\right]}\left[\kappa_{H^+} + \kappa_{P_{CO_2}}\right]\varepsilon^*_{H^+}\,;\;\; \kappa_{H^+} > 0 \;\;; \kappa_{P_{CO_2}} > 0 \tag{A-47-p}$$

By integration of Equation (A-47-p), we get

$$\varepsilon^{*}_{H^{+}} = \varepsilon^{0}_{H^{+}} \, exp\left[-\frac{P^{(eq)}_{CO_2}\left(\kappa_{H^{+}} + \kappa_{P_{CO_2}}\right)}{m^{(eq)}_{H^{+}}\left(\frac{1}{a_{int}k_1} + \frac{1}{k_2 K_1}\right)}\left(t - t_0\right) \right] \qquad \text{(A-47-q)}$$

Chapter (2)

Characterisation of an artificial source of radiative energy: Commercial grow-LED tubes

(1). - Summary

Knowledge of the characteristics of the radiation source chosen for a microalgae cultivation system and of its radiant energy becomes a crucial aspect in the design, characterisation and optimisation stages of a photobioreactor (PBR) in terms of light. The most important characteristics of a source are: i] the number of photons per unit of time that emerge from its surface (photon flux), ii] the directions these photons take (photon directional distribution function), and iii] the composition of the photon population in terms of wavelength λ (photon spectral distribution function).

Throughout the chapter, these properties are found for the LEDs used in this thesis. To begin with, a model for the radiation exchange between surfaces is adopted and described, and the proper expressions for the calculation of the mentioned properties are derived. In addition, the experimental and computational simulation methodology implemented in the calculation is detailed.

From the results, it can be concluded that LEDs have an isotropic emission type and that the spectral composition of the lamp is known thoroughly for the construction of the necessary directional and spectral distribution functions, which are unique features of each lamp, and these will be employed in the following chapters of the thesis.

(2). - Introduction

The composition of microalgae biomass can be altered due to changes in the environmental conditions of cultivation, growth rate, life cycle stages, etc. The quality and quantity of supplied light, natural or artificial, are essential parameters for the growth of phototrophic organisms, as they are involved in photosynthesis and morphological changes [104].

Although sunlight is the most cost-effective source of radiant energy for growing microalgae, artificial light is an economically viable alternative when the biomass is used as raw material for the generation of high-added-value products, such as functional foods, dietary supplements (e.g. carotenoids and polyunsaturated fatty acids), nutraceuticals, among others [105]. Artificial light makes it possible to avoid fluctuations in sunlight (due to geography, climate, time of day, day of the year, presence of objects, and so on), control the amount of light supplied per unit of time, hours of illumination and spectrum, which in some cases could lead to gains in productivity and biomass quality.

The most common artificial light sources include fluorescent lamps, incandescent lamps, halogen lamps and LEDs. Today, microalgae biotechnology has migrated to the use of LEDs due to their long lifetime (50.000-100.000 [hs], vs 12.000-20.000 [hs] of fluorescent lamps, and 1.000 [hs] of incandescent lamps), stable emission, small size in relation to the radiant energy supplied, a wide range of commercially available lamp packages (in relation to integrated power and diode arrangements), simple installation, adaptability to various substrates, wide or narrow bandwidth spectra (20-40 [nm]), an adjustable quantity of emitted light, high photoelectric conversion efficiency, fast emission response (nanosecond scale) allowing intermittent operation (flashes), ability to operate immersed in liquid media, a multi-colour option with independent selection (RGB), high mechanical resistance due to the absence of filaments, reduced environmental pollution and fully ecological models, the ability for the emitted light to be transferable by fibre optics, among others [106], [107].

LED technology is still under development, with companies now offering the possibility of customised design of the LED emission spectrum through the choice of housing components and the proportion of each component. One potentially disruptive example in the area of algal biotechnology has been the creation of high-power LEDs that simulate the spectrum of sunlight reaching the earth's surface, something impossible to achieve with conventional LEDs due to the shape of their spectra [108]. Although this type of device currently has a high economic cost, its use in the scientific-technological field could reduce the gap between productivity predictions made with information generated at the laboratory scale and those observed in outdoor cultivation systems.

During the objectives carried out throughout this thesis, the characterisation of a lighting module consisting of eight commercial LED tubes with a particular spectral composition was compulsory. The module forms part of a production unit belonging to MINT Engineering GmbH (Dresden, Germany). In view that all the LED tubes that compose the custom-made lighting arrangement are the same, the following sections present details and the assessment of the essential properties (directional and spectral mathematical functions) calculated for one of these lamps.

(3). – Objectives

- To include a model for radiation exchange and derive the properties of the radiant energy emitted by LED tubes chosen by MINT Engineering GmbH.
- To design experiments and develop ad hoc computational algorithms to find the properties of interest.

(4). - Materials and methods

(4.1). - LED tubes

The LED tubes purchased by MINT Engineering GmbH and used in this study correspond to the VALOYA brand (Valoya oy, Helsinki, Finland). They belong specifically to the L-18 model for vegetative solid and generative growth [109]. These lamps consist of 1200-mm-length white-plastic T8 tubes of 26-mm diameter, containing 100 LED units each (fig. (1)). The latter is supposed to produce minimal heat while preserving maximal uniformity on the light produced. Each lighting set-up has been connected directly to the main power supply (220 V) without control of the photon flux they emit.

(4.2). - Measurement of the Valoya-L18 lighting-system emitted radiation

A DK-PHAR 2.010BS PAR-quantum sensor (deka Sensor + Technologie Entwicklungs- und Vertriebsgesellschaft GmbH, Teltow, Germany) was used to record the radiation emitted by the LED arrays [110]. The device gives the reading of the number of photons reaching the radiometer's detection surface per unit time [µmol m-2 s-1] but not the spectral distribution of the photon population (λ).

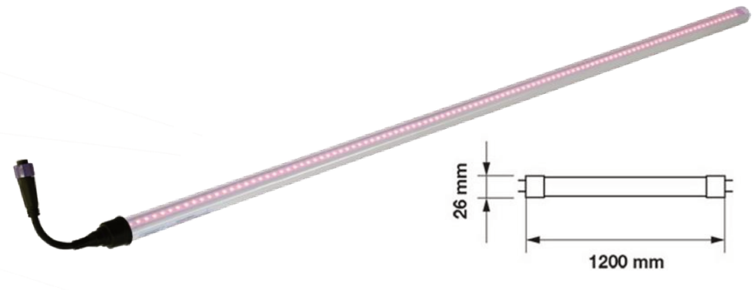

Figure (1). An image o the L18 model of Valoya, fully operational, with a scheme of its dimensions.

(4.3). - Directional emission distribution function

In order to find the directional distribution function of the photons emitted by the LEDs, it is necessary to have radiation measurements corresponding to different points on the surface of a semi-sphere, which contains the LEDs at its centre. In other words, radiation measurements are required for different angles θ and φ (spherical coordinates) for the LED mounted on the tubes. For this purpose, an ad hoc designed and built device was used, which consists of a metal housing with a black interior (to avoid reflection, refraction, and environmental radiation phenomena), provided with a circular glass fixing site at the base that allows the centring of the LED plates, Fig. (2C). A rotation axis located in the base allows the angular movement of the device (rotation around the z-axis in the xy plane), with a non-adjustable variation of 5°, resulting in values of φ contained in the range [0°-90°]. To achieve the angular variation in θ, the detector is moved on the sphere reaching different heights with respect to the base, starting from a fixed height of 10 [cm] determined by the construction.

Readings were recorded with the radiometer sweeping θ (from $\theta=0°$ to $\theta= 90°$ with $\Delta\theta= 5°$) and φ (from $\varphi=0°$ to $\varphi=90°$ with $\Delta \varphi=10°$) for a single LED board since all the diodes belong to the same model (SMD).

(4.4). - Spectral distribution of emission

A portable Ocean Insight Red Tide 650 (Ocean Insight, Ostfildern, Germany) fibre-optic spectrophotometer was used, which contains a system of mirrors and diffraction gratings that make it capable of splitting the photon beam into its component photons (λ) and recording them individually using a CCD detector. CCD detectors, like photovoltaic cells, are based on the photoelectric effect and the spontaneous conversion of the received light into electric current. The response measured by the equipment gives the spectral distribution of the radiant energy density from light sources in [counts s^{-1} nm^{-1}].

The spectral distribution of emission is independent of the value of the photon flux at which the LEDs operate. This is why the experiments were carried out with a short section of the Valoya L18 lamps, positioning the spectrophotometer detector, of the fibre optic type, at a distance that avoids equipment saturation [111]. Another way of calibrating the measurements is selecting a suitable integration time for the experiments. In the present case, the lowest value possible in every essay (3 ms) was selected.

(4.5). - Photosynthetic photon flux (PPF)

PPF (photosynthetic photon flux) and PPFD (photosynthetic photon flux density) are both acronyms that deal with the amount of light for a light source or location. PPF and PPFD measure the quantity of photosynthetic active (PAR) photons. The critical difference is that PPFD measures the density of these photons falling on a particular surface, while PPF measures the total number of photons released from a light source in every direction. The worldwide accepted unit for PPF is [μmol s^{-1}] and in the case of PPFD is [μmol s^{-1} m^{-2}].

Taking into account the pieces above of information, in the present study, it was chosen to express the PPF of the lighting system employed by MINT Engineering in the units of [μmol s^{-1}], as the total flux of light is the best property of the radiant energy field that serves to characterise this system, as every one of the nineteen tubes composing the TPBR under the study has been treated independently. The experiments to measure the PPF of the LED tubes provided by MINT Engineering GmbH were performed in the following two ways. Firstly, the ad-hoc device described in Section (4.3) and schematized in Fig. (2B) was used. The LED plate was located at a distance of 10 [cm] from the radiometer, and the detector's centre coincided with the LED in the centre of the plate. In addition, another ad-hoc device was used, consisting of a black plastic cylinder with two holes at the ends. The first of these, which has a larger diameter and is located at the top, allows the radiometer to be inserted and fixed, while the other allows the central LED to be isolated from the plate, and thus only the radiation coming from it to be recorded. In this configuration, the centre of the detector coincided with the LED located in the centre of the plate, separated by a distance of 10 [cm]. Fig. (2A) schematizes the device used for these LEDs. Lastly, the plates were placed on a black cloth, and the measurements were carried out in a darkened room to avoid external radiation and optical phenomena of reflection and refraction in nearby materials.

In all cases, before taking the measurements, sufficient time was allowed for the emission to stabilise [112].

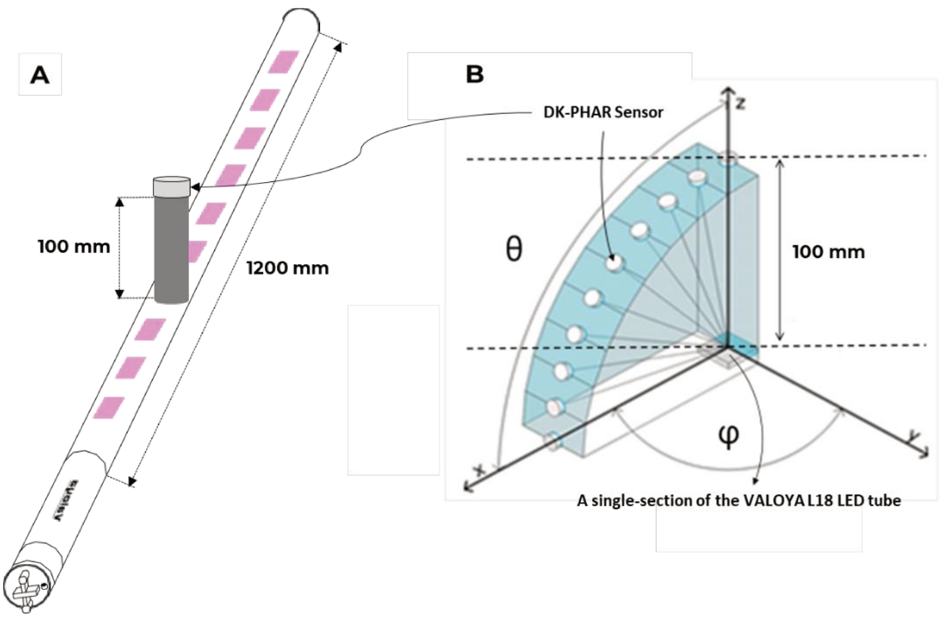

Figure (2). A] Schematic of the device built ad hoc for the calculation of the photon flux at fixed distances from the LED tube. B] Schematic of the alternative device used to determine the emission directional distribution function and LED tube's PPF. At the centre of the (x, y, z) coordinate system, (0, 0, 0), the central LED of the tube is positioned, and at the different angles θ and φ, the radiometer is positioned.

(4.6). - Computational algorithms

MATLAB 2022b, with a valid education licence, was used to calculate each LED model's intensity and photosynthetic photon flux. The calculation algorithm implemented is detailed in Section (5.4) of the Results and Discussion.

(5). - Results and discussion

(5.1). - The transfer of radiant energy

Radiative transfer is the physical phenomenon of energy transfer in the form of electromagnetic radiation. The power from a real or virtual surface element dA_1 incident on a real or virtual surface element dA_2, both in a medium transparent to radiation of wavelength λ (i.e., a medium "non-participating" in that λ), can be represented by the following expression [113]:

$$dN_{\lambda}^{(1,2)} = n_{\lambda}^{(1,2)}\left(\underline{r}_1, \underline{\hat{\Omega}}_{1,2}, t\right) d\lambda\, dt \frac{\left(\underline{\hat{n}}_1 \cdot \underline{\hat{\Omega}}_{1,2}\right) dA_1 \left(\underline{\hat{n}}_2 \cdot \underline{\hat{\Omega}}_{2,1}\right) dA_2}{r_{1,2}^2} \tag{1}$$

In Eq. (1), $dN_{\lambda}^{(1,2)}$ [μmol] is the infinitesimal number of photons with wavelength λ [nm] coming from the elementary surface dA_1 [m^2] incident on the elementary surface dA_2 [m^2] during time dt [s]; $n_\lambda^{(1,2)}(\underline{r}_1, \hat{\underline{\Omega}}_{1,2}, t)$ [µmol s^{-1} m^{-2} nm^{-1} sr^{-1}] is the intensity of monochromatic radiation with wavelength λ associated with the emerging photon beam from the elementary surface dA_1, propagating in the direction $\hat{\underline{\Omega}}_{1,2}$ at instant t; dA_1 is an elementary surface (real or virtual) located at a position $\underline{r}_1$; dA_2 is an elementary surface (real or virtual) located at a position $\underline{r}_2$; $\hat{\underline{n}}_1$ is a unit vector normal to the face exposed to the radiant exchange of dA_1 with dA_2; $\hat{\underline{n}}_2$ is a unit vector normal to the face exposed to the radiant exchange of dA_2 with dA_1; $\hat{\underline{\Omega}}_{1,2}$ is a unit vector joining the elementary surfaces in a photon exchange situation, oriented from surface dA_1 towards dA_2; $\hat{\underline{\Omega}}_{2,1}$ is a unit vector joining the surfaces, oriented from surface dA_2 towards dA_1; and dA_1; and $r_{1,2} = r_{2,1}$ [m] is the distance between surfaces dA_1 and dA_2. The photon exchange between two elementary surfaces is schematised in Fig. (3A).

In the right-hand member of Eq. (1), two sets of terms can be defined, one called the "energy factor" and the other the "geometric factor":

$$dN_\lambda^{(1,2)} = \underbrace{n_\lambda^{(1,2)}\left(\underline{r}_1, \hat{\underline{\Omega}}_{1,2}, t\right) d\lambda\, dt}_{''\,energy\ factor\,''} \quad \underbrace{\frac{\left(\hat{\underline{n}}_1 \cdot \hat{\underline{\Omega}}_{1,2}\right) dA_1 \left(\hat{\underline{n}}_2 \cdot \hat{\underline{\Omega}}_{2,1}\right) dA_2}{r_{1,2}^2}}_{''\,geometric\ factor\,''} \tag{1}$$

The "geometric factor" remains unchanged for a permutation of indices, but for the same operation, the "energetic" factor changes the meaning of the photon exchange.

A solid angle element around $\hat{\underline{\Omega}}_{1,2}$ may be defined as follows:

$$d\hat{\underline{\Omega}}_{1,2} = \frac{\left(\hat{\underline{n}}_2 \cdot \hat{\underline{\Omega}}_{2,1}\right) dA_2}{r_{1,2}^2} \tag{2}$$

In Eq. (2), the scalar product of unit vectors $(\hat{\underline{n}}_1 \cdot \hat{\underline{\Omega}}_{1,2})$ is equivalent to the cosine of the angle formed by these vectors, Fig. (3A). The term $(\hat{\underline{n}}_1 \cdot \hat{\underline{\Omega}}_{1,2}) dA_2$ corresponds to the projection of the surface dA_2, whose normal is $\hat{\underline{n}}_2$, on the plane perpendicular to the direction $\hat{\underline{\Omega}}_{2,1}$, where $\hat{\underline{\Omega}}_{2,1} = -\hat{\underline{\Omega}}_{1,2}$.

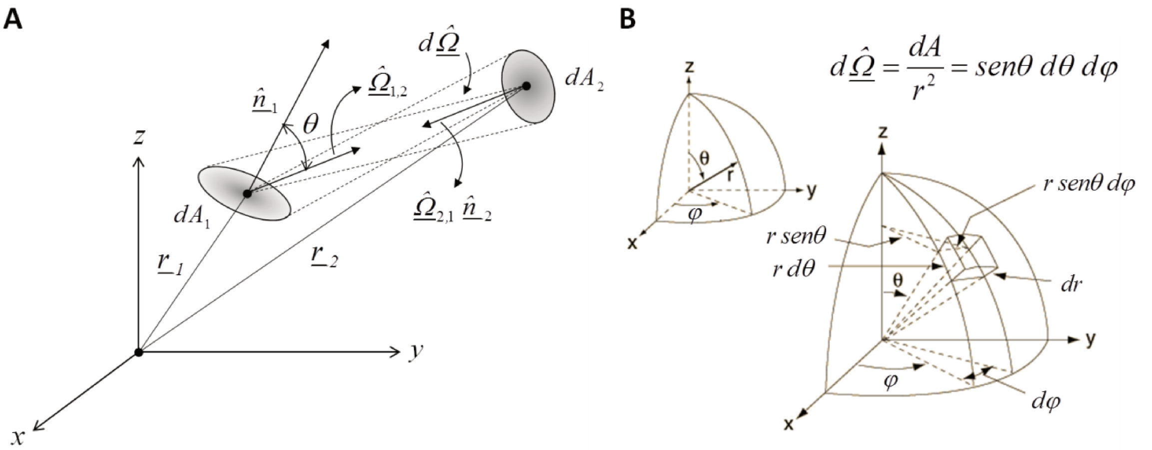

Figure (3). A] Schematic of the radiant energy exchange between two elementary surfaces dA_1 and dA_2. B] The definition of the solid angle differential $d\underline{\hat{\Omega}}$ in a spherical coordinate system.

Incorporating the definition of $d\underline{\hat{\Omega}}_{1,2}$ the radiant energy transfer equation in terms of the number of photons, Eq. (1), can be written as:

$$dN_\lambda^{(1,2)} = n_\lambda^{(1,2)}\left(\underline{r}_1, \underline{\hat{\Omega}}_{1,2}, t\right) cos\,\theta_1 \, d\underline{\hat{\Omega}}_{1,2} \, dA_1 \, d\lambda \, dt \tag{3}$$

The expression for the solid angle element, $d\underline{\hat{\Omega}}_{1,2}$, around the direction $\underline{\hat{\Omega}}_{1,2}$ in a spherical coordinate system, as a function of the angles θ and φ, turns out to be:

$$d\underline{\hat{\Omega}}_{1,2} = sen\;\theta_1 \, d\theta_1 \, d\varphi = -d(cos\,\theta_1)\, d\varphi = -d\,u_1 \, d\varphi \tag{4}$$

where is the cosine of the angle between the unit vectors $\underline{\hat{n}}_1$ and $\underline{\hat{\Omega}}_{1,2}$, $\cos\theta_1$.

Adopting the alternative definition for $d\underline{\hat{\Omega}}_{1,2}$, Eq. (3) can be written as:

$$dN_\lambda^{(1,2)} = n_\lambda^{(1,2)}\left(\underline{r}_1, \underline{\hat{\Omega}}_{1,2}, t\right) cos\,\theta_1 \, sen\;\theta_1 \, d\theta_1 \, d\varphi \, dA_1 \, d\lambda \, dt \tag{5}$$

$$dN_\lambda^{(1,2)} = -n_\lambda^{(1,2)}\left(\underline{r}_1, \underline{\hat{\Omega}}_{1,2}, t\right) u_1 \, du_1 \, d\phi_1 \, dA_1 \, d\lambda \, dt \tag{6}$$

The number of photons exchanged between surfaces dA_1 and dA_2, for a given surface dA_2, will be the same as long as their projection onto the plane transverse to the direction $\underline{\hat{\Omega}}_{1,2}$ is proportional to the square of the distance between the two elementary surfaces, $r_{1,2}^2$, Eq. (2). The most important consequence of defining a solid angle element $d\underline{\hat{\Omega}}$ around the direction $\underline{\hat{\Omega}}_{1,2}$, is that it renders the elementary surface dA_2 unnecessary.

On the elementary surface dA_1 located at position $\underline{r}_1$, the infinitesimal number of photons with wavelength λ propagating in the direction $\underline{\hat{\Omega}}$ during time dt is:

$$dq_{\lambda,\underline{\hat{\Omega}}}^{(1,2)} = \frac{dN_{\lambda}^{(1,2)}}{dt\ d\lambda\ dA_1} = n_{\lambda}^{(1,2)}\left(\underline{r}_1, \underline{\hat{\Omega}}_{1,2}, t\right)\left(\underline{\hat{n}}_1 \cdot \underline{\hat{\Omega}}_{1,2}\right) d\underline{\hat{\Omega}} \tag{7}$$

Considering all possible directions $\underline{\hat{\Omega}}$ it is possible to obtain the infinitesimal contribution to the spectral photon flux density, $dq_{VIS}^{(1,2)}$ [μmol s^{-1} m^{-2}], Eq. (8).

$$dq_{\lambda}^{(1,2)} = \int_{\underline{\hat{\Omega}}} dq_{\lambda,\underline{\hat{\Omega}}}^{(1,2)} d\underline{\hat{\Omega}} = \int_{\underline{\hat{\Omega}}} n_{\lambda}^{(1,2)}\left(\underline{r}_1, \underline{\hat{\Omega}}_{1,2}, t\right)\left(\underline{\hat{n}}_1 \cdot \underline{\hat{\Omega}}_{1,2}\right) d\underline{\hat{\Omega}} \tag{8}$$

The infinitesimal contribution to the photon flux density, considering only photons in the visible region of the electromagnetic spectrum, $dq_{VIS}^{(1,2)}$ [μmol s^{-1} m^{-2}], is obtained by integration of $dq_{\lambda}^{(1,2)}$ in the range 400 ≤ λ ≤700 [nm], Eq. (9).

$$dq_{VIS}^{(1,2)} = \int_{VIS} dq_{\lambda}^{(1,2)} d\lambda = \int_{VIS}\int_{\underline{\hat{\Omega}}} n_{\lambda}^{(1,2)}\left(\underline{r}_1, \underline{\hat{\Omega}}_{1,2}, t\right)\left(\underline{\hat{n}}_1 \cdot \underline{\hat{\Omega}}_{1,2}\right) d\underline{\hat{\Omega}}\, d\lambda \tag{9}$$

It is important to note that the intensity of the photon beam can depend on $\underline{\hat{\Omega}}$ y λ.

Consider the emission of radiant energy by an elementary surface dA_1. The intensity of the radiation emitted by the elementary surface can be rewritten as $n'^{(1,2)}_{\lambda}(\underline{r}_1, \underline{\hat{\Omega}}_{1,2}, t) = n_{\lambda}^{(1,2)}(\underline{r}_1, \underline{\hat{\Omega}}_{1,2}, t) dA_1$. Then, the infinitesimal contribution to the spectral photon flux, defined as the infinitesimal number of photons emitted by the elementary surface per unit of time and wavelength, dQ_{λ} [μmol s^{-1} nm^{-1}], contained in the set of directions $d\underline{\hat{\Omega}}$ around the direction $\underline{\hat{\Omega}}$, turns out to be:

$$dQ_{\lambda} = n_{\lambda}^{(1,2)}\left(\underline{r}_1, \underline{\hat{\Omega}}_{1,2}, t\right) dA \left(\underline{\hat{n}}_1 \cdot \underline{\hat{\Omega}}_{1,2}\right) d\underline{\hat{\Omega}} = n'^{(1,2)}_{\lambda}\left(\underline{r}_1, \underline{\hat{\Omega}}_{1,2}, t\right)\left(\underline{\hat{n}}_1 \cdot \underline{\hat{\Omega}}_{1,2}\right) d\underline{\hat{\Omega}} \tag{10}$$

It is possible to see that dQ_λ depends on the emission direction $\underline{\hat{\Omega}}$ through the scalar product ($\underline{\hat{n}} \cdot \underline{\hat{\Omega}}$). The infinitesimal flux turns out to be maximum when the vectors $\underline{\hat{\Omega}}$ and $\underline{\hat{n}}$ are oriented parallel and decrease as the angle formed between these vectors increases. When $\underline{\hat{\Omega}}$ and $\underline{\hat{n}}$ are perpendicular, the infinitesimal flux emitted by the elementary surface is zero.

The photon flux, considering all possible directions $\underline{\hat{\Omega}}$, and photons in the visible region of the electromagnetic spectrum, Q_{VIS} [μmol s^{-1}] is obtained from:

$$Q_{VIS} = \int_{VIS} \int_{\underline{\hat{\Omega}}} dQ_\lambda = \int_{VIS} \int_{\underline{\hat{\Omega}}} n_\lambda'^{\,(1,2)} \left(\underline{r}_1, \underline{\hat{\Omega}}_{1,2}, t\right) \left(\underline{\hat{n}}_1 \cdot \underline{\hat{\Omega}}_{1,2}\right) d\underline{\hat{\Omega}}\, d\lambda \tag{11}$$

The properties deduced from adopting a model for the exchange of radiant energy between surfaces will be helpful in understanding the results of the experiments carried out.

(5.2). - Directional emission distribution

Fig. (4A) shows the photon flux density values q_{VIS} recorded with the radiometer, corresponding to different angles θ and φ (see Fig. (2B)). In Fig. (4B), the experimental measurements of q_{VIS} are compared with the $\cos(\theta)$ function. As can be seen, q_{VIS} remains constant for all angles φ of each angle θ, which allows us to conclude that the emission at φ is independent of θ. However, as θ increases, a decrease in the value of q_{VIS} is evident. The way in which the decay occurs is proportional to $\cos(\theta)$. From this, and taking into account the expression for the flux of photons emitted by an elementary surface, Eq. (11), it is possible to conclude that the intensity of the LEDs is independent of the direction of emission $\underline{\hat{\Omega}}(\theta, \varphi)$. An emission with these characteristics is known as "isotropic emission".

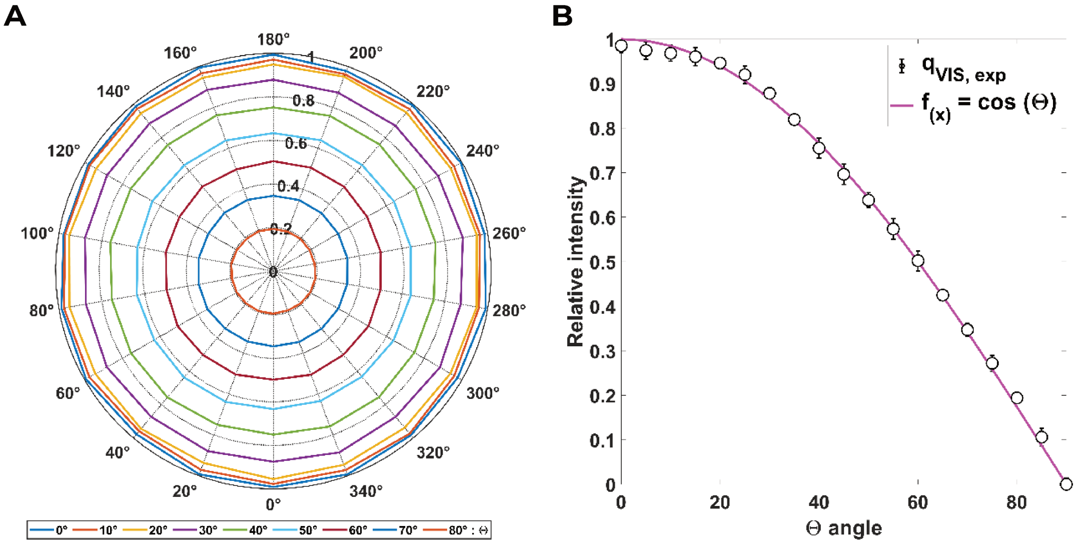

Figure (4). A] Each curve describes the value of q_{VIS} for an angle θ and its corresponding angles φ. θ (from 0° to 90° with 10° variation), φ (from 0° to 360°, every 20°). B] Measurements of q_{VIS} and $\cos(\theta)$ for different θ (from θ=0° to θ=90° with Δθ=5°). In both figures, the measurements were normalised to 1, with the highest value recorded for q_{VIS} (θ=0°).

From the information obtained from the experimental measurements of q_{VIS}, it is possible to define the directional distribution function of the photons emitted by the LEDs. On the one hand, φ can take values between $0 \leq \varphi \leq 2\pi$, being all of them equally probable and independent of θ; while θ can take values between $0 \leq \theta \leq \pi/2$, whose distribution is related to cos (θ). The distribution functions for θ and φ, E_θ and E_φ, are defined according to:

$$\int_0^{2\pi} E_\varphi d\varphi = E_\varphi \int_0^{2\pi} k d\varphi = 1 \tag{12}$$

$$E_\varphi = \frac{1}{2\pi} \tag{13}$$

$$\int_0^{\pi/2} E_\theta d\theta = \int_0^{\pi/2} k\cos(\theta) d\theta = k\int_0^{\pi/2} \cos(\theta) d\theta = 1 \tag{14}$$

In Eq. (14), k is a normalisation constant so that the area under E_θ, over the whole possible range of values of θ, is 1.

$$k\, sen(\theta)\Big|_0^{\pi/2} = 1 \quad ; \quad k = 1 \tag{15}$$

$$E_\theta = \cos(\theta) \tag{16}$$

The directional distribution function of LED emission, $E_{\theta,\varphi}$, where the distribution functions of θ and φ are independent, can be expressed as follows:

$$E_{\theta,\varphi} = E_{\varphi} E_{\theta} = \frac{1}{2\pi} cos(\theta) \tag{17}$$

(5.3). - Spectral distribution of emission

The absorption of radiant energy in photosystems depends on the wavelength λ of the radiation, so it is essential to know how the reactor's light "feeding" is composed. This characterisation may be performed by calculating a spectral distribution function of energy, $E_{\lambda,w}(\lambda)$ [nm^{-1}], or of photons, $E_{\lambda,f}(\lambda)$ [nm^{-1}]. These distribution functions $E_{\lambda,w}(\lambda)$ and $E_{\lambda,f}(\lambda)$ must satisfy the following condition:

$$\int_{\lambda} E(\lambda) d\lambda = 1 \tag{18}$$

The Red Tide 650 spectrophotometer records the spectral energy density, $q_{\lambda,w}$ [Joule m^{-2} s^{-1} nm^{-1}], considering narrow wavelength ranges λ (± 0.36 [nm]). The photons emitted by the LEDs around a direction $\underline{\hat{\Omega}}$ correspond to the whole spectrum emitted by the diodes, i.e., there is no wavelength distribution λ as a function of the emission direction $\underline{\hat{\Omega}}$.

The measurement of $q_{\lambda,w}$ depends on the relative position of the emission source concerning the spectrophotometer detector. The spectral distribution function must be independent of the devices' relative positions; to achieve this, a normalisation is necessary, Eq. (19).

$$E_{\lambda,w}(\lambda) = \frac{q_{\lambda,w}}{\int_{VIS} q_{\lambda,w} \, d\lambda} \tag{19}$$

To find the distribution function in terms of the number of photons, $E_{\lambda,f}(\lambda)$, the spectral flux density $q_{\lambda,w}$ can be defined through $E_{\lambda,w}(\lambda)$, as described by Eq. (20).

$$q_{\lambda,w} E_{\lambda,w}(\lambda) = \frac{hc}{\lambda} q_{\lambda,f} E_{\lambda,f}(\lambda) \tag{20}$$

where *h* is Planck's constant and *c* is the vacuum speed of light.

Integrating Eq. (20) in λ, and remembering that $q_{\lambda,w}$ and $q_{\lambda,f}$ are not a function of λ, and that the integrals of $E_{\lambda,w}(\lambda)$ and $E_{\lambda,f}(\lambda)$ fulfil specific requirements (Eq. (18)), allows us to obtain the mathematical expression of the factor that grants the conversion of energy to photons (Eq. (21)).

$$\frac{q_{\lambda,w}(\underline{r},t)}{hc}\int_{\lambda}\lambda E_{\lambda,w}(\lambda)\,d\lambda = q_{\lambda,f}(\underline{r},t)\underbrace{\int_{\lambda}E_{\lambda,f}(\lambda)\,d\lambda}_{1} \tag{21}$$

$$q_{\lambda,f}(\underline{r},t) = \frac{q_{\lambda,w}(\underline{r},t)}{hc}\int_{\lambda}\lambda E_{\lambda,w}(\lambda)\,d\lambda \tag{22}$$

Knowing the values of $q_{\lambda,f}$ it is possible to assess $E_{\lambda,f}(\lambda)$ via Eq. (23).

$$E_{\lambda,f}(\lambda) = \frac{q_{\lambda,f}}{\int_{VIS} q_{\lambda,f}\,d\lambda} \tag{23}$$

Fig. (6A) shows $E_{\lambda,f}(\lambda)$ for the different LED models.

(5.4). - PPF

For the determination of the photosynthetic photon flux, a series of experiments were carried out, which consisted of recording with a radiometer, located in different positions, the radiant energy coming from the LED tube (see Figs. (2)). The measurement provided by the detector corresponds to the photon flux density over the detector, considering the photons included in the following wavelength spectral range of 400 ≤ λ ≤ 700 [nm], q_{VIS} [μmol s^{-1} m^{-2}].

For modelling purposes, each LED will be considered as an indivisible unit with an area small enough to be considered an elementary surface, ΔA_i. Such an LED exchanges photons with the detector, and the area of the detector happens to be large compared to the LED, and therefore the number of photons exchanged varies with the position of the detector. This is why the surface of the radiometer is divided into more minor surface elements, ΔA_j, and the number of photons exchanged between each LED and each of the ΔA_j, is calculated.

The number of photons exchanged per unit of time, $\Delta N/\Delta t$ [μmol s^{-1}], between an LED "i" and a surface element "j" of the detector, is:

$$\frac{\Delta N_\lambda}{\Delta t} = n_\lambda\left(r, \underline{\hat{\Omega}}_{i,j}, t\right)\Delta\lambda \frac{\left(\underline{\hat{n}}_i \cdot \underline{\hat{\Omega}}_{i,j}\right)\Delta A_i \left(\underline{\hat{n}}_j \cdot \underline{\hat{\Omega}}_{j,i}\right)\Delta A_j}{r_{j,i}^2} \tag{24}$$

In Eq. (24), ΔN_λ refers to the number of photons [μmol] with wavelength λ arriving at a surface element "j" of the detector, ΔA_j, coming from an LED "i" on the tube's inner surface, ΔA_i, and n_λ to the spectral intensity of the photon beam [μmol s^{-1} m^{-2} nm^{-1} sr^{-1}]. Since the LED is assumed to be an elementary surface, the spectral intensity of the photon beam per LED can be rewritten as: $n'_\lambda(\underline{\hat{r}}, \underline{\hat{\Omega}}, t) = n_\lambda(\underline{\hat{r}}, \underline{\hat{\Omega}}, t)\Delta A_i$.

The intensity n'_λ can be expressed in terms of $E_\lambda(\lambda)$ [nm^{-1}] as follows:

$$n'_\lambda = n'_{VIS} E(\lambda) \tag{25}$$

where:

$$n'_{VIS} = \int_{VIS} n'_\lambda \, d\lambda \tag{26}$$

Then, the PPFD, q_{VIS}, on the detector surface is the result of the number of photons per unit of time exchanged by each ΔA_j on the detector, with each of the LEDs divided by the detector area, A_D.

$$q_{VIS} = \frac{1}{A_D} \sum_{LED_i} \sum_{\Delta A_j} \sum_{\lambda} \left(\frac{\Delta N_\lambda}{\Delta t}\right) \tag{27}$$

$$q_{VIS} = \frac{1}{A_D} \sum_{LED_i} \sum_{\Delta A_j} \sum_{\lambda} \left(n'_\lambda \Delta\lambda \frac{\left(\underline{\hat{n}}_i \cdot \underline{\hat{\Omega}}_{i,j}\right)\left(\underline{\hat{n}}_j \cdot \underline{\hat{\Omega}}_{j,i}\right)\Delta A_j}{r_{j,i}^2} \right) \tag{28}$$

Incorporating into Eq. (29) the relationship between n'_λ y n'_{VIS} given by Eq. (25), it follows:

$$q_{VIS} = \frac{1}{A_D} \sum_{LED_i} \sum_{\Delta A_j} \sum_{\lambda} \left(n'_{VIS} E(\lambda) \Delta\lambda \frac{\left(\underline{\hat{n}}_i \cdot \underline{\hat{\Omega}}_{i,j}\right)\left(\underline{\hat{n}}_j \cdot \underline{\hat{\Omega}}_{j,i}\right) \Delta A_j}{r^2_{j,i}} \right) \tag{29}$$

The distribution function $E_\lambda(\lambda)$ is independent of the emission direction and the receiving surface and fulfils the condition stated in Eq. (18).

$$q_{VIS} = \frac{1}{A_D} \sum_{LED_i} \sum_{\Delta A_j} \left(n'_{VIS} \frac{\left(\underline{\hat{n}}_i \cdot \underline{\hat{\Omega}}_{i,j}\right)\left(\underline{\hat{n}}_j \cdot \underline{\hat{\Omega}}_{j,i}\right) \Delta A_j}{r^2_{j,i}} \right) \tag{30}$$

Considering an isotropic type of emission, it results:

$$n'_{VIS} = \frac{q_{VIS} A_D}{\sum_{LED_i} \sum_{\Delta A_j} \left(\frac{\left(\underline{\hat{n}}_i \cdot \underline{\hat{\Omega}}_{i,j}\right) \Delta A_i \left(\underline{\hat{n}}_j \cdot \underline{\hat{\Omega}}_{j,i}\right) \Delta A_j}{r^2_{j,i}} \right)} \tag{31}$$

In Eq. (31), n'_{VIS} is the intensity in terms of the number of photons considering the range 400 ≤ λ ≤ 700 [nm], A_D is the radiometer area [m^2] and is a known quantity, q_{VIS} is the measurement recorded by the radiometer, and the term in the denominator is the geometrical factor (see Eq. (1)) and can be calculated numerically. The calculation methodology adopted for the numerical resolution was implemented in MATLAB 2022b programming language and is schematized in Fig. (5). The relevant data are detailed in Table (1) and Figure (6).

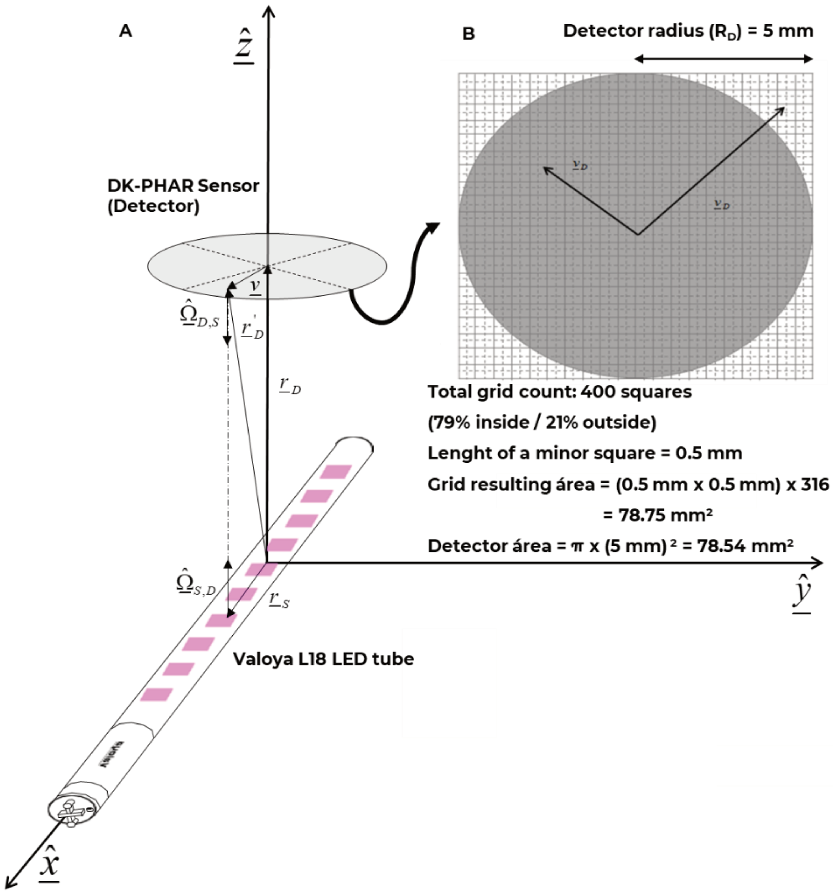

Figure (5). A] The numerical calculation methodology for the geometrical factor of Eq. (31). B] Division of the circular area of the detector into square surface elements, ΔA_j, of 0.5 mm side, in order to simulate all the radiant energy exchanges between these elements and the "i" LEDs of the plate, ΔAi, considered as elementary surfaces.

Table (1). The numerical calculation details and methodology for assessing the system's geometric factor of Eq. (31) are schematized in Fig. (5A).

▹ The light sensor position is: $\underline{r}_D$

▹ The positions of the surface elements on the detector, ΔA_j, are: $\underline{r}_D^{'} = \underline{r}_D + \underline{v}$

▹ Exists a vector $\underline{v}$ for each position over the sensor's surface:

$$\begin{pmatrix} -R_D + \Delta x_D/2 < v_x < R_D - \Delta x_D/2 \\ -R_D + \Delta z_D/2 < v_y < R_D - \Delta z_D/2 \\ v_z = 0 \end{pmatrix}$$

$$\Delta x = 0.5mm \;\; ; \;\; \Delta y = 0.5mm$$

▹ If the norm of the $\underline{v}$, $|\underline{v}|$, surpasses R_D (5 [mm]), the contribution of that position to the radiant energy exchange is not considered. Where: $|\underline{v}| = \sqrt{v_x^2 + v_y^2 + v_z^2}$.

▹ The corresponding area of each ΔA_j is: $\Delta A_D = \Delta A_x \Delta A_y$.

▹ The normal vector for each ΔA$_j$, $\underline{\hat{n}}_D$, is the same for every position: $\underline{\hat{n}}_D = (0\underline{\hat{x}}, 0\underline{\hat{y}}, -1\underline{\hat{z}})$

▹ The position of each LED over the tube facing side is: $\underline{r}_L = (x_i\underline{\hat{x}}, y_i\underline{\hat{y}}, z_i\underline{\hat{z}})$.

▹ The normal surface vector of each "i" LEDs, $\underline{\hat{n}}_L$, is the same for every: $\underline{\hat{n}}_L = (0\underline{\hat{x}}, 0\underline{\hat{y}}, 1\underline{\hat{z}})$.

The expression for the total flux of photons emerging from a LED, considering photons with wavelengths λ contained in the range 400 ≤ λ ≤700 [nm], and taking into account all possible emission directions for an LED, turns out to be:

$$Q_{VIS} = \int_{\hat{\Omega}} n'_{VIS} d\underline{\hat{\Omega}} \tag{32}$$

Incorporating the expression of $d\underline{\hat{\Omega}}$ present in Eq. (4) results:

$$Q_{VIS} = -\int_{\varphi} \int_{u} n'_{VIS} \; u \; d\varphi \; du = -\int_0^{2\pi}\int_1^0 n'_{VIS} \; u \; d\varphi \; du = -n'_{VIS} \int_0^{2\pi} d\varphi \int_1^0 u \; du \tag{33}$$

$$Q_{VIS} = n'_{VIS}\pi \tag{34}$$

Following the application of the latter procedure, a Q_{VIS} equal to 0.3008 [μmol s^{-1} LED^{-1}] (30.08 [μmol s^{-1}] in total) was assessed and n'_{VIS} resulted in a value of 0.09575 [μmol s^{-1} nm^{-1} sr^{-1} LED^{-1}].

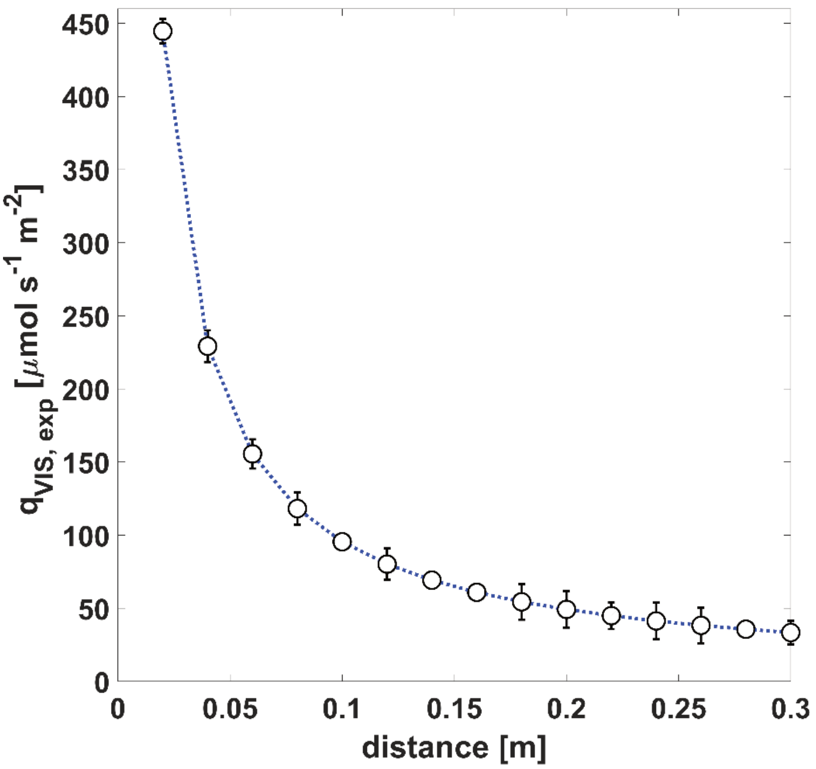

Figure (6). A] The assessment of the Valoya L18 PPFD at different distances. The blue dot line does not represent experimental points.

The spectral photon flux distribution function, or spectral photon flux, [μmol s^{-1} nm^{-1} LED^{-1}], can be obtained by multiplying Q_{VIS} [μmol s^{-1} LED^{-1}] by the function $E_{\lambda,f}(\lambda)$ [nm^{-1}], Fig. (7).

The LEDs described here are industrially manufactured in series, i.e., they are all built similarly. For the experiments in the following chapters of this thesis, it is assumed that the PPF, the angular emission distribution and the spectral emission distribution are identical for all the experiments carried out with different microorganisms.

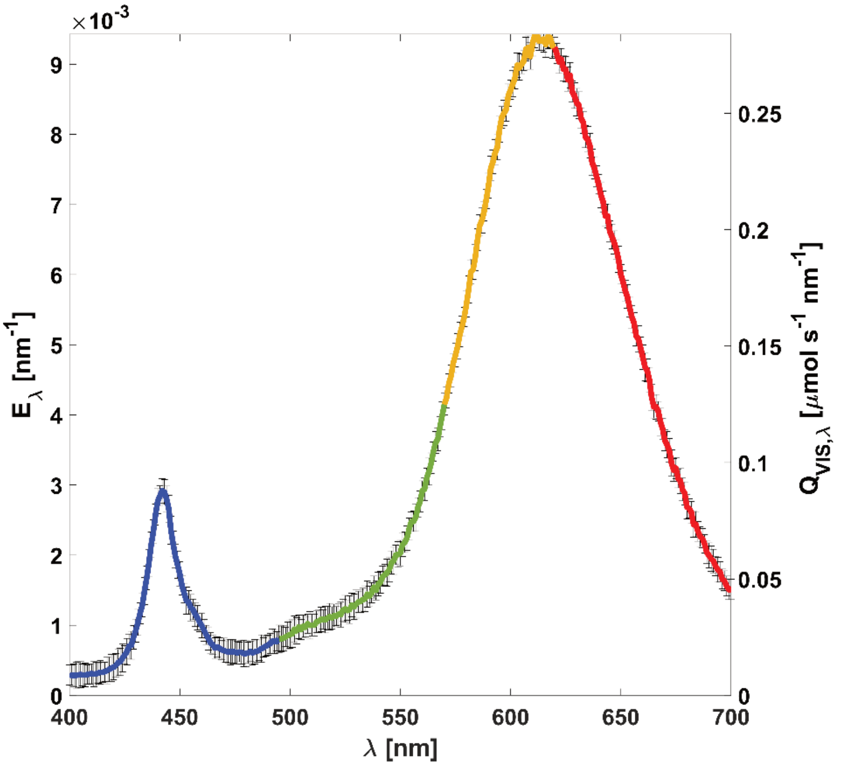

Figure (7). A] Spectral distribution function $E_{\lambda,f}(\lambda)$ [nm^{-1}] (left) and PPF spectral distribution function [μmol s^{-1} nm^{-1}] (right) were experimentally obtained from the light source's characterisation.

(6). - Conclusions

In this chapter, a comprehensive characterisation of the radiant energy emitted by the LEDs chosen to design and build radiation sources for microalgae cultivation in PBRs was carried out.

From the experiments, it can be concluded that the LEDs emit isotropically, i.e., the intensity does not depend on the angle of emission, i.e., the photon flux remains constant at all angles φ for the same angle θ, and there is a decrease proportional to $\cos(\theta)$ in the value of the photon flux as the angle θ increases. The intensity is a scalar property, and like the spectral distribution function, it varies according to the LED model.

Chapter (3)

Physical-mathematical modelling of the radiant energy field in microalgae suspensions: simulation through Monte Carlo methodology.

---

(1). – Abstract

Knowledge of the radiant energy field (REF) in a microalgae culture system, partly due to the interaction between light and microorganism cells, is an essential aspect in the context of biological studies and the design, optimisation and scale-up stages of photobioreactors (PBRs).

In this chapter, computational algorithms are developed for the simulation of REF within microalgae suspensions in MATLAB programming language and based on the Monte Carlo (MC) methodology, a calculation method based on the generation of random numbers for the determination of probabilities. The algorithms take into account the characteristics of the radiant energy source, the reactor geometry, the orientation and arrangement of the light source-PBR configuration, the physical phenomena of light reflection and refraction at the reactor physical boundaries (walls), and the absorption and scattering phenomena within the microalgae suspension.

(2). – Introduction

Knowledge of the REF in a microalgae cultivation system allows i) the search for kinetic expressions for biomass growth and metabolite accumulation based on local properties of the REF [114]–[116] or the average values of the distribution of such properties [117], e.g. absorption rate of photons of wavelength λ; ii) the calculation of yields in terms of light supplied or absorbed; iii) the analysis and understanding of the results of tests performed under certain operating conditions, e.g. specific growth rate, productivity, biomass composition (proteins, lipids, carbohydrates, nucleic acids, pigments); iv) the choice of radiation source and reactor, lighting policy (in terms of the amount of light to be delivered and duration), scaling-up methodology.

Typical aquatic microalgae cultures are inhomogeneous suspensions consisting of a cloud of algal cells dispersed throughout the volume of a saline solution. A bubbling gas, usually atmospheric air, is used as a medium to deliver CO_2 and stir the suspension. If the culture medium is transparent to visible light, each beam of light can be absorbed or scattered as it travels through the suspension.

Solving the Radiative Transfer Equation (RTE) for a system of interest provides insight into the spatial and directional distribution of the radiation intensity. To solve the RTE within the PBR, the spectral radiative properties of the microalgae suspension are required (spectral absorption coefficient, κ_λ [mm^{-1}], spectral scattering coefficient; σ_λ [mm^{-1}], and the parameters of the chosen phase function $B(\underline{\widehat{\Omega}} \cdot \underline{\widehat{\Omega}}')$. These properties can be estimated either with experimental methods [118]–[120] or with theoretical approaches [121] (e.g., Mie's theory).

Due to the complexity of the RTE, an analytical resolution is only possible in elementary systems. For most PBRs used for microalgae cultivation, the application of various methods involving simplifications is necessary to solve the RTE, e.g., the Lambert-Beer Law, the two-flux approximation and the discrete ordinate method [121]–[123]. An alternative to solving the RTE and its inherent complications is the physical simulation of the REF distribution. In this regard, a commonly used method is Monte Carlo (MC) [124]–[126], which has the advantage that it does not require the imposition of simplifications on the system for the purpose of ruling out an analytical resolution.

(3). – Objectives

- To build computational algorithms based on the MC methodology for the simulation of REF in PBRs illuminated with LED light tubes, which allow the calculation of the spatial distribution in the PBR of the photon density and the volumetric absorption velocity of photons of wavelength λ.

(4). - Materials and methods

(4.1). - Computational algorithms and inputs

The algorithms were written and implemented in MATLAB 2022b. A detailed description of the flowchart for these computational programs is given in Fig (3).

(5). - Results and discussion

(5.1). - Fundamentals of MC simulation and structure of computational algorithms

The REF may be considered as a collection of photons moving at the speed of light. Each photon is assumed as a particle, and then the REF as a non-uniform fluid of photons moving at the speed of light.

To simultaneously include the phenomena of absorption and scattering of radiant energy within the solution, the culture medium will be treated as a homogeneous and continuous suspension, with absorption and scattering centres randomly distributed within the suspension. Under these conditions, the algae lose their identity as particles, and the suspension is considered as a continuous medium with photon absorption and scattering centres homogeneously distributed throughout the suspension.

The MC method is a numerical simulation method based on random numbers, which allows the statistical estimation of the final value of a sequence of non-deterministic events, i.e., subject to variability. The absolute error of the estimate decreases as $1/\sqrt{N}$, where N is the number of times the procedure is repeated, concluding that an increase in N leads to more accurate results.

In the REF simulation using MC, the trajectory of each photon from the radiation source until it is absorbed, or leaves the crop through the PBR boundaries, is described on a probabilistic basis. Although photons are fired successively during the computation time, all photons are considered as being emitted simultaneously for the purposes of the REF simulation. By repeating the simulation for many photons, a continuous field of radiation properties, unevenly distributed in space and wavelength λ, is constructed.

The local number density of photons with wavelength λ, with a trajectory through the position $\underline{r}$ in the direction $\underline{\hat{\Omega}}$, $p_{\lambda,\underline{\hat{\Omega}}}(\underline{r},\underline{\hat{\Omega}},t)$, is the property of the REF on which an MC simulation algorithm can be constructed. If $p_{\lambda,\underline{\hat{\Omega}}}(\underline{r},\underline{\hat{\Omega}},t)$ is known, the local spectral photon density, $e_\lambda(\underline{r},t)$, may be obtained as:

$$e_\lambda(\underline{r},t)=\int_{\hat{\Omega}} p_{\lambda,\underline{\hat{\Omega}}}\left(\underline{r},\underline{\hat{\Omega}},t\right)d\underline{\hat{\Omega}} \tag{1}$$

From $e_\lambda(\underline{r},t)$, it is possible to obtain the local spectral volumetric rate of photon absorption, $r_\lambda(\underline{r},t)$, which allows us to understand how light within the PBR is locally absorbed by the microalgae, Eq. (2).

$$r_\lambda(\underline{r},t)=c\,\alpha_\lambda e_\lambda(\underline{r},t) \tag{2}$$

In Eq. (2), c represents the speed of light.

To find the relations between the REF properties of interest, let us consider a volume element immersed in the REF at position $\underline{r}$, which receives radiation due to the beams passing through it in all possible directions $\underline{\hat{\Omega}}$. This elementary volume contains, at any instant t a certain amount of radiant energy residing in it, resulting from the presence of photons of wavelength λ. If we consider one of such monochromatic beams, as shown in Fig. (1A), the number of photons per unit area and per unit time passing through the transverse projection to the beam propagation direction $\underline{\hat{\Omega}}$ of an elementary surface dA, located at position $\underline{r}$, is:

$$dq_{\lambda}\left(\underline{r},\underline{\hat{\Omega}},t\right)=\frac{dN_{\lambda}}{dA\ \ cos\theta\ \ d\lambda\ \ dt}=n_{\lambda}\left(\underline{r},\underline{\hat{\Omega}},t\right)d\underline{\hat{\Omega}} \tag{3}$$

Eq. (3) represents the contribution to the local photon flux density λ, due to the photon beam with an intensity $n_{\lambda}(\underline{r},\underline{\hat{\Omega}},t)$.

Inasmuch as the beam propagates at speed equal to the speed of light, contributing an amount $de_{\lambda}(\underline{r},\underline{\hat{\Omega}},t)$ to the local photon flux density λ at position $\underline{r}$, $dq_{\lambda}(\underline{r},\underline{\hat{\Omega}},t)$ may also be written as:

$$dq_{\lambda}\left(\underline{r},\underline{\hat{\Omega}},t\right)=c\ de_{\lambda}\left(\underline{r},\underline{\hat{\Omega}},t\right) \tag{4}$$

From Eq. (3) and (4), it immediately follows that the contribution of the considered beam to the spectral photon density around the position $\underline{r}$ is:

$$de_{\lambda}\left(\underline{r},\underline{\hat{\Omega}},t\right)=\frac{1}{c}\ dq_{\lambda}\left(\underline{r},\underline{\hat{\Omega}},t\right)=\frac{1}{c}\ n_{\lambda}\left(\underline{r},\underline{\hat{\Omega}},t\right)d\underline{\hat{\Omega}} \tag{5}$$

From Eq. (5), the local photon spectral density, $e_{\lambda}(\underline{r},t)$, is found to be:

$$e_{\lambda}\left(\underline{r},t\right)=\int_{\hat{\Omega}}de_{\lambda}\left(\underline{r},\underline{\hat{\Omega}},t\right)d\underline{\hat{\Omega}}=\frac{1}{c}\int_{\hat{\Omega}}n_{\lambda}\left(\underline{r},\underline{\hat{\Omega}},t\right)d\underline{\hat{\Omega}} \tag{6}$$

Following, it is possible to define the direction of motion of the photon according to the polar angle θ and the azimuthal angle φ, $\underline{\hat{\Omega}}(\theta,\varphi)$. Incorporating the definition of $\mathrm{d}\underline{\hat{\Omega}}$ (see Eq. (4) of Chapter (2)), the expression for $e_{\lambda}(\underline{r},t)$ results:

$$e_{\lambda}\left(\underline{r},t\right)=\frac{1}{c}\int_{0}^{2\pi}d\varphi\int_{-1}^{1}n_{\lambda}\left(\underline{r},\mu,\varphi,t\right)d\mu \tag{7}$$

where $\mu = cos\,\theta$.

It is possible to establish the following identity with respect to the definitions of the local photon spectral density $e_{\lambda}(\underline{r},t)$, calculated from the photon beam intensity $n_{\lambda}(\underline{r},\underline{\hat{\Omega}},t)$, and the local photon number density $p_{\lambda,\underline{\hat{\Omega}}}(\underline{r},\underline{\hat{\Omega}},t)$:

$$e_{\lambda}\left(\underline{r},t\right)=\frac{1}{c}\int_{\underline{\hat{\Omega}}}n_{\lambda}\left(\underline{r},\underline{\hat{\Omega}},t\right)d\underline{\hat{\Omega}} \;=\int_{\underline{\hat{\Omega}}}p_{\lambda,\underline{\hat{\Omega}}}\left(\underline{r},\underline{\hat{\Omega}},t\right)d\underline{\hat{\Omega}} \tag{8}$$

(5.2). - Choice of the emitted photon direction and wavelength

In Chapter (2), the properties of the radiant energy emitted by the LED tubes used in this Thesis were assessed. It should be remembered that LEDs are considered as differential radiant energy emitting surfaces. That is why the emission of photons in the simulations takes place from a point in space coincident with the centre of the LED.

For the choice of LED model, in cases of arrays composed of more than one LED, a random number in the range of $0 \leq \delta_{LED} \leq 1$ is generated, and δ_{LED} is compared with the fraction that each LED model contributes to the total radiant flux of the source. To determine the position of the LED that will emit the photon, a random integer $1 \leq \delta_P \leq n_{LED}$ is generated, where n_{LED} is the number of LEDs corresponding to the selected model. Each δ_P is associated with a position vector in a primary coordinate system of convenience.

To choose the wavelength λ of the photon, we will use the spectral distribution functions of each LED model, $E_{\lambda,f}$(λ), present in Fig. (7) of Chapter (2). We have seen that the integral of $E_{\lambda,f}$(λ) [nm^{-1}], considering the range $0 \leq \lambda < \infty$, takes the value of 1. The magnitude of the integral of $E_{\lambda,f}$(λ) in the interval, λ+dλ [nm], represents the probability that the photon has a wavelength λ contained in that interval, Eq. (9).

$$P\left(\lambda\right)=\frac{\int_{0}^{\lambda}E_{\lambda,\mathrm{f}}\left(\lambda'\right)d\lambda'}{\int_{0}^{\infty}E_{\lambda,\mathrm{f}}\left(\lambda\right)d\lambda} \tag{9}$$

The range of 400 ≤ λ ≤ 700 [nm], the region in which the LEDs emit, was divided into intervals Δλ of 10 [nm], resulting in 31 values for the wavelength λ. To determine the wavelength λ of the emitted photon, a random number of $0 \leq \delta_\lambda \leq 1$ is generated, and the interval λ+Δλ is identified by comparing δ_λ with the values taken by the integral of $E_{\lambda,f}(\lambda)$. The cumulative distribution functions, $P_{\lambda,f}(\lambda)$, for the LEDs described in Chapter (2) are shown in Fig. (1B).

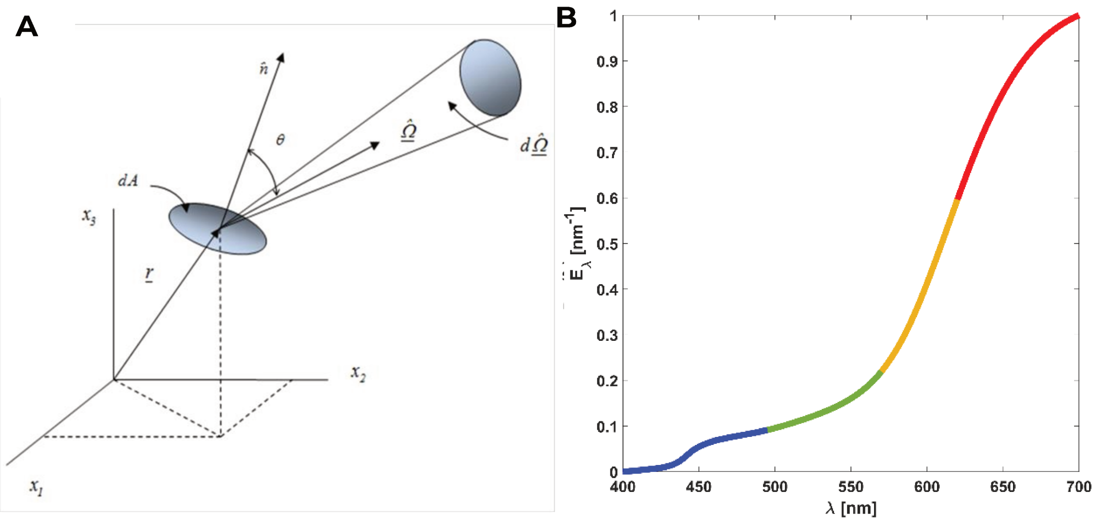

Figure (1). A]. An elemental surface immersed in the REF located at the position $\underline{r}$. B] The cumulative distribution function $P_{\lambda,f}(\lambda)$ for the Valoya L18 model.

For the choice of the direction of the emitted photon, $\hat{\Omega}$, we will resort to the directional distribution function of the LEDs, Eq. (10).

$$E_{\theta,\varphi} = E_\varphi E_\theta = \frac{1}{2\pi} cos(\theta) \tag{10}$$

On the one hand, φ can take values between 0 ≤ φ ≤ 2π, all of them being equally likely, while θ can take values between 0 ≤ θ ≤ $\pi/2$, whose distribution is related to the function $\cos(\theta)$. The cumulative probability distribution functions, $P(\theta)$ and $P(\varphi)$ arise from integrating the directional distribution functions E_θ and E_φ (Eqs. (11) and (13)). In the context of MC, these probabilities are replaced by random numbers, $0 \leq \delta_\theta, \delta_\varphi \leq 1$ (Eqs. (12) and (14)).

$$P(\varphi)=\int_0^{\varphi} E_{\varphi} d\varphi=\frac{1}{2\pi}\int_0^{\varphi} d\varphi=\frac{1}{2\pi}\varphi \tag{11}$$

$$\varphi=2\pi P(\varphi)=2\pi\delta_{\varphi} \tag{12}$$

$$P(\theta)=\int_0^{\theta} E_{\theta} d\theta=\int_0^{\theta} cos(\theta)d\theta=sen(\theta) \tag{13}$$

$$sen(\theta)=\delta_{\theta} \tag{14}$$

The unit vector describing the direction of the photon, $\underline{\hat{\Omega}}(\theta,\varphi)$, in an orthonormal auxiliary coordinate system $\{\underline{\hat{e}}_1,\underline{\hat{e}}_2,\underline{\hat{e}}_3\}$ turns out to be:

$$\underline{\hat{\Omega}}(\theta,\varphi)=\left(sen\,(\theta)cos\,(\varphi)\right)\underline{\hat{e}}_1+\left(sen\,(\theta)\,sen\,(\varphi)\right)\underline{\hat{e}}_2+\left(cos\,(\theta)\right)\underline{\hat{e}}_3 \tag{15}$$

$$\underline{\hat{\Omega}}(\theta,\varphi)=\left(\delta_{\theta} sen\left(2\pi\delta_{\varphi}\right)\right)\underline{\hat{e}}_1+\left(\delta_{\theta}\,cos\left(2\pi\delta_{\varphi}\right)\right)\underline{\hat{e}}_2+\left(\left(1-\delta_{\theta}{}^{2}\right)^{1/2}\right)\underline{\hat{e}}_3 \tag{16}$$

where $\underline{\hat{e}}_2,\underline{\hat{e}}_3$ are vectors located on the flat emission surface of the LED and $\underline{\hat{e}}_3$ is the unit vector normal to the surface, whose position coincides with the centre of the LED.

Last but not least, the direction of the photon must be expressed in the principal coordinate system (coordinate transformation), which is achieved by perpendicular projections. One crucial aspect that has been included in the present thesis in difference from the previous work published by the other research group members is the utilisation of a different methodology for assessing the position of the impacting photons over the reactor walls. The latter implies using fzero, a MATLAB function that employs Newton’s Golden rule. In Fig. (3A), it is possible to follow the sequence of events that involves the generation of potential random directions of photons from the light source until they reach the reactor's transparent physical limits. Here, the main advantage of employing *fzero* is avoiding the necessity of parameterising the reactor walls' surface in the selected coordinate system. The latter is advantageous in adapting Monte Carlo algorithms to further geometries.

(5.3). - Photon reflection and refraction at PBR physical boundaries

In the case where the source of radiant energy is not in intimate contact with the PBR content, it is necessary to assess whether the emitted photon impacts the boundaries of the PBR, e.g., the walls of the reactor vessel and the surface of the suspension in the case of ponds. The impact is assessed from the knowledge of the position and direction of the emitted photon and through expressions that take into account characteristics of the PBR, such as geometry and orientation. In case of a negative impact, the photon is removed from the REF, while a positive impact involves two possible optical events, reflection and refraction. Fig. (2A) schematises the reflection and refraction of photons for the case of two media, 1 and 2. On the one hand, in reflection, the photon propagating in medium 1, with an angle of incidence σ_1 defined with respect to the normal vector to the surface at the point of impact, $\underline{\hat{n}}$, acquires a direction $\underline{\hat{\Omega}}^{(R)}$ (equal angle σ_1 with respect to $\underline{\hat{n}}$). The reflected photon is removed from the REF if no other surfaces allow it to return to the boundaries (i.e., black plastic covering at the bottom of raceway reactors). On the other hand, in refraction, the photon propagating in medium 1 with an angle of incidence σ_1 enters medium 2, adopting a direction $\underline{\hat{\Omega}}_2$.

The reflectivity, $\rho_{1,2}$, refers to the fraction of the reflected incident radiation, and at the interface between media 1 and 2 is determined according to the Fresnel equations, Eq. (17).

$$\rho_{1,2}\left(\underline{\hat{\Omega}},\underline{\hat{\Omega}}_2,\underline{\hat{n}}\right)=\frac{1}{2}\left[\frac{n_1\left(\underline{\hat{n}}\cdot\underline{\hat{\Omega}}\right)-n_2\left(\underline{\hat{n}}\cdot\underline{\hat{\Omega}}_2\right)}{n_1\left(\underline{\hat{n}}\cdot\underline{\hat{\Omega}}\right)+n_2\left(\underline{\hat{n}}\cdot\underline{\hat{\Omega}}_2\right)}\right]^2+\frac{1}{2}\left[\frac{n_1\left(\underline{\hat{n}}\cdot\underline{\hat{\Omega}}_2\right)-n_2\left(\underline{\hat{n}}\cdot\underline{\hat{\Omega}}\right)}{n_1\left(\underline{\hat{n}}\cdot\underline{\hat{\Omega}}_2\right)+n_2\left(\underline{\hat{n}}\cdot\underline{\hat{\Omega}}\right)}\right]^2 \tag{17}$$

In Eq. (17), $\underline{\hat{\Omega}}$ y $\underline{\hat{\Omega}}_2$ are unit direction vectors of incidence and refraction, n_1 and n_2 are the refractive indices of media 1 and 2; and $\underline{\hat{n}}$ is the normal unit vector to the interface, pointing towards any of the interfaces. The direction $\underline{\hat{\Omega}}_2$ is constructed from the angle σ_2, which is obtained from Snell's law, Eq. (18).

$$n_1 sen\ \sigma_1 = n_2 sen\ \sigma_2 \tag{18}$$

The transmissivity, $T_{1,2}$, which refers to the fraction of incident radiation passing through the interface, is determined from $\rho_{1,2}$ with Eq. (19).

$$T_{1,2}\left(\underline{\hat{\Omega}},\underline{\hat{\Omega}}_2,\underline{\hat{n}}\right)=1-\rho_{1,2}\left(\underline{\hat{\Omega}},\underline{\hat{\Omega}}_2,\underline{\hat{n}}\right) \tag{19}$$

The case of media 1 and 2 corresponds to open pond reactors, where the photons emitted by the source reach the surface of the suspension, i.e., the air-suspension interface. The microalgae suspension is considered an aqueous medium.

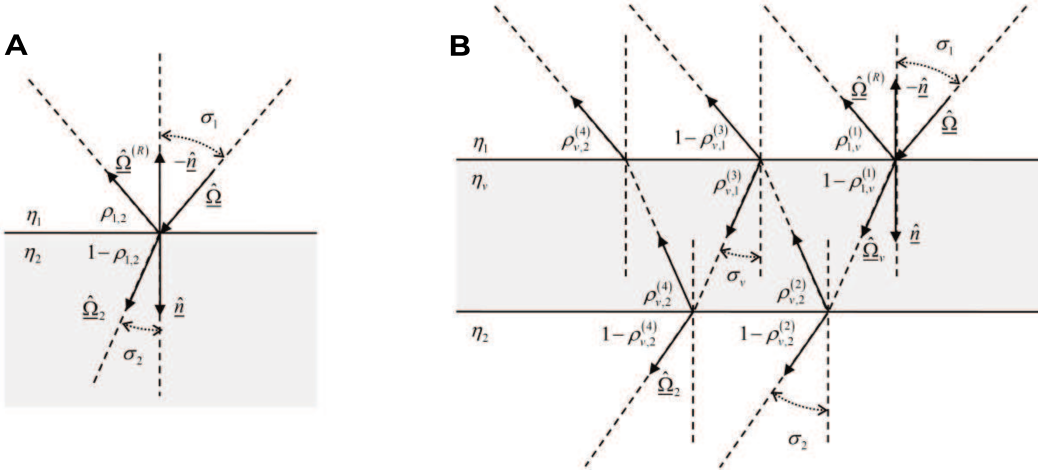

Figure (2). Representation of the reflection or refraction event on [A] An interface between media 1 and 2, [B] A thin sheet of transparent material between media 1 and 2.

In the case of glass walls, acrylic, or other materials, the system can be composed of three phases, air-material-water (Fig. (2B)). The system is modelled as an air-water double film, assuming that the material thickness is negligible, and considering the possibility of multiple internal reflections.

The reflectivity for this type of system, ρ_{Total}, is calculated with Eq. (20).

$$\rho_{Total} = \rho_{1,V}^{(1)} + \rho_{2,V}^{(2)}\left(1-\rho_{1,V}^{(1)}\right)\left(1-\rho_{V,1}^{(3)}\right) + \rho_{V,1}^{(3)}\rho_{2,V}^{(2)}\rho_{2,V}^{(4)}\left(1-\rho_{1,V}^{(1)}\right) \tag{20}$$

In the MC context, to find out whether the photon reflects or passes through the interface between the media, a random number $0 \leq \delta_R \leq 1$ is generated and compared to the value of ρ_{Total}. If $0 \leq \delta_R \leq \rho_{Total}$ the photon reflects. Otherwise, the photon is transmitted across the boundary and enters the microalgae suspension. The simulation pseudocode for evaluating photon reflection and refraction in various systems is described in detail in [116], [125].

(5.4). - Photon inside the microalgae suspension

The photon, in its movement within the suspension, can be absorbed by the microalgae cells through the pigments that integrate the photosynthetic apparatus or modify the direction of movement as a result of a collision with cellular components, a phenomenon known as scattering. The occurrence of photon absorption and scattering events of wavelength λ and direction $\underline{\hat{\Omega}}$, is related to the optical properties of the microalgae suspension, namely: i) the spectral absorption coefficient, κ_λ [mm^{-1}]; and ii) the spectral scattering coefficient; σ_λ [mm^{-1}]. These coefficients and their challenging accurate evaluation have been the objective of numerous pieces of research over the last forty years. In chapter (4) of the current thesis, a new contribution to the existing methodologies for their assessment is presented. Consequently, this information will not be thoroughly presented in this section. Moreover, the only possible way for a scattering event to occur is as a result of photon impact over any microalga cell because the composition of the culture medium involves inorganic species and water. We will consider elastic scattering, i.e., the energy carried by the photon after a scattering event is not altered. Hence the wavelength λ does not change. It is also considered that there is no emission of radiant energy within the suspension, i.e., phenomena such as fluorescence are not considered. Regarding the presence of a gas stream in the suspension, the photon-bubble interaction phenomenon has not been modelled because the REF simulations performed with or without the phenomenon are very similar, thus saving computational simulation time.

The scattering phase function, $B(\underline{\hat{\Omega}} \cdot \underline{\hat{\Omega}}')$, describes how the scattered radiation is redistributed in directions $\underline{\hat{\Omega}}'$ around the original direction $\underline{\hat{\Omega}}$, and must satisfy the normalisation condition in Eq. (21).

$$\frac{1}{4\pi}\int_{\underline{\hat{\Omega}}} B\left(\underline{\hat{\Omega}}\cdot\underline{\hat{\Omega}'}\right) d\underline{\hat{\Omega}'} = 1 \qquad (21)$$

If we consider that $B(\underline{\hat{\Omega}} \cdot \underline{\hat{\Omega}}')$ is axially symmetric concerning the original direction $\underline{\hat{\Omega}}$, where all angles $0 \leq \varphi \leq 2\pi$ are equally probable, $B(\underline{\hat{\Omega}} \cdot \underline{\hat{\Omega}}')$ depends only on the dot product ($\underline{\hat{\Omega}} \cdot \underline{\hat{\Omega}}' = cos\theta = \mu$), where θ is the angle formed between the vectors $\underline{\hat{\Omega}}$ and $\underline{\hat{\Omega}}'$. Adopting a $B(\underline{\hat{\Omega}} \cdot \underline{\hat{\Omega}}')$ with these characteristics results:

$$\frac{1}{4\pi}\int_{\hat{\underline{\Omega}}} B\left(\hat{\underline{\Omega}}\cdot\hat{\underline{\Omega}}'\right)d\hat{\underline{\Omega}}' = \frac{1}{2\pi}\left(\int_{0}^{2\pi} d\varphi\right)\frac{1}{2}\left(\int_{-1}^{1} B(\mu)\,d\mu\right) = 1 \tag{22}$$

Many phase functions $B(\hat{\underline{\Omega}}\cdot\hat{\underline{\Omega}}')$ for phototropic suspensions has been proposed as models for evaluating the scattering phenomenon. Among these, one expression based on a series expansion of Legendre polynomials was extensively employed for the research group associated with the actual thesis:

$$B\left(\hat{\underline{\Omega}}\cdot\hat{\underline{\Omega}}'\right) = \sum_{n=0}^{\infty} c_n P_n\left(\hat{\underline{\Omega}}\cdot\hat{\underline{\Omega}}'\right) = \sum_{n=0}^{\infty} c_n P_n(\mu) \tag{23}$$

Where c_n corresponds to the nth coefficient multiplying the nth polynomial of the series P_n.

The expression for $P_n(\mu)$ turns out to be:

$$P_n(\mu) = \frac{1}{2^n n!}\frac{d^n}{d\mu^n}\left(\mu^2 - 1\right)^n \tag{24}$$

The polynomial series was truncated upon reaching the desired degree of precision, resulting in a total of 5 coefficients.

The probability that a photon with direction $\hat{\underline{\Omega}}$ changes its direction to $\hat{\underline{\Omega}}'$ in a scattering event turns out to be:

$$P(\varphi,\mu) = P(\varphi)P(\mu) = \left(\frac{\varphi}{2\pi}\right)\left(\frac{1}{2}\int_{-1}^{\mu} B(\mu')\,d\mu'\right) \tag{25}$$

Again, the three possible events for a photon during its passage in suspension are absorption (A), scattering (S), and neither (NA, NS). The events are complementary and mutually exclusive, so the probability of either occurring can be written as:

$$P(A) + P(S) + P(NA, NS) = 1 \tag{26}$$

Mathematical expressions for the probabilities of these events, Eq. (27-29), were derived from radiation balances for a volume element located in purely dispersive *(P(S)+P(NS)=1)* and absorbing *(P(A)+P(NA)=1)* media, and from proposed constitutive expressions for the rate of absorption and scattering of radiant energy.

$$P(A)=\frac{\kappa_\lambda}{(\kappa_\lambda+\sigma_\lambda)}\left[1-e^{-(\kappa_\lambda+\sigma_\lambda)\Delta S}\right] \tag{27}$$

$$P(S)=\frac{\sigma_\lambda}{(\kappa_\lambda+\sigma_\lambda)}\left[1-e^{-(\kappa_\lambda+\sigma_\lambda)\Delta S}\right] \tag{28}$$

$$P(NA,NS)=e^{-(\kappa_\lambda+\sigma_\lambda)\Delta S} \tag{29}$$

In Eq. (27) to (29), ΔS is the distance advanced by the photon in each movement inside the microalgae suspension.

The magnitude of ΔS for the REF computational simulation cannot be chosen randomly but must be chosen systematically. A possibility in assigning a value for ΔS arises from calculating the expected mean path or free path, Eq. (30).

$$s_{LM}=\frac{1}{(\kappa_\lambda+\sigma_\lambda)} \tag{30}$$

In the research group's previous work associated with the current thesis's experimental essays, a distance ΔS equal to 1 [mm] was used for the REF simulation [116], [125]–[127]. The basic structure of the simulation algorithm in the algae suspension, in those works, consists of calculating the probabilities of events (A), (S) and (NA, NS) at distances of 1 [mm] through the generation of a random number $0 \leq \delta_M \leq 1$. If δ_M meets the condition $0 \leq \delta_M \leq P(A)$ the photon is absorbed, and the photon position is recorded for the construction of the REF distribution. If δ_M meets the condition $P(A) < \delta_M \leq P(S)$ the photon undergoes scattering, assigning it a new direction through the phase function $B(\underline{\hat{\Omega}} \cdot \underline{\hat{\Omega}}')$. The latter requires the generation of two random numbers, $0 \leq \delta_\mu \leq 1$ and $0 \leq \delta_\varphi \leq 1$ (see Eq. (25)). Finally, with the new direction $\underline{\hat{\Omega}}'$ the photon advances a new distance ΔS equal to 1 [mm], and a new event evaluation cycle starts. In the case that δ_M fulfils the condition $\delta_M > P(A) + P(S)$ the photon does not undergo absorption or scattering events, i.e., it maintains the original direction of motion $\underline{\hat{\Omega}}$, and continues to move forward in suspension. At each step, it is necessary to assess whether the photon is on the boundaries of the PBR (culture medium surface, the base, the side walls, and the rest). If so, the probabilities of the events are calculated according to the nature of the boundary, e.g., if the photon reaches the sidewalls, it is necessary to evaluate its reflection, returning to the suspension, or refraction, leaving the PBR and being removed from the REF (see Section (5.1.2)).

The described methodology to build the REF inside PBRs, which uses a distance ΔS of 1 [mm], chosen according to the mean free path s_{LM}, involves a significant expenditure of computational resources, and the simulation time is ample. This last is due to the fact that the probabilities of occurrence of the considered phenomena must be evaluated for each trajectory, and the impact of the photon on the PBR boundaries must also be checked. Besides, depending on the wavelength λ of the photon, the number of movements in the suspension before it is absorbed can be considerable.

In this Thesis, it has been proposed and applied a computational methodology that allows us to reduce the computational simulation time while achieving the same quality in the results in terms of simulation and visual description of the REF inside the PBR. The proposal arises from the analysis of Eq. (26), which can be rearranged as follows:

$$P(A)+P(S)=1-P(NA,NS) \tag{31}$$

If Eq. (29) is replaced in Eq. (31), it results:

$$P(A)+P(S)=1-e^{-(\kappa_\lambda+\sigma_\lambda)\Delta S} \tag{32}$$

When clearing ΔS, it arises:

$$\Delta S=-\frac{ln\left[1-\left(P(A)+P(S)\right)\right]}{(\kappa_\lambda+\sigma_\lambda)} \tag{33}$$

Now, ΔS is the distance that the photon with direction $\underline{\widehat{\Omega}}$ is expected to travel to undergo an absorption or scattering event. In the MC context, it is possible to replace the term P(A)+P(S) with a random number $0 \leq \delta_{AS} \leq 1$.

$$\Delta S = -\frac{ln\left(1-\delta_{AS}\right)}{\left(\kappa_{\lambda}+\sigma_{\lambda}\right)} \tag{34}$$

It may be the case that when travelling this distance ΔS, the photon is outside the limits of the PBR, so it is logical to contemplate the calculation over the PBR physical boundaries. To do so, all the distances ΔS to the boundaries of the system under consideration are evaluated. **The most likely event is associated with the smallest positive ΔS distance**. If the distance turns out to be that leading to a scattering or absorption event, it is necessary to generate a random number of $0 \leq \delta_S \leq 1$ to see whether the photon is absorbed or scattered. The expressions for the probabilities of the absorption (A) and scattering (S) events in this situation turn out to be:

$$P\left(A\right)=\frac{\kappa_{\lambda}}{\left(\kappa_{\lambda}+\sigma_{\lambda}\right)} \tag{35}$$

$$P\left(S\right)=\frac{\sigma_{\lambda}}{\left(\kappa_{\lambda}+\sigma_{\lambda}\right)} \tag{36}$$

In the case that $\delta_S \leq P(A)$ the photon is absorbed, and in the opposite case, the photon is scattered, acquiring a new direction of motion $\underline{\hat{\Omega}}$, as described above.

The elementary decision flow diagram for the REF simulation in the PBRs is schematised in Fig. (3).

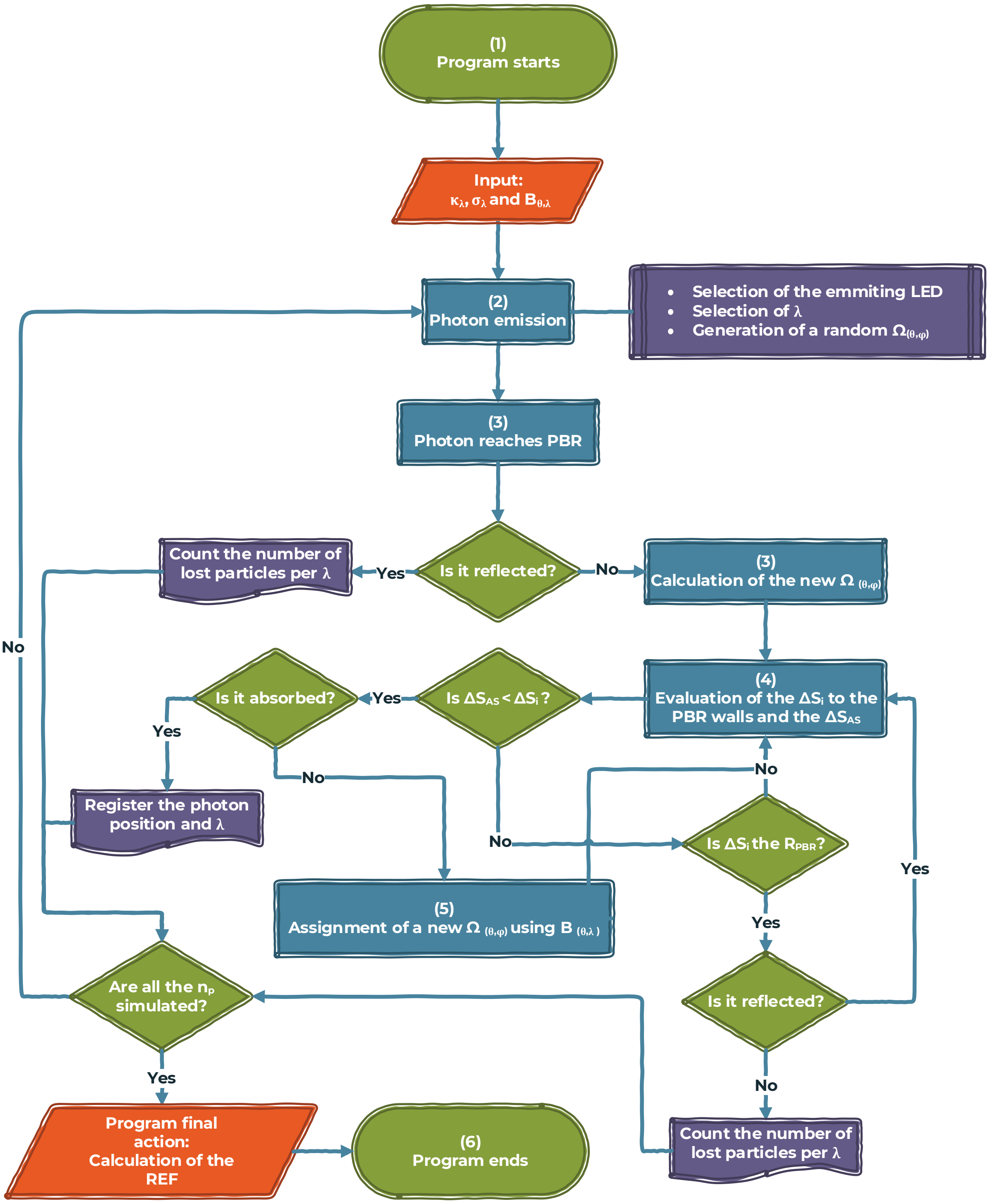

Figure (3). Computational flowchart including the decision nodes of the stochastic algorithm developed for the MC simulation of the REF. References: ΔS_{AS} is the distance at which an absorption (A) or scattering (S) event occurs.

(6). - Conclusions

In this chapter, computational algorithms were developed in MATLAB to simulate the REF using the MC methodology. A simulation strategy was proposed and applied to decrease the computational time significantly.

The algorithms allow the calculation of the spatial distribution in the PBR of the volumetric absorption velocity of photons of wavelength λ.

Chapter (4)

Development of a methodology for assessing real-time radiative properties

---

(1). - Summary

Regardless if a kinetic expression of a light-dependent bioprocess is being sought, the parameters of that kinetic function are being adjusted, or a scaling-up process is being carried out to predict the productivity of a reactor, it is necessary to know the light availability in the culture volume. The emission characteristics of the radiation source, the geometry of the reactor as well as the optical properties of the suspension that resides within it must be known to achieve the latter. Here, an approach is presented to quantify the optical properties of microalgae suspensions. A simple methodology, consisting in illuminating a suspension of microalgae with a characterised polychromatic radiation source and assessing how the directions are modified and the amount of energy carried by the light beams after crossing the suspension, was successfully employed. Subsequently, through an optimisation program, the experimental culture data has been used to determine the spectral absorption and scattering coefficients of photons and the suspension's scattering phase function. For a given microalgal culture, eight samples corresponding to a cultivation time of one week were analysed, utilising an energy balance, independently of the biomass or pigment concentration. Altogether the results presented here suggest that this methodology could be adapted to other suspensions, allowing accessible ways to evaluate the radiative characteristics of phototrophic microorganisms in the complex context of the evolution through time of the radiant energy field inside a photobioreactor.

(2). - Introduction

Photobioreactors (PBRs) are the preferable units for the cultivation of photosynthetic microorganisms. Even if the culture is mixotrophic or autotrophic, light must reach the suspension by passing through the unit's walls. Consequently, the optimisation and control of light transfer in PBRs are bound to the close relationship between the characteristics of the source of light, the geometry of the system and the radiative properties of the microorganisms dependent on the physiological state of the cell at any given time [128]. The combination of these three features in the radiative transfer equation (RTE) allows access to the radiant energy field (REF) in a PBR and, subsequently, the knowledge of the light availability inside the unit and the local volumetric rates of absorption of light (r_{abs}) in the photosynthetic active radiation (PAR) spectral range [129]. The absorption rates can be translated into growth rate values linked to a growth kinetic expression and, further, the productivity of a particular configuration. Nonetheless, during the progression of a run, the radiant energy field in, and the composition of the liquid medium underlies a significant dynamic change. Thus photo-adaptative biological processes and the physical chemistry of the system might alter the radiation properties of the suspension through variations in the composition of biomass and morphology of the cells, altering growth directly [128], [130].

The spectral optical properties of the suspensions (OPs) are the absorption coefficient (κ_λ), the scattering coefficient (σ_λ) and the scattering phase function ($\beta_{\theta,\lambda}$). They account for a fraction of incoming light that is effectively absorbed, scattered and, in case of scattering, the distribution of a beam in a new direction around the previous one, respectively (Fig. (1)) [128]. Due to the heterogeneous and non-spherical nature of the cells and the limited information concerning the radiative properties of intracellular constituents, numerous works have been published regarding its determination, explaining the interaction between cells with light as an equivalent homogeneous molecular medium that must reckon for the cells' internal heterogeneities [120], [131], [132]. Microalgae are, whence, pictured as composite material whose volume is divided into organelles assuming a homogeneous refraction index and a negligible scattering effect of separate molecules [133]. Then, complex refraction indexes of the suspension, which are dependent on the wavelength and the density of the material, stand for this simplification, composed of an imaginary part linked to the absorption behaviour and quantity of pigments present and the real part, which counts for the detailed description of the other non-absorbing cellular components, and usually is approximated.

The inclusion of different cell geometries and size distributions with experimental data such as biomass concentration, pigments content, normal-normal and normal-hemispherical spectral transmittance, in either analytical solutions or experimental approaches aimed to solve the RTE, have provided sets of refractive indexes, absorption and scattering cross-sections in the PAR region, as well as analytical or empirical models of phase functions whose parameters were regressed from experimental data [134], [135]. Although these OPs have been effectively used in the calculation of light availability inside a PBR unit, there is a lack of consensus about some discrepancies (i.e., nonlinear behaviour of pigments and adopted models regarding the cells' shape) previously reported. The pigment molecules are typically modelled as diluted enough to be characterised by an *in vivo* absorption cross-section and an internal pigment concentration. The latter leads to taking the system as independent of the microorganism characteristics (cellular shape, metabolism) and becoming strongly dependent on the medium's chemical composition and culture conditions. Consequently, the spectral absorption coefficients can be estimated, expressing it as the sum of *in vivo* previously reported absorption cross-sections under the PAR region, with a linear dependence on cells' pigments concentration [136], [137]. However, due to the none considered biological aspects, it has been reported that a first-order approximation could not be accurate enough due to a 'package effect' of the pigments, supporting the fact that the OPs must be experimentally determined due to a potential lack of reproducibility [138]. As for the scattering phase function, making use of the cell's size distribution models and experimental data, usually different expressions are employed, assuming forward scattering and dependence only on the azimuthal angles [120]. One of them was found to be nearly dependent on wavelength over the PAR region [137]. It was posited, though, that the majority of the models are sufficient in predicting light absorption yet inaccurate regarding scattering distribution. Besides, it is not clear if there is no effect whatsoever of the polarised properties of the scattered light throughout the evolution of the REF [139].

Given the necessity of applying rigorous solutions to these complex reflective systems, another published alternative to calculating the REF is the simulation of the radiation through Monte Carlo (MC) method, avoiding the inherent difficulties in solving the RTE [111]. This method emulates physical reality by tracking photons along their paths through an algal suspension. A considerable advantage of such a procedure relies on the premise that it enables the handling of the optical phenomena occurring within the suspensions and on their physical limits, with the characteristics of the light emitted by radiant energy sources (in direction and spectral composition) without the need of introducing simplifications to make the problem mathematically accessible [124]. Here the liquid medium must be treated as a continuum, and the cells are replaced as a homogeneous dispersion of absorption and scattering centres of energy [140]. After firing a large number of photons from the source of light, the OPs are utilised then to track the steps of the photons flying in the suspension. These are different since the absorption and scattering probabilities assigned to the cells depend on the simulated wavelengths and their interaction with the ensuing OPs.

The present study aims to calculate the microalgae suspensions' OPs under the foundation that the pigment content and all of the non-absorbing components of individual cells are highly dynamic variables. However, overall these produce a particular REF in its interaction with the light, which holds for the photo-adaptative phenomena and environmental conditions of a unique moment (Fig. (1)). Cellular metabolism is not as fast as the radiative phenomena on which the OPs are involved. Thus, the evolution of the REF is here assessed, utilising an energy balance which reckons for the considerable variations in the medium's composition, including the inner structure and shape of the cell in the same model. Based on the latter, a simple methodology was employed, consisting of (i) the design and construction of a device that allows recording the values of the photon flux density through different angles with respect to the main emission direction of the radiation source; (ii) the characterisation of the light source's spectral and emission distribution functions; (iii) the development of an algorithm which allows the physical simulation of a system comprised by the light spring, the cuvette holding microalgae' suspension and the position and orientation of the detector; (iv) nest the algorithm obtained in (iii) inside a stochastic algorithm to calculate the values of the radiative properties through the utilisation of recorded experimental data. By means of this methodology, eight sets of OPs over the PAR spectral region were obtained, corresponding to samples from a culture of *Chromochloris zofingiensis*, obtained through eight different times alongside a typical one-week batch culture. Since the methodology is based on an energy balance, it did not require the knowledge of the medium's composition, pigment content or microorganism' nature. Consequently, this method might be thought of as a more natural way of calculating the radiative properties of other microalgae suspensions in a faster and more reliable way, designed for laboratory or industrial applications.

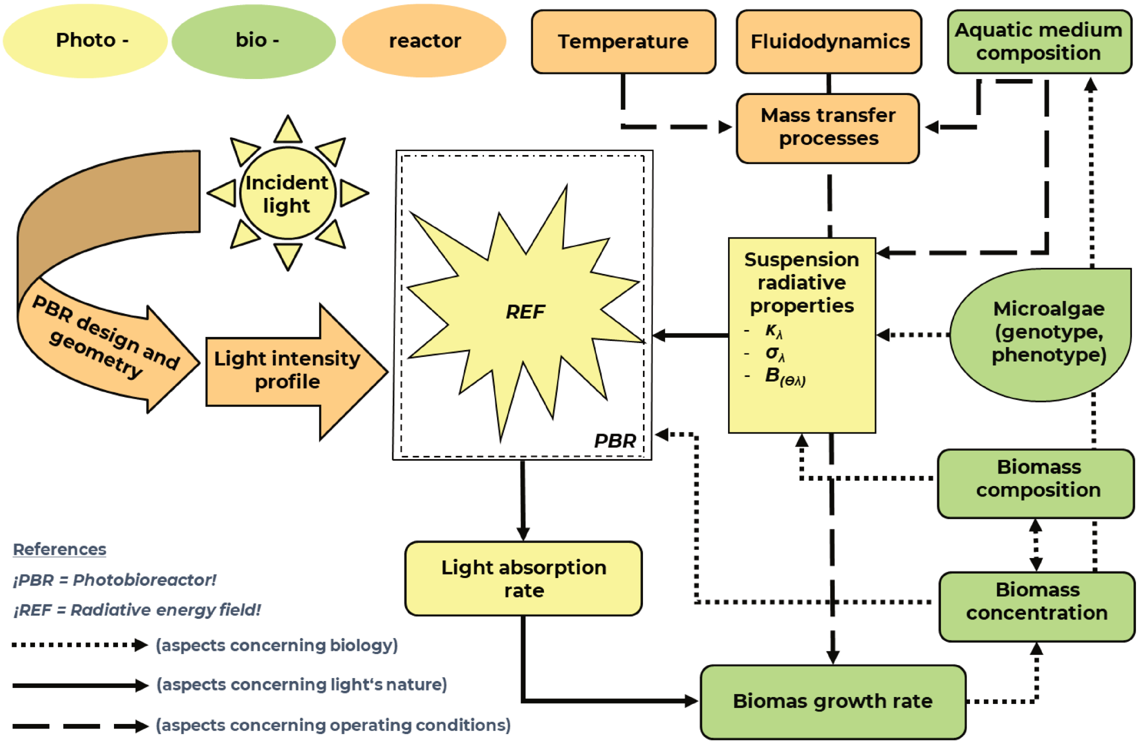

Figure (1): a PBR can be understood by treating the three major components of the system separately: the light (yellow), the geometry of the system and operating conditions (orange) and every aspect concerning the microorganism present (green). The incident light, in its interaction with the physical boundaries of the system, generates a unique light profile. Further, the microalgae' OPs (κ_λ, σ_λ, $\beta_{\theta,\lambda}$) and the physicochemical system conditions in the interaction with this light profile create the REF, which allows the calculation of r_{abs} and r_x for a particular moment alongside the cultivation time.

(3). - Objectives

- To make a contribution to the existing techniques for the evaluation of the radiative properties of microorganisms' suspensions.

(4). - Materials and methods

(4.1). - Light emission and collection system.

The source of light utilised in this work is a tungsten halogen HL-2000 lamp (Ocean Optics). The lamp's stable wavelength range is 360 – 2400 [nm], and it maximises light throughput with adjustable focus and alignment through an SMA 905 connector (Ocean Optics), which provides accuracy to the light collection of optical fibres.

The detector employed was a Red Tide 650 spectrometer (Ocean Optics). The spectrometer's resolution is 2 [nm] with a detectable spectrum ranging from 350 to 1000 [nm]. The spectral data were obtained employing the manufacturer's SpectraSuite (Ocean Optics) software. The latter was configured with the lowest integration time and default options disabled.

The optical fibres used were two pieces of stainless steel QP400-2-UV-BX fibres (Ocean Optics), with a robust transmission capacity from 300 – 1100 [nm] and 400 [µm] diameter size.

(4.2). - Strain and cultivation conditions

The batch cultivation of *Chromochloris zofingiensis SAG 221-2* (SAG – Göttingen, Germany) was performed in a 100 [L] tubular photobioreactor of MINT Engineering GmbH (Dresden, Germany). The PBR has 19 plastic tubes with an external diameter of 0.63 [m] and a length equal to 1.4 [m]. The liquid circulates with a pumping rate of 1 [L min^{-1}] and air and CO_2 gassing rates of 5 10^{-5} and 2.5 10^{-6} [vvm], respectively. The CO_2 input was utilised to maintain the pH level at a value equal to 7. The temperature was fixed at 23 [°C]. A concentrated inoculum was prepared in an illuminated chamber to start the cultivation with a biomass concentration equal to 0.1 [g L^{-1}] in the exponential phase.

The culture medium employed either for the inoculum or the PBR is BM, with the following composition: $NaNO_3$ - 7.5 10^{-1} [g L^{-1}], $MgSO_4.7H_2O$ - 7.5 10^{-2} [g L^{-1}], $CaCl_2.2H_2O$ - 2.5 10^{-2} [g L^{-1}], K_2HPO_4 - 7.5 10^{-2} [g L^{-1}], KH_2PO_4 - 1.75 10^{-1} [g L^{-1}], NaCl - 2.5 10^{-2} [g L^{-1}], $ZnSO_4.7H_2O$ - 2.87 10^{-4} [g L^{-1}], H_3BO_3 - 6.10 10^{-5} [g L^{-1}], $MnCl_2.6H_2O$ - 1.69 10^{-4} [g L^{-1}], $CuSO_4.5H_2O$ - 2.5 10^{-6} [g L^{-1}], $(NH_4)_6Mo_7O_{24}.7H_2O$ - 1.24 10^{-6} [g L^{-1}] and $FeCl_3.6H_2O$ - 5 10^{-3} [g L^{-1}].

(4.3). - Experimental set-up

The experimental set-up was composed of a light source, a detector, two optical fibres connected to both devices and the other edge of the fibres into a plastic 3D-printed device (Fig. (2)). The latter is a semicircle of 0.1 [m] of diameter made of PA2200, which holds a space for a rectangular custom-made cuvette sized:

(0.028 x 0.028 x 0.0025) [m]. On the left-hand side of the cuvette, there is a hole designed for holding an optical fibre, which carries the light coming from the light source. On the right-hand side, there is a mobile holder designed for the detector's optical fibre, whose position can be adjusted throughout different equidistant marks placed on the semicircle's surface, from 0 to 180°, each 2.5°. The two holders are aligned to ensure proper measurement (Fig. (3)).

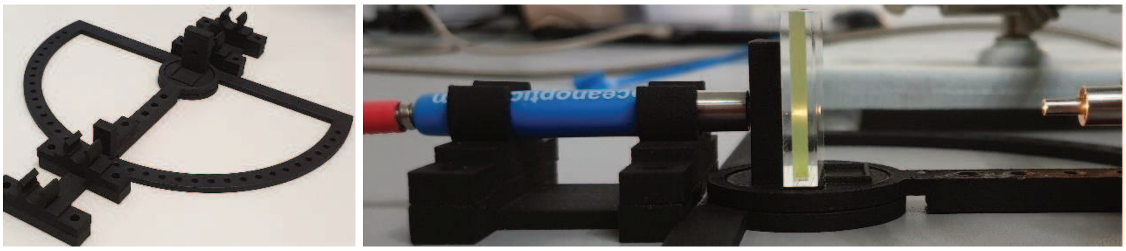

Figure (2): real pictures of the experimental set-up.

Every measurement was performed by filling the cuvette with 2 [mL] of culture and utilising the intensity-recording function of the *SpectraSuite* software (Ocean Optics). The spectral intensity of each sample $I_\lambda'^*\left(\underline{\hat{\Omega}}\right)$ (section 3.1) was then calculated as the average of three different spectra, each 2.5°, starting in the zero-position taken as the total alignment of both optical fibres and recording the spectral data from 0° to 90°, and further 0° to -90°. With every averaged sample's continuous spectrum, 31 intervals of $\lambda \pm 5.0$ [nm] were considered for each angle, corresponding to the spectral range $400 \le \lambda \le 700[nm]$. Further, each of these 31 dependencies was divided by $I_\lambda'\left(\mu = 1\right)$, the spectral intensity of the two fibres fully aligned (section 3.1-3.2), allowing us to obtain the normalised relative spectral intensity of the sample $I_\lambda^{R,*}\left(\mu\right)$, for each angle and each one of the 31 wavelength intervals. Finally, through the system's symmetry, it was calculated the average of the $I_\lambda^{R,*}\left(\mu\right)$ correspondent to each one of the positive and negative angles into one unique value of relative spectral intensity in the range from 0° to 90° for each PAR spectral interval under study. The latter bestowed the construction of a matrix of $I_\lambda^{R,*}\left(\mu\right)$, with many columns corresponding to the number of considered angles, and 31 rows related to each wavelength's interval.

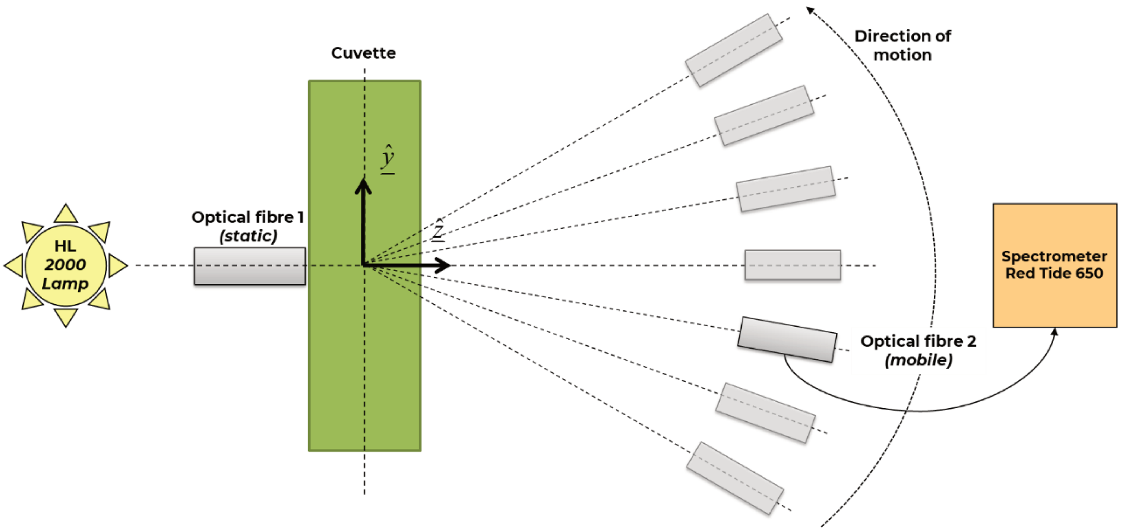

Figure (3): schematics of the 3D-printed device made of PA2200 with the correspondent reference system and the two optical fibres with the cuvette.

As for the system's calibration, the different continuous spectra were recorded only for the ensuing relative spectral intensities in every angle without the cuvette. Every matrix has then utilised in an optimisation routine (Fig. 1.2) to obtain the values of the samples' radiative properties. All the regressions were performed utilising the *fmincon + globalsearch* solver of MATLAB. The latter is a nonlinear least-squares solver that finds the coefficients necessary to minimise the difference between observed and input data. Every independent data series was adjusted utilising the trust-region-reflective algorithm, under a default step tolerance and function tolerance. Finally, the nonlinear 90% confidence intervals of any calculated parameter of interest were calculated through the *nlparci* solver of MATLAB. This last required the Jacobian regression matrix of each experimental data series obtained.

(5). - Theoretical approach and mathematical model

In this section, the mathematical basis that allows the calculation of the absorption coefficients (κ_λ), scattering coefficients (σ_λ) and the scattering phase function ($\beta_{\theta,\lambda}$) is described. The first step is to define the energy exchange between the detector (D) and the source of light (L), which grants access to calculate the total photon flux independently from the receiving surface, with or without another element among them (i.e., the system can be used with or without a cuvette with a phototropic suspension inside). Later, these definitions are further employed to define the directional probability functions linked to the experimental data and, last but not least, the simulation of the different tracks of the light and its interaction with the particles are explained as part of the subroutine, which works with the MC method. Making use of the equations defined in the first part, the latter brings the feedback loop to a stochastic algorithm (*globalsearch*), which reproduces the experiment, creating a scattering phase function whose coefficients are bounded to the experimental data with the t κ_λ and σ_λ previously calculated.

(5.1). – The radiant energy emission by the light source

The number of photons ΔE_λ^{LD} with a wavelength corresponding within the range $\lambda + \Delta\lambda$, which arrives at (D) coming from (L) (Fig. 4) during an interval of time Δt, may be known through utilising the radiant energy exchange equation [113]:

$$\Delta E_\lambda^{LD} = I_\lambda\left(\underline{\hat{\Omega}}\right)\Delta\lambda\Delta t\frac{A_L\left(\underline{\hat{n}}_L\cdot\underline{\hat{\Omega}}_{LD}\right)A_D\left(\underline{\hat{n}}_D\cdot\underline{\hat{\Omega}}_{DL}\right)}{r_{LD}^2} \tag{1}$$

In eq. (1), $I_\lambda\left(\underline{\hat{\Omega}}\right)$ is the emission source spectral Irradiadiance [μmol s^{-1} m^{-2} sr^{-1} nm^{-1}]; A_D y A_L the areas of (D) and (L) [m^2]; r_{LD} is the distance between (D) and (L) [m]; Δt is the duration of the energy exchange over time [s]; $\Delta\lambda$ is the wavelength range considered [nm]; $\underline{\hat{\Omega}}_{LD}$, and $\underline{\hat{\Omega}}_{DL}$ are directional unitary vectors corresponding to (D) and (L); and, $\underline{\hat{n}}_L$ and $\underline{\hat{n}}_D$ are the normal vectors of each flat surface.

Further rearrangement of eq. (1) allows the calculation of the spectral photon flux density $q_{\lambda,\alpha}^D$ [μmoles s^{-1} m^{-2} nm^{-1}], which arrives at (D) in terms of the angle α and, the respective distance between the origin and, (L) and (D), d_L and d_D [m] respectively (Fig. (4)):

$$q_{\lambda,\alpha}^{D} = \frac{\Delta E_{\lambda}^{LD}}{\Delta t\, \Delta\lambda A_D} = I_{\lambda}\left(\hat{\underline{\Omega}}\right) A_L \frac{\left(\hat{\underline{n}}_L \cdot \hat{\underline{\Omega}}_{LD}\right)\left(\hat{\underline{n}}_D \cdot \hat{\underline{\Omega}}_{DL}\right)}{r_{LD}^2} \tag{2.1}$$

$$r_{LD} = \left|\underline{r}_{LD}\right| \tag{2.2}$$

$$\underline{r}_{LD} = \underline{r}_D - \underline{r}_L \tag{2.3}$$

$$\underline{r}_L = -d_L \hat{\underline{z}} \tag{2.4}$$

$$\underline{r}_D = d_D \cos\alpha\, \hat{\underline{z}} + d_D \sin\alpha\, \hat{\underline{y}} \tag{2.5}$$

If we consider A_L sufficiently smaller in comparison with A_D (differential surface), it is possible to call $I'_{\lambda}\left(\hat{\underline{\Omega}}\right)$ to the number of photons that are emitted from (L) per unit of time, wavelength and solid angle [μmol s^{-1} nm^{-1} sr^{-1}], accounting for the light source surface. Then, $I'_{\lambda}\left(\hat{\underline{\Omega}}\right)$ may be assessed through equation (3):

$$I'_{\lambda}\left(\hat{\underline{\Omega}}\right) = I_{\lambda}\left(\hat{\underline{\Omega}}\right) A_L = \frac{q_{\lambda,\alpha}^{D}\, r_{LD}^2}{\left(\hat{\underline{n}}_L \cdot \hat{\underline{\Omega}}_{LD}\right)\left(\hat{\underline{n}}_D \cdot \hat{\underline{\Omega}}_{DL}\right)} \tag{3}$$

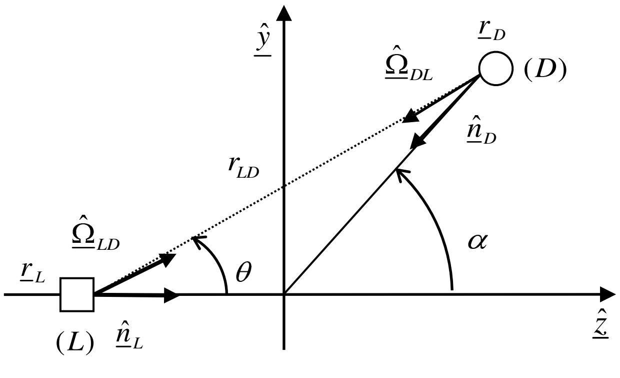

Figure (4): Schematics of the device. Geometrical definition of the system employed.

Additionally, for our purposes, with the definition of a solid angle:

$$\Delta\underline{\hat{\Omega}}_D = \frac{A_D\left(\underline{\hat{n}}_D\cdot\underline{\hat{\Omega}}_{DL}\right)}{r_{LD}^2} = \sin\theta\,\Delta\theta\Delta\phi = -\Delta cos\theta\Delta\phi \tag{4}$$

Eq. (1) can be rewritten in the following way to achieve a different shape of Eq. (2):

$$\Delta E^L_{\lambda,\underline{\hat{\Omega}}} = I_\lambda\left(\underline{\hat{\Omega}}\right) A_L \Delta t\Delta\lambda\left(\underline{\hat{n}}_L\cdot\underline{\hat{\Omega}}_{LD}\right)\frac{A_D\left(\underline{\hat{n}}_D\cdot\underline{\hat{\Omega}}_{DL}\right)}{r_{DL}^2} = -I'_\lambda\left(\underline{\hat{\Omega}}\right)\Delta t\Delta\lambda\left(\underline{\hat{n}}_L\cdot\underline{\hat{\Omega}}_{LD}\right)\Delta\underline{\hat{\Omega}}_D$$

$$Q^L_{\lambda,\underline{\hat{\Omega}}} = \frac{\Delta E^L_{\lambda,\underline{\hat{\Omega}}}}{\Delta t\,\Delta\lambda} = I'_\lambda\left(\underline{\hat{\Omega}}\right)\left(\underline{\hat{n}}_L\cdot\underline{\hat{\Omega}}\right)\Delta\underline{\hat{\Omega}} \tag{5}$$

The final shape of eq. (5) grants the calculation of the spectral photon flux $Q^L_{\lambda,\underline{\hat{\Omega}}}$ [μmoles s^{-1} m^{-2} nm^{-1}] with a direction corresponding to the range $\underline{\hat{\Omega}}$ and $\underline{\hat{\Omega}}+\Delta\underline{\hat{\Omega}}$. The replacement of $\Delta\underline{\hat{\Omega}}$ by $-\Delta\phi\,\Delta\cos\theta$, $\left(\underline{\hat{n}}_L\cdot\underline{\hat{\Omega}}\right)$ by $\cos\theta$ and computing the limit of eq.(5) under $\Delta\cos\theta\to 0$ and $\Delta\phi\to 0$; gives:

$$dQ^L_{\lambda,\underline{\hat{\Omega}}} = -I'_\lambda\left(\underline{\hat{\Omega}}\right)\cos\theta\,d\cos\theta\,d\phi = -I'_\lambda\left(\underline{\hat{\Omega}}\right)\mu\,d\mu\,d\phi \tag{6}$$

In Eq. (6), $\cos\theta$ was replaced by μ for the sake of simplifying. Finally, *the total spectral photon flux* across every ϕ and θ possible directions is:

$$Q_\lambda = -\int_0^{2\pi}\int_1^0 I'_\lambda\left(\underline{\hat{\Omega}}\right)\mu' d\mu' d\phi' = \int_0^{2\pi} d\phi' \int_1^0 I'_\lambda\left(\mu'\right)\mu' d\mu' = 2\pi\int_0^1 I'_\lambda\left(\mu'\right)\mu' d\mu' \tag{7}$$

(5.2). – The photon emission probability in the directions $\underline{\hat{\Omega}}(\theta,\phi)$

The differential probability that a photon during the emission was emitted in one direction μ is:

$$dP(\mu)=\frac{dP(\mu)}{d\mu}d\mu=\xi(\mu)\,d\mu \tag{8}$$

In eq. (8), $\xi(\mu)$ is the distribution function of photon emission probabilities in different directions. Then, the cumulative probability that said photon has been emitted in a direction between 1 and μ can be calculated, and, at the same time, this probability may be thought of as the fraction of emitted photon flux within the range $1<\mu'<\mu$:

$$P(\mu)=\int_1^{\mu}\xi(\mu')\,d\mu'=\frac{\int_0^{2\pi}\int_1^{\mu}dQ^{L}_{\lambda,\underline{\hat{\Omega}}}}{\int_0^{2\pi}\int_1^{0}dQ^{L}_{\lambda,\underline{\hat{\Omega}}}}=\frac{\int_1^{\mu}I'_{\lambda}(\mu')\,\mu'd\mu'}{\int_1^{0}I'_{\lambda}(\mu')\,\mu'd\mu'} \tag{9}$$

Moreover, to evaluate if the emitted light has the same directional distribution over the wavelength, it is useful to calculate *the relative spectral intensity* $I^{R}_{\lambda}\left(\underline{\hat{\Omega}}\right)$, relative to the relation among the different $I'_{\lambda}\left(\underline{\hat{\Omega}}\right)$, divided by $I'_{\lambda}(\mu=1)$ (i. e. $I'_{\lambda}(\theta=0)$). Inasmuch as the latter is valid, eq. (9) can be reshaped to:

$$P(\mu)=\frac{\int_1^{\mu}I^{R}_{\lambda}(\mu')\mu'd\mu'}{\int_1^{0}I^{R}_{\lambda}(\mu')\mu'd\mu'} \tag{10}$$

Eq. (10) can, whence, be solved by numerical integration from the $I^{R}_{\lambda}(\mu)$ values obtained experimentally. As for $\xi(\mu)$, the probabilities can be calculated utilising eq. (8) as the derivative of $P(\mu)$ concerning μ.

As for the ϕ component angles, every direction is possible to be selected; thus:

$$\xi(\phi)=\frac{1}{2\pi}\ \text{and subsequently,}\ P(\phi)=\frac{1}{2\pi}\int_0^{\phi}d\phi'=\frac{\phi}{2\pi} \tag{11}$$

(5.3). – The interaction of the light with the phototrophic suspension

In this study, a stochastic algorithm based on the Monte Carlo method is devised for the simulation of the REF in the algal suspensions, the methodology developed and described in Chapter 3 of the present manuscript. The simulated experiment starts generating a total quantity of photons $n_p\left(\underline{r},\underline{\hat{\Omega}},\lambda\right)$ coming from the light source. These moves through the PBR walls and phototrophic suspension like a nonuniform gas at light speed, in varying directions. For each value in the spectral range: $400<\lambda+10<700[nm]$, the fate of the algorithm is to produce 31 dependencies of *the relative spectral intensity through the suspension*, $I_{\lambda}^{R,*}(\mu)$, reproducing the experiment for the 31 $n_p\left(\underline{r},\underline{\hat{\Omega}},\lambda\right)$ photon densities composing each wavelength under study. Each one of the photons starts with the position $\underline{r}_L$ (Fig. (4)) and with an initial direction $\underline{\hat{\Omega}}_0\left(\mu_0,\phi_0\right)$. The latter is provided through the generation of two random numbers δ_μ and δ_φ, between 0 and 1, and the use of the known $P(\mu)$ and $P(\phi)$ functions (eq. 10-11). Then, the reflectivity on the interface between air and the culture medium $\rho_{1,2}$ is computed according to Fresnel's law.

Once each photon is inside the phototrophic continuous suspension, their respective trajectories are described on a probabilistic base. These pathways might be deflected by scattering effects due to elastic interactions between photons and suspended cells, or even reach a sudden end due to absorption. The algorithm requires the radiative properties (κ_λ, σ_λ, $\beta_{\theta,\lambda}$) to simulate these events. In this approach, these were provided by the global search (GS) algorithm employed (Fig. (5)). **Therefore, κ_λ and σ_λ are calculated with the matrix of spectral intensity, and a set of parameters belonging to $\beta_{\theta,\lambda}$ are created to reproduce each $I_{\lambda}^{R,*}(\mu)$ under analysis**, respecting the following expressions:

$$\left(\kappa_\lambda+\sigma_\lambda\right)=\frac{-\log\left(\dfrac{I_{\lambda}^{R,*}\left(\mu=1\right)}{I_{\lambda}^{R}\left(\mu=1\right)}\right)}{d_C} \tag{12}$$

$$\kappa_{\lambda} = \frac{-\log\left(\dfrac{\int_{1}^{0} I_{\lambda}^{R,*}(\mu')\mu' d\mu'}{\int_{1}^{0} I_{\lambda}^{R}(\mu')\mu' d\mu'}\right)}{d_C} \tag{13}$$

In eq. (12), the term $\frac{I_{\lambda}^{R,*}(\mu=1)}{I_{\lambda}^{R}(\mu=1)}$ is the division among the value of the relative spectral intensity with, and without cuvette in the system, accounting for $\theta = 0$. d_C is the narrow optical path of the cuvette [m]. The term $\frac{\int_{1}^{0} I_{\lambda}^{R,*}(\mu')\mu' d\mu'}{\int_{1}^{0} I_{\lambda}^{R}(\mu')\mu' d\mu'}$ in eq. (13) represents the division between the total emitted energy from the light source with, and without the cuvette, respectively.

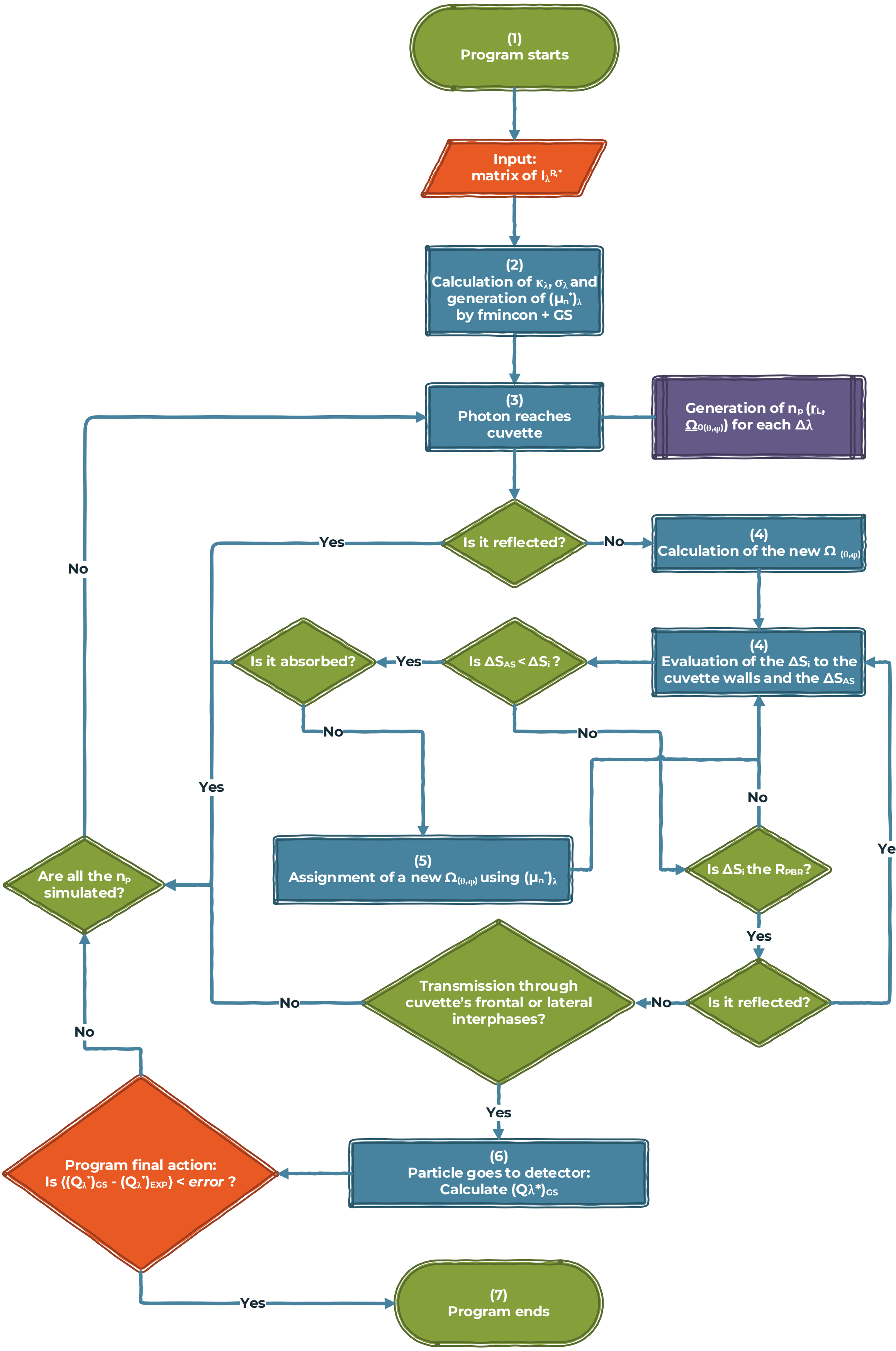

Figure (5): Computational flowchart, including the decision nodes in the stochastic algorithm developed for the Monte Carlo simulation of the REF inside the cuvette.

Regarding the scattering phase function, under this model $\beta_{\theta,\lambda}$ is meant as the differential probability function (i. e. same in shape as eq. (8)), which allows the assessment of the most probable azimuthal angles that the photons might take after experiencing the event of scattering, following the next procedure:

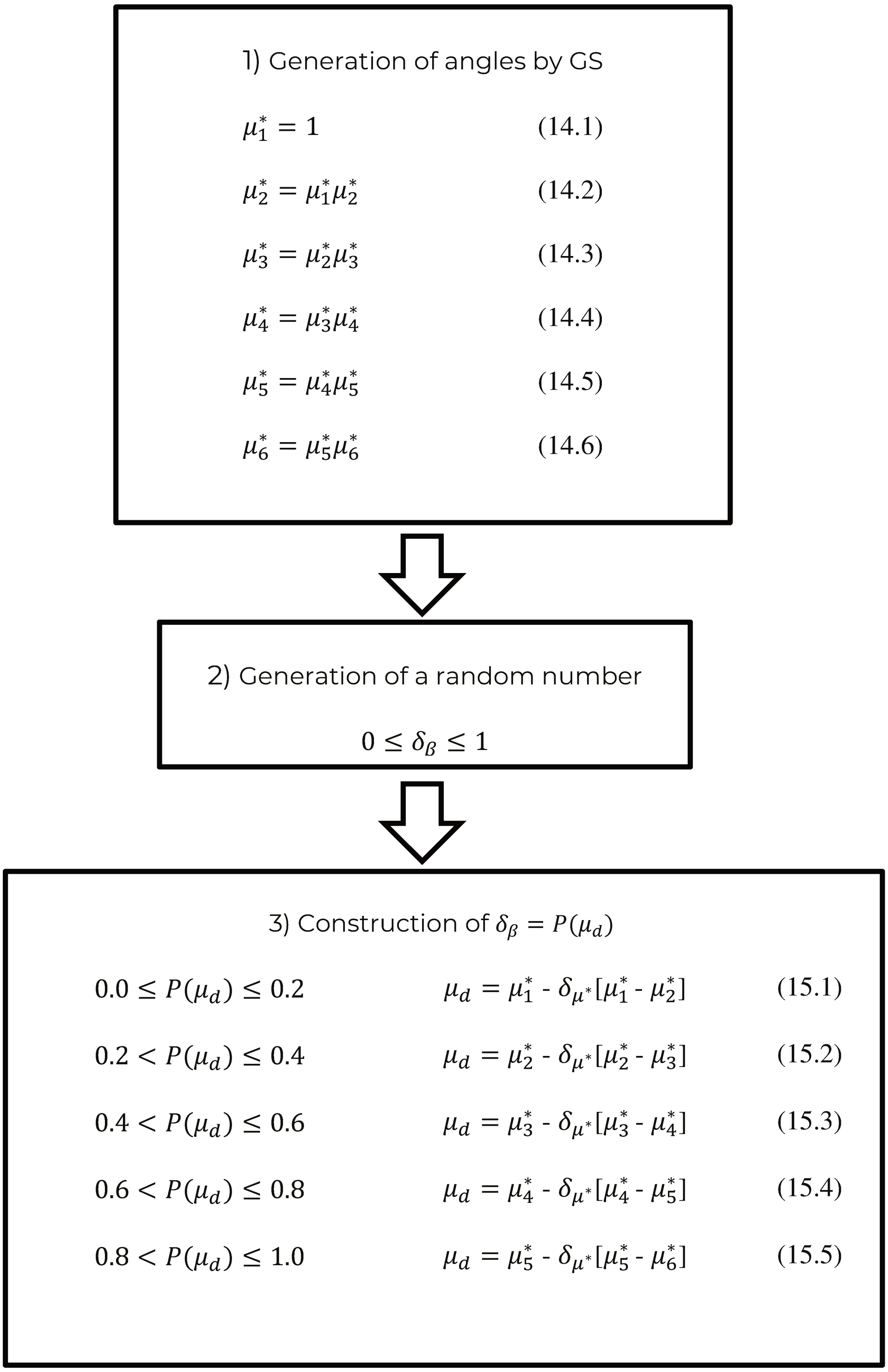

1) Generation of angles by GS

$$\mu_1^* = 1 \tag{14.1}$$

$$\mu_2^* = \mu_1^*\mu_2^* \tag{14.2}$$

$$\mu_3^* = \mu_2^*\mu_3^* \tag{14.3}$$

$$\mu_4^* = \mu_3^*\mu_4^* \tag{14.4}$$

$$\mu_5^* = \mu_4^*\mu_5^* \tag{14.5}$$

$$\mu_6^* = \mu_5^*\mu_6^* \tag{14.6}$$

2) Generation of a random number

$$0 \leq \delta_\beta \leq 1$$

3) Construction of $\delta_\beta = P(\mu_d)$

$0.0 \leq P(\mu_d) \leq 0.2$ $$\mu_d = \mu_1^* - \delta_{\mu^*}[\mu_1^* - \mu_2^*] \tag{15.1}$$

$0.2 < P(\mu_d) \leq 0.4$ $$\mu_d = \mu_2^* - \delta_{\mu^*}[\mu_2^* - \mu_3^*] \tag{15.2}$$

$0.4 < P(\mu_d) \leq 0.6$ $$\mu_d = \mu_3^* - \delta_{\mu^*}[\mu_3^* - \mu_4^*] \tag{15.3}$$

$0.6 < P(\mu_d) \leq 0.8$ $$\mu_d = \mu_4^* - \delta_{\mu^*}[\mu_4^* - \mu_5^*] \tag{15.4}$$

$0.8 < P(\mu_d) \leq 1.0$ $$\mu_d = \mu_5^* - \delta_{\mu^*}[\mu_5^* - \mu_6^*] \tag{15.5}$$

In eq. (14.1-14.6), the $\left(\mu_n^*\right)_\lambda$ coefficients are azimuthal angles generated by the GS in such a way that from $\left(\mu_1^*\right)_\lambda$ to $\left(\mu_6^*\right)_\lambda$, the probability of occurrence of each generated angle is decreasing or, in other words, the most favoured directions to be selected are the ones in the surroundings of $\left(\mu_d\right)_\lambda = 1$ (i. e. $\theta = 0$). A function $P\left(\mu_d\right)$, which is bounded to fulfil this feature, represents a $\beta_{\theta,\lambda}$ function in a forward scattering scenario, which is appropriate for the analysis of the light interaction with particles holding sizes similar to the magnitude of the incident wavelength over them. The new $\underline{\hat{\Omega}}'\left(\mu_d,\phi_d\right)$ direction is provided then by eq. (15.1-15.6) making use of a random number δ_{μ^*} and, a polar angle provided by a dependence similar to eq. (11).

After a succession of scattering events, the particles which were not removed from the light field have the chance to pass through the physical boundaries of the cuvette, and if they are not reflected inside again, they continue their way to reach the detector. Eq. (3) is used then to calculate the ensuing $I_\lambda'^*\left(\mu\right)$, and after using $I_\lambda'\left(\mu=1\right)$, the corresponding $I_\lambda^{R,*}$. Finally, making use of eq. (9) *the total photon flux through the suspension* $\left(Q_\lambda^*\right)_{GS}$ is calculated by the subroutine that works employing the MC method. The latter is given to the GS, thereby allowing the comparison with the experimental total photon flux previously measured $\left(Q_\lambda^*\right)_{EXP}$ and the estimation of the absolute error to start again with the next evolution of the coefficients from eq. (15.1-15.6). The best fit of the GS is, whence, the result of eq. (14.1-14.6), which allows the best estimation of $\left(Q_\lambda^*\right)_{EXP}$, fulfilling the restriction imposed by eq. (12) and (13).

(6). - Results and discussion

The optimisation and control of light transfer in PBRs on which an autotrophic process is carried out are bound to the close relationship between the radiation source's emission characteristics, the geometry of the reactor as well as the optical properties of the suspension that resides within it. The combination of these three components in the radiative transfer equation (RTE) allows access to knowledge of the light availability inside the unit, which accounts for the physiological state of the culture at a given time. Since photo-adaptative biological processes and the physical chemistry of the system alters during the progression of a run, it is necessary to assess the changes in these radiative properties throughout time. A model of interaction linking light and the culture must be applied to do so, and due to the system's complexity, there is up to date a lack of agreement between the different empirical approaches, and still, there are no studies where both the inner structures and the shape of the cell are included to the model when describing algal cells with complex shapes.

Here, an approach to measure the optical properties of microalgae suspensions is presented based on the simulation of the radiation employing the Monte Carlo method. The latter's advantage is that it allows handling complex reflexive systems and the optical phenomena occurring within them without simplifying them to solve complicated mathematical approaches. Under this perspective, the culture is a continuum, and the cells are centres of absorption and scattering with associated probabilities accounting for these events. Below the assumption that detectable changes in light passing through the culture are faster in comparison with the biological processes involved in the progressive changes of the OPs, a simple methodology has been proposed, consisting in illuminating a *C. zofingiensis* suspension with a characterised polychromatic radiation source and assessing how the directions were modified, and the amount of energy carried by the light beams after crossing the suspension. Subsequently, through an optimisation program, the experimental culture data will be used to determine the spectral absorption and scattering coefficients of photons, and the phase function of the suspension. Collectively, the results presented here are independent of pigments' concentration and biomass' concentration, suggesting that this methodology allows more intuitive ways of calculating the radiative characteristics of phototrophic microorganisms in the complex context of the evolution through time of the radiant energy field inside a photobioreactor.

(6.1). – Simulation of the source of light

In the present work, a system composed of a polychromatic source of light, two optical fibres meant for carrying the source's light and collecting it, respectively, and a spectrometer was placed upon a 3D-printed device made from PA2200 to quantify the radiative properties of a suspension of a phototrophic microorganism. The light modelling of a similar system, on which the photons move at lightspeed like a gaseous fluid, and the corresponding resolution of the RTE were published in previous reports [17]. The application of the Monte Carlo method over this system to solve an energy balance first required the knowledge of the light source spectral distribution and the directional distribution of the emitted wavelengths. The latter has been evaluated here utilising the average relative spectral intensity $\bar{I}_R\left(\underline{\hat{\Omega}}\right)$ values, obtained as the average of the ensuing $I_\lambda^R\left(\underline{\hat{\Omega}}\right)$ quantities in the spectral range $400 < \lambda + 10 < 700[nm]$. Fig. (6) shows the $I'_\lambda\left(\underline{\hat{\Omega}}\right)$ registered values inherent to the HL-2000 lamp (eq. 3), and Fig. (7) display the $\bar{I}_R\left(\underline{\hat{\Omega}}\right)$ corresponding to 11 angles in the range: $0.9 < \mu < 1$. While the light source's spectral emission is not homogeneous, the wavelengths' directions on the PAR spectral range are. Likewise, since the directional distribution must fulfil with eq. (9-10), the following expression is valid for the range $0 < \mu < 1$ and $0 < \bar{I}_R\left(\underline{\hat{\Omega}}\right) < 1$ has been employed:

$$\bar{I}_R\left(\underline{\hat{\Omega}}\right) = \frac{a_1 - a_2}{1 + e^{\frac{\mu - \mu_0}{\delta}}} + a_2 \tag{16}$$

In eq. (16), a_1, a_2, μ_0 y δ are four regressed parameters, with values: 0.00 ± 2.30 10^{-2}, 1.08 ± 2.49 10^{-2}, 9.80 ± 2.25 10^{-2}, 8.02 10^{-3} ± 1.84 10^{-4}. The latter allowed the simulation of the light source emission on the printed device (Fig. (7)) and the reproduction of the $\bar{I}_R^*\left(\underline{\hat{\Omega}}\right)$ values obtained with, firstly, the empty cuvette present and further with the cuvette and de-ionised water inside. Finally, the application of eq. (7) over $\bar{I}_R\left(\hat{\underline{\Omega}}\right)$, and $\bar{I}_R^*\left(\hat{\underline{\Omega}}\right)$ quantities facilitated the estimation of Q_{PAR}, and Q_{PAR}^* correspondingly (Appendix – Table 2). In the case of Figure (6), the acquisition of experimental data was performed through the measurement of ten spectra. The dots in this figure are the average values of these spectra, and the error bars are the standard deviation of these magnitudes with a 90% confidence interval. For the case of Figure (7), the procedure has been the same, except for the data series, since only three series of data have been acquired, and the values presented are the average relative spectral intensities (The (○,□,◊) blue dots by triplicate), with their corresponding standard deviations of the mean of these experimental values (error bars with 90% confidence interval).

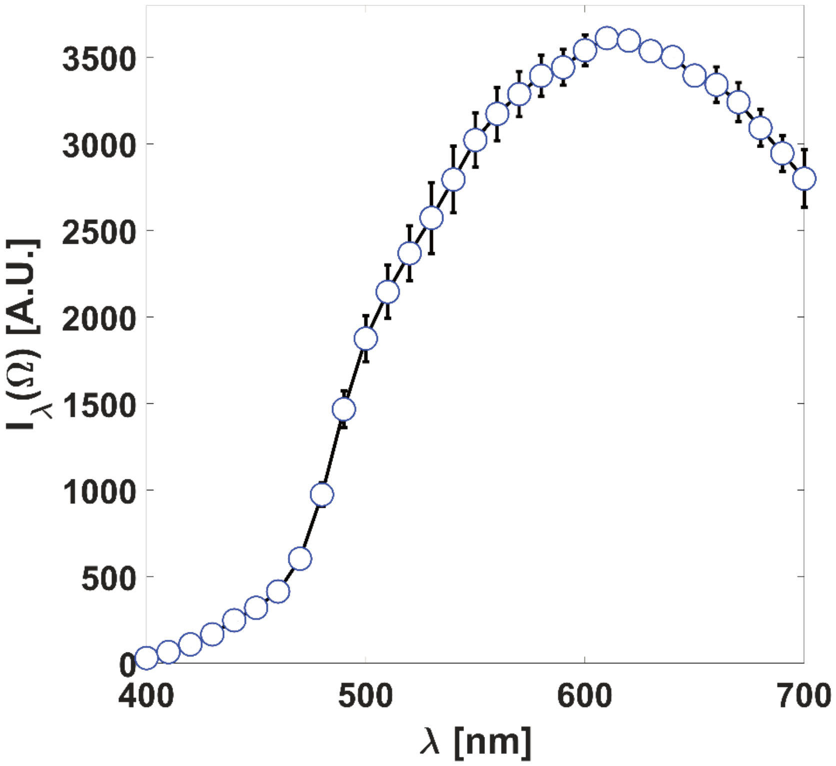

Figure (6): Light source continuous spectra of the $I'_\lambda\left(\hat{\underline{\Omega}}\right)$ [A.U. – Arbitrary Units/Counts] of the HL-2000 Halogen lamp obtained in the spectral range $400 < \lambda + 10 < 700[nm]$. The acquisition of experimental data was performed through the measurement of ten spectra. The (○) blue dots are the ensuing spectral intensity values obtained for the PAR spectral region with the spectrometer RedTide 650. The black error bars are the standard deviation of these average spectra (blue dots) with a 90% confidence interval.

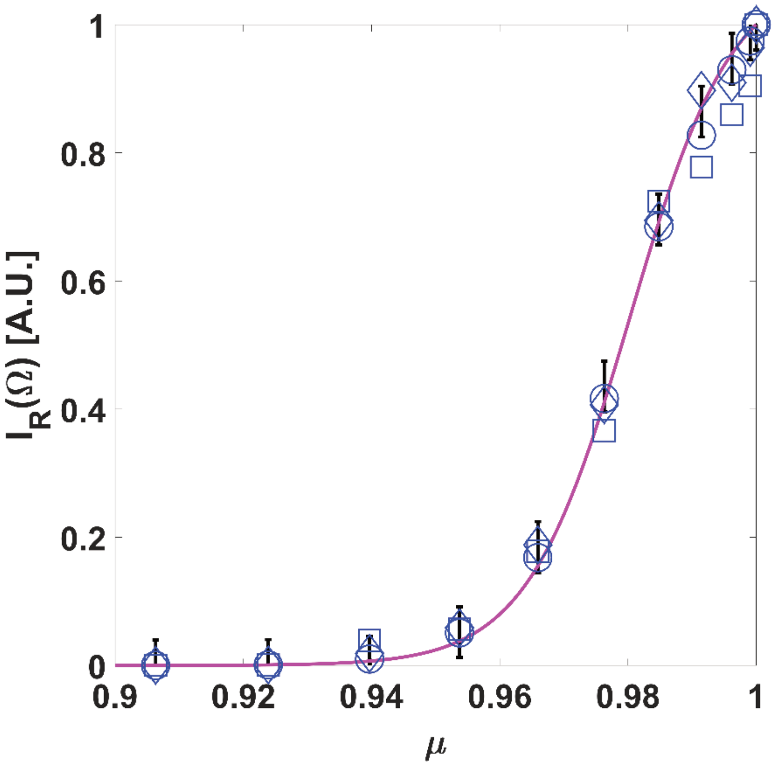

Figure (7): Corresponding average relative intensity and its directional distribution concerning the azimuthal angles. The (○,□,◊) blue dots are the triplicate of the same experiment performed in the light source simulation. The magenta line with black error bars is the continuous distribution regressed, making use of eq. (16) with a 90% confidence interval.

The total light source flux is required later for the application of eq. (13), taking the value of 2.91 10^{-4} ± 2.78 10^{-5} [μmol s^{-1}]. The reproducible Q^*_{PAR} values of the experiments with the empty cuvette and with pure water were 2.82 10^{-4} ± 2.64 10^{-5} [μmol s^{-1}] and 2.53 10^{-4} ± 2.56 10^{-5} [μmol s^{-1}], 3% and 13% lower than Q_{PAR} on an individual basis.

(6.2). – Absorption and scattering coefficients of a suspension of a phototrophic microorganism.

C. zofingiensis is a member of the *Chlorophyta* microalgae family. In recent years this strain has been used as a model for the study of the carotenoids' biosynthetic pathway since it is possible to isolate from its interior either primary pigments like chlorophyll, α- and β-carotene, subsequently, lutein and violaxanthin under standard growth conditions, and secondary pigments as astaxanthin and canthaxanthin under stress conditions [10], [141]. As for its potential as an industrially relevant alga, *C. zofingiensis* can assimilate different carbon sources, and it might produce proper astaxanthin and lutein levels with a robust, specific growth rate, either in an autotrophic cultivation mode or in the dark [142]. Under nutrient-limiting conditions, it was found that this strain also produces high lipid content, pointed as a promising feedstock for biodiesel production [142]. Therefore, there is a severe concern about the development of tools for the scaling up of this microorganism [10].

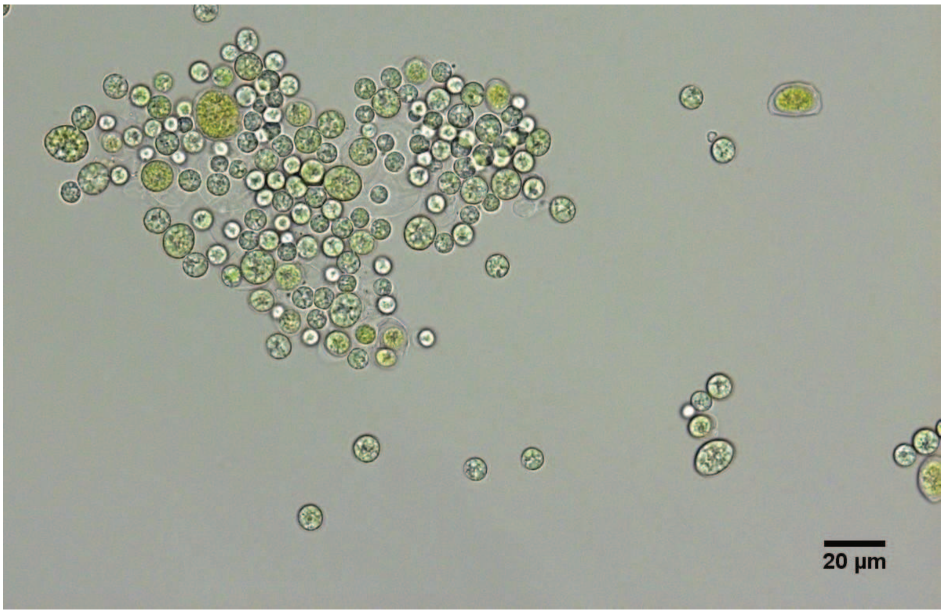

Figure (8): a standard culture of *C. zofingiensis* cells.

In *C. zofingiensis,* depending on the culture conditions, it was found that the size of the cells can vary from 4 to 9 [µm] (Appendix – Fig.(11)), whether the lighting conditions change in quality and quantity or there are organic carbon sources present in the liquid [143]. The quantity and size of chloroplasts can also change in response to the environment in this strain, exhibiting larger photosynthetic starch storage capacity and changes in the carbon concentrating mechanisms [144]. Likewise, lipid accumulation may take place by the overexpression of acetyl-CoA carboxylase and the degradation of chlorophyll *a* and *b* [145]. Concomitantly, astaxanthin lipid bodies are synthesised outside chloroplasts, designed for photoprotection, as well as phenolic compounds, which increase the overall antioxidant activity, among other components [146]. Although there are no studies so far related to the influence of the light stratification over *C. zofingiensis*, as this phenomenon appears with the growth in biomass quantity and the latter modify the REF, changes in the architecture and composition of photosystems might happen like in other members of the Chlorophyta family [20].

Here, it is sought to investigate the radiative properties of a *C. zofingiensis* phototrophic culture based on an energy balance. The latter allows the construction of a continuum medium of radiation properties in the culture volume in a single period, although unevenly distributed in space and wavelength. Then, the OPs, which are related to the REF at this moment, fated to every chemical or biological alteration in the system, like the ones mentioned in previous paragraphs, were calculated under the restrictions imposed by eq. (12, 13 and 14-1,6). In Fig. (4-a,d), eight sets of κ_λ and σ_λ coefficients in the PAR spectral range are presented. The trend in the coefficients' variations in the wavelength region from 400 to 700 [nm] has shown expectable results in comparison with other members of Chlorophyta [136].

As for absorption, there are larger values at those wavelengths where the chlorophyll pigments are active to light. Free Chl *a* absorb around 435 and 676 [nm] while free Chl *b* presents maxima peaks around 475 and 650 [nm] [120]. In Fig. (9-a) and (9-c), these peaks are smoother and present shifts due mainly to two effects: firstly, Chl molecules are supported by other proteins in the core antennas of the light-harvesting complexes in chloroplasts, which creates an overlapping in the spectrum of these free substances; secondly, as it was mentioned before, it is natural in *C. zofingiensis* the synthesis of carotenoids and xanthophylls [147]. Lutein and astaxanthin, as representative of all the different α- and β-carotene intermediates, have absorption maxima around 445 and 474 [nm], and 480 [nm] on an individual basis [120], [148]. The latter contributes as well to the spectral peaks overlapping alongside the PAR spectral range, which also explains the other variations present in the wavelength range from 550 to 650 [nm].

Regarding the fate of the non-absorbed light, when absorption occurs in the LHC and the amplitude of an electromagnetic field changes, its phase will change accordingly, producing inelastic scattering. From Fig. (9-b) and (9-d), it can be observed the habitual trending in light dispersion's behaviour for a phototrophic suspension. Light scattering tends to be higher than microalgae absorption efficiency [149], [150]. Even though the σ_λ coefficients depend on wavelength as the κ_λ coefficients, this wavelength selectivity is not as sharp for the microalgae scattering spectrum. The latter may be attributed to the dominant influence of the non-absorbing cell components over the σ_λ, although pigments exert an effect through fluorescence and selective absorption [5]. The ensuing σ_λ to the spectral range 500-560 [nm] are the highest values (Fig. 9-c and 9-d), corresponding to the lowest κ_λ in Fig. (9-a) and (9-c), except for κ_{500} and κ_{510} which reckons for carotenoids nature in each sample. As for the two dips present in the blue and red areas of the wavelengths' range analysed, these are analogous in behaviour (but reciprocal) to the ensuing chlorophylls' κ_λ, in every biomass sample studied.

Last but not least, the sum of scattering and absorption from all the cell parts and its interaction with the REF in the continuous medium, determines the total optical response of the cell, in the form of attenuation coefficients. In many works, the molecular medium of microalgae cells is adequately characterised as homogeneous, having a complex refractive index [130], [151], [152]. However, if the heterogeneous nature of the cells is considered on the organelle level, the attenuation coefficients might not be reproducible, which is the case in the listed experiments from Figures (9-a,d). Here a batch culture, with non-nutrient depletion and sufficient light amount, has displayed an alteration in the OPs over cultivation time. Even when towards the final moments of the cultivation, biomass concentration started to decrease and, κ_λ and σ_λ decreased as well, it was not possible to find a linear relationship between these OPs and the biomass quantity. However, in the case of the σ_λ, a lack of linear dependence on the biomass concentration may be explained due to a lack of photo-acclimation of the cells, which cannot be seen in Fig. (10) on which a potential linear relationship in β_{PAR} was found. This last highlights the necessity of measuring the radiative properties rapidly and accessibly to calculate the varying light availability inside a PBR correctly.

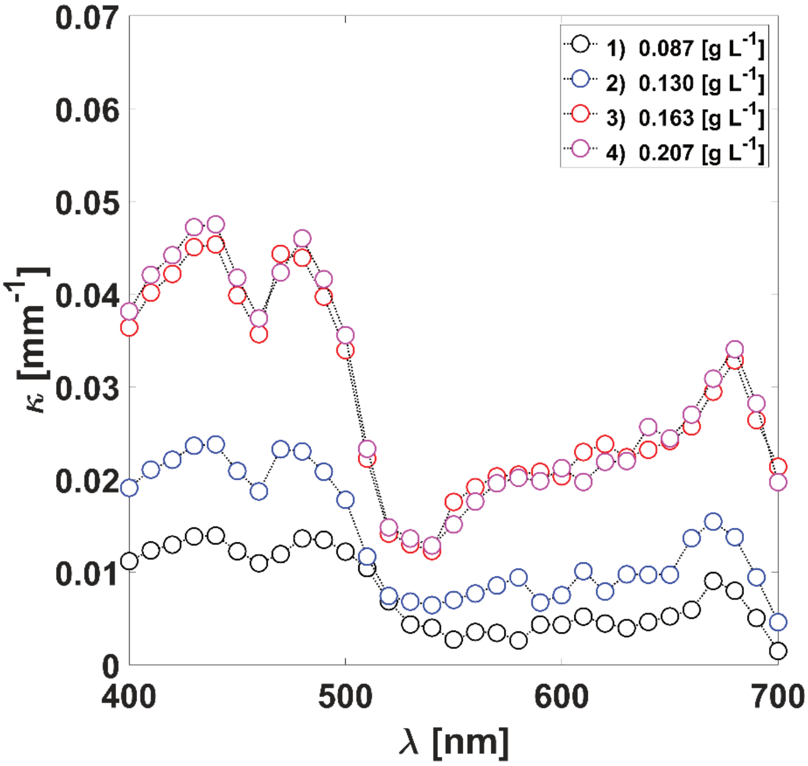
0.07
0.06
0.05
0.04
0.03
0.02
0.01
0
400
500
600
700
κ [mm^{-1}]
λ [nm]
1) 0.087 [g L^{-1}]
2) 0.130 [g L^{-1}]
3) 0.163 [g L^{-1}]
4) 0.207 [g L^{-1}]

(a)

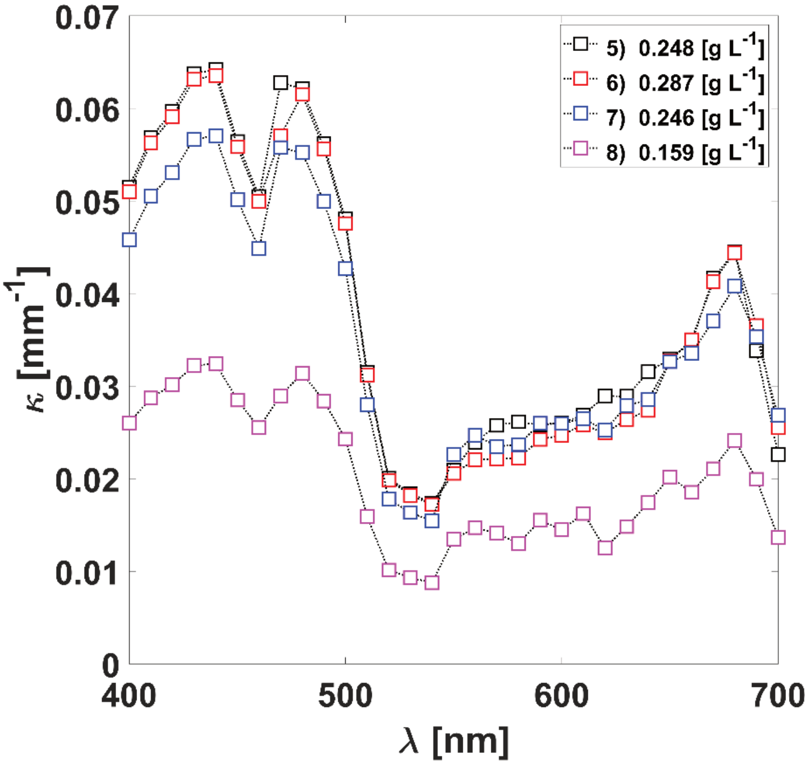
0.07
0.06
0.05
0.04
0.03
0.02
0.01
0
400
500
600
700
κ [mm^{-1}]
λ [nm]
5) 0.248 [g L^{-1}]
6) 0.287 [g L^{-1}]
7) 0.246 [g L^{-1}]
8) 0.159 [g L^{-1}]

(b)

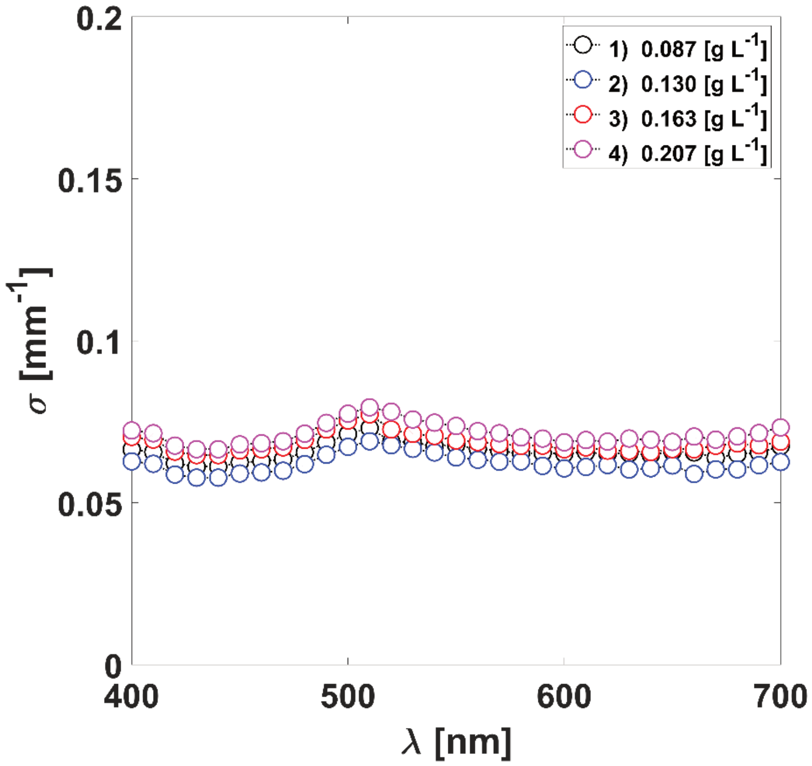
0.2
0.15
0.1
0.05
0
σ [mm^{-1}]
400
500
600
700
λ [nm]
1) 0.087 [g L^{-1}]
2) 0.130 [g L^{-1}]
3) 0.163 [g L^{-1}]
4) 0.207 [g L^{-1}]

(c)

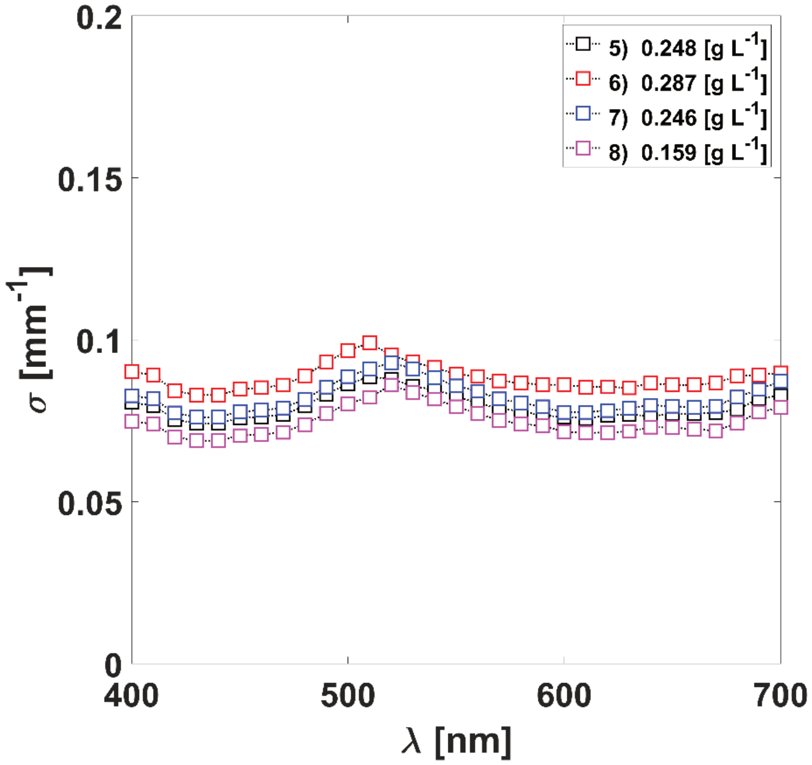
0.2
0.15
0.1
0.05
0
σ [mm^{-1}]
400
500
600
700
λ [nm]
5) 0.248 [g L^{-1}]
6) 0.287 [g L^{-1}]
7) 0.246 [g L^{-1}]
8) 0.159 [g L^{-1}]

(d)

Figure (9-a,d): The absorption and scattering coefficients of eight samples. The (○) black, red, blue, and magenta dots are correspondent with the κ_λ of samples 1-4 (Fig. (9-a)) and σ_λ respectively (fig. (9-b)). The (▫) black, red, blue, and magenta dots are correspondent with the κ_λ of samples 5-8 (fig. (9-c)) and σ_λ respectively (fig. (9-d)).

(6.3). – The scattering phase function.

The three size regimes assert the primary electromagnetic interaction mechanisms: (1) If particles are smaller than the wavelength of light, on which the interaction is determined chiefly by scattering and absorption, and the impacting beams' angular distribution is firmly dependent on polarization. (2) when the particle size almost reaches the wavelengths' size scale, on which the scattering pattern becomes forward peaking. (3) if the particles' diameter is more massive than the wavelength, on which the interaction is explained through classical-geometrical approaches. The algae' scattering pattern is firmly forward, as many of the more abundant organelles and the cell itself catalogues in between (2) and (3). Roughly 90% of the dispersed light is generally contained within a solid angle of 20 degrees around the optical axis in the forward direction [133], [150].

At the time of calculating the microalgae's OPs, the most general assumptions treat the microorganisms as well mixed and randomly oriented, on which the cells are presented as symmetric spheroids, and the phenomenon of single scattering prevails due to the consideration of low concentration suspension. Further, the $\beta_{\theta,\lambda}$ is taken as a function dependent on θ angles and, finally, as a first-order estimation, $\beta_{\theta,\lambda}$ is assumed to be constant over the PAR spectral region [135], [153]. In this section, it was used a simple physical model of the REF interaction with biological suspensions, relying on the modelling of algae as a continuum where the cells have been replaced with centres of absorption and scattering, randomly distributed throughout the suspension. Later on, a Monte Carlo algorithm can be developed to reproduce the elementary steps of photons flying in the suspension and eventually being removed of it by absorption and scattering events. The likelihood of the latter is linked to the cells' OPs. In our approach, these are provided by *fmincon* (MATLAB), making use of eq. (12, 13, 14-1,6 and 15-1,6).

Based on solid grounds, our proposal here was to reproduce the total light flux and the directional distribution of the beams after travelling throughout a microalgae suspension, constructing 31 independent distribution functions in the wavelength's region $400 < \lambda + 10 < 700[nm]$, giving to the MC subroutine the possible forward angles to be selected under the restrictions imposed by eq. (12) and (13). In the table (1), the average in the PAR spectral range of the μ_n^* angles is presented. It can be seen that to simulate the $\left(Q_\lambda^*\right)_{EXP}$ values in each sample, up to 80% of the angles took values of $0 < \theta < 6$ degrees with respect to the optical axis. In a further individual basis, between 80 and 60% of the angles hold values of $9 < \theta < 13$ degrees. The chances for azimuthal angles ranged $15 < \theta < 24$ is 60 to 40%, while the probabilities of holding $\theta \le 40$ degrees were 40 to 20%. Finally, a likelihood of less than 20% was found for azimuthal angles ranging $43 < \theta < 55$ degrees.

	X [g L^{-1}]	**0.087**	**0.130**	**0.163**	**0.207**	**0.248**	**0.287**	**0.246**	**0.159**
$\mathbf{P(\mu_d) \ge 0.8}$	$\left(\overline{\mu}_2^*\right)_{PAR}$	0.9956	0.9946	0.9950	0.9955	0.9935	0.9932	0.9944	0.9941
$\mathbf{0.8 > P(\mu_d) \ge 0.6}$	$\left(\overline{\mu}_3^*\right)_{PAR}$	0.9874	0.9800	0.9818	0.9842	0.9723	0.9861	0.9795	0.9848
$\mathbf{0.6 > P(\mu_d) \ge 0.4}$	$\left(\overline{\mu}_4^*\right)_{PAR}$	0.9665	0.9081	0.9451	0.9529	0.9241	0.9685	0.9353	0.9509
$\mathbf{0.4 > P(\mu_d) \ge 0.2}$	$\left(\overline{\mu}_5^*\right)_{PAR}$	0.7939	0.7696	0.7677	0.8607	0.7918	0.8714	0.7599	0.9247
$\mathbf{0.2 > P(\mu_d)}$	$\left(\overline{\mu}_6^*\right)_{PAR}$	0.6786	0.7300	0.6891	0.5607	0.6145	0.6851	0.6602	0.6732

Table (1): The average value under the PAR spectral range of the coefficients generated by the algorithm employed, corresponding to each sample studied.

Rather than using $\left(\mu_n^*\right)_\lambda$, the values of $\left(\overline{\mu}_n^*\right)_{PAR}$ coefficients have been used here mainly for two reasons. In the first place, the variation coefficient of the average of the most probable azimuthal angles is less than 0,3%, while in contrast, a 30% of variation can be found in the less possible angles produced. A priori, the latter might lead to thinking that the 31 sets of $\left(\mu_n^*\right)_\lambda$ are wavelength-dependent. However, since the cumulative distribution functions $P\left(\mu_d\right)$ were constructed in such a way that the coefficients in the surroundings of $\left(\mu_d\right)_\lambda = 1$ hold high chances of being produced, all of the errors associated with the measuring process weight on the less favoured angles to be produced. Therefore, it is expectable to find huge variations among the different $\left(\mu_n^*\right)_\lambda$ values. In closing, rather than elucidate the specific influence of a single element, the nature of these variations is related generally to all of the complex non-absorbing components. So far, the understanding of the individual organelle-light interaction is not sufficiently wide to present a $\beta_{\theta,\lambda}$ function more than partially biased by wavelength [137], like the experiments we have shown in this research.

(7). - Conclusions

In a purely phototrophic culture, microalgae are dependent on absorbing light energy to meet their demand for cellular functions and growth. This growth is dependent on the light availability inside the reactor, and both quantities are linked through a growth kinetic expression. Addressing the optical properties of a suspension is one of the significant concerns in calculating the intrinsic parameters within these dynamics. Cells modify the light field, and light modifies the cells. Light exposure and nutrient-level alterations trigger a set of physiological processes in microalgae on both transcriptional and metabolic levels. These processes affect the OPs of the cells. Therefore, radiation characteristics and the size of the cells are not constant but continually changing as a response to variations in light intensity and colour, among other factors.

In this work, it has been presented an approach to measure the optical properties of microalgae suspensions. The use of a 3D-printed device in combination with a Monte Carlo approach grant access to how motion and energy carried by photons change throughout culture samples. Utilising an optimisation algorithm/program constrained properly to simulate the light emission in the forward direction, reproducible sets of absorption and scattering coefficients have been calculated, as well as the scattering phase function of the suspension. Further use of the previous information can provide a way of solving the radiative transfer equation for a given system regardless of the assessment of biomass or medium composition.

(8). – *Appendix for chapter 4*

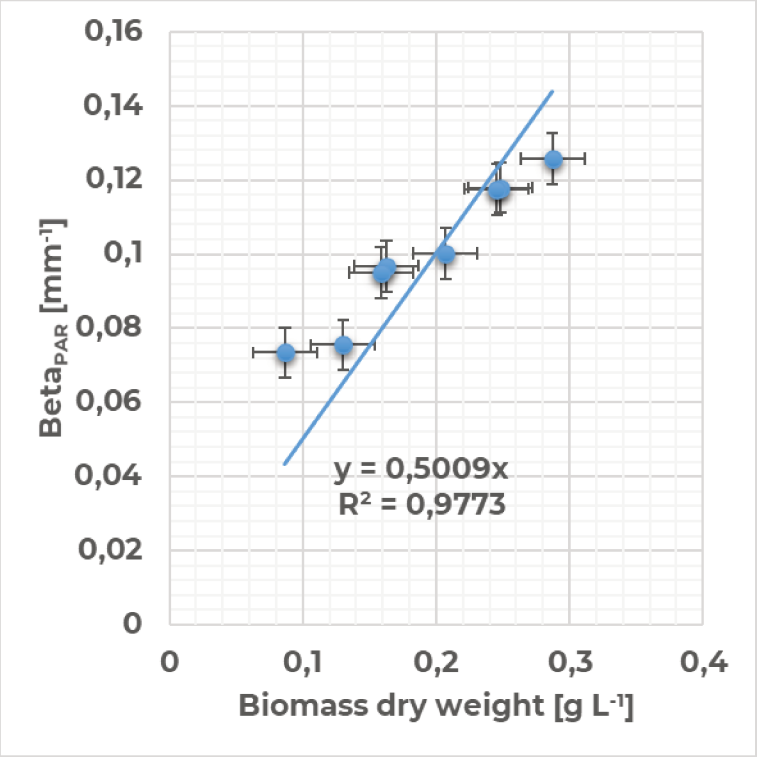

Figure (10): Evolution of the PAR spectral range attenuation coefficients with the cell dry weight content. These coefficients are the average values resulting from adding the spectral absorption and scattering coefficients.

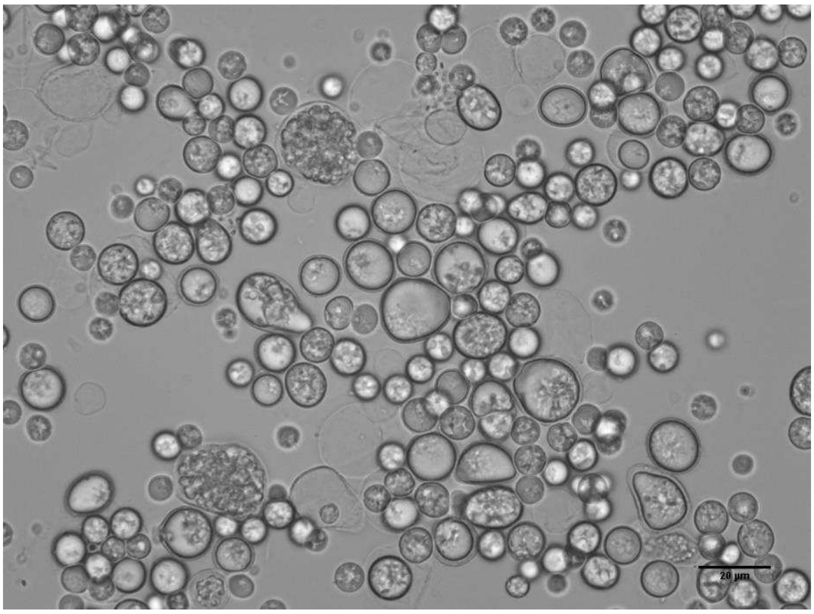

Figure (11): microscopic image of *Chromochloris zofingiensis* SAG 221-2 (SAG - Göttingen). The distribution of different cell sizes and morphologies is present in the evolution of a typical culture during the cultivation time.

Table (2): Values of the average relative spectral irradiance $\bar{I}_R\left(\underline{\hat{\Omega}}\right)$ in the PAR spectral range for the calibrations performed without any interference between the two optical fibres, including the empty plastic cuvette in the middle and utilising de-ionised water inside.

Angles [rad]	**Calibration without cuvette**			**Calibration + cuvette**			**Calibration + cuvette + water**		
1,0000	1,0000	1,0000	1,0000	0,9640	0,9680	0,9730	0,8740	0,8710	0,8620
0,9990	0,9043	0,9743	0,9643	0,8717	0,9431	0,9383	0,7904	0,8486	0,8312
0,9962	0,8593	0,9293	0,9093	0,8284	0,8996	0,8848	0,7511	0,8094	0,7838
0,9914	0,7774	0,8274	0,8974	0,7494	0,8009	0,8732	0,6794	0,7207	0,7735
0,9848	0,7245	0,6845	0,6945	0,6985	0,6626	0,6758	0,6332	0,5962	0,5987
0,9763	0,3666	0,4166	0,4066	0,3534	0,4033	0,3956	0,3204	0,3629	0,3505
0,9659	0,1783	0,1683	0,1883	0,1719	0,1629	0,1832	0,1558	0,1466	0,1623
0,9537	0,0566	0,0508	0,0587	0,0546	0,0492	0,0572	0,0495	0,0443	0,0506
0,9397	0,0389	0,0101	0,0189	0,0375	0,0098	0,0184	0,0340	0,0088	0,0163
0,9239	0,0010	0,0009	0,0010	0,0009	0,0009	0,0009	0,0008	0,0008	0,0008

Chapter (5)

The construction of a predictive tool for estimating the performance of Tubular Photobioreactors

---

(1). - Summary

The development of tools to predict the productivity of photobioreactors (PBRs) is a significant concern in biotechnology. To this end, it is required to know the light availability inside the cultivation unit and combine this information with a suitable kinetic expression that links the distribution of radiant energy with the cell growth rate. In the previous chapter, we presented and validated a methodology for assessing the radiative properties necessary to address the light distribution inside a PBR for varying illuminating conditions through the cultivation process of a phototrophic microorganism. Here, we sought to utilise this information to construct a predictive tool to estimate the productivity of an autotrophic bioprocess carried out in a 100 [L] tubular photobioreactor (TPBR). Firstly, the time-dependent optical properties over ten batch cultures of *L. platensis* were calculated. Secondly, the local volumetric rate of photon absorption was assessed based on a physical model of the interaction of the radiant energy with the suspended biomass, together with a Monte Carlo simulation algorithm. Lastly, a kinetic expression valid for low illumination conditions has been utilised to reproduce all the experimentally obtained dry-weight biomass concentration values of the cultures. Taken together, time-dependent radiative properties and the kinetic model produced a valuable tool for the study and scaling up of TPBRs.

(2). - Introduction

The ability of eukaryotic microalgae and cyanobacteria to convert light and carbon dioxide into chemical energy has attracted biotechnologists as well as various companies for the last six decades [154]. Besides the possibility of cultivating microalgae in arid areas, flood plains or lands not fit for agriculture, these organisms can produce a wide variety of products, from high-value proteins, pigments or fatty acids to energy-rich lipids [10], [155]. Among these, the cyanobacterium *Limnospira platensis* [156], [157] is considered a safe (GRAS) species and a natural producer of vitamin B12, antioxidants and proteins [8]. Its biomass is widely used as a health superfood, feed supplement and source of fine chemicals, representing a worldwide annual production of around 10,000 tons [158].

Concerning the cultivation of photoautotrophic microorganisms, abundant work has been published that considers different lighting conditions, alternative geometries for the PBRs and the impact of low and high values of the biomass concentration on the performance of PBRs [98], [159], [160]. While open PBRs, such as ponds and raceways, are economically efficient choices for the mass production of low-value biomass or processes such as wastewater depuration, high-value applications typically demand a level of quality, control and homogeneity that closed systems can only meet [120], [161]. Among these, TPBRs are an established technology that gained popularity in photobiotechnology over the last two decades [72]. These units are composed of two different parts: on the one hand, the place on which the radiant energy collection takes place, namely the solar loop, and on the other hand, a degasser, on which mass transfer processes take place, especially O_2 desorption [110]. This spatial differentiation of light-harvesting and gas exchange processes allows the optimisation of the photosynthetic performance of the PBR via modifying some parameters, such as the diameter and length of the tubes or the linear velocity of the liquid. Although the latter and the easiness of scalability of a TPBR make them more attractive than other PBR types, there are some drawbacks related to high economic costs concerning their installation, biofilm formation and sufficient oxygen removal to avoid photooxidative stress [162].

In the last few years, the knowledge regarding the REF in microalgae cultures, including light scattering and absorption, has expanded rapidly, as light is the most crucial factor driving photosynthesis [78], [160]. It is recognised that algae growth rate and biomass content depend on light availability and spectral composition [7], [163], [164]. At the same time, during the progression of a batch run, the REF within it, and the composition of the liquid medium underlies a significant dynamic change [136], [165]. Consequently, these variations trigger different adaptative processes, such as adjusting strategies for capturing and dissipating radiative energy or the modification of cellular physiology and cell cycle control [131], [135]. Thus, the performance of the culture results from considering these environmental conditions throughout the assessment of the phototrophic suspension radiative properties [126], [140] (Figure 1).

In a previous investigation, we presented a model of well-mixed microalgal suspensions, considering them as a continuum with absorption and scattering centres homogeneously dispersed within the PBR volume [128]. Given the temperatures involved in microalgal cultures, light could be assimilated as a gas of photons which move in different directions with the speed of light. Based on this physical model, Monte Carlo algorithms were developed and computationally implemented with different purposes: one for the determination of the optical properties (OPs) of the suspensions of photosynthetic microorganisms (the spectral absorption (κ_λ) and scattering (σ_λ) coefficients, and the scattering phase function ($\beta_{\theta,\lambda}$)) [20], [111], [116], [126]and the other for the simulation of the REF in PBRs. As a result, it was possible to predict the value of the local volumetric absorption rate of photons ($r_\lambda^{abs}(\underline{r},t)$) and its change with the microalgal culture growth, including the changing degree of stratification of light in the reactor [24].

Recently, we presented and validated a methodical perspective about the reproduction of outdoor lighting conditions at the laboratory scale and how this information may be employed for scaling up PBRs [108], [166]. Later on, we published and validated a methodology for calculating the optical properties necessary to address the light distribution inside a TPBR for changing illuminating conditions through the cultivation process of an eukaryotic microalga [140]. Here, we sought to utilise this information to construct a predictive tool to estimate the autotrophic bioprocess productivity in a TPBR of 100 litres for a commercially well-known cyanobacterial strain, considering the geometry of the system, the nature of the lighting system in quantity and quality and the physiological state of the cyanobacterial cells measured as the radiative properties of the autotrophic suspension.

Lastly, this preliminary study provides information about the kinetic behaviour of *L. platensis* under industrially relevant culturing conditions for ten cultivations, solely calculated from an energy balance. The latter highlights the possibility of considering the time-dependent radiative properties of autotrophic cultures as a design variable. Some authors have pointed out the necessity of considering time-dependent radiative properties for improving the predictions about the PBR production performance [160], [162]. Even though our perspective holds the potential of allowing the design of cultivation strategies that considers adjusting light quantity or quality in response to the monitoring of the OPs, the experiments of this section were not meant to optimise the PBR under study. Proper optimisation is possible, but firstly the OPs of the unit under analysis should be addressed to commence pointing in this direction. Inasmuch as we faithfully continue reproducing the behaviour of eukaryotic algae and cyanobacteria in this way, more accessible ways of optimising PBRs based on quantifying the microalgal optical properties as a design, control or operating variable may take place.

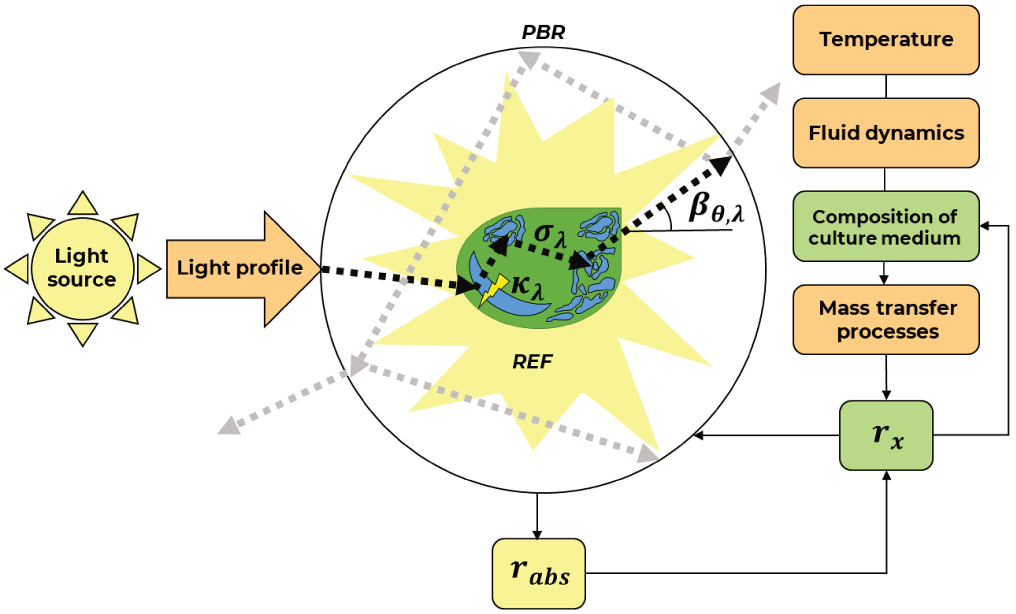

Figure (1). a T*PBR may be studied through its three major components: the light (yellow), the geometry of the system and operating conditions (orange) and every aspect concerning the biology of the cultured microorganism (green). In its interaction with the physical boundaries of the system, the incident light generates a unique light profile. Further, the microalgal OPs* $(\kappa_\lambda, \sigma_\lambda, \beta_{\theta,\lambda})$ *and the physicochemical system conditions in the interaction with this light profile create the REF, which allows the calculation of* r_λ^{abs} *and* r_x *for a particular moment alongside the cultivation time.*

(3). - Objectives

- To produce a model that link the CER calculated through measuring real-time radiative properties and operating variables.

(4). - Material and methods

(4.1). - Strain and Cultivation Conditions

The batch cultivations of *L. platensis* PCC7345 (PCC, Paris) were performed in a 100 [L] TPBR of MINT Engineering GmbH (Dresden, Germany). This TPBR is mainly composed of two units: the solar loop in which biomass growth occurs and the degassing tank. The PBR has 19 plastic tubes with an inner diameter of 0.0606 [m] and a total tube length of approximately 33 [m]. The liquid circulates with a pumping rate of 0.35 [m s^{-1}] (15 [W]) and air gassing rates of 0.03 [vvm]. Additionally, oxygen is removed from the suspension by introducing air to the liquid in the degassing tank. The gas insertion is supposed to be accomplished by the outflow of the solar loop encountering the liquid surface in the degassing tank and the resulting mixing movements (Figure 2). In the exponential growth phase, a concentrated inoculum was prepared in an illuminated chamber to start the cultivation with a biomass concentration equal to 0.1 [g L^{-1}]. To the end of cultivating cyanobacterial cells under industrially relevant physiological conditions, all the cultivations were carried out in a simplified Spirulina medium, including an inorganic plant fertiliser as the source of macro- and micro-nutrients (dosed as 0.5 mL of liquid fertiliser per litre of growth medium). The approximated composition of these reduced growth medium is: $NaHCO_3$ - 8.0 [g L^{-1}], $NaNO_3$ - 0.21 [g L^{-1}], NaCl - 1.0 [g L^{-1}], KNH_4 - 1.85×10^{-2} [g L^{-1}], KH_2PO_4 - 1.5×10^{-2} [g L^{-1}], K_2O - 3×10^{-2} [g L^{-1}] and traces of boron, copper, iron, molybdenum and zinc.

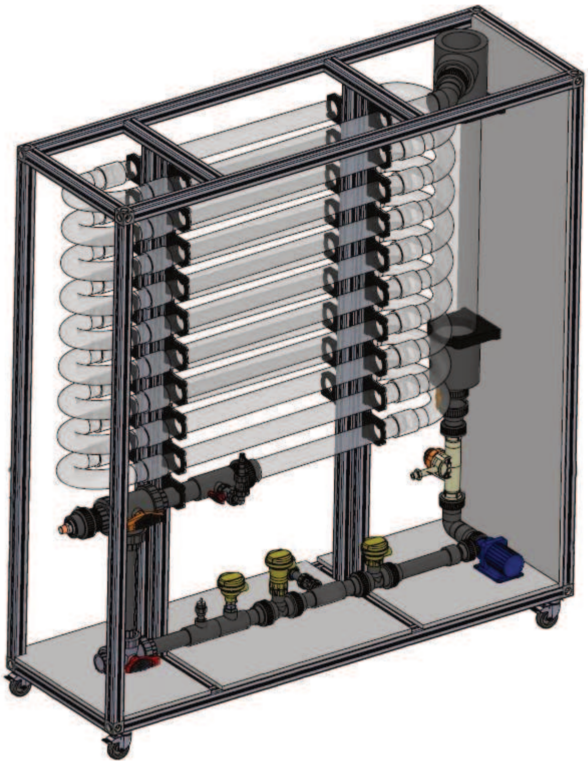

Figure (2): CAD rendering of 100L MINT PBR.

The reactor was unilaterally illuminated with warm-enriched light by four pairs of facing LED tubes (18 [W]) that were vertically mounted in the interspace of the solar loop. The whole lighting system (Figure 3) was fully characterised in its spectral (Figure 1b – Chapter 3) and directional composition (Figure 4 a,b – Chapter

2). The total length of each LED lamp is 1.2 [m] and the inner diameter is 0.26 [mm]. Each lamp provides a total photosynthetic photon flux (PPF) equal to 30.08 ± 0.12 [μmol s^{-1}], making a total PPF of 240.64 [μmol s^{-1}] that is emitted in the direction of the PBR tubes. The distance from each LED lamp to the nearest point of the PBR walls is 60 [mm].

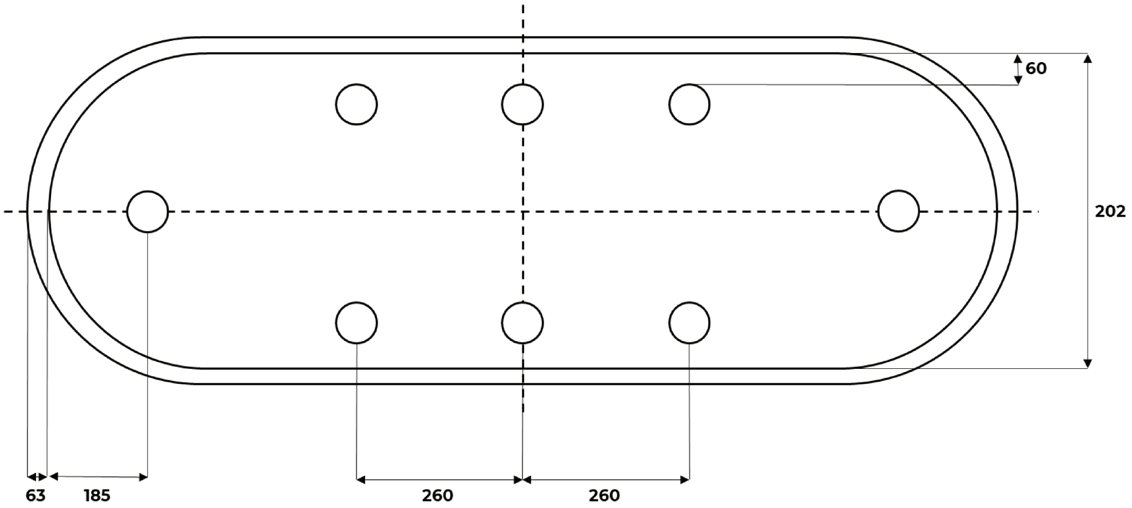

Figure (3): The schematic cross-section of the 100-L-MINT PBR. The figure is not a scaled representation but shows the position of the LED lamps from the PBR walls. All the measures are expressed in [mm].

(4.2). - Cell Dry Weight Concentration (C_x) & Optical Density (OD_{750})

Culture samples of *L. platensis* PCC7345 were analysed using a UV/VIS spectrophotometer (GENESYS 150, Thermo Fisher, Waltham, MA, USA). The optical density (OD_{750}) was measured at 750 [nm] and was calibrated against C_x [g L^{-1}] of *L. platensis* PCC7345 using the following correlation (in triplicate [110], [167], [168]):

$$C_x = 0.86 \times OD_{750} \tag{1}$$

Aiming to assess C_x, 15 mL of *L. platensis* PCC7345 suspension was passed through a glass microfiber filter (VWR International, Delaware Valley, PA, USA, mesh size: 1 [μm], in triplicate) and was then washed three times using 15 mL deionised water and dried for 24 h at 103 °C (Memmert GmbH + Co.KG, Schwabach, Germany). Finally, the weight difference of dried biomass was determined to calculate C_x.

(4.3). - Assessment of the radiative properties (OPs)

The optical properties corresponding to each sample (κ_λ, σ_λ, $\beta_{\theta,\lambda}$) were evaluated using the methodology presented in Chapter 4. There were no further considerations concerning the nature of the suspension between cyanobacterial or eukaryotic microalgal cells.

(4.4). - Modelling, simulation and analysis of radiant energy field (REF)

The physical and mathematical model upon which the simulation of the REF in the culturing medium relied was carried out following the methodology developed and described in Chapter 3. In the present study, the trajectory of each light beam may lead them to pass through the space between the tubes of the TPBR and be lost or have the chance to impact any of the 19 tubes composing the geometry of this culture system. Therefore, each tube and connector were treated as independent of each other.

The computational steps diagram, including the MC algorithm’s decision nodes, was presented in Chapter 3 – Figure (4). The ad-hoc simulation algorithm was designed and run in MATLAB (2022b). Concerning the REF properties, the definitions and units recommended in Alfano et al. were employed. Lastly, the regression of kinetic parameters was carried out using *globalsearch + fmincon* solver. Here, the error function was established as the non-linear squares minimising the sum of the differences between the experimental and model-predicted values. Every independent data series was adjusted utilising the trust-region-reflective algorithm under a default step tolerance and function tolerance. Finally, the model’s performance and the consequent calculation of the associated errors were performed utilising *fitnml* from the MATLAB Statistics and Machine Learning toolbox.

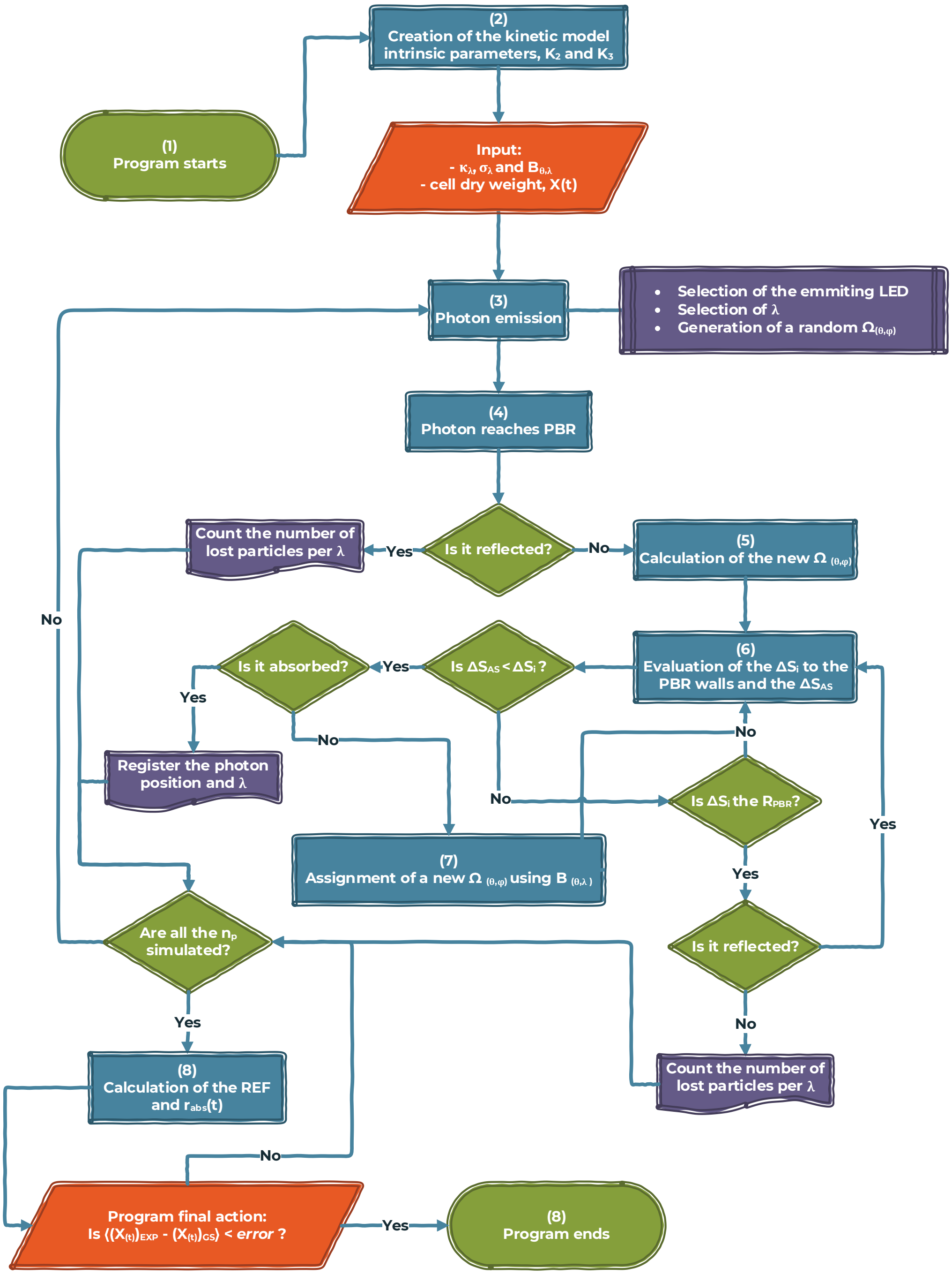

Figure (4): Computational flowchart, including the decision nodes in the stochastic algorithm developed for the Monte Carlo simulation of the REF inside the cuvette.

(5). - Results and discussion

In a purely phototrophic culture, microalgae are dependent on absorbing light energy to meet their demand for cellular functions and growth. Massive culture of cyanobacterial biomass in industrial PBRs requires a high biomass concentration and optically dense cultures capable of absorbing a high proportion of the collected light through its boundaries. Therefore, in PBRs, intense light gradients may be present naturally, especially in outdoor units. Not all the photons are equally absorbed in the suspension. Not all reactor zones are equally productive regarding photosynthetic growth because their productivity depends on the local photon availability and their wavelength. This last may lead to the coexistence of oversaturating and unlit zones, a phenomenon that is widely known as *self-shading*, giving place to the generation of simultaneous oversaturating, or further, photoinhibition zones and respiration zones, which could cause a noticeable loss of photosynthetic efficiency and a significant decrease in the TPBR productivity if not managed properly.

The local volumetric spectral rate of photon absorption $r_\lambda^{abs}(\underline{r},t)$ is the number of photons of wavelength λ locally absorbed per unit time and unit volume of culture for a particular moment throughout the length of a cultivation process [169]. Accessing $r_\lambda^{abs}(\underline{r},t)$ at every location in the culturing medium is key to understanding the factors affecting light absorption by microalgae for a given reactor setup and comparing the performance of different reactor configurations operating under different conditions concerning this process [20], [135].

The present section of this manuscript presents an approach to measure the optical properties of microalgae suspensions based on the radiation simulation employing an MC method and the employment of these in the evaluation of the light field inside a TPBR. The latter's advantage is that it allows the handling of complex reflexive systems and the optical phenomena occurring within industrial-scale TPBRs without introducing simplifications to solve complicated mathematical approaches. Under this perspective, the culture is a continuum and the cells are centres of absorption and scattering, with associated probabilities accounting for these events. After that, through an optimisation program, the experimental culture data will be used to determine (κ_λ, σ_λ, $\beta_{\theta,\lambda}$) based on the assumption that detectable changes in light passing through the culture are faster in comparison with the biological processes involved in the progressive changes regarding the OPs. It is essential to note that this way of assessing the REF is independent of pigments and biomass concentrations. The latter is not a minor statement, as a model of interaction linking light and the culture must be applied to do so, and due to the system's complexity, there is a lack of agreement between the different empirical approaches [134]. Still, there are no studies where the inner structures and the cell's shape are included in the model when describing cyanobacterial cells with complex shapes [133].

Lastly, as this methodology allows more intuitive ways of calculating the OPs of phototrophic microorganisms in the complex context of the evolution through the time of the REF inside a TPBR, a suitable kinetic expression was chosen to link the properties of the light field with cell growth. The accuracy and extension of this approach are analysed in the present section.

(5.1). – The study of the light collected by the 100-L-MINT TPBR

First and foremost, in Chapter 3 we introduced the necessary steps for assessing the amount of light that reaches a surface, and how to evaluate the phenomena of reflection and refraction across this area. The latter is a matter of concern, either in PBR illuminated with natural or artificial light, as each of these events depends on the directional nature of the impacting light [169]. In the case of sunlight, for example, there is a percentage of reflected light that is lost over the PBR physical boundaries that changes with the hourly sun's position and with the alteration in the seasonal trajectories [170].

In table 1, it is possible to see the result of evaluating the exchange of radiant energy between the eight LED tubes composing MINT's lighting module and the 19 tubes of the 100-L TPBR. Noticeably, 59.16 % of the light produced by the lighting module is not impacting over the reactor walls. The latter value is strictly related to the geometry of the system, in particular, with the spacing between tubes. A study of these characteristics allows to find a compromise between the geometry of a TPBR and the potential production values. Concerning the 40.84 % corresponding to the impacting energy fraction, 2.37 % is lost via reflection over the PBR walls. Due to this last number was considered as non-influential for the rest of the calculations, the contribution of these reflected particles to the rest of the tubes has been neglected.

Last but not least, in Fig. (5) it is pictured the distribution of the PPFD over the TPBR facing sections to the tubes. The distribution values present a maximum at the centre of the tube height (radius) in coincidence too with the centre of each LED tube. This is not surprising, as these areas are the closest to the lighting module. For the remaining heights, the energy decreases, as the light must travel a longer distance to reach this curvy surface.

λ [nm]	% impact	% no impact	% reflected	% refracted
400	0.01056	0.01716	0.00058	0.00998
410	0.10648	0.15850	0.00648	0.10000
420	0.13806	0.20228	0.00770	0.13036
430	0.24862	0.36038	0.01446	0.23416
440	0.70930	1.03874	0.04112	0.66818
450	1.01672	1.46616	0.05870	0.95802
460	0.52348	0.75724	0.02918	0.49430
470	0.31324	0.44998	0.01884	0.29440
480	0.25132	0.36300	0.01470	0.23662
490	0.26136	0.37888	0.01510	0.24626
500	0.32548	0.46998	0.01896	0.30652
510	0.38768	0.56884	0.02184	0.36584
520	0.43944	0.63794	0.02472	0.41472
530	0.49628	0.71048	0.02822	0.46806
540	0.58946	0.84116	0.03466	0.55480
550	0.74010	1.07778	0.04328	0.69682
560	0.99896	1.44596	0.05800	0.94096
570	1.40422	2.04166	0.08420	1.32002
580	1.98380	2.86284	0.11770	1.86610
590	2.64132	3.81240	0.15222	2.48910
600	3.26674	4.75812	0.18878	3.07796
610	3.67680	5.31956	0.21332	3.46348
620	3.80234	5.53138	0.21996	3.58238
630	3.63536	5.26332	0.21058	3.42478
640	3.21630	4.68458	0.18664	3.02966
650	2.73994	3.94230	0.15980	2.58014
660	2.20958	3.19124	0.12922	2.08036
670	1.72754	2.49060	0.09882	1.62872
680	1.30024	1.89636	0.07638	1.22386
690	0.96734	1.39302	0.05458	0.91276
700	0.70898	1.03112	0.04002	0.66896
Total	**40.84**	**59.16**	**2.37**	**38.47**

Table 1. Summary of the early steps of the simulation program. It concerns the events of production of radiant energy by the lighting module and the event of reflection occurring from the interaction of the light and the TPBR.

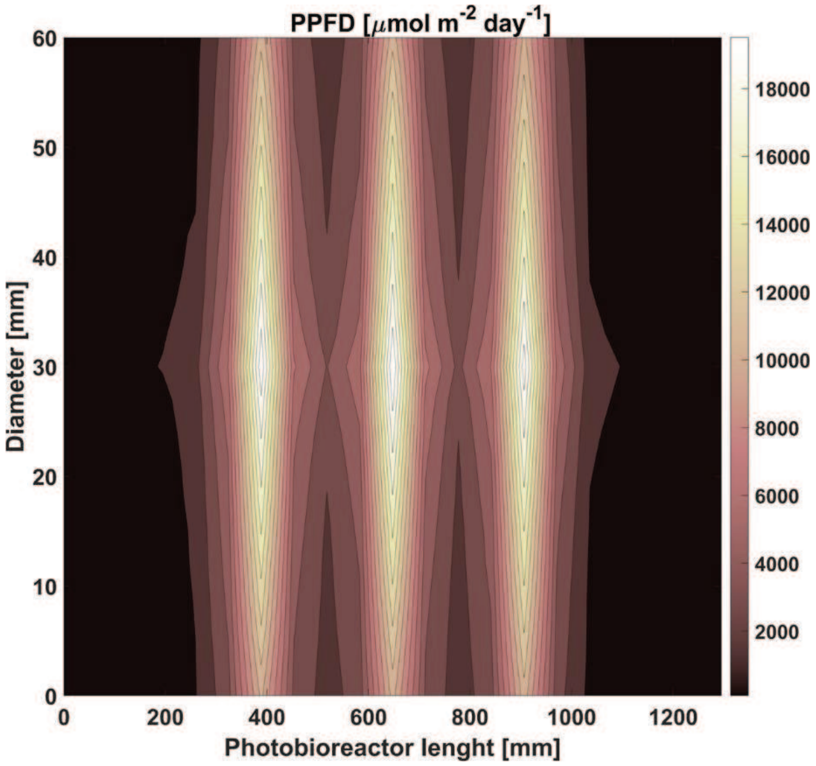

Figure (5): Photosynthetic photon flux density values over the photobioreactor surface facing the light source for the central tube of the 100-L-MINT PBR. This image is related to the previously presented Figure (3). The three LED lamps that face the reactor walls are related to the central position of the light dispersion presented in the PPFD of the present figure.

(5.2). - Absorption, Scattering coefficients and the scattering phase function of *L. platensis*.

The cyanobacterium *Limnospira platensis*, often referred to as Spirulina for commercial purposes, forms multicellular, filamentous structures known as coiled trichomes [43]. The cylindrical cells with diameters of 6–12 [μm] are arranged in helices with diameters ranging from 30 to 70 [μm] that typically possess a length of around five to seven coils (Figure 11 – appendix). The ultrastructure of an *L. platensis* cell exhibits a similar cell organisation to that of a typical prokaryotic cell with a Gram-negative cell wall. Nevertheless, *L. platensis* consists of thylakoids formed by membrane systems arranged in bundles parallel to the longitudinal cell wall. This cyanobacterium may conduct oxygenic photosynthetic processes due to the thylakoid membrane-integrated photosystem II (PSII), which is, among others, composed of chlorophyll *a*, and the presence of phycobilisomes (PBS) [17]. PBS are supramolecular light-harvesting complexes composed widely of phycobiliproteins, such as phycocyanin or allophycocyanin, having the presence of other polypeptides. Phycobiliproteins exhibit colouring chromophores, the so-called phycobilins attached by covalent bindings. Thus, the bluish colour of *L. platensis* is caused by its primary composing pigment, phycocyanin, among others. Moreover, carboxysomes that possess polyhedral inclusion bodies can be found in central cytoplasmic regions of *L. platensis*. These micro-compartments of a crystal-like structure store the enzyme ribulose-1,5-bisphosphate carboxylase/oxygenase (RuBisCO) [19].

In *L. platensis*, depending on the culture conditions, it was found that the size of the cells can vary in response to low or high PAR lighting conditions, whether the lighting conditions change in quality and quantity or there are organic carbon sources present in the liquid [171]. Additionally, a morphological alteration is regulated by light to the transcriptional level [17]. At the beginning of a cultivation process, a photo-acclimation effect is related to the loosening process of *L. platensis* spirals, which enables the cells to receive more light for photosynthesis [171]. On the contrary, a tightening process also allows the cells to shade themselves when solar radiation becomes excessive [172]. The quantity and size of PSII can also change in response to the environment in this cyanobacterium and the composition of the accessory pigments. Chlorophyll *a* levels were reported to be altered in response to different illuminating conditions, as well as beta-carotene and phycobiliproteins [173]. Furthermore, the architecture of PBSs changes drastically due to high radiation in the PAR spectral range [174].

Here, it is sought to investigate the radiative properties of a phototrophic culture of *L. platensis* based on an energy balance. The latter allows the construction of a continuum medium of radiation properties in the culture volume in a single period, although unevenly distributed in space and wavelength. Then, the OPs related to the REF at this moment, fated to every chemical or biological alteration in the system, such as the ones mentioned in previous paragraphs, were calculated. Figure 6 - a,d present ten sets of κ_λ and σ_λ coefficients in the PAR spectral range. The trend in the coefficients' variations in the wavelengths region from 400 to 700 [nm] has shown expectable results in comparison with other members of Cyanophyceae [175].

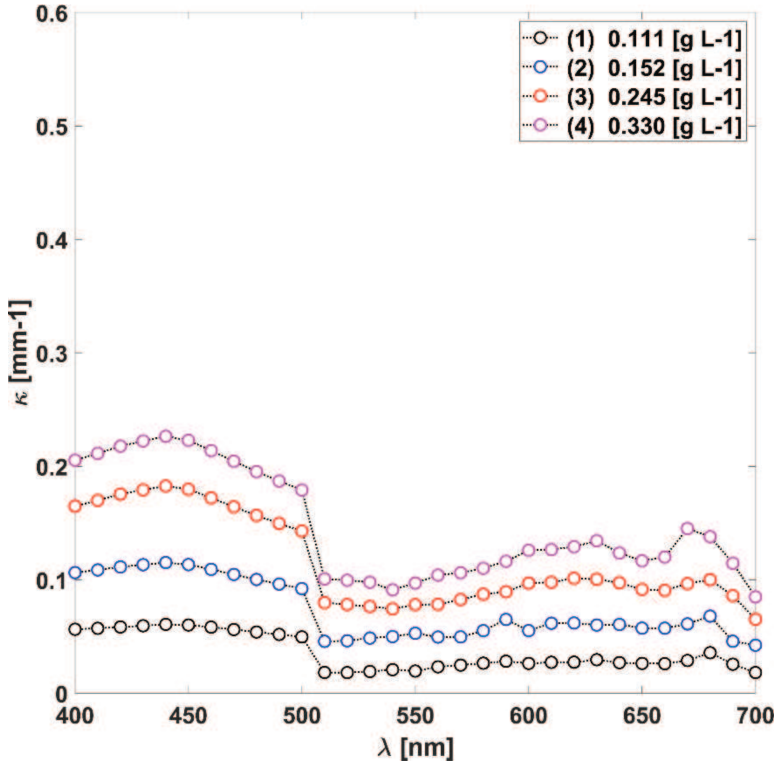
0.6
0.5
0.4
0.3
0.2
0.1
0
κ [mm-1]
400
450
500
550
600
650
700
λ [nm]
(1) 0.111 [g L-1]
(2) 0.152 [g L-1]
(3) 0.245 [g L-1]
(4) 0.330 [g L-1]

(**a**)

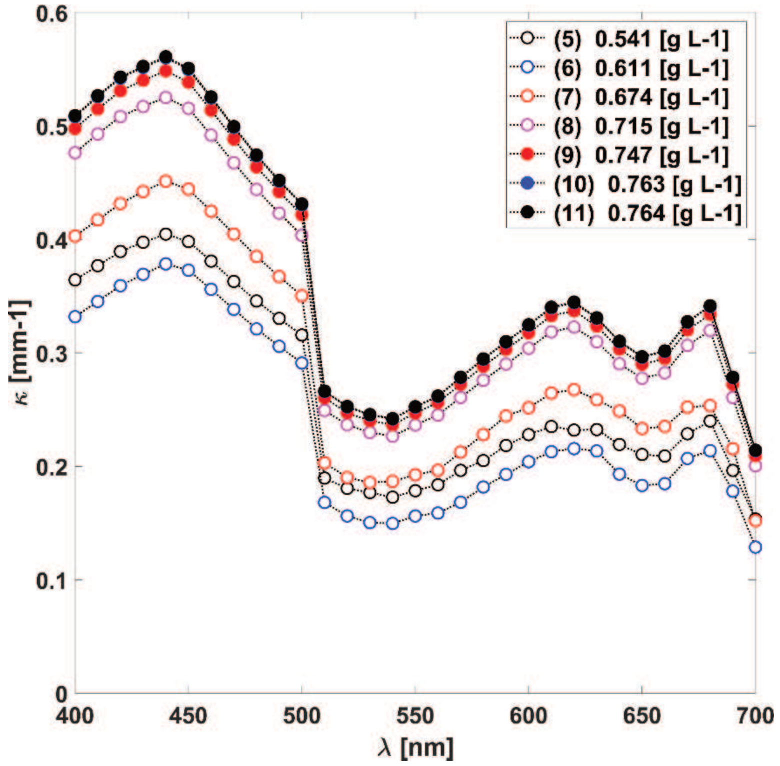
0.6
0.5
0.4
0.3
0.2
0.1
0
κ [mm-1]
400
450
500
550
600
650
700
λ [nm]
(5) 0.541 [g L-1]
(6) 0.611 [g L-1]
(7) 0.674 [g L-1]
(8) 0.715 [g L-1]
(9) 0.747 [g L-1]
(10) 0.763 [g L-1]
(11) 0.764 [g L-1]

(**b**)

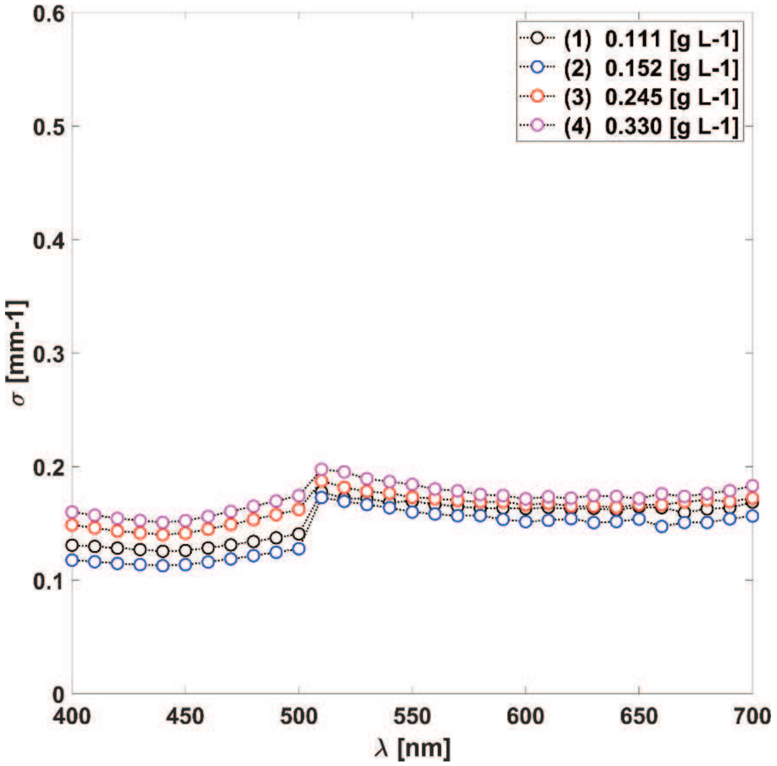

(**c**)

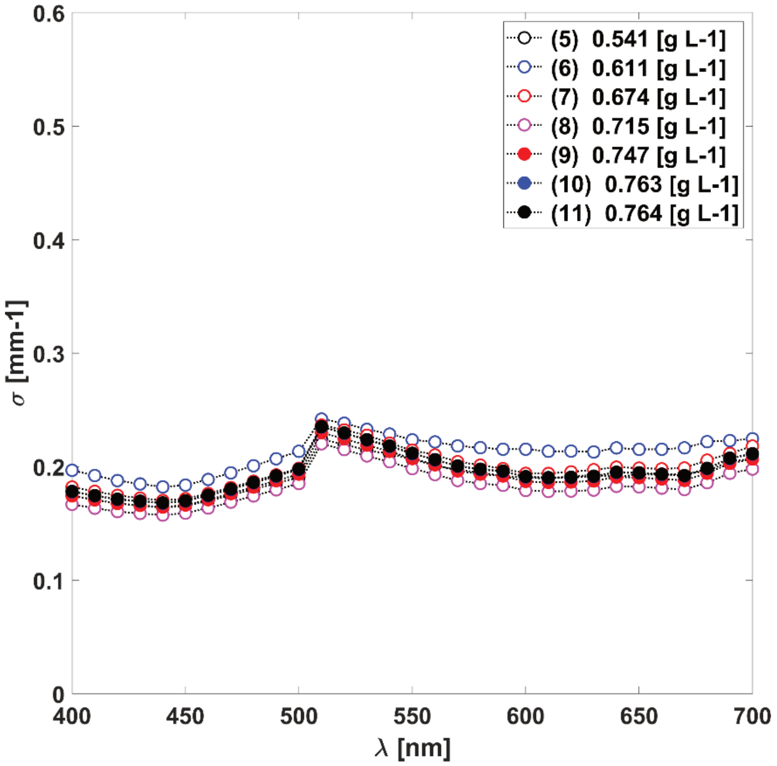

(**d**)

Figure (6) (**a**,**b**). The absorption κ_λ and scattering coefficients of eleven samples. (**c**,**d**). The spectral scattering σ_λ coefficients of eleven samples.

As for absorption, there are larger values at those wavelengths where the chlorophyll pigments are active to light. Free Chl *a* absorb around 435 and 676 [nm]. In Figure (6- a, b), these peaks are smoother and present shifts due to two effects: firstly, Chl molecules are supported by other proteins in the core antennas of the LHC, which creates an overlapping in the spectrum of these free substances; secondly, as it was mentioned before, it is natural in *L. platensis* and in the synthesis of carotenoids [173]. Lutein and zeaxanthin, as representatives of all the different α- and β-carotene intermediates, have absorption maxima around 445 and 474 [nm] and 480 [nm] on an individual basis [120]. The latter also contributes to the spectral peaks overlapping the PAR spectral range, explaining the other wavelength variations ranging from 550 to 650 [nm]. Lastly, the PBSs that take shape in antenna-like arrangements absorb light in the wavelength range of around 540 to 650 [nm], as they capture sections of the solar spectrum not used by chlorophyll molecules and very efficiently transmit energy to the photosystems where charge separation takes place [176]. It is notable to see how the peaks related to phycobiliproteins become more important towards the increasing biomass content relative to the peaks of Chl *a* (Fig. 7).

Regarding the fate of the non-absorbed light, when absorption occurs in the LHC and the amplitude of an electromagnetic field changes, its phase will change accordingly, producing inelastic scattering [177]d. From Figure 6 - c,d, the habitual trending in the light dispersion's behaviour for an autotrophic suspension can be observed. Light scattering tends to be higher than microalgae absorption efficiency [163]. Even though the σ_λ depends on wavelength as the κ_λ, this wavelength selectivity is not that sharp for the cyanobacterium scattering spectrum. The latter may be attributed to the dominant influence of the non-absorbing cell components over the σ_λ, although pigments exert an effect through fluorescence and selective absorption [133]. The ensuing σ_λ to the spectral range 500–560 [nm] are the highest values (Figure 6 - c,d), corresponding to the lowest κ_λ in Figure 6 - a,b.

Last but not least, the $\left(\bar{\mu}_n^*\right)_{PAR}$ values composing the most favourable angles represent the forward scattering pattern of *L. platensis* and $\beta_{\theta,\lambda}$ are listed in (appendix - Table 3). As it has been observed for *C. zofingiensis*, there are variations in the calculated values of $\left(\overline{\mu}_n^*\right)_{PAR}$. Here, rather than elucidate the specific influence of a single element, the nature of these variations is generally related to all of the complex non-absorbing components that may be present within the cells [135], [178]. So far, the understanding of the individual organelle–light interaction is not sufficiently wide to present a $\beta_{\theta,\lambda}$ function more than partially biased by wavelength. Therefore, the values of $\beta_{\theta,\lambda}$ will be utilised as the averaged values across the entire PAR spectral range.

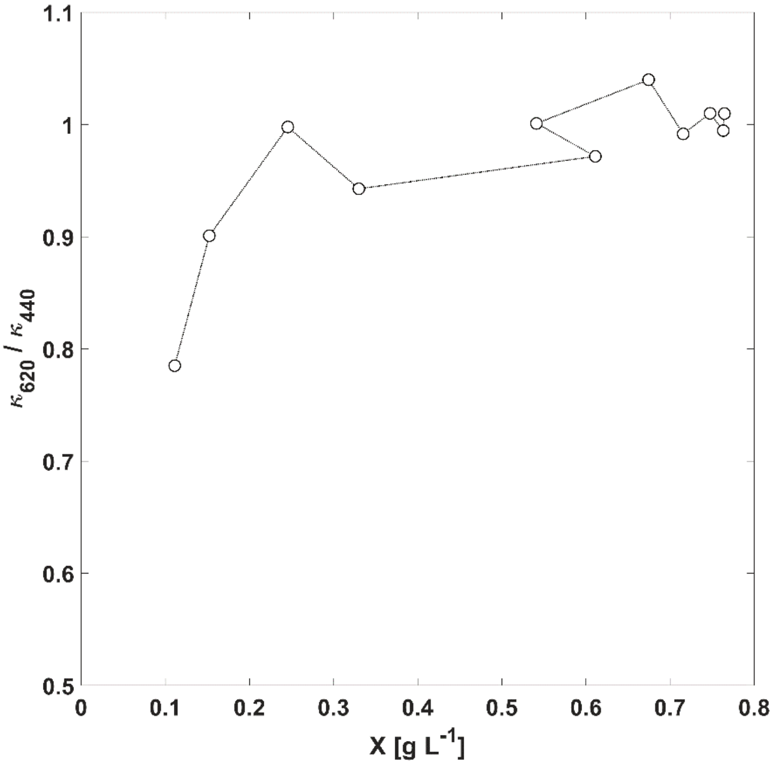

Figure (7): ratio of the κ_{620} and κ_{440} to observe the relative changes among the highest Chl-*a*-related and phycobiliprotein-related peaks.

(5.3). - Modelling and analysis of radiant energy field within the TPBR.

The optimisation and control of light transfer in PBRs on which an autotrophic process is carried out are bound to the close relationship between the radiation source's emission characteristics, the reactor's geometry and the suspension's OPs that reside within it. Combining these three components in the radiative transfer equation (RTE) allows access to know the light availability inside the unit, which accounts for the physiological state of the culture at a given time. Cells modify the light field, and light affects the life of the cells [163]. Light exposure and nutrient-level alterations trigger a set of physiological processes in microalgae on both transcriptional and metabolic levels. These processes affect the OPs of the cells. Therefore, radiation characteristics and the size of the cells are changing not constantly but continually as a response to variations in the spectral density distribution of photons $e_{\lambda}(r,t)$, among other factors [151].

If κ_{λ}, σ_{λ} and $\beta_{\theta,\lambda}$ were calculated experimentally, $e_{\lambda}(\underline{r},t)$ may be addressed as follows:

$$e_{\lambda}(\underline{r},t) = \int_{\hat{\underline{\Omega}}} n_{\lambda}(\underline{r},\hat{\underline{\Omega}},t)\, d\hat{\underline{\Omega}} \qquad (2)$$

In Equation (2), $n_{\lambda}(\underline{r},\hat{\underline{\Omega}},t)$ is the local density number of photons with wavelength λ with a trajectory through the position $\underline{r}$ in the direction $\hat{\underline{\Omega}}$, for a particular time t in the cultivation process. Thus, in agreement with the radiation transfer theory, $r_{\lambda}^{abs}(\underline{r},t)$ may be readily obtained through the use of the light speed constant and the spectral absorption coefficients:

$$r_{\lambda}^{abs}(\underline{r},t) = c\, \kappa_{\lambda}(t)\, e_{\lambda}(\underline{r},t) \qquad (3)$$

In Figure 7, it is possible to see the outcome of the numerical simulation of $\overline{r}_{PAR}^{abs}(t)$ and $\overline{r}_{PAR}^{abs,SP}(t)$, which is the result of summing up all the contributions within the photosynthetically active wavelength range for the total PBR positions, where:

$$\overline{r}_{PAR}^{abs}(t) = \frac{1}{V_{PBR}} \int_{0}^{\infty} \int_{400}^{700} r_{\lambda}^{abs}(\underline{r},t)\, g(r_{\lambda}^{abs},t)\, d\lambda\, dr_{\lambda}^{abs}, \qquad (4)$$

And

$$\overline{r}_{PAR}^{abs,SP}(t)=\frac{\overline{r}_{PAR}^{abs}(t)}{\overline{x}(t)} \tag{5}$$

In Equation (4), $\overline{r}_{PAR}^{abs}(t)$ is the average rate of PAR photon absorption in the TPBR, V_{PBR} is the culture volume within the TPBR and $g(r_{\lambda}^{abs},t)$ is a measure of the frequency of occurrence of $r_{\lambda}^{abs}(\underline{r},t)$ values in the TPBR, or the volume distribution function in terms of the photon absorption rates, subject to the following normalisation condition:

$$V_{PBR}=\int_{0}^{\infty} g(r_{\lambda}^{abs},t)dr_{\lambda}^{abs} \tag{6}$$

In Equation (5), $\overline{r}_{PAR}^{abs,SP}(t)$ is the average specific rate of PAR photon absorption in the TPBR, while $\overline{x}(t)$ is the cell biomass concentration for a given time alongside the cultivation process.

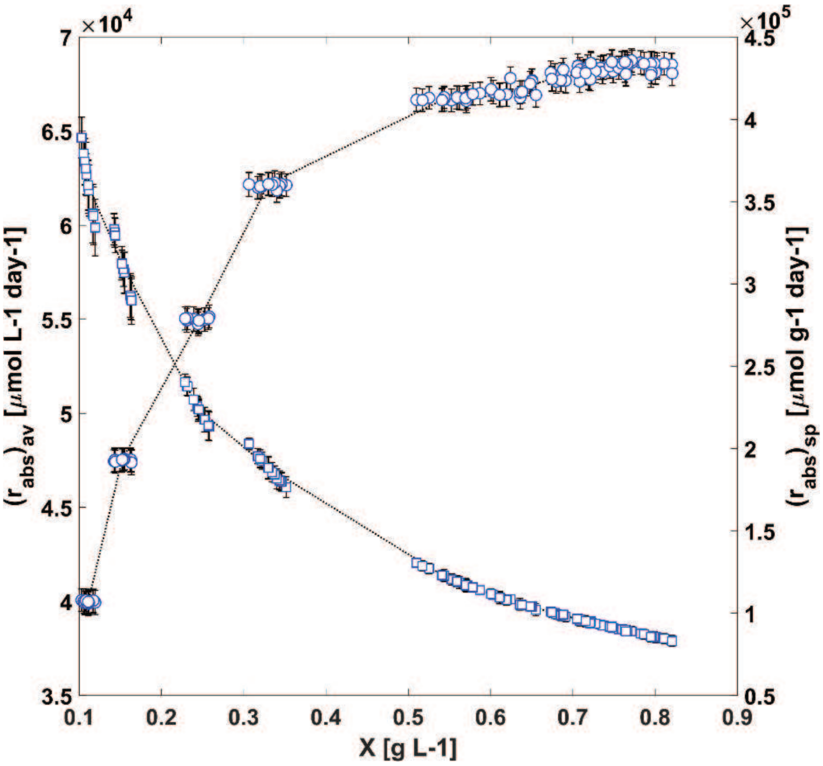

Figure (7) The evolution of the average ($\overline{r}_{PAR}^{abs}$, ○) and specific average ($\overline{r}_{PAR}^{abs,SP}$, ▫) rate of PAR photon absorption in the TPBR.

In the experimental cultivations carried out, the amount of radiation absorbed increases with the biomass concentration. However, when a larger number of cells captures light, the amount of light absorbed per biomass unit is reduced and vice versa (Figure 7). Even though the $\overline{r}_{PAR}^{abs}(t)$ values increased with the amount of suspended biomass, it should be considered that, as the $\kappa_{\lambda}(t)$ coefficients evolved, the contribution of each $r_{\lambda}^{abs}(\underline{r},t)$ to the average rate value changed drastically.

Light is unevenly distributed in the reactor because of the phenomena of absorption, scattering and reflection associated with the transfer of radiant energy and with the configuration of the PBR. Figure 8 - a,c present how the stratification of light changes along with the cyanobacterial growth for a single tube of the 100L-TPBR, giving rise to zones with different local volumetric absorption rates $r_{\lambda}^{abs}(\underline{r},t)$ and different spectral volumetric densities $e_{\lambda}(\underline{r},t)$ of photons within the PAR spectral range. In Figure 4a, the $r_{PAR}^{abs}(\underline{r},t)$ values are very low for all radial distances, irrespective of the biomass concentration. For high biomass concentrations (Figure 8c), a significant fraction of the photons that enter the suspension are absorbed in zones close to the irradiated boundary, and only a tiny fraction is left to be absorbed in more distant zones. Whether this evolution of the light stratification effect is advantageous or adverse to biomass performance will depend on if the positive impact of an increase in the $r_{PAR}^{abs}(\underline{r},t)$ values is outdone by the negative effect of a decrease in the efficiency in the utilisation of the radiant energy.

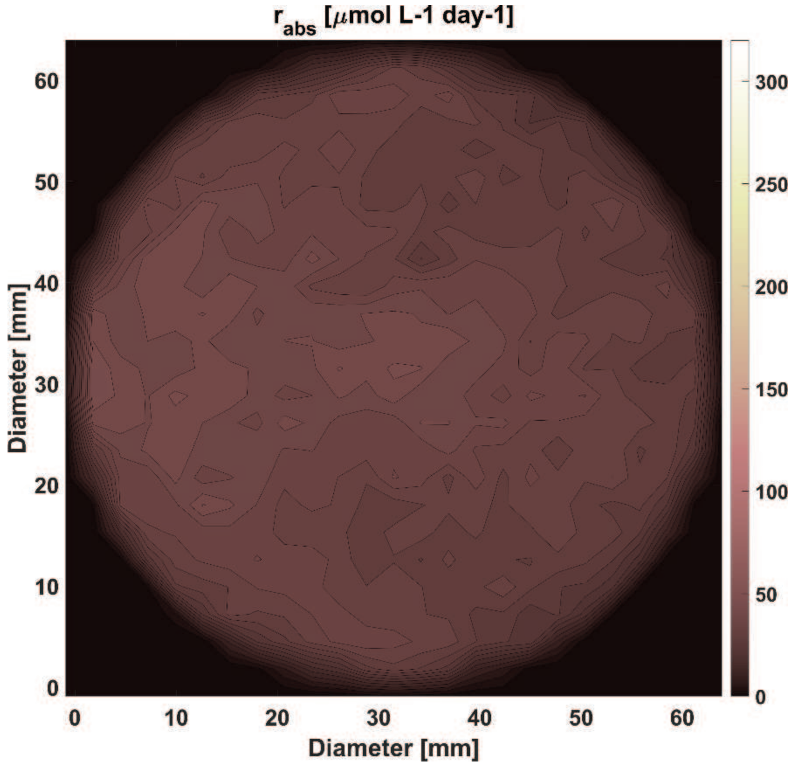

(**a**)

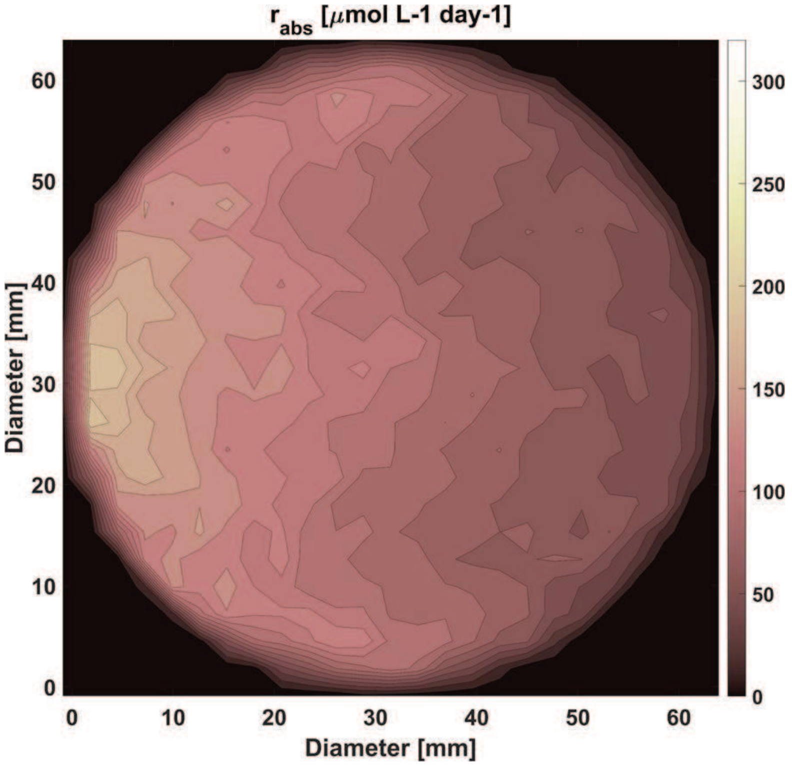

(**b**)

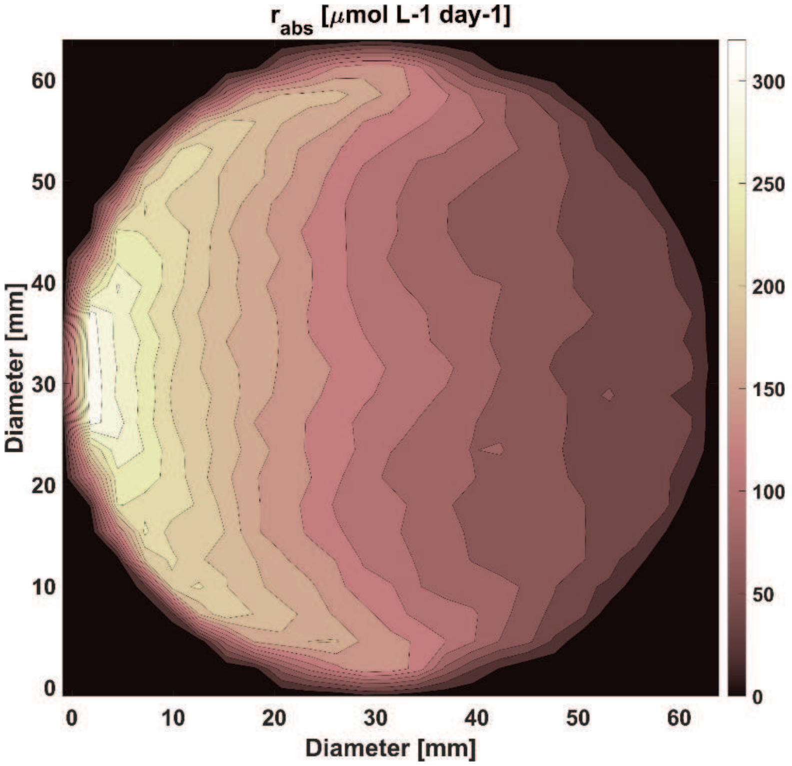

(**c**)

Figure (8) (**a**,**c**). $r_{PAR}^{abs}(\underline{r},t)$ distribution profiles as a function of the diameter of the central tube of the TPBR solar loop at a corresponding cross-section equal to the median length of the tube. The suspended biomass concentration for a, b and c particular moments alongside the cultivation process is 0.111 (**a**), 0.541 (**b**) and 0.764 (**c**) [g L^{-1}], respectively.

Finally, in light of this analysis and concerning the light source, it is possible to propose using radiation sources of higher energy output to circumvent the stratification effect. Nonetheless, this is not an option without shortcomings because the increase in the availability of radiant energy in the zones of concentrated suspensions already exposed to high light intensity may cause the saturation of the photosynthetic systems or may even be harmful to them [171]. Because of the latter, it is tempting to robustly support the previous selection and employment of the radiation source already chosen for this illuminating system, as it emits photons in wavelengths corresponding to a low or middle value of the absorption coefficient (Figure 1b – Chapter 3) and this helps to facilitate light penetration into the culture avoiding the generation of excessively irradiated areas or respiration zones [179].

(5.4). - The autotrophic growth in the TPBR and regression of intrinsic kinetic parameters.

As far as $r_{\lambda}^{abs}(r,t)$ values are concerned, the biomass concentration is an essential operating variable, which can be manipulated to balance the relative importance of deeper zones into the suspension with the contribution of zones near the irradiated boundary, which will be reflected in that the profiles of rates of photon absorption will be less steep and vary across the PAR spectral range [162]. These differences in $r_{\lambda}^{abs}(\underline{r},t)$ values for different wavelengths could be an interesting parameter in PBR operation conditions and design. In the case of concentrated suspensions, photons whose wavelength corresponds to the higher values of the absorption coefficient are absorbed in the zones closest to the irradiated boundary [6]. Consequently, the deepest zones in a homogeneous suspension are relatively poorly illuminated by the energy of high photosynthetic value. These regions, "ill-lit" than the rest in what valuable energy for photosynthesis is concerned, have a meagre rate of photon absorption in the wavelength ranges of interest for photosynthesis [180].

In order to gain a deeper insight into the cyanobacterial biomass light dependence when light availability fluctuates, it is necessary to follow the REF changes alongside the cultivation process and link the growth kinetics with a suitable property of the light field [127]. In the 100L-TPBR under analysis, the $r_\lambda^{abs}(\underline{r},t)$ values are not uniform (Figure 8c). Nonetheless, from previous studies performed with the unit, there is an agreement that the culture circulates in a turbulent regime [110]. Thus, it is generally assumed that fluids circulating in turbulent conditions through pipes are radially well mixed [72]. In accordance with this notion, the fluid elements move from the centre to the surface of the tube lines several times per second. In addition, this unit possesses a degassing tank on which several volume elements perfectly mix with each other before starting a new run into the pipes. This evidence solidly supports the conclusion that the solar loop of the 100L-TPBR operates through a well-developed plug flow regime. Then, the typical mixing time inside each of the “plugs” is much smaller than the typical time of cyanobacterial growth [181]. Under these conditions, the cyanobacterial cells frequently turn from lighted zones to dark zones (and vice versa) many times and also perform several runs alongside the tubes before cellular replication occurs. Therefore, it is tempting to assume an integrated scenario and that the kinetics of cell growth is driven by $\overline{r}_{PAR}^{abs}(t)$ [162].

In this work, a kinetic expression based on a simplified pathway of the light-dependent step of photosynthesis and the inclusion of time-dependent radiative properties have been applied [127]:

$$\overline{r}_X(t) = K_3\left(\sqrt{1+K_2\,\overline{r}_{PAR}^{abs,SP}(t)}-1\right) \tag{7}$$

In Equation (7), $\overline{r}_{PAR}^{abs,SP}(t)$ has been previously defined in Equation (5), while K_2 and K_3 are kinetic constants related to the intracellular rate of ferredoxin formation and the rate of net photosynthesis, as the energy harvesting stage is the growth limiting step [182]. $\overline{r}_X(t)$ is the average biomass growth rate. Furthermore, the mass balance proposed for this TPBR operated in batch mode was established and later solved as follows:

$$\frac{d\,\bar{x}(t)}{d\,t} = \bar{r}_X(t) \tag{8}$$

In Figure 9, the solid magenta line represents the predicted biomass values for every one of the batch cultivation processes analysed in this study. The kinetic parameters related to physical quantities concerning the photosynthetic process are shown in Table 2a. Moreover, and for the sake of comparing with other methodologies previously published, the same kinetic model was employed for evaluating the REF in the geometry of an “infinite tube” [108], i.e. assuming every curvy section of the 100-L MINT TPBR as straight, maintaining the same diameter in each tube. Additionally, the same evaluation employing the scattering phase function proposed by Heinrich et al. [128] has also been considered. From Figure 9, it is possible to conclude that around the fourth day of cultivation for each one of the cultures, the rising biomass growth rate $\bar{r}_X(t)$ started to decrease. This corresponds to the situation shown in Figure 8b, in which it is pictured that the influence of ill-lit areas, far away from the irradiated boundaries of the tubes, starts to have a major contribution to the dispersion of the $r_{\lambda}^{abs}(\underline{r},t)$ around $\bar{r}_{PAR}^{abs}(t)$ [20].

In relation to the simulations carried out with the “infinite tube” geometry, in Fig. 9 and Table 2b is shown the results of the non-linear regressions performed, and it is possible to see an overestimation of the predicted results in comparison with the experimental values. In the same direction, it is crystal clear that with the utilisation of a phase function obtained as an expansion of Legendre polynomials, the simulated values underestimated the experimental ones (Fig. 9 and Table 2b). The first case has been explored as it holds the advantage of taking less amount of computation time in producing results in comparison with the normal geometry. Some authors have proposed that TPBRs may be simulated as infinite bubble columns as long as the radius of the two units is similar [61]. As it is pictured in Fig. 9, the difference in considering the curvy junctions of the longer tubes in comparison with treating them as straight sections produces a difference with a degree of uncertainty of around 15-20% in comparison with the more complex geometry. It should be noticed that this last is an effect of changing the geometry, while the nature of the light involved and the radiative properties of the microorganisms were maintained across these simulations. A possible explanation for these results arises from considering that the light collected by an “infinite tube” turns out to be higher in contrast with a semicircular surface (Table 1), which is translated into higher growth rates.

Contrarily, in the second case, the nature of the light source and the system's geometry were the same, but the model for the scattering phase function was different. The result of considering an average scattering phase function for a different strain resulted in differences of up to 40% between the predicted and experimental dry weight biomass concentration values (Fig. 9 and Table 2c). To the end of explaining this outcome, it should be taken into account that both methodologies consider the cells as points of the space across the REF on which the direction of photons could be altered or not, without imposing any restriction over the complex geometry of the cells. In this direction, Heinrich et al. [128] proposed a model for *Tetradesmus sp* and *Chlorella sp* cells, while here, the morphology of *L. platensis* is markedly different. As it was pointed out in the previous chapter, it is necessary to gain further insight into the relationship between the non-absorbing components of the cells and the impact that this has on the forward and backward scattering phenomena [183].

Furthermore, as the REF evolves, changes in the architecture and composition of the photosystems (PS), depending on the lighting conditions, have been observed in many species of cyanobacteria and green microalgae [165]. *L. platensis* increased their Chl content per biomass unit weight when they were grown at low light intensities [184]. Contrarily, some members of the green microalgae showed lower pigmentation content as light distribution in the TPBR became homogeneous [185]. Under low light-intensity conditions, algae produce photosynthetic systems with a greater capacity to capture photons. This increase in the photon uptake capacity is achieved by enhancing the synthesis of primary and accessory pigments [186]. In *L. platensis,* it has been observed that the ratio between the PSI and PSII is altered under the self-shading effect [187].

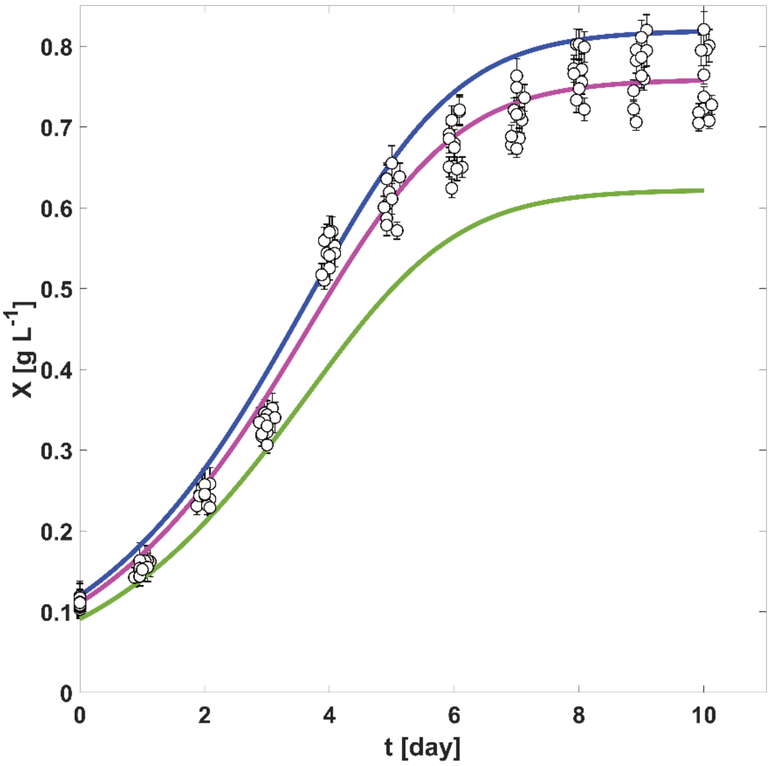

Figure (9) Experimental (○) and predicted (solid lines) biomass values for every one of the batch cultivation processes analysed in this study. (magenta) evaluation with the normal geometry already described in Figure (2). (blue) “infinite tube” geometry was considered. (green) kinetic model including a scattering phase function composed of an expansion of Legendre polynomials.

The light-to-biomass yield ($Y_{xp}(t)$) depends on the proper kinetic coupling between the absorption of light, electron transport and carbon fixation processes.

Parameter	**Value**	**Unit**	**Adjusted R²**
K_2	$7.60\ 10^{-12} \pm\ 0.71\ 10^{-12}$	$\left[\text{day g }\mu\text{mol}^{-1}\right]$	0.937
K_3	$2.66\ 10^{4} \pm\ 0.14\ 10^{4}$	$\left[\text{g L}^{-1}\text{ day}^{-1}\right]$	

(a)

Parameter	**Value**	**Unit**	**Adjusted R²**
K_2	$8.51\ 10^{-12} \pm\ 0.84\ 10^{-12}$	$\left[\text{day g }\mu\text{mol}^{-1}\right]$	0.884
K_3	$3.19\ 10^{4} \pm\ 0.17\ 10^{4}$	$\left[\text{g L}^{-1}\text{ day}^{-1}\right]$	

(b)

Parameter	Value	Unit	Adjusted R²
K_2	$6.46\ 10^{-12} \pm\ 0.61\ 10^{-12}$	$\left[\text{day g }\mu\text{mol}^{-1}\right]$	0.779
K_3	$2.26\ 10^{4} \pm\ 0.12\ 10^{4}$	$\left[\text{g L}^{-1}\text{ day}^{-1}\right]$	

(c)

Table 2. Model parameters resulted by fitting the experimental average specific rate of PAR photon absorption in the TPBR and biomass concentration values. (a) normal geometry described in Figure (2). (b) “infinite tube” geometry was considered. (c) kinetic model including a scattering phase function composed of an expansion of Legendre polynomials.

In Figure 10, is possible to see the photosynthetic yield, $Y_{xp}(t)$, where:

$$Y_{xp}(t) = \frac{\bar{r}_X(t)}{\bar{r}_{PAR}^{abs}(t)} \tag{9}$$

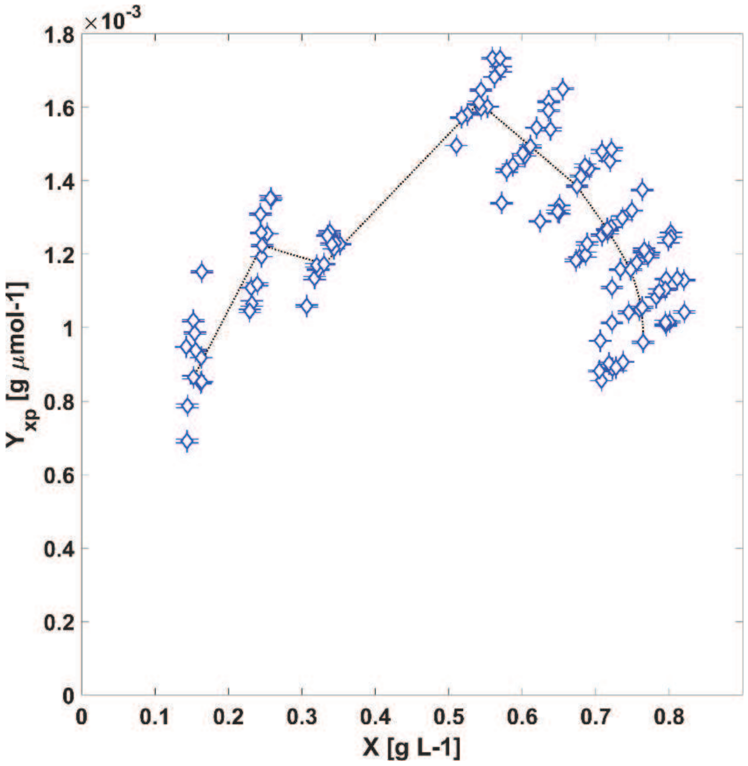

Figure (10) Light-to-biomass conversion values (◊) as a function of biomass concentration values studied in the TPBR.

Here, an increase in biomass concentration brings about an increase in the amount of energy absorbed up to a certain biomass concentration value [188], [189]. Afterwards, the biomass productivity is reduced due to a lowering photoautotrophic growth efficiency. This reduction is related to the adaptive mechanisms discussed in previous paragraphs (Section 5.2). On the one hand, if the light absorption rate is greater than the speed at which electrons generated in the reaction centres are transported, a depletion in the available electron carriers takes place, and due to a lack of processing capacity, a more significant fraction of the absorbed energy is dissipated mainly as thermal energy to the adjacent volume acting as a thermal sink [7]. On the other hand, the efficiency in the use of photons is associated with the size of the complex light-capture antenna, which, as was highlighted in previous sections, in *L. platensis* suffers morphological changes regulated at the molecular level triggered by the naturally occurring stratification of light [171]. Even though there exists a clear dispersion over the biomass cultivation values that could be attributed to variations in other growth factors (such as varying temperatures or nutrient starvation, oxygen mass transfer limitations and toxic effects of the oxygen evolution within the tubes and poor mixing regime [110], [168]), the predicted values show good agreement with the experimental values and the notion that light availability is the controlling factor driving the growth kinetics in the system under study. Lastly, the calculated TPBR mean areal productivity oscillates around 2.48 ± 0.06 [g m^{-2} day^{-1}]. The latter value is up to six times lower than the reported areal productivities for similar PBRs [190], confirming the fact that the amount of light collected by the TPBR may be improved, and the amount of energy supplied could be increased to boost the biomass productivity.

(6). - Conclusion

From a biotechnological point of view, the study of the light behaviour of photobioreactors is compulsory to find and employ a light exposure regime that provides the maximum conversion of light to biomass and high-value compound production. Unluckily, achieving high biomass growth rates and the best productivity of the desired target products is usually tricky. In this preliminary work, a kinetic expression for *L. platensis* growth under light-controlling conditions has been applied based on an energy balance evaluated by assessing the cultivations' time-dependent radiative properties. The $\overline{r}_{PAR}^{abs}$ values were calculated considering the photobioreactor's uneven light distribution because of the absorption and scattering phenomena associated with the transfer of radiant energy and with the configuration of the PBR. Based on $\overline{r}_{PAR}^{abs}$, the growth of *L. platensis* as a function of time was simulated, showing good agreement with experimental data for similar cultivations carried out in the same unit and influenced by the same operating conditions. Even though the original focus of this work was not the optimisation of the TPBR, the possibility of assessing the suspension's radiative properties through the cultivation time by this methodology highlights the option of designing experiments in which these coefficients may be taken as variables to optimise. Considering that a high degree of light stratification may affect *L. platensis*, measuring the optical properties could help adjust the light source's quantity and quality to keep these parameters constant and regulate the light-to-biomass conversion values up to a maximum level.

(7). – Appendix for Chapter 5

	X [g L^{-1}]	0.111	0.152	0.245	0.330	0.541	0.611	0.674	0.715	0.747	0.763	0.764
$P(\mu_d) \geq 0.8$	$\left(\bar{\mu}_2^*\right)_{PAR}$	0.9979	0.9969	0.9950	0.9955	0.9969	0.9932	0.9944	0.9927	0.9953	0.9947	0.9941
$0.8 > P(\mu_d) \geq 0.6$	$\left(\bar{\mu}_3^*\right)_{PAR}$	0.9839	0.9919	0.9818	0.9842	0.9919	0.9861	0.9795	0.9911	0.9917	0.9916	0.9915
$0.6 > P(\mu_d) \geq 0.4$	$\left(\bar{\mu}_4^*\right)_{PAR}$	0.9223	0.9669	0.9451	0.9529	0.9491	0.9685	0.9353	0.9671	0.9781	0.9631	0.9541
$0.4 > P(\mu_d) \geq 0.2$	$\left(\bar{\mu}_5^*\right)_{PAR}$	0.7599	0.8079	0.7677	0.8607	0.7871	0.8714	0.7599	0.8171	0.8172	0.8121	0.7599
$0.2 > P(\mu_d)$	$\left(\bar{\mu}_6^*\right)_{PAR}$	0.5012	0.5508	0.6891	0.5607	0.5402	0.6851	0.6602	0.5307	0.4999	0.6710	0.6633

Table (3): The PAR average value of the coefficients generated by the optimisation algorithm, corresponding to the same series of absorption and scattering coefficients presented before.

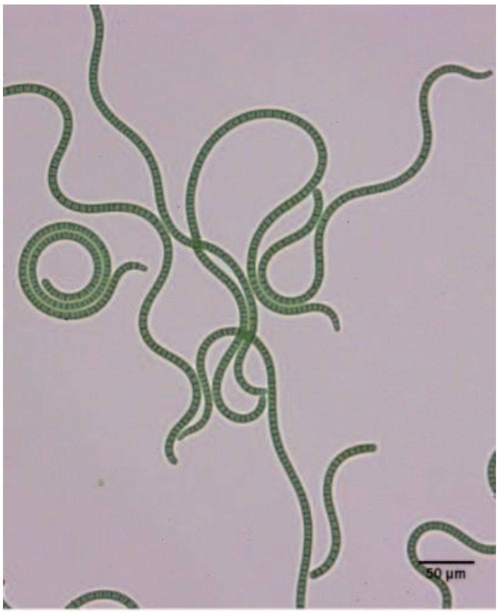

Figure 11: a microscopy picture of *Limnospira platensis* PCC7345.

Concluding remarks

To begin with, a physicochemical model was developed to simulate the culture medium and liquids with similar thermodynamic properties. This model makes it possible to determine the final composition of each of the species present in the culture medium from its original formulation, as well as the pH of the solution. In addition, it is possible to analyse the variations in the composition when the formulation is modified or when CO_2 is added to the gas stream. Lastly, with this perspective, it is also possible to design artificial wastewater or to study natural wastewater, simulating its behaviour accurately to the end of incorporating the physical-chemical properties of these complex aquatic environments into the study of relevant phenomena for microalgae cultivation, like the course of enzymatic kinetics or the gas-liquid mass transfer processes.

Furthermore, the liquid-gas transfer CO_2 was modelled using a model produced from systematically studying the kinetics of multiple equilibria taking place simultaneously. The latter has been achieved by employing irreversible thermodynamics. In addition, the parameters included in the model were determined, considering the exchanges of CO_2 between the aqueous phase and the bubbles residing in the culture medium and between the aqueous phase and the air chamber above the aqueous phase, as this spatial separation is irrelevant for modelling the gaseous phase in contact with the liquid. This study's main result highlights this perspective's potential for considering it into future contributions like modelling the O_2 mass transfer process or the kinetics of carbonic anhydrases.

Secondly, the emission of a commercial LED tube was characterised by defining and quantifying three properties, the intensity (related to the radiant flux) and the directional and spectral distribution functions. To this end, a model for the exchange of radiant energy between surfaces was adopted. Moreover, experiments were carried out with a radiometer and calculation algorithms were built in MATLAB. With the knowledge of the properties of the artificial radiant energy source, it was possible to design experiments in photobioreactors (PBRs) to demonstrate and study different phenomena related to the quantity, quality and distribution of light.

In addition, a methodology based on the Monte Carlo (MC) method was developed to simulate the radiant energy field inside horizontal tubular photobioreactors. So far, this methodology has been applied solely to the study of bubble column PBRs. This methodology assumes the radiant energy field as a set of photons moving at the speed of light and the microalgae suspension as a homogeneous medium with absorption and scattering centres distributed throughout the suspension. Modifications were made to the computational routine, which significantly reduced the calculation time and complexity (flexibility improved to be adapted to run in different computers/processing units and the network/cloud) of the algorithms for the calculation of the REF properties. With the newly proposed method, ad hoc algorithms were generated in MATLAB for all the cultivation systems and light sources used in this Thesis.

Thirdly, a method for determining the real-time radiative properties of microalgae suspensions was designed, presented and validated with a microorganism of commercial interest. This method is based on a previous methodology that utilises integrating spheres. It comprises a set of experimental measurements that resembles the so-called linear transmittance, diffuse transmittance and diffuse reflectance measurements, the numerical simulation of the experimental procedure (through the reproduction of the experiments employing the same MC way of solving the energy balance of the system under study) and the use of a stochastic optimisation programme (*fmincon + globasearch* of MATLAB). These optical properties are the spectral coefficients of absorption and scattering of radiant energy and the scattering phase function. The spectral absorption and scattering coefficients were also correlated with the respective cell dry weight in the suspension.

In conclusion, the construction of a predictive tool for estimating the performance of tubular photobioreactors was presented and applied to characterise a commercial unit for the production of *L. platensis* (Spirulina) dried powder in a start-up located in Dresden, Germany. The coefficients of absorption, scattering, and the scattering phase function were evaluated for different samples, and with these data, a mathematical model relating the REF properties with the cell growth has been used. Lastly, considering the accessibility granted for these new perspectives for characterising the optical properties of phototrophic suspensions, this presents a new milestone for proposing and designing experiments to optimise the production of target metabolites or to consider these parameters as a scaling-up variable to equalise among different production units.

Future perspectives

First and foremost, the present thesis was developed between the UNL and the TUD, and three academic research articles were produced through its completion. Additionally, the topics of the thesis presented a framework to work in collaboration for the master thesis of three students from the TU Dresden who contributed to it: Mr Esteban Lopera Corredor, Ms Sabine Franke and Mr Niklas Foerster. Further, in Argentina as well, for the Master Thesis of Mr Maximiliano Palmier and Mr Agustin Eduardo Tacca. Moreover and concerning funding, with the topics arising from the Thesis, Mr Manuel Ibañez became the beneficiary of two Capital Semilla research grants belonging to the UNL. These research funds were employed in constructing and improving new versions of the methodology presented in Chapters 4 and 5.

In relation to the mass transfer process of CO_2, further progress has been achieved in collaboration with other researchers of the UNL, and now this produced sufficient information to allow the presentation of a new research article for the study of the relationship between the modelling of the kinetics of gas-liquid CO_2 transfer and other operating variables like the temperature, flow rate and the composition of the carbon present in the gas phase. Due to the desorption of O_2 is a hotspot in what to microalgal bioprocesses are concerned, there is a possibility to apply the irreversible thermodynamic perspectives in quantifying the evolution of O_2 in photobioreactors. Nonetheless, the methodology for obtaining the kinetics of CO_2 evolution presented in this thesis is just one possible application of this perspective's full potential. Further studies should be conceived to address the kinetic relationship between carbonic anhydrases and CO_2 dissolution.

Last but not least, the topics related to radiant energy transfer were applied for the construction of three industrial-scale raceway reactors in the wastewater treatment facility of AYSA, located in Ezeiza, Buenos Aires, Argentina. The latter is the result of participating in a massive public-private funding project to establish an intelligent system of monitoring and modelling through machine learning, the evolution of open photobioreactors financed by the Argentinian government. Here, the participation of Mr Ibañez comprised the assessment of the directional and spectral composition of the solar radiation and the characteristics of the geographical location and the design of three raceway PBRs that were built at the beginning of 2022 and are currently fully operational at testing mode. The latter is a collaboration between AYSA (an Argentinian company), the University of Buenos Aires, and the University of the Litoral.

References

[1] A. Richmond, ‘Handbook of Microalgal Culture: Biotechnology and Applied Phycology’.

[2] R. E. Blankenship, *Molecular Mechanisms of PhotosynthesiS*.

[3] P. Physiology, L. Taiz, and E. Zeiger, ‘Chapter 7 - Photosynthesis: The Light Reactions -’, in *Plant physiology*, USA: Sinauer Associates, 2003, pp. 111–143.

[4] A. Kumar, A. Nath, and A. Brett, *Stress Biology of Cyanobacteria*.

[5] L. O. Björn *et al.*, ‘Technical discussion I underwater light measurement and light absorption by algae’, *Sci Mar*, vol. 60, no. SUPPL. 1, pp. 293–297, 1996.

[6] A. F. De Iorio, ‘Unicellular microalgae vs . filamentous algae for wastewater treatment and nutrient recovery’, vol. 59, no. August, 2021, doi: 10.1016/j.algal.2021.102442.

[7] J. R. F. Malapascua, C. G. Jerez, M. Sergejevová, and F. L. Figueroa, ‘Photosynthesis monitoring to optimize growth of microalgal mass cultures : application of chlorophyll fluorescence techniques’, vol. 22, pp. 123–140, 2014, doi: 10.3354/ab00597.

[8] J. Masojídek and G. Torzillo, ‘Mass Cultivation of Freshwater Microalgae’, *Encyclopedia of Ecology, Five-Volume Set*, pp. 2226–2235, 2008, doi: 10.1016/B978-008045405-4.00830-2.

[9] M. C. Mendes *et al.*, ‘Algae as Food in Europe: An Overview of Species Diversity and Their Application†’, *Foods*, vol. 11, no. 13, pp. 1–36, 2022, doi: 10.3390/foods11131871.

[10] G. Perspectives, *Global Perspectives on Astaxanthin*. Academic Press ELSEVIER.

[11] A. S. T. Ingenier, L. Creative, and C. Atribuci, ‘Aplicaciones de las microalgas: estado de la técnica’.

[12] L. S. Rizza, M. Eugenia, S. Smachetti, M. Do Nascimento, G. L. Salerno, and L. Curatti, ‘Bioprospecting for native microalgae as an alternative source of

sugars for the production of bioethanol', *Algal Res*, vol. 22, pp. 140–147, 2017, doi: 10.1016/j.algal.2016.12.021.

[13] F. Gabriel, A. Fernández, and C. Gómez-serrano, 'Recovery of Nutrients From Wastewaters Using Microalgae', vol. 2, no. September, pp. 1–13, 2018, doi: 10.3389/fsufs.2018.00059.

[14] J. Copia, H. Gaete, G. Zúñiga, M. Hidalgo, and E. Cabrera, 'Efecto de la radiación ultravioleta B en la producción de polifenoles en la microalga marina Chlorella sp . Effect of ultraviolet B radiation on the production of polyphenols in the marine microalga Chlorella sp .', vol. 40, no. 1, pp. 113–123, 2012, doi: 10.3856/vol40-issue1-fulltext-11.

[15] *BIOCHEMISTRY & MOLECULAR BIOLOGY OF PLANTS*.

[16] W. G. T. Willats, 'The cell walls of green algae : a journey through evolution and diversity', vol. 3, no. May, pp. 1–7, 2012, doi: 10.3389/fpls.2012.00082.

[17] A. M. Collins, M. Liberton, H. D. T. Jones, O. F. Garcia, H. B. Pakrasi, and J. A. Timlin, 'Photosynthetic pigment localization and thylakoid membrane morphology are altered in Synechocystis 6803 phycobilisome mutants', *Plant Physiol*, vol. 158, no. 4, pp. 1600–1609, 2012, doi: 10.1104/pp.111.192849.

[18] S. Baldanta, G. Guevara, and J. M. Navarro-Llorens, 'SEVA-Cpf1, a CRISPR-Cas12a vector for genome editing in cyanobacteria', *Microb Cell Fact*, vol. 21, no. 1, pp. 1–13, 2022, doi: 10.1186/s12934-022-01830-4.

[19] M. Giordano, J. Beardall, and J. A. Raven, 'CO 2 Concentrating Mechanisms in Algae : Mechanisms , Environmental Modulation , and Evolution', 2005, doi: 10.1146/annurev.arplant.56.032604.144052.

[20] R. J. Leonardi, M. V. Ibañez, M. N. Morelli, H. A. Irazoqui, and J. M. Heinrich, 'Influence of light stratification on the growth of Scenedesmus quadricauda', *Biochem Eng J*, vol. 148, no. April, pp. 97–107, 2019, doi: 10.1016/j.bej.2019.04.022.

[21] K. A. Publishers *et al.*, 'Chromatic regulation in Chlamydomonas reinhardtii alters photosystem stoichiometry and improves the quantum efficiency of photosynthesis', pp. 253–265, 1996.

[22] A. Lehmuskero, M. Skogen Chauton, and T. Boström, ‘Light and photosynthetic microalgae: A review of cellular- and molecular-scale optical processes’, *Prog Oceanogr*, vol. 168, pp. 43–56, 2018, doi: 10.1016/j.pocean.2018.09.002.

[23] T. Cardona, ‘Tansley insight On the origin of oxygenic photosynthesis and’, 2019, doi: 10.1111/nph.16249.

[24] M. V. Ibañez, R. J. Leonardi, and F. Krujatz, ‘The Assessment of the Real-Time Radiative Properties and Productivity of Limnospira platensis in Tubular Photobioreactors’, 2022.

[25] D. Shevela, ‘Adventures with cyanobacteria : a personal perspective’, vol. 2, no. July, pp. 1–17, 2011, doi: 10.3389/fpls.2011.00028.

[26] N. Bishop, K. Humbeck, and S. Romer, ‘The Mode of Adaptation of the Photosynthetic Apparatus of a Pigment Mutant of’, vol. 135, pp. 144–149, 1989, doi: 10.1016/S0176-1617(89)80167-1.

[27] A. Vadiveloo, N. R. Moheimani, J. J. Cosgrove, D. Parlevliet, and P. A. Bahri, ‘Effects of different light spectra on the growth , productivity and photosynthesis of two acclimated strains of Nannochloropsis sp .’, 2017, doi: 10.1007/s10811-017-1083-9.

[28] M. V. Ibañez, R. J. Leonardi, M. N. Morelli, H. A. Irazoqui, and J. M. Heinrich, ‘A colourimetric method for the measuring of the mass transfer kinetics of carbon dioxide in aqueous media’, *Algal Res*, vol. 45, no. October 2019, p. 101717, 2020, doi: 10.1016/j.algal.2019.101717.

[29] R. P. Rastogi, *Ecophysiology and Biochemistry of Cyanobacteria*.

[30] H. Sun, W. Zhao, X. Mao, Y. Li, T. Wu, and F. Chen, ‘Biotechnology for Biofuels High - value biomass from microalgae production platforms : strategies and progress based on carbon metabolism and energy conversion’, *Biotechnol Biofuels*, pp. 1–23, 2018, doi: 10.1186/s13068-018-1225-6.

[31] B. W. B. Holman, ‘Spirulina as a livestock supplement and animal feed’, 2012, doi: 10.1111/j.1439-0396.2012.01328.x.

[32] F. Camacho and A. Macedo, ‘Potential Industrial Applications and Commercialization of Microalgae in the Functional Food and Feed Industries : A Short Review’, no. i, 2019.

[33] P. Janczyk, B. Halle, and W. B. Souffrant, ‘Microbial community composition of the crop and ceca contents of laying hens fed diets supplemented with Chlorella vulgaris’, *Poult Sci*, vol. 88, no. 11, pp. 2324–2332, 2009, doi: 10.3382/ps.2009-00250.

[34] Y. Jiang, W. Zhang, J. Wang, Y. Chen, S. Shen, and T. Liu, ‘Bioresource Technology Utilization of simulated flue gas for cultivation of Scenedesmus dimorphus’, *Bioresour Technol*, vol. 128, no. X, pp. 359–364, 2013, doi: 10.1016/j.biortech.2012.10.119.

[35] J. C. B. Nutr, A. Satoh, S. Tsuji, Y. Okada, N. Murakami, and M. Urami, ‘Preliminary Clinical Evaluation of Toxicity and Efficacy of A New Astaxanthin-rich Haematococcus pluvialis Extract’, no. May, pp. 280–284, 2009.

[36] R. E. Mendoza, I. v García, L. de Cabo, C. F. Weigandt, A. Fabrizio, and D. Iorio, ‘Science of the Total Environment The interaction of heavy metals and nutrients present in soil and native plants with arbuscular mycorrhizae on the riverside in the Matanza-Riachuelo River Basin (Argentina)’, *Science of the Total Environment, The*, vol. 505, pp. 555–564, 2015, doi: 10.1016/j.scitotenv.2014.09.105.

[37] V. Matamoros and Y. Rodríguez, ‘Batch vs continuous-feeding operational mode for the removal of pesticides from agricultural run-off by microalgae systems : A laboratory scale study’, *J Hazard Mater*, vol. 309, pp. 126–132, 2016, doi: 10.1016/j.jhazmat.2016.01.080.

[38] B. Petrie, R. Barden, and B. Kasprzyk-hordern, ‘ScienceDirect A review on emerging contaminants in wastewaters and the environment : Current knowledge , understudied areas and recommendations for future monitoring’, *Water Res*, vol. 72, no. 0, pp. 3–27, 2014, doi: 10.1016/j.watres.2014.08.053.

[39] J. Stevenson, ‘R EVIEW ECOLOGICAL ASSESSMENTS WITH ALGAE : A REVIEW AND SYNTHESIS 1’, vol. 461, pp. 437–461, 2014, doi: 10.1111/jpy.12189.

[40] X. Tang *et al.*, ‘Construction of an artificial microalgal-bacterial consortium that efficiently degrades crude oil’, vol. 181, pp. 1158–1162, 2010, doi: 10.1016/j.jhazmat.2010.05.033.

[41] M. A. Borowitzka, ‘High-value products from microalgae — their development and commercialisation’, 2013, doi: 10.1007/s10811-013-9983-9.

[42] H. Zhang *et al.*, ‘Fucoxanthin : A Promising Medicinal and Nutritional Ingredient’, vol. 2015, 2015.

[43] S. K. Ali and A. M. Saleh, ‘Spirulina - An overview’, *Int J Pharm Pharm Sci*, vol. 4, no. SUPPL.3, pp. 9–15, 2012, doi: 10.1201/9780203025901.ch14.

[44] N. Korbee, ‘Acumulación de aminoácidos tipo micosporina (MAAs): biosíntesis , fotocontrol y funciones ecofisiológicas’, pp. 119–132, 2006.

[45] J. Liu, M. Sommerfeld, and Q. Hu, ‘Screening and characterization of Isochrysis strains and optimization of culture conditions for docosahexaenoic acid production’, pp. 4785–4798, 2013, doi: 10.1007/s00253-013-4749-5.

[46] P. K. Kumar, S. V. Krishna, K. Verma, K. Pooja, D. Bhagawan, and K. Srilatha, ‘Bio oil production from microalgae via hydrothermal liquefaction technology under subcritical water conditions’, *J Microbiol Methods*, vol. 153, no. July, pp. 108–117, 2018, doi: 10.1016/j.mimet.2018.09.014.

[47] S. Li, F. Li, X. Zhu, Q. Liao, J. Chang, and S. Ho, ‘Chemosphere Biohydrogen production from microalgae for environmental sustainability’, *Chemosphere*, vol. 291, no. P1, p. 132717, 2022, doi: 10.1016/j.chemosphere.2021.132717.

[48] R. Ramaraj and N. Dussadee, ‘Biological purification processes for biogas using algae cultures : A review’, vol. 4, pp. 20–32, 2015, doi: 10.11648/j.ijrse.s.2015040101.14.

[49] P. H. Baudelet, G. Ricochon, M. Linder, and L. Muniglia, ‘A new insight into cell walls of Chlorophyta’, *Algal Res*, vol. 25, no. October 2016, pp. 333–371, 2017, doi: 10.1016/j.algal.2017.04.008.

[50] M. J. Scholz *et al.*, ‘Ultrastructure and Composition of the Nannochloropsis gaditana Cell Wall’, no. September, 2014, doi: 10.1128/EC.00183-14.

[51] J. Alberto, V. Costa, and M. G. De Morais, ‘Bioresource Technology The role of biochemical engineering in the production of biofuels from microalgae’, *Bioresour Technol*, vol. 102, no. 1, pp. 2–9, 2011, doi: 10.1016/j.biortech.2010.06.014.

[52] M. Mondal, S. Goswami, A. Ghosh, and G. Oinam, ‘Production of biodiesel from microalgae through biological carbon capture : a review’, *3 Biotech*, vol. 7, no. 2, pp. 1–21, 2017, doi: 10.1007/s13205-017-0727-4.

[53] B. Singh, A. Guldhe, P. Singh, A. Singh, I. Rawat, and F. Bux, ‘Sustainable Production of Biofuels from Microalgae Using a Biorefinary Approach’, 2015, doi: 10.1007/978-81-322-2123-4.

[54] K. K. Sharma, H. Schuhmann, and P. M. Schenk, ‘High Lipid Induction in Microalgae for Biodiesel Production’, pp. 1532–1553, 2012, doi: 10.3390/en5051532.

[55] Y. Chisti, ‘Biodiesel from microalgae beats bioethanol’, no. January, 2008, doi: 10.1016/j.tibtech.2007.12.002.

[56] Y. Collos and P. J. Harrison, ‘Acclimation and toxicity of high ammonium concentrations to unicellular algae’, *Mar Pollut Bull*, vol. 80, no. 1–2, pp. 8–23, 2014, doi: 10.1016/j.marpolbul.2014.01.006.

[57] D. Vandamme, I. Foubert, I. Fraeye, B. Meesschaert, and K. Muylaert, ‘Bioresource Technology Flocculation of Chlorella vulgaris induced by high pH : Role of magnesium and calcium and practical implications’, *Bioresour Technol*, vol. 105, pp. 114–119, 2012, doi: 10.1016/j.biortech.2011.11.105.

[58] F. G. Acién, J. M. Fernández, J. J. Magán, and E. Molina, ‘Production cost of a real microalgae production plant and strategies to reduce it’, *Biotechnol Adv*, vol. 30, no. 6, pp. 1344–1353, 2012, doi: 10.1016/j.biotechadv.2012.02.005.

[59] K. L. Terry and L. P. Raymond, ‘System design for the autotrophic production of microalgae’, vol. 7, pp. 474–487, 1985.

[60] M. A. Borowitzka, ‘Commercial production of microalgae : ponds , tanks , tubes and fermenters’, vol. 70, pp. 313–321, 1999.

[61] N. Norsker, M. J. Barbosa, M. H. Vermuë, and R. H. Wijffels, ‘Microalgal production — A close look at the economics’, *Biotechnol Adv*, vol. 29, no. 1, pp. 24–27, 2011, doi: 10.1016/j.biotechadv.2010.08.005.

[62] J. B. K. Park, R. J. Craggs, and A. N. Shilton, ‘Bioresource Technology Wastewater treatment high rate algal ponds for biofuel production’, *Bioresour Technol*, vol. 102, no. 1, pp. 35–42, 2011, doi: 10.1016/j.biortech.2010.06.158.

[63] J. P. Hoffmann, ‘MINIREVIEW WASTEWATER TREATMENT WITH SUSPENDED AND NONSUSPENDED ALGAE 1’, vol. 763, pp. 757–763, 1998.

[64] J. C. Weissman and R. P. G. M. Products, ‘Microalgal Open Pond Systems for the Purpose of Producing Fuels’.

[65] A. Richmond and Z. Cheng-wu, ‘Optimization of a flat plate glass reactor for mass production of Nannochloropsis sp . outdoors’, vol. 85, pp. 259–269, 2001.

[66] R. Bosma, J. H. de Vree, P. M. Slegers, M. Janssen, R. H. Wijffels, and M. J. Barbosa, ‘Design and construction of the microalgal pilot facility AlgaePARC’, 2014.

[67] F. G. Aci *et al.*, *Photobioreactors for the production of microalgae 1 ´*. 2017. doi: 10.1016/B978-0-08-101023-5.00001-7.

[68] M. Huesemann *et al.*, ‘Simulation of outdoor pond cultures using indoor LED-lighted and temperature-controlled raceway ponds and Phenometrics photobioreactors’, *ALGAL*, vol. 21, pp. 178–190, 2017, doi: 10.1016/j.algal.2016.11.016.

[69] P. Stephen and R. John, *Microalgal Production*.

[70] S. Africa and C. Republic, ‘Variation in some photosynthetic characteristics of microalgae cultured in outdoor thin-layered sloping reactors’, vol. 2, pp. 175–184, 1995.

[71] A. P. Carvalho, A. Meireles, and F. X. Malcata, ‘Microalgal Reactors : A Review of Enclosed System Designs and Performances’, no. ii, pp. 1490–1506, 2006.

[72] E. Molina, J. Ferna, F. G. Acie, and Y. Chisti, ‘Tubular photobioreactor design for algal cultures’, vol. 92, pp. 113–131, 2001.

[73] M. R. Tredici *et al.*, ‘Energy balance of algal biomass production in a 1-ha “‘ Green Wall Panel ’” plant : How to produce algal biomass in a closed reactor achieving a high Net Energy Ratio q’, *Appl Energy*, vol. 154, pp. 1103–1111, 2015, doi: 10.1016/j.apenergy.2015.01.086.

[74] M. Lemar, E. Vermel, and R. Pradelles, ‘Appraisal of a horizontal two-phase flow photobioreactor for industrial production of delicate microalgae species’, pp. 349–355, 2012, doi: 10.1007/s10811-012-9820-6.

[75] M. R. Tredici, ‘Photobiology of microalgae mass cultures : understanding the tools for the next green revolution’, vol. 1, pp. 143–162, 2010.

[76] S. Jørgensen and B. Fath, Eds., ‘Mass Cultivation of Freshwater Microalgae’, in *Encyclopedia of Ecology*, London: Academic Press Oxford, 2008, pp. 2226–2235.

[77] G. Zittelli, N. Biondi, L. Rodolfi, and M. Tredici, ‘Photobioreactors for Microalgal Biofuel Production’, in *Handbook of Microalgal Culture: Applied Phycology and Biotechnology*, 2nd editio., Q. H. A Richmond, Ed. John Wiley and Sons, 2013, pp. 225–266.

[78] A. Martins, N. S. Caetano, and T. M. Mata, ‘Microalgae for biodiesel production and other applications : A review’, vol. 14, pp. 217–232, 2010, doi: 10.1016/j.rser.2009.07.020.

[79] K. J. Lauersen *et al.*, ‘Phototrophic production of heterologous diterpenoids and a hydroxy- functionalized derivative from Chlamydomonas reinhardtii’, *Metab Eng*, vol. 48, no. July, pp. 0–1, 2018, doi: 10.1016/j.ymben.2018.07.005.

[80] T. Duarte-santos, J. L. Mendoza-martín, F. G. A. Fernández, E. Molina, and J. A. Vieira-costa, ‘Bioresource Technology Optimization of carbon dioxide supply in raceway reactors : Influence of carbon dioxide molar fraction and gas flow rate’, *Bioresour Technol*, vol. 212, pp. 72–81, 2016, doi: 10.1016/j.biortech.2016.04.023.

[81] J. M. F. Sevilla, F. G. A. Fernandez, and A. C. Gomez, ‘in Light-Limited Chemostat Culture’, pp. 167–173, 1994.

[82] G. V. Swarnalatha, N. S. Hegde, V. S. Chauhan, and R. Sarada, ‘The effect of carbon dioxide rich environment on carbonic anhydrase activity, growth and metabolite production in indigenous freshwater microalgae’, *Algal Res*, vol. 9, pp. 151–159, 2015, doi: 10.1016/j.algal.2015.02.014.

[83] N. M. Langley, S. T. L. Harrison, and R. P. van Hille, ‘A critical evaluation of CO 2 supplementation to algal systems by direct injection’, *Biochem Eng J*, vol. 68, pp. 70–75, 2012, doi: 10.1016/j.bej.2012.07.013.

[84] K. K. Vasumathi, M. Premalatha, and P. Subramanian, ‘Parameters influencing the design of photobioreactor for the growth of microalgae’, *Renewable and Sustainable Energy Reviews*, vol. 16, no. 7, pp. 5443–5450, 2012, doi: 10.1016/j.rser.2012.06.013.

[85] M. Caia, O. Bernard, and Q. Béchet, ‘Optimizing CO2 transfer in algal open ponds’, *Algal Res*, vol. 35, no. May, pp. 530–538, 2018, doi: 10.1016/j.algal.2018.09.009.

[86] C. Shene, Y. Chisti, M. Bustamante, and M. Rubilar, ‘Effect of CO2 in the aeration gas on cultivation of the microalga Nannochloropsis oculata: Experimental study and mathematical modeling of CO2 assimilation’, *Algal Res*, vol. 13, no. 3, pp. 16–29, 2016, doi: 10.1016/j.algal.2015.11.005.

[87] R. Pohorecki and W. Moniuk, ‘Kinetics of reaction between carbon dioxide and hydroxyl ions in aqueous electrolyte solutions’, *Chem Eng Sci*, vol. 43, no. 7, pp. 1677–1684, 1988, doi: 10.1016/0009-2509(88)85159-5.

[88] J. Elhajj, M. Al-Hindi, and F. Azizi, ‘A review of the absorption and desorption processes of carbon dioxide in water systems’, *Ind Eng Chem Res*, vol. 53, no. 1, pp. 2–22, 2014, doi: 10.1021/ie403245p.

[89] L. Van Den Berg, ‘Carbon dioxide absorption and desorption in a packed tower using water and solutions of sodium carbonate and of triethanolamine’, *Can J Chem Eng*, vol. 40, no. 6, pp. 250–253, 1962, doi: 10.1002/cjce.5450400605.

[90] G. A. Hill, ‘Measurement of overall volumetric mass transfer coefficients for carbon dioxide in a well-mixed reactor using a pH probe’, *Ind Eng Chem Res*, vol. 45, no. 16, pp. 5796–5800, 2006, doi: 10.1021/ie060242t.

[91] M. Kordač and V. Linek, ‘Dynamic measurement of carbon dioxide volumetric mass transfer coefficient in a well-mixed reactor using a pH probe: Analysis of the salt and supersaturation effects’, *Ind Eng Chem Res*, vol. 47, no. 4, pp. 1310–1317, 2008, doi: 10.1021/ie0711776.

[92] M. Al-Hindi and F. Azizi, ‘Absorption and desorption of carbon dioxide in several water types’, *Canadian Journal of Chemical Engineering*, vol. 96, no. 1, pp. 274–284, 2018, doi: 10.1002/cjce.22901.

[93] B. Tamburic, C. R. Evenhuis, J. R. Crosswell, and P. J. Ralph, ‘An empirical process model to predict microalgal carbon fixation rates in photobioreactors’, *Algal Res*, vol. 31, no. May 2017, pp. 334–346, 2018, doi: 10.1016/j.algal.2018.02.014.

[94] R. W. Babcock, J. Malda, and J. A. C. Radway, ‘Hydrodynamics and mass transfer in a tubular airlift photobioreactor’, *J Appl Phycol*, vol. 14, no. 3, pp. 169–184, 2002, doi: 10.1023/A:1019924226457.

[95] S. K. Dahod, ‘Dissolved Carbon Dioxide Measurement and Its Correlation with Operating Parameters in Fermentation Processes’, *Biotechnol Prog*, vol. 9, no. 6, pp. 655–660, 1993, doi: 10.1021/bp00024a014.

[96] R. A. Robinson and R. H. Stokes, ‘Electrolyte Solutions’, in *Electrolyte Solutions*, Second Edi., London: Butterworth & Co., 197AD, p. 518.

[97] K. Michaelian, ‘A non-linear irreversible thermodynamic perspective on organic pigment proliferation and biological evolution’, *J Phys Conf Ser*, vol. 475, no. 1, 2013, doi: 10.1088/1742-6596/475/1/012010.

[98] G. Breuer, P. P. Lamers, D. E. Martens, R. B. Draaisma, and R. H. Wijffels, ‘Effect of light intensity, pH, and temperature on triacylglycerol (TAG) accumulation induced by nitrogen starvation in Scenedesmus obliquus’, *Bioresour Technol*, vol. 143, pp. 1–9, 2013, doi: 10.1016/j.biortech.2013.05.105.

[99] A. W. D. Larkum, I. L. Ross, O. Kruse, and B. Hankamer, ‘Selection, breeding and engineering of microalgae for bioenergy and biofuel production’, *Trends Biotechnol*, vol. 30, no. 4, pp. 198–205, 2012, doi: 10.1016/j.tibtech.2011.11.003.

[100] A. Melis, ‘Photosynthesis-to-fuels: From sunlight to hydrogen, isoprene, and botryococcene production’, *Energy Environ Sci*, vol. 5, no. 2, pp. 5531–5539, 2012, doi: 10.1039/c1ee02514g.

[101] E. Stephens *et al.*, ‘Future prospects of microalgal biofuel production systems’, *Trends Plant Sci*, vol. 15, no. 10, pp. 554–564, 2010, doi: 10.1016/j.tplants.2010.06.003.

[102] Q. Béchet, A. Shilton, and B. Guieysse, ‘Modeling the effects of light and temperature on algae growth : State of the art and critical assessment for productivity prediction during outdoor cultivation’, *Biotechnol Adv*, vol. 31, no. 8, pp. 1648–1663, 2013, doi: 10.1016/j.biotechadv.2013.08.014.

[103] E. Rodríguez-Miranda, J. L. Guzmán, F. G. Acién, M. Berenguel, and A. Visioli, ‘Indirect regulation of temperature in raceway reactors by optimal management of culture depth’, *Biotechnol Bioeng*, vol. 118, no. 3, pp. 1186–1198, 2021, doi: 10.1002/bit.27642.

[104] N. Yeh and J. P. Chung, ‘High-brightness LEDs-Energy efficient lighting sources and their potential in indoor plant cultivation’, *Renewable and Sustainable Energy Reviews*, vol. 13, no. 8, pp. 2175–2180, 2009, doi: 10.1016/j.rser.2009.01.027.

[105] E. G. Nwoba, D. A. Parlevliet, D. W. Laird, K. Alameh, and N. R. Moheimani, ‘Light management technologies for increasing algal photobioreactor e ffi ciency’, *Algal Res*, vol. 39, no. September 2018, p. 101433, 2019, doi: 10.1016/j.algal.2019.101433.

[106] P. S. C. Schulze, L. A. Barreira, H. G. C. Pereira, J. A. Perales, and J. C. S. Varela, ‘Light emitting diodes (LEDs) applied to microalgal production’, *Trends Biotechnol*, vol. 32, no. 8, pp. 422–430, 2014, doi: 10.1016/j.tibtech.2014.06.001.

[107] M. Glemser, M. Heining, J. Schmidt, A. Becker, D. Garbe, and R. Buchholz, ‘Application of light-emitting diodes (LEDs) in cultivation of phototrophic

microalgae : current state and perspectives', 2015, doi: 10.1007/s00253-015-7144-6.

[108] R. J. Leonardi, M. V. Ibañez, E. N. Osella, and J. M. Heinrich, 'Laboratory-scale reproduction of lighting conditions for an outdoor vertical column photobioreactor: Theoretical fundamentals and operation of a programmable LED module', *Algal Res*, vol. 55, no. December 2020, 2021, doi: 10.1016/j.algal.2021.102227.

[109] F. Ferrón-Carrillo *et al.*, 'LED Enhances Plant Performance and Both Carotenoids and Nitrates Profiles in Lettuce', *Plant Foods for Human Nutrition*, vol. 76, no. 2, pp. 210–218, 2021, doi: 10.1007/s11130-021-00894-8.

[110] S. Franke, J. Steingröwer, T. Walther, and F. Krujatz, 'The Oxygen Paradigm—Quantitative Impact of High Concentrations of Dissolved Oxygen on Kinetics and Large-Scale Production of Arthrospira platensis', *ChemEngineering*, vol. 6, no. 1, pp. 1–22, 2022, doi: 10.3390/chemengineering6010014.

[111] R. J. Leonardi, I. Niizawa, H. A. Irazoqui, and J. M. Heinrich, 'Modeling and simulation of the influence of fractions of blue and red light on the growth of the microalga Scenedesmus quadricauda', *Biochem Eng J*, vol. 129, pp. 16–25, 2018, doi: 10.1016/j.bej.2017.10.014.

[112] S. Astolfi, C. Marianello, S. Grego, and R. Bellarosa, 'Preliminary investigation of LED lighting as growth light for seedlings from different tree species in growth chambers', *Not Bot Horti Agrobot Cluj Napoca*, vol. 40, no. 2, pp. 31–38, 2012, doi: 10.15835/nbha4028221.

[113] M. N. Özisik, 'Radiative Transfer and Interactions with Conduction and Convection', 1973, pp. 249–253.

[114] E. M. Grima, F. G. Acie, and Y. Chisti, 'Photobioreactors : light regime , mass transfer , and scaleup', vol. 70, pp. 231–247, 1999.

[115] M. Janssen *et al.*, 'Scale-up aspects of photobioreactors : effects of mixing-induced light / dark cycles', pp. 225–237, 2000.

[116] I. Niizawa, J. Miguel, H. Antonio, J. M. Heinrich, and H. A. Irazoqui, 'Modeling of the influence of light quality on the growth of microalgae in a laboratory scale

photo-bio-reactor irradiated by arrangements of blue and red LEDs', *Biochem Eng J*, vol. 90, pp. 214–223, 2014, doi: 10.1016/j.bej.2014.05.002.

[117] J. M. Ferna, F. G. Acie, and E. M. Grima, 'Photobioreactors for the production of microalgae', pp. 131–151, 2013, doi: 10.1007/s11157-012-9307-6.

[118] H. BERBEROGLU, L. PILON, and A. MELIS, 'Radiation characteristics of Chlamydomonas reinhardtii CC125 and its truncated chlorophyll antenna transformants tla1, tlaX and tla1-CW+', *Int J Hydrogen Energy*, vol. 33, no. 22, pp. 6467–6483, 2008, doi: 10.1016/j.ijhydene.2008.07.071.

[119] H. Berberoglu and L. Pilon, 'Experimental measurements of the radiation characteristics of Anabaena variabilis ATCC 29413-U and Rhodobacter sphaeroides ATCC 49419', *Int J Hydrogen Energy*, vol. 32, no. 18, pp. 4772–4785, 2007, doi: 10.1016/j.ijhydene.2007.08.018.

[120] L. Pilon, H. Berberoĝlu, and R. Kandilian, 'Radiation transfer in photobiological carbon dioxide fixation and fuel production by microalgae', *J Quant Spectrosc Radiat Transf*, vol. 112, no. 17, pp. 2639–2660, 2011, doi: 10.1016/j.jqsrt.2011.07.004.

[121] L. Pottier, J. Pruvost, J. Deremetz, J. Cornet, J. Legrand, and C. G. Dussap, 'A Fully Predictive Model for One-Dimensional Light Attenuation by Chlamydomonas reinhardtii in a Torus Photobioreactor', 2005, doi: 10.1002/bit.20475.

[122] J. Pruvost, J. Legrand, P. Legentilhomme, and A. Muller-Feuga, 'Simulation of microalgae growth in limiting light conditions: Flow effect', *AIChE Journal*, vol. 48, no. 5, pp. 1109–1120, 2002, doi: 10.1002/aic.690480520.

[123] J. F. Cornet, C. G. Dussap, and G. Dubertret, 'A structured model for simulation of cultures of the cyanobacterium Spirulina platensis in photobioreactors: I. Coupling between light transfer and growth kinetics', *Biotechnol Bioeng*, vol. 40, no. 7, pp. 817–825, 1992, doi: 10.1002/bit.260400709.

[124] J. Dauchet, S. Blanco, J. F. Cornet, M. El Hafi, V. Eymet, and R. Fournier, 'The practice of recent radiative transfer Monte Carlo advances and its contribution to the field of microorganisms cultivation in photobioreactors', *J*

Quant Spectrosc Radiat Transf, vol. 128, pp. 52–59, 2013, doi: 10.1016/j.jqsrt.2012.07.004.

[125] J. M. Heinrich, I. Niizawa, F. A. Botta, A. R. Trombert, and H. A. Irazoqui, 'Analysis and design of photobioreactors for microalgae production I: Method and parameters for radiation field simulation', *Photochem Photobiol*, vol. 88, no. 4, pp. 938–951, 2012, doi: 10.1111/j.1751-1097.2012.01141.x.

[126] J. M. Heinrich, I. Niizawa, F. A. Botta, A. R. Trombert, and H. A. Irazoqui, 'Stratification of the radiation field inside a photobioreactor during microalgae growth', *Photochem Photobiol*, vol. 89, no. 5, pp. 1127–1134, 2013, doi: 10.1111/php.12095.

[127] J. M. Heinrich and H. A. Irazoqui, 'Kinetic Model of Photoautotrophic Growth of Chlorella sp. Microalga, Isolated from the Setúbal Lagoon', *Photochem Photobiol*, vol. 91, no. 5, pp. 1095–1102, 2015, doi: 10.1111/php.12468.

[128] J. M. Heinrich, I. Niizawa, F. A. Botta, A. R. Trombert, and H. A. Irazoqui, 'Analysis and design of photobioreactors for microalgae production II: Experimental Validation of a radiation field simulator based on a Monte Carlo algorithm', in *Photochemistry and Photobiology*, Jul. 2012, vol. 88, no. 4, pp. 952–960. doi: 10.1111/j.1751-1097.2012.01149.x.

[129] C. Posten and C. Walter, *Microalgal biotechnology: potential and production*. Walter de Gruyter, 2012.

[130] J. Pruvost, J. F. Cornet, F. Le Borgne, V. Goetz, and J. Legrand, 'Theoretical investigation of microalgae culture in the light changing conditions of solar photobioreactor production and comparison with cyanobacteria', *Algal Res*, vol. 10, pp. 87–99, 2015, doi: 10.1016/j.algal.2015.04.005.

[131] R. Kandilian, E. Lee, and L. Pilon, 'Radiation and optical properties of Nannochloropsis oculata grown under different irradiances and spectra', *Bioresour Technol*, vol. 137, pp. 63–73, 2013, doi: 10.1016/j.biortech.2013.03.058.

[132] R. L. Heng and L. Pilon, 'Radiation characteristics and effective optical properties of dumbbell-shaped cyanobacterium Synechocystis sp.', *J Quant Spectrosc Radiat Transf*, vol. 174, pp. 65–78, 2016, doi: 10.1016/j.jqsrt.2016.01.023.

[133] J. Dauchet, S. Blanco, J. F. Cornet, and R. Fournier, ‘Calculation of the radiative properties of photosynthetic microorganisms’, *J Quant Spectrosc Radiat Transf*, vol. 161, pp. 60–84, 2015, doi: 10.1016/j.jqsrt.2015.03.025.

[134] S. Bellini *et al.*, ‘Simulation Method Linking Dense Microalgal Culture Spectral Properties in the 400 – 750 nm Range to the Physiology of the Cells’, vol. 0, no. 0, pp. 1–16, 2016, doi: 10.1177/0003702816641270.

[135] J. Hoeniges *et al.*, ‘Effect of colony formation on light absorption by Botryococcus braunii’, *Algal Res*, vol. 50, no. June, p. 101985, 2020, doi: 10.1016/j.algal.2020.101985.

[136] E. Lee, R. L. Heng, and L. Pilon, ‘Spectral optical properties of selected photosynthetic microalgae producing biofuels’, *J Quant Spectrosc Radiat Transf*, vol. 114, pp. 122–135, 2013, doi: 10.1016/j.jqsrt.2012.08.012.

[137] R. L. Heng and L. Pilon, ‘Time-dependent radiation characteristics of Nannochloropsis oculata during batch culture’, *J Quant Spectrosc Radiat Transf*, vol. 144, pp. 154–163, 2014, doi: 10.1016/j.jqsrt.2014.04.008.

[138] R. Kandilian, J. Pruvost, A. Artu, C. Lemasson, J. Legrand, and L. Pilon, ‘Comparison of experimentally and theoretically determined radiation characteristics of photosynthetic microorganisms’, *J Quant Spectrosc Radiat Transf*, vol. 175, pp. 30–45, 2016, doi: 10.1016/j.jqsrt.2016.01.031.

[139] K. Witkowski, T. Król, A. Zieliński, and E. Kuteń, ‘A light-scattering matrix for unicellular marine phytoplankton’, *Limnol Oceanogr*, vol. 43, no. 5, pp. 859–869, 1998, doi: 10.4319/lo.1998.43.5.0859.

[140] M. V. Ibañez, R. J. Leonardi, J. M. Heinrich, J. Steingroewer, T. Walther, and K. Felix, ‘A rapid assessment of the radiative properties from a suspension of Chromochloris zofingiensis’, *J Photochem Photobiol*, vol. 3–4, no. June, p. 100007, 2020, doi: 10.1016/j.jpap.2020.100007.

[141] J. hui Chen, L. Liu, and D. Wei, ‘Enhanced production of astaxanthin by Chromochloris zofingiensis in a microplate-based culture system under high light irradiation’, *Bioresour Technol*, vol. 245, pp. 518–529, 2017, doi: 10.1016/j.biortech.2017.08.102.

[142] K. S. Khoo *et al.*, 'Recent advances in downstream processing of microalgae lipid recovery for biofuel production', *Bioresour Technol*, vol. 304, no. December 2019, p. 122996, 2020, doi: 10.1016/j.biortech.2020.122996.

[143] S. N. Ani Azaman, N. Nagao, F. M. Yusoff, S. W. Tan, and S. K. Yeap, 'A comparison of the morphological and biochemical characteristics of chlorella sorokiniana and chlorella zofingiensis cultured under photoautotrophic and mixotrophic conditions', *PeerJ*, vol. 2017, no. 9, 2017, doi: 10.7717/peerj.3473.

[144] Z. Zhang, D. Sun, Y. Zhang, and F. Chen, 'Chloroplast morphogenesis in Chromochloris zofingiensis in the dark', *Algal Res*, vol. 45, no. November 2019, p. 101742, 2020, doi: 10.1016/j.algal.2019.101742.

[145] X. Mao, T. Wu, D. Sun, Z. Zhang, and F. Chen, 'Differential responses of the green microalga Chlorella zofingiensis to the starvation of various nutrients for oil and astaxanthin production', *Bioresour Technol*, vol. 249, no. September 2017, pp. 791–798, 2018, doi: 10.1016/j.biortech.2017.10.090.

[146] J. Liu, X. Mao, W. Zhou, and M. T. Guarnieri, 'Simultaneous production of triacylglycerol and high-value carotenoids by the astaxanthin-producing oleaginous green microalga Chlorella zofingiensis', *Bioresour Technol*, vol. 214, pp. 319–327, 2016, doi: 10.1016/j.biortech.2016.04.112.

[147] Z. Zhang, J. J. Huang, D. Sun, Y. Lee, and F. Chen, 'Two-step cultivation for production of astaxanthin in Chlorella zofingiensis using a patented energy-free rotating floating photobioreactor (RFP)', *Bioresour Technol*, vol. 224, pp. 515–522, 2017, doi: 10.1016/j.biortech.2016.10.081.

[148] Y. Zhang, M. Shi, X. Mao, Y. Kou, and J. Liu, 'Time-resolved carotenoid profiling and transcriptomic analysis reveal mechanism of carotenogenesis for astaxanthin synthesis in the oleaginous green alga Chromochloris zofingiensis', *Biotechnol Biofuels*, vol. 12, no. 1, pp. 1–19, 2019, doi: 10.1186/s13068-019-1626-1.

[149] H. Berberoglu and L. Pilon, 'Experimental measurements of the radiation characteristics of Anabaena variabilis ATCC 29413-U and Rhodobacter sphaeroides ATCC 49419', *Int J Hydrogen Energy*, vol. 32, no. 18, pp. 4772–4785, 2007, doi: 10.1016/j.ijhydene.2007.08.018.

[150] A. Lehmuskero, M. Skogen Chauton, and T. Boström, ‘Light and photosynthetic microalgae: A review of cellular- and molecular-scale optical processes’, *Prog Oceanogr*, vol. 168, no. September, pp. 43–56, 2018, doi: 10.1016/j.pocean.2018.09.002.

[151] D. Fuente, J. Keller, J. A. Conejero, M. Rögner, S. Rexroth, and J. F. Urchueguía, ‘Light distribution and spectral composition within cultures of micro-algae: Quantitative modelling of the light field in photobioreactors’, *Algal Res*, vol. 23, pp. 166–177, 2017, doi: 10.1016/j.algal.2017.01.004.

[152] F. Krujatz *et al.*, ‘Light-field-characterization in a continuous hydrogen-producing photobioreactor by optical simulation and computational fluid dynamics’, *Biotechnol Bioeng*, vol. 112, no. 12, pp. 2439–2449, 2015, doi: 10.1002/bit.25667.

[153] R. Kandilian, J. Pruvost, J. Legrand, and L. Pilon, ‘Influence of light absorption rate by Nannochloropsis oculata on triglyceride production during nitrogen starvation’, *Bioresour Technol*, vol. 163, pp. 308–319, 2014, doi: 10.1016/j.biortech.2014.04.045.

[154] M. A. Borowitzka and N. R. Moheimani, ‘Algae for biofuels and energy’, *Algae for Biofuels and Energy*, pp. 1–288, 2013, doi: 10.1007/978-94-007-5479-9.

[155] K. Schediwy, A. Trautmann, C. Steinweg, and C. Posten, ‘Microalgal kinetics — a guideline for photobioreactor design and process development’, *Eng Life Sci*, vol. 19, no. 12, pp. 830–843, 2019, doi: 10.1002/elsc.201900107.

[156] G. Papapanagiotou and S. Gkelis, ‘Taxonomic revision of commercially used Arthrospira (Cyanobacteria) strains : a polyphasic approach Taxonomic revision of commercially used Arthrospira (Cyanobacteria) strains : a polyphasic approach’, *Eur J Phycol*, vol. 54, no. 4, pp. 595–608, 2019, doi: 10.1080/09670262.2019.1624832.

[157] P. Nowicka-krawczyk, R. Mühlsteinová, and T. Hauer, ‘Detailed characterization of the Arthrospira type species separating commercially grown taxa into the new genus Limnospira (Cyanobacteria)’, no. August 2018, pp. 1–11, 2019, doi: 10.1038/s41598-018-36831-0.

[158] D. Yuan *et al.*, 'Biodiversity and distribution of microzooplankton in Spirulina (Arthrospira) platensis mass cultures throughout China', *Algal Res*, vol. 30, no. December 2017, pp. 38–49, 2018, doi: 10.1016/j.algal.2017.12.009.

[159] I. Niizawa, R. J. Leonardi, H. A. Irazoqui, and J. M. Heinrich, 'Light wavelength distribution effects on the growth rate of Scenedesmus quadricauda', *Biochem Eng J*, vol. 126, pp. 126–134, 2017, doi: 10.1016/j.bej.2016.09.006.

[160] C. E. Pfaffinger, T. S. Severin, A. C. Apel, J. Göbel, J. Sauter, and D. Weuster-Botz, 'Light-dependent growth kinetics enable scale-up of well-mixed phototrophic bioprocesses in different types of photobioreactors', *J Biotechnol*, vol. 297, no. January, pp. 41–48, 2019, doi: 10.1016/j.jbiotec.2019.03.003.

[161] B. Šantek, M. Ivančić, P. Horvat, S. Novak, and V. Marić, 'Horizontal tubular bioreactors in biotechnology', *Chem Biochem Eng Q*, vol. 20, no. 4, pp. 389–399, 2006.

[162] P. Fernández del Olmo, F. G. Acién, and J. M. Fernández-Sevilla, 'Productivity analysis in tubular photobioreactors using a dynamic photosynthesis model coupled to computational fluid dynamics particle tracking', *Bioresour Technol*, no. September, p. 126277, 2021, doi: 10.1016/j.biortech.2021.126277.

[163] A. Lehmuskero, M. Skogen Chauton, and T. Boström, 'Light and photosynthetic microalgae: A review of cellular- and molecular-scale optical processes', *Prog Oceanogr*, vol. 168, no. September, pp. 43–56, 2018, doi: 10.1016/j.pocean.2018.09.002.

[164] C. G. Jerez, J. R. Malapascua, M. Sergejevová, and F. L. Figueroa, 'Chlorella fusca (Chlorophyta) grown in thin-layer cascades : Estimation of biomass productivity by in-vivo chlorophyll a fl uorescence monitoring', vol. 17, pp. 21–30, 2016, doi: 10.1016/j.algal.2016.04.010.

[165] G. C. Zittelli *et al.*, 'Effects of blue , orange and white lights on growth , chlorophyll fluorescence , and phycocyanin production of Arthrospira platensis cultures', *Algal Res*, vol. 61, no. December 2021, p. 102583, 2022, doi: 10.1016/j.algal.2021.102583.

[166] M. Nicol, R. Jorge, and M. Vicente, ‘Evaluation of the phototrophic growth of Haematococcus pluvialis under outdoor lighting conditions inside a bubble column reactor at a laboratory scale’, vol. 66, no. June, 2022, doi: 10.1016/j.algal.2022.102800.

[167] F. Krujatz *et al.*, ‘Think outside the box: 3D bioprinting concepts for biotechnological applications – recent developments and future perspectives’, *Biotechnol Adv*, vol. 58, no. September 2021, 2022, doi: 10.1016/j.biotechadv.2022.107930.

[168] A. Nosratimovafagh, A. E. Fereidouni, and F. Krujatz, ‘Modeling and Optimizing the Effect of Light Color , Sodium Chloride and Glucose Concentration on Biomass Production and the Quality of Arthrospira platensis Using Response Surface Methodology (RSM)’, pp. 1–19, 2022.

[169] A. E. Cassano, C. A. Martín, R. J. Brandi, and O. M. Alfano, ‘Photoreactor Analysis and Design: Fundamentals and Applications’, *Ind Eng Chem Res*, vol. 34, no. 7, pp. 2155–2201, 1995, doi: 10.1021/ie00046a001.

[170] A. K. Sahu, K. K. Vasumathi, and M. Premalatha, ‘Simulation of solar light intensity distribution in open pond photobioreactor’, pp. 50–57, 2011.

[171] Z. Ma and K. Gao, ‘Photoregulation of morphological structure and its physiological relevance in the cyanobacterium Arthrospira (Spirulina) platensis’, *Planta*, vol. 230, no. 2, pp. 329–337, 2009, doi: 10.1007/s00425-009-0947-x.

[172] A. E. Solovchenko, O. B. Chivkunova, and I. P. Maslova, ‘Pigment Composition , Optical Properties , and Resistance to Photodamage of the Microalga Haematococcus pluvialis Cultivated under High Light’, vol. 58, no. 1, pp. 12–20, 2011, doi: 10.1134/S1021443710061056.

[173] M. Olaizolal and E. O. Duerr, ‘Effects of light intensity and quality on the growth rate and photosynthetic pigment content of Spirulina platensis’, *J. Appl. Phycol.*, vol. 2, pp. 97–104, 1990.

[174] P. Nomsawai, N. Tandeau De Marsac, J. C. Thomas, M. Tanticharoen, and S. Cheevadhanarak, ‘Light regulation of phycobilisome structure and gene

expression in Spirulina platensis C1 (Arthrospira sp. PCC 9438)', *Plant Cell Physiol*, vol. 40, no. 12, pp. 1194–1202, 1999, doi: 10.1093/oxfordjournals.pcp.a029507.

[175] A. Morel, Yu-Hwan Ahn, F. Partensky, D. Vaulot, and H. Claustre, 'Prochlorococcus and Synechococcus: a comparative study of their optical properties in relation to their size and pigmentation', *J Mar Res*, vol. 51, no. 3, pp. 617–649, 1993, doi: 10.1357/0022240933223963.

[176] M. M. Jangir and S. Chowdhury, 'Differential response of photosynthetic apparatus towards alkaline pH treatment in NIES-39 and PCC 7345 strains of Arthrospira platensis', pp. 219–231, 2021.

[177] C. P. Dullemond, 'Chapter 4: What makes radiative transfer hard , and how to solve it - An introduction', *Radiative transfer in astrophysics*, pp. 26–54.

[178] A. Bhowmik and L. Pilon, 'Can spherical eukaryotic microalgae cells be treated as optically homogeneous?', *Journal of the Optical Society of America A*, vol. 33, no. 8, p. 1495, 2016, doi: 10.1364/josaa.33.001495.

[179] L. López-rosales, F. García-camacho, A. Sánchez-mirón, E. M. Beato, and Y. Chisti, 'Bioresource Technology Pilot-scale bubble column photobioreactor culture of a marine dinoflagellate microalga illuminated with light emission diodes', vol. 216, pp. 845–855, 2016, doi: 10.1016/j.biortech.2016.06.027.

[180] M. A. Liebert *et al.*, 'Photochemistry and Photobiology of Light Absorption by Living Cells', vol. 24, no. 2, pp. 179–185, 2006.

[181] J. U. Grobbelaarl, L. Nedbal, and V. Tichy, 'Influence of high frequency light / dark fluctuations on photosynthetic characteristics of microalgae photoacclimated to different light intensities and implications for mass algal cultivation', pp. 335–343, 1996.

[182] D. B. Stengel, 'Chlorophyll a fluorescence responses of temperate Phaeophyceae under submersion and emersion regimes : a comparison of rapid and steady-state light curves', 2012, doi: 10.1007/s11120-012-9776-z.

[183] C. P. Dullemond, 'Chapter 6. Dust scattering off particles', *Radiative transfer in astrophysics*, vol. 0, pp. 92–98, 2013.

[184] E. D. G. Danesi, C. O. Rangel-Yagui, J. C. M. Carvalho, and S. Sato, 'Effect of reducing the light intensity on the growth and production of chlorophyll by Spirulina platensis', *Biomass Bioenergy*, vol. 26, no. 4, pp. 329–335, 2004, doi: 10.1016/S0961-9534(03)00127-2.

[185] M. E. Martínez, S. Sánchez, J. M. Jiménez, F. El Yousfi, and L. Muñoz, 'Nitrogen and phosphorus removal from urban wastewater by the microalga Scenedesmus obliquus', *Bioresour Technol*, vol. 73, no. 3, pp. 263–272, 2000, doi: 10.1016/S0960-8524(99)00121-2.

[186] A. P. Carvalho, S. O. Silva, J. M. Baptista, and F. X. Malcata, 'Light requirements in microalgal photobioreactors: An overview of biophotonic aspects', *Appl Microbiol Biotechnol*, vol. 89, no. 5, pp. 1275–1288, 2011, doi: 10.1007/s00253-010-3047-8.

[187] F. Delrue *et al.*, 'Optimization of Arthrospira platensis (Spirulina) Growth : From Laboratory Scale to Pilot Scale', doi: 10.3390/fermentation3040059.

[188] G. Perin *et al.*, 'Biotechnological Optimization of Light Use Efficiency in Nannochloropsis Cultures for Biodiesel Production', vol. 37, pp. 763–768, 2014, doi: 10.3303/CET1437128.

[189] E. Sforza, D. Simionato, G. M. Giacometti, A. Bertucco, and T. Morosinotto, 'Adjusted Light and Dark Cycles Can Optimize Photosynthetic Efficiency in Algae Growing in Photobioreactors', vol. 7, no. 6, 2012, doi: 10.1371/journal.pone.0038975.

[190] R. W. Babcock, J. Malda, and J. A. C. Radway, 'Hydrodynamics and mass transfer in a tubular airlift photobioreactor', *J Appl Phycol*, vol. 14, no. 3, pp. 169–184, 2002, doi: 10.1023/A:1019924226457.

Statement of authorship

I hereby declare that I have written the present work entitled:

OPTIMISATION OF BIOTECHNOLOGICAL PROCESSES RELATED TO THE CULTIVATION OF MICROALGAE IN PHOTOBIOREACTORS FOR OBTAINING METABOLITES OF INDUSTRIAL INTEREST

I also declare that I have written this thesis independently and have listed all used sources and aids. I am submitting this thesis for the first time as part of an examination. The electronic version of the thesis corresponds to the printed version.

Name: Manuel Vicente Ibañez.

Doctoral candidate code: 7629D1.

Date: 29.11.2022

Signature: